THE UNIVERSITY OF MANITOBA

LOW TEMPERATURE NUCLEAR MAGNETIC RESONANCE AND RELAXATION IN MANGANESE FERRITE

by

JAMES H. DAVIS

A THESIS
SUBMITTED TO THE FACULTY OF GRADUATE STUDIES
IN PARTIAL FULFILMENT OF THE REQUIREMENTS FOR THE DEGREE
OF DOCTOR OF PHILOSOPHY

DEPARTMENT OF PHYSICS

WINNIPEG, MANITOBA

February 1976

"LOW TEMPERATURE NUCLEAR MAGNETIC RESONANCE AND RELAXATION IN MAGANESE FERRITE"

by

JAMES H. DAVIS

A dissertation submitted to the Faculty of Graduate Studies of the University of Manitoba in partial fulfillment of the requirements of the degree of

DOCTOR OF PHILOSOPHY

PREFACE

The ^{55}Mn nuclear magnetic resonance of the A-site ions in manganese ferrites provides an opportunity to study many of the features characteristic of magnetic materials. The strong signal and the cubic symmetry of the A-sites make this a relatively easy system to study although the presence of two strongly overlapping signal components and the fairly complex structure of the spinel lattice result in some difficulty in the interpretation of the spectra.

Nuclear magnetic resonance in ordered magnetic materials has many distinctive features and some special problems, these are discussed in Chapter I, as an introduction, with particular reference to the properties of manganese ferrites. The strong magnetic hyperfine interaction, the spin-wave interactions, and the existence of domain-walls lead to most of the interesting properties of this system, including the Suhl-Nakamura or indirect nuclear spin-spin interaction, spin-wave relaxation processes, and the contrast in the behaviour of the two components of the signal (due to nuclei in domains and in domain walls).

Chapter II gives a detailed discussion of the Suhl-Nakamura interaction with particular reference to its role in the formation of multiple echoes following a two pulse rf excitation of the spin system.

Chapter III is a general discussion of relaxation processes in magnetic materials, including dipole-dipole and spin-wave relaxation as well as the dominant Suhl-Nakamura relaxation. The frequency dependent relaxation due to the Suhl-Nakamura interaction is compared to the experimental data for the first three echoes, followed by a discussion of the two-component nature of the spectrum in low external fields.

Chapter IV discusses and compares the temperature and field dependences of the two components of the spectrum. The technique of fitting a set of partially relaxed spectra to a function (made up of two independently relaxing components) of two independent variables, frequency and rf pulse separation, allows the effective separation of the spectrum into its domain and domain-wall components.

Finally, Chapter V gives a brief discussion and conclusion, pointing out some areas where the techniques used here may be usefully applied.

I would like to thank my supervisor Dr. C. W. Searle for his help and encouragement during the course of this work, and Dr. Akira Hirai of Kyoto University, Kyoto, Japan, who assembled much of the equipment and pointed out the existence of multiple echoes in manganese ferrite. The practical advice and assistance in many areas given by Dr. Iman Maartense has been especially helpful. Finally, I would like to thank my wife for her patience and for her help in drawing the figures.

TABLE OF CONTENTS

ABSTRACT

The A-site ^{55}Mn nuclear magnetic resonance at low temperatures consists of two overlapping signal components, one due to nuclei within the domain walls, the other due to nuclei within the bulk domains. The resonance is inhomogeneously broadened and characterized by strongly frequency dependent relaxation. Two-pulse spin-echo measurements show that the Suhl-Nakamura or indirect spin-spin interaction is responsible for most of the low temperature relaxation near resonance, and provides a mechanism for the formation of multiple echoes. By studying a series of partially relaxed spectra it is possible to separate the two signal components leading to the observation of the different temperature dependences of the frequency-independent part of the relaxation of the two components. This difference is felt to be due to the narrowing of the longitudinal dipole-dipole interaction's contribution to the homogeneous linewidth of the domain-wall component but not of the domain component. Spin-wave scattering, in particular the dipolar-induced two-magnon process, provides the strongly temperature dependent contribution to the total relaxation rate.

CHAPTER I

Introduction to NMR in Magnetic Materials

The features that distinguish the nuclear magnetic resonance in magnetic materials from that in other solids are: i) the presence, in the ordered state, of strong magnetic hyperfine fields ($\sim 10^5 - 10^6$ Oe), ii) the distribution of these hyperfine fields and the subsequent severe broadening of the resonance lines, iii) the existence of domain walls in non-saturated samples and the complicated enhancement mechanisms associated with these domain walls, iv) the possibility of the existence of two signal components--one from domain walls, the other from the bulk domains--which strongly overlap each other, and v) the interaction of the nuclear spins with unpaired electronic spins or, in the ordered state, with spin waves. These strictly magnetic effects profoundly alter the nature of the nuclear resonance and, therefore, must be carefully considered and understood before any analysis of the spectra can be attempted.

1. Manganese Ferrite

Manganese ferrite ($MnFe_2O_4$) is a magnetic insulator and has the spinel ($MgAl_2O_4$) structure with the magnetic (Mn, Fe) ions located on two crystallographically inequivalent sites, the tetrahedral A-sites and the octahedral B-sites. The ionic distribution has been studied in some detail[1-4] and can be described by the formula unit $Mn^{2+}_{0.8}Fe_{0.2}[Mn^{3+}_{0.2}Fe_{1.8}]O_4$, where the cations outside the brackets occupy the tetrahedral sites and the cations inside the brackets occupy the octahedral sites. The nuclear resonance of the ^{55}Mn nuclei on the two different sites have been reported and identified[4] as being from Mn^{2+} ions on the A-sites and Mn^{3+} ions on the B-sites. The B-site resonance will be quadrupolar split into 2I = 5 components due to the non-cubic symmetry of the octahedral sites (the octahedral symmetry does not extend beyond the O^{2-} ions forming the octahedron), while the A-site, due to its tetrahedral symmetry, has a single resonance line. The work reported here is concerned only with the ^{55}Mn resonance from ions on the A-sites.

The spinel A-site, illustrated in Figure 1, is at the center of a tetrahedron formed by four O^{2-} ions. Each of the oxygen ions is connected to three B-site cations (Mn^{3+}, Fe^{3+}) in such a way as to preserve the tetrahedral symmetry of the A-site. Because of this symmetry, the dipolar field at the A-site is expected to be zero, as is the quadrupole splitting. Some small contribution to the local field may exist due to the presence of different ions on the B-sites, however, there is no indication of this in the nuclear resonance data.

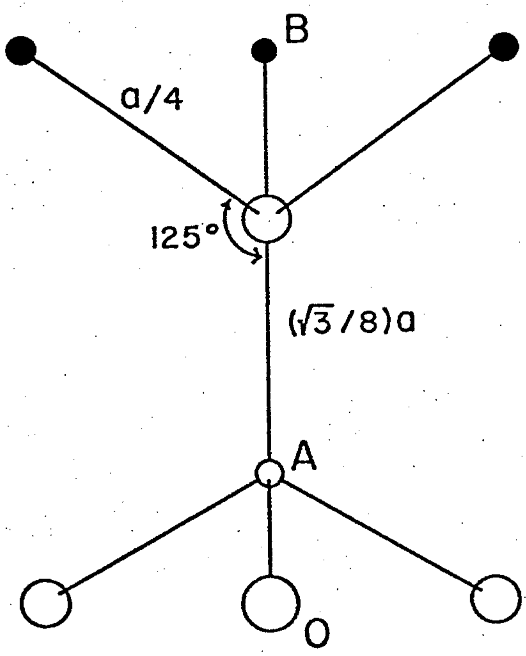

Figure 1. The spinel A-site. Large circles are oxygen ions and the dark circles are B-sites. a = 8.5 Å.

2. The Magnetic Field at the Nucleus

The magnetic field at a nucleus in a magnetic material is the sum of the externally applied field, the magnetic field due to the distribution of the magnetic dipoles surrounding the ion containing the nucleus, and the electronic hyperfine field.

2.1 The dipolar contributions--the Lorentz and demagnetizing fields

The total dipolar contribution to the microscopic magnetic field at nucleus i in a single domain sample is

$$\vec{h}_{dd} = g\mu_B \sum_j \left(\frac{1}{r_{ij}}\right)^5 \left(\vec{S}_j r_{ij}^2 - 3\vec{r}_{ij}(\vec{S}_j \cdot \vec{r}_{ij})\right) \tag{1}$$

where Σ_j is over all spins $\vec{S}_j$ located at position $\vec{r}_{ij}$ with respect to spin i, g is the electronic spectroscopic splitting factor and μ_B is the Bohr magneton. (The field due to nuclear dipoles may be neglected.) This sum may be evaluated by breaking it up into the sums over spins in two regions separated by a surface, called the Lorentz sphere, such that the volume enclosed by the sphere is large by atomic dimensions but small on a macroscopic scale. Then, the sum is evaluated explicitly for spins inside the sphere and the contribution from spins outside the sphere can be evaluated as an integral over the volume enclosed by the sample's surface and the Lorentz sphere. If we define, after Keffer[5]

$$D_V^{IJ} = D_L^{IJ} + D_{V-L}^{IJ} = \sum_\ell (3r_\ell^I r_\ell^J - r_\ell^2 \delta^{IJ}) r_\ell^{-5}$$

for cartesian components I,J of r_ℓ, where D_L^{IJ} is the sum over the interior of the Lorentz sphere, then,

$$D_{V-L}^{IJ} \to \delta^{IJ} \int_{V-L} (\partial/\partial r^I)(-r^I/r^3)\, d\vec{r} = -\delta^{IJ} \int (r^I/r^3)\hat{I}\cdot(d\vec{S}_1 - d\vec{S}_2)$$

where $\delta^{IJ} = 0$ unless I = J, and S_1 is the surface of the sample, and S_2 is the Lorentz sphere. Then, assuming an ellipsoidal sample,

$$D^{IJ}_{V-L} = (\frac{4\pi}{3} - N^I)\delta^{IJ}$$

The factor $4\pi/3$ is due to the uncompensated poles at the surface of the Lorentz sphere, while the factor N^I, called the demagnetizing factor, is due to uncompensated magnetic poles on the surface of the sample. For a spherical sample, $N^I = 4\pi/3$ and $D^{IJ}_{V-L} = 0$.

The contribution to the field from spins inside the Lorentz sphere is called the dipolar field and can be readily evaluated by direct summation over lattice sites. For sites (of the spin i) of cubic symmetry the dipolar field vanishes.

2.2 The electronic hyperfine field

By far the largest contribution to the magnetic field at the nucleus is the field produced by it's ion's own electrons--the electronic hyperfine field. The magnetic hyperfine interaction can be written as[6]

$$\mathcal{H}_{hf} = -gg_N\mu_B\mu_N \sum_i \left(\frac{8\pi}{3}\delta(r_i)\vec{S}_i\cdot\vec{I} + \frac{(\vec{L}_i - \vec{S}_i)\cdot\vec{I}}{r_i^3} + \frac{3(\vec{S}_i\cdot\vec{r}_i)(\vec{I}\cdot\vec{r}_i)}{r_i^5} \right) \quad (2)$$

where g_N is the nuclear spectroscopic splitting factor, μ_N is the nuclear magneton; $\vec{L}$, $\vec{S}$, $\vec{I}$ are the electronic orbital angular momentum, electronic spin, and nuclear spin, respectively; r_i is the distance of the ith electron from the nucleus, and the sum is over all of the ion's electrons.

The term in $\vec{L}_i$ will be neglected here since in many iron-group compounds (as in this case) the orbital angular momentum is almost completely quenched by the crystal field[6]. The last two terms involving $\vec{S}_i$ are the dipole-dipole terms and will be non-zero only for unpaired electrons. The first term, called the Fermi contact term, involves, through the delta function, the density of electrons at the nucleus. This is non-zero only for s-electrons and thus should vanish here since all s-electrons are paired. However, the presence of unpaired d-electrons causes a polarization[6] of the s-electrons through the exchange interaction and a substantial hyperfine field results. In fact, the largest contribution to the field at the nucleus is due to s-electron polarization.

The details of the polarization of the s-electrons are very complicated and include contributions from the unpaired d-electrons of neighboring ions through polarization by them of the oxygen anions which in turn polarize the original cation's s-electrons (super-transferred hyperfine interaction)[7].

The dipolar part of Equation 2 gives rise to an anisotropic hyperfine field. For Mn^{3+} ions on the B-sites considerable anisotropy is observed[4] but for Mn^{2+} ions on the A-sites, since Mn^{2+} is an S-state ion (five 3-d electrons → half-filled shell), the hyperfine field is isotropic.

Writing the interaction in Equation 2 in terms of the effective hyperfine field yields

$$\mathcal{H}_{hf} = - g_N \mu_N \vec{I}\cdot\vec{H}_s = A\vec{I}\cdot\vec{S} \tag{3}$$

where, $$A = - g_N \mu_N \vec{H}_s \cdot \vec{S}/(\vec{S}\cdot\vec{S})$$

and S is the total spin of the ion (for Mn^{2+}, $S = 5/2$). For the isotropic case A is simply a constant while in the anisotropic case A would be a second rank tensor.

Finally, in manganese ferrite, as in many other magnetic materials, the hyperfine field at an A- or B-site is anti-parallel to the sublattice magnetization at that site. The A-site hyperfine field has been found to be proportional to the sublattice magnetization at low temperatures[8], and at $T = 4.2\ ^{o}K$ has a magnitude of $H_{hf}^{A} \simeq 560$ kOe, while at the same temperature, the B-site hyperfine field is $H_{hf}^{B} \simeq 360$ kOe.

3. Magnetic Ordering

Below a temperature $T_F \simeq 600\ ^{o}K$ the unpaired spins of the magnetic ions in manganese ferrite are spontaneously ordered in such a way that all of the A-site moments are parallel to each other and anti-parallel to the B-site moments. This type of order is called ferrimagnetic and T_F is the ferrimagnetic Neel point. The A and B sites can be considered to form sublattices whose magnetizations are oppositely directed but do not have the same magnitude[9]. This results in a net moment of 4.6 μ_B per formula unit along the B-site magnetization, since there are twice as many occupied B-sites as there are A-sites. Because of this net moment many of the properties of ferromagnets are present in ferrimagnets; e.g., the existence of domains, magnetic hysteresis, etc.

3.1 The exchange interaction

The interaction responsible for the spontaneous ordering of the magnetic ions' spins is the exchange interaction, which can be described in insulators by the Heisenberg exchange Hamiltonian

$$\mathcal{H}_{ex} = -\sum_{i<j} J_{ij}\vec{S}_i\cdot\vec{S}_j \tag{4}$$

where $\vec{S}_i$ is the spin of the ith ion, and J_{ij} is the exchange constant representing the strength of the interaction between ions i and j. In these materials, as mentioned earlier in connection with the hyperfine interaction, the orbital contribution to the magnetic moment is quenched and therefore the contribution of the orbital angular momentum to the exchange interaction will be neglected. The exchange interaction is very short ranged and only very near neighbors in the sums over i and j in Equation 4 need to be considered.

As shown in Figure 1 there is an oxygen anion between an A-site ion and each of its nearest B-site neighbors. The exchange interaction must proceed via a polarization of the anion's electronic p-orbitals[10]. Such an interaction is called superexchange (analagous to the super-transferred hyperfine fields mentioned earlier) and is found to be very common in iron-group salts[11]. Superexchange allows the exchange interaction to be effective over quite large distances when compared with direct exchange[10] which would require significant overlap of the magnetic ions' d-orbitals. Even so, the strength of the superexchange is strongly dependent on distance between cations and on the angle formed by the cation-anion-cation system[11]. Table 1 gives a list of the possible exchange couplings between cations in a spinel together with the distances and angles between the cations.[12]

Table 1: Superexchange in Spinels

Interaction	Angle	Distance	Sign
A-O-B	125° 9'	$\sqrt{11}a/8$	−
A-O-B	154° 34'	$3\sqrt{3}a/8$	−
A-O-A	79° 38'	$\sqrt{3}a/4$	+
B-O-B	90°	$\sqrt{2}a/4$	+
B-O-B	125° 2'	$\sqrt{6}a/4$	+

The minus sign corresponds to antiparallel or antiferromagnetic exchange and the plus sign to parallel or ferromagnetic exchange.

The superexchange interaction is strongest for short distances and for angles closest to 180° [11], thus the A-B exchange (especially the first type shown in Table 1) is the strongest in these materials[12] and is responsible for the antiparallel alignment of the two sublattices. The other contributions (of which the 125° B-B is the largest) can be safely neglected[12] in many instances.

3.2 Molecular field theory

As postulated by Weiss[13] the exchange interaction in a ferromagnetic material can be represented by an effective magnetic field $H_{ex} = \lambda M$, where M is the sample magnetization and λ is the molecular field constant. Extending this concept to the ferrimagnetic case[9,14] one obtains an exchange field acting on A-site spins due to the B-sublattice magnetization and a similar field on the B-site spins due to the A-sublattice magnetization (neglecting intrasublattice interactions).

$$H^A_{ex} = \lambda M_B \quad , \qquad H^B_{ex} = \lambda M_A$$

where the molecular field constant λ represents the same quantity in both cases and is given by

$$\lambda = 3k_B T_F / N g^2 \mu_B^2 (S_A(S_A + 1) S_B(S_B + 1))^{\frac{1}{2}} \qquad (5)$$

where $S_A = 5/2$ is the A-site spin (both Mn^{2+} and Fe^{3+} have spin 5/2) and $S_B = 2.40$ is the average B-site spin. N is the total number of magnetic ions, k_B is the Boltzmann constant, and T_F is the ferrimagnetic ordering temperature.

Since $M_B = N_B g\mu_B S_B$ and $N_B = \frac{2}{3} N$, the exchange field acting on the A-site ions is

$$H_{ex}^A = \frac{2}{3} S_B \left(\frac{3k_BT_F}{g\mu_B(S_A(S_A+1)S_B(S_B+1))^{\frac{1}{2}}}\right) \tag{6}$$

Then, for g = 2 and $T_F = 600\ {}^oK$, the exchange field is

$$H_{ex}^A = (2zS_B/g\mu_B)J \simeq 2.6 \times 10^6 \text{ Oe}$$

where z = 12 is the number of magnetic nearest neighbors of the A-site ion and J is the A-B exchange constant as used in Equation 4.

4. Spin Waves

The Hamiltonian of a ferromagnet including only an isotropic exchange interaction and the electronic Zeeman interaction with an external field H_o is

$$\mathcal{H} = -\sum_{(i,j)} J_{ij}\vec{S}_i\cdot\vec{S}_j - g\mu_BH_o\sum_i S_i^z \tag{7}$$

where $\Sigma_{(i,j)}$ is the sum over all "distinct" pairs of spins. The ground state of a ferromagnet, denoted by $|\uparrow\rangle$, is the state with all spins aligned parallel. Introducing the spin raising and lowering operators $S^{\pm} = S^x \pm iS^y$ the Hamiltonian can be written as

$$\mathcal{H} = -\sum_{(i,j)} J_{ij}(S_i^zS_j^z + \tfrac{1}{2}S_i^+S_j^- + \tfrac{1}{2}S_i^-S_j^+) - g\mu_BH_o\sum_i S_i^z$$

Then, the ground state energy is given by

$$\mathcal{H}|\uparrow\rangle = -N(g\mu_BH_oS + \tfrac{1}{2}S^2\sum_j J_{ij})|\uparrow\rangle \tag{8}$$

since $S_i^z|\uparrow\rangle = S$, $S_i^+|\uparrow\rangle = 0$. The factor of 1/2 preceding Σ_j is to insure that the contribution from each pair of spins is counted only once.

Then, taking the commutator of $\mathcal{H}$ and the spin lowering operator S_i^- and applying it to $|\uparrow\rangle$ yields

$$\begin{aligned}\left[\mathcal{H}, S_i^-\right]|\uparrow\rangle &= \left(g\mu_B H_o S_i^- + \sum_j J_{ij}(S_i^- S_j^z - S_i^z S_j^-)\right)|\uparrow\rangle \\ &= \left(g\mu_B H_o S_i^- + S\sum_j J_{ij}(S_i^- - S_j^-)\right)|\uparrow\rangle\end{aligned} \tag{9}$$

This forms a new state which is a linear combination of states where a spin i has been flipped, $(S_i^-|\uparrow\rangle)$. Then, replacing S_i^- by its Fourier transform $\Sigma_i \exp(i\vec{k}\cdot\vec{r}_i)S_i^-$,

$$\begin{aligned}&\left[\mathcal{H}, \sum_i \exp(i\vec{k}\cdot\vec{r}_i)S_i^-\right]|\uparrow\rangle \\ &= \left(g\mu_B H_o + S\sum_j J_{ij}(1 - \exp(i\vec{k}\cdot(\vec{r}_i - \vec{r}_j)))\right)\sum_i \exp(i\vec{k}\cdot\vec{r}_i)S_i^-|\uparrow\rangle\end{aligned} \tag{10}$$

it can be seen that the states

$$|k\rangle = \frac{1}{\sqrt{2SN}} \sum_i \exp(i\vec{k}\cdot\vec{r}_i)S_i^-|\uparrow\rangle \tag{11}$$

are the normalized eigenstates of the Hamiltonian $\mathcal{H}$ with eigenvalues given by

$$E_k = E_o + g\mu_B H_o + S\sum_i J_{ij}\{1 - \exp(i\vec{k}\cdot(\vec{r}_i - \vec{r}_j))\} \tag{12}$$

where E_o is the ground state energy. These new states $|k\rangle$ are called Bloch spin-wave states[15,16] and the excitations of wavevector $\vec{k}$ are called spin waves.

The minimum energy required to excite a spin wave $(E - E_o = g\mu_B H_o)$ is much lower than that required to flip a single spin since, for a spin-wave excitation, neighboring spins are still very nearly parallel (on the average) and their exchange energy is only slightly increased.

The interaction of the ^{55}Mn nuclear moments with these spin waves via the hyperfine ($A\vec{I}\cdot\vec{S}$) interaction and the effective nuclear spin-spin interaction--the Suhl-Nakamura interaction--which is a result of the virtual excitation, by the hyperfine interaction, of electronic spin waves as intermediate states, require a detailed understanding of these excitations.

4.1 Holstein-Primakoff diagonalization

The eigenstates of the Hamiltonian are expanded in terms of the eigenstates $|n_\ell>$ of the spin-deviation operator η_ℓ defined by

$$\eta_\ell|n_\ell> = (S - S_\ell^z)|n_\ell> = n_\ell|n_\ell>$$

In this notation, the ferromagnetic ground state is $|0>$, the state of zero spin deviation. Then the raising and lowering operators acting on these states give[17]

$$\begin{aligned} S_\ell^+|n_\ell> &= \{(S - S_\ell^z)(S + S_\ell^z + 1)\}^{\frac{1}{2}}\,|n_\ell - 1> \\ S_\ell^-|n_\ell> &= \{(S + S_\ell^z)(S - S_\ell^z + 1)\}^{\frac{1}{2}}\,|n_\ell + 1> \end{aligned} \qquad (13)$$

The spin-deviation operator η_ℓ is actually the boson occupation number operator defined by

$$\eta_\ell = a_\ell^+ a_\ell \quad , \text{ with } \quad \left[a_\ell, a_m^+\right] = \delta_{\ell,m} \quad , \text{ all others zero}$$

where the a_ℓ^+ and a_ℓ are the spin-deviation creation and annihilation operators. Then, since

$$a_\ell^+|n_\ell> = (n_\ell + 1)^{\frac{1}{2}}\,|n_\ell + 1>$$

and, (14)

$$a_\ell |n_\ell\rangle = (n_\ell)^{\frac{1}{2}} |n_\ell - 1\rangle$$

we may express the spin operators in the Hamiltonian in terms of these operators as

$$\begin{aligned} S_\ell^+ &= (2S)^{\frac{1}{2}}(1 - a_\ell^+ a_\ell/2S)^{\frac{1}{2}}\, a_\ell \\ S_\ell^- &= (2S)^{\frac{1}{2}} a_\ell\, (1 - a_\ell^+ a_\ell/2S)^{\frac{1}{2}} \qquad (15) \\ S_\ell^z &= S - a_\ell^+ a_\ell \end{aligned}$$

Expanding these expressions for S_ℓ^+ , S_ℓ^- in powers of (1/S) yields

$$S_\ell^+ = (2S)^{\frac{1}{2}} \left(1 - \frac{a_\ell^+ a_\ell}{4S} - \frac{a_\ell^+ a_\ell a_\ell^+ a_\ell}{32S^2} - \cdot\cdot\right) a_\ell$$

$$S_\ell^- = (2S)^{\frac{1}{2}}\ a_\ell^+ \left(1 - \frac{a_\ell^+ a_\ell}{4S} - \frac{a_\ell^+ a_\ell a_\ell^+ a_\ell}{32S^2} - \cdot\cdot\right)$$

where for many applications only the terms linear in the spin-deviation operators need to be retained[5,18,19]. When spin wave scattering becomes important, as in the derivation of spin-wave relaxation processes, higher order terms may be necessary.

For a two sublattice system, with the B-sublattice aligned along the positive z-axis (the direction of H_o), the spin operators are given by[20]

$$\begin{aligned} S_{B_j}^+ &= (2S_B)^{\frac{1}{2}} (1 - b_j^+ b_j/2S_B)^{\frac{1}{2}}\, b_j \qquad \text{,(plus complex conjugates)} \\ S_{A_i}^+ &= (2S_A)^{\frac{1}{2}}\, a_i^+ (1 - a_i^+ a_i/2S_A)^{\frac{1}{2}} \qquad (16) \\ S_{B_j}^z &= S_B - b_j^+ b_j \quad , \quad S_{A_i}^z = -S_A + a_i^+ a_i \end{aligned}$$

where S_A and S_B are the A- and B-site spin and the operators a_i^+ , b_j^+ create a spin-deviation on their respective sublattices.

The next step in diagonalizing the Hamiltonian is to Fourier transform the spin-deviation operators, which become

$$a_i = (N_A)^{-\frac{1}{2}} \sum_k \exp(i\vec{k}\cdot\vec{r}_i)a_k$$

$$b_j = (N_B)^{-\frac{1}{2}} \sum_k \exp(-i\vec{k}\cdot\vec{r}_j)b_k$$

4.2 The diagonalized Hamiltonian

The Hamiltonian we wish to consider is

$$\begin{aligned}\mathcal{H} &= \mathcal{H}_A^z + \mathcal{H}_B^z + \mathcal{H}_{A-B}^{ex} + \mathcal{H}^{dd} \\ &= -g\mu_B H \sum_i^A S_{A_i}^z - g\mu_B H \sum_j^B S_{B_j}^z + \frac{1}{2} J \sum_{i,j}^{nn} \vec{S}_i\cdot\vec{S}_j \\ &\quad + \frac{1}{2} \sum_{i,j} \frac{g^2\mu_B^2}{R_{ij}^5} \left(R_{ij}^2\{\vec{S}_i\cdot\vec{S}_j - 3(\vec{R}_{ij}\cdot\vec{S}_i)(\vec{R}_{ij}\cdot\vec{S}_j)\}\right)\end{aligned} \qquad (17)$$

This Hamiltonian consists of Zeeman, exchange, and dipole-dipole terms. The sum Σ_i^A is over all spins on the A-sublattice, Σ_j^B is over all spins on the B-sublattice, $\Sigma_{i,j}^{nn}$ is over all pairs (i,j) of nearest neighbor spins, and $\Sigma_{i,j}$ is over all spins ($i \neq j$). When the spin has a subscript it refers to a particular sublattice and when no subscript is present, S can refer to either sublattice. Thus, for example,

$$\frac{1}{2} J \sum_{i,j}^{nn} \vec{S}_i\cdot\vec{S}_j = \frac{1}{2} J\left(\sum_i^A \sum_{i+\delta}^B \vec{S}_{A_i}\cdot\vec{S}_{B_{i+\delta}} + \sum_j^B \sum_{j+\delta}^A \vec{S}_{B_j}\cdot\vec{S}_{A_{j+\delta}}\right)$$

where $\vec{\delta}$ is the vector joining nearest neighbors. Similarly, the dipole-

dipole part of the Hamiltonian can be written as

$$\frac{1}{2}\sum_{i\neq j}\mathcal{H}^{dd}_{i,j}(\vec{S}_i,\vec{S}_j) = \frac{1}{2}\left(\sum_{i\neq\ell}^{A}\mathcal{H}^{dd}_{i,\ell}(\vec{S}_{A_i},\vec{S}_{A_\ell}) + \sum_{i}^{A}\sum_{j}^{B}\mathcal{H}^{dd}_{i,j}(\vec{S}_{A_i},\vec{S}_{B_j}) + \sum_{j}^{B}\sum_{\ell}^{A}\mathcal{H}^{dd}_{j,\ell}(\vec{S}_{B_j},\vec{S}_{A_\ell}) + \sum_{j\neq m}^{B}\mathcal{H}^{dd}_{j,m}(\vec{S}_{B_j},\vec{S}_{B_m})\right)$$

The factor of $\frac{1}{2}$ on both sides of these equations is to insure that the interaction between any two spins is included only once.

By breaking up the Hamiltonian in this manner we can more easily carry out the steps in diagonalization of the total Hamiltonian. The dipole-dipole Hamiltonian can be written in terms of spin operators S^+, S^-, and S^z as

$$\mathcal{H}_{dd} = \frac{1}{2}\sum_{i\neq j}\Big[A^{(z,z)}_{i,j}S^z_iS^z_j + A^{(+,-)}_{i,j}(S^+_iS^-_j + S^-_iS^+_j) - A^{(z,+)}_{i,j}(S^z_iS^+_j + S^+_iS^z_j) - A^{(z,-)}_{i,j}(S^z_iS^-_j + S^-_iS^z_j) - A^{(+,+)}_{i,j}S^+_iS^+_j - A^{(-,-)}_{i,j}S^-_iS^-_j\Big] \tag{18}$$

where,

$$A^{(z,z)}_{i,j} = \frac{g^2\mu_B^2}{R^5_{ij}}\left(R^2_{ij} - 3(R^z_{ij})^2\right)$$

$$A^{(+,-)}_{i,j} = \frac{1}{2}\,\frac{g^2\mu_B^2}{R^5_{ij}}\left(R^2_{ij} - \frac{3}{2}R^+_{ij}R^-_{ij}\right) \tag{19}$$

$$A^{(z,\pm)}_{i,j} = \frac{3}{2}\,\frac{g^2\mu_B^2}{R^5_{ij}}\,R^z_{ij}R^{\mp}_{ij}$$

$$A_{i,j}^{(\pm,\pm)} = \frac{3}{4}\,\frac{g^2\mu_B^2}{R_{ij}^5}\,(R_{ij}^{\mp})^2$$

Each of the four parts (A-A, A-B, B-A, B-B) of the dipole-dipole Hamiltonian will be written in this fashion, where the sums involved will be over a particular sublattice.

Applying the Holstein-Primakoff transformation to the Zeeman and exchange terms leads, to second order in magnon operators, to

$$\mathcal{H}'^{(2)} = \sum_k (\mu_{AA}^o a_k^+ a_k + \mu_{AB}^o a_k^+ b_k^+ + \mu_{BA}^o a_k b_k + \mu_{BB}^o b_k^+ b_k) + \text{const.} \qquad (20)$$

where,

$$\begin{aligned}
\mu_{AA}^o &= -g\mu_B H + \hat{z}JS_B(N_B/N_A)^{\frac{1}{2}} \\
\mu_{AB}^o &= \frac{1}{2}J(S_AS_B)^{\frac{1}{2}}\{Z_B(N_B/N_A)^{\frac{1}{2}}\gamma_{-k}^B + Z_A(N_A/N_B)^{\frac{1}{2}}\gamma_{-k}^A\} \\
\mu_{BA}^o &= \frac{1}{2}J(S_AS_B)^{\frac{1}{2}}\{Z_B(N_B/N_A)^{\frac{1}{2}}\gamma_k^B + Z_A(N_A/N_B)^{\frac{1}{2}}\gamma_k^A\} \\
\mu_{BB}^o &= g\mu_B H + \hat{z}JS_A(N_A/N_B)^{\frac{1}{2}}
\end{aligned} \qquad (21)$$

with, $\hat{z} = \frac{1}{2}\{(N_B/N_A)^{\frac{1}{2}} Z_B + (N_A/N_B)^{\frac{1}{2}} Z_A\}$

and $\gamma_k^{A,B} = Z_{A,B}^{-1}\sum_{\delta}^{A,B} \exp(i\vec{k}\cdot\vec{\delta})$

where $\vec{\delta}$ is the vector joining nearest neighbors and N_A, N_B, Z_A, Z_B are the numbers of A-, B-site ions and the number of A-, B-site nearest neighbors.

The dipole-dipole Hamiltonian can be transformed in the same fashion to obtain the total Hamiltonian to second-order in magnon operators

$$\mathcal{H}^{(2)} = \sum_k (\mu_{AA} a_k^+ a_k + \mu_{AB} a_k^+ b_k^+ + \mu_{BA} a_k b_k + \mu_{BB} b_k^+ b_k) \qquad (23)$$

In this equation we have neglected terms such as $a_k a_{-k}$, $a_k^+ b_{-k}$, $b_k^+ b_{-k}$, etc., which arise from terms in S^+S^+, S^-S^- and are expected to be small compared to the remaining terms[5,20]. The coefficients in this Hamiltonian are

$$\mu_{AA} = \mu^{o}_{AA} + \mu^{dd}_{AA}\,, \qquad \mu_{AB} = \mu^{o}_{AB} + \mu^{dd}_{AB}\,, \qquad \text{etc., and}$$

$$\begin{aligned}
\mu^{dd}_{AA} &= S_A\{(C^{(+,-)}_{AA}(-\vec{k}) + C^{(+,-)}_{AA}(\vec{k})) - C^{(z,z)}_{AA}(0)\} \\
&\quad + (S_AS_B)^{\frac{1}{2}}\,(N_B/N_A)^{\frac{1}{2}}\,\{(N_A/N_B)^{\frac{1}{2}}\,C^{(z,z)}_{AB}(0) + (N_B/N_A)^{\frac{1}{2}}\,C^{(z,z)}_{BA}(0)\} \\
\mu^{dd}_{AB} &= (S_AS_B)^{\frac{1}{2}}\,\{(N_A/N_B)^{\frac{1}{2}}\,C^{(+,-)}_{AB}(-\vec{k}) + (N_B/N_A)^{\frac{1}{2}}\,C^{(+,-)}_{BA}(\vec{k})\} \\
\mu^{dd}_{BA} &= (S_AS_B)^{\frac{1}{2}}\,\{(N_A/N_B)^{\frac{1}{2}}\,C^{(+,-)}_{AB}(\vec{k}) + (N_B/N_A)^{\frac{1}{2}}\,C^{(+,-)}_{BA}(-\vec{k})\} \\
\mu^{dd}_{BB} &= S_B\{(C^{(+,-)}_{BB}(\vec{k}) + C^{(+,-)}_{BB}(-\vec{k})) - C^{(z,z)}_{BB}(0)\} \\
&\quad + (S_AS_B)^{\frac{1}{2}}(N_A/N_B)^{\frac{1}{2}}\,\{(N_A/N_B)^{\frac{1}{2}}\,C^{(z,z)}_{AB}(0) + (N_B/N_A)^{\frac{1}{2}}\,C^{(z,z)}_{BA}(0)\}
\end{aligned} \tag{24}$$

Here we have defined the expressions $C^{(\mu,\nu)}_{XY}$ by

$$C^{(\mu,\nu)}_{XY}(\vec{k}) = \sum_{\delta_X}^{Y} A^{(\mu,\nu)}_{\delta_X}\,\exp(i\vec{k}\cdot\vec{\delta}_X) \tag{25}$$

where the sum $\sum^{Y}_{\delta_X}$ is over all vectors $\vec{\delta}_X$ originating on a site on the X-sublattice (X = A or B) and terminating on the Y-sublattice, and the $A^{(\mu,\nu)}_{\delta}$ are as defined in Equation 19 with $\vec{\delta} = R_{ij}$.

The Hamiltonian in Equation 23 is still not diagonal since it contains terms coupling the operators a_k and b_k. To bring the Hamiltonian into normal-mode form, the transformation to normal-mode operators α_k, β_k is made.

$$b_k = u_k\alpha_k - v_k\beta_k^+ \qquad (26)$$

$$a_k = -v_k\alpha_k^+ + u_k\beta_k$$

$$[\alpha_k, \alpha_k^+] = [\beta_k, \beta_k^+] = 1, \text{ all others zero.}$$

The transformation coefficients u_k, v_k are chosen to bring the Hamiltonian into diagonal decoupled form. The Hamiltonian then takes the form

$$\mathcal{H}^{(2)} = \sum_k (\hbar\omega_\alpha\, \alpha_k^+\alpha_k + \hbar\omega_\beta\, \beta_k^+\beta_k) \qquad (27)$$

which is the desired result.

4.3 The ferrimagnon dispersion relation

The normal-mode energies in Equation 27 are given by

$$\hbar\omega_\alpha = \mu_{BB}u_k^2 - (\mu_{AB} + \mu_{BA})u_kv_k + \mu_{AA}v_k^2$$

$$\hbar\omega_\beta = \mu_{BB}v_k^2 - (\mu_{AB} + \mu_{BA})v_ku_k + \mu_{AA}u_k^2 \qquad (28)$$

$$= \hbar\omega_\alpha - (\mu_{BB} - \mu_{AA})$$

The transformation coefficients are determined from the equations of motion of the magnon operators α_k , β_k , a_k , b_k, i.e.,

$$i\frac{d\alpha_k}{dt} = [\alpha_k, \mathcal{H}_k] = \omega_\alpha\alpha_k \qquad (29)$$

and since, from Equation 26, $u_k^2 - v_k^2 = 1$, we obtain the equation

$$\begin{pmatrix} \mu_{BB} - \omega & -\mu_{BA} \\ \mu_{AB} & -\mu_{AA} - \omega \end{pmatrix} \begin{pmatrix} u_k \\ v_k \end{pmatrix} = 0 \qquad (30)$$

and the coefficients may be defined by the relations

$$u_k = \{1 - (v_k/u_k)^2\}^{-\frac{1}{2}} \quad , \quad v_k = (v_k/u_k)\{1 - (v_k/u_k)^2\}^{-\frac{1}{2}}$$

To obtain the dispersion relation (Equation 29) in terms of recognizable quantities we must substitute for the μ's from Equations 21 and 24. First we consider the ratio of the transformation coefficients.

$$(v_k/u_k) = \frac{\mu_{BB} - \omega}{\mu_{BA}} \simeq \frac{\hat{z}(N_A/N_B)^{\frac{1}{2}}\,(S_A/S_B)^{\frac{1}{2}}}{\frac{1}{2}\,\{Z_B(N_B/N_A)^{\frac{1}{2}}\,\gamma_k^B + Z_A(N_A/N_B)^{\frac{1}{2}}\,\gamma_k^A\}} = \eta(S_A/S_B)^{\frac{1}{2}}$$

This equation is used to define a parameter η which, since it depends on N_A , N_B , Z_A , Z_B , describes the nonequivalence of the two sublattices. For small k, $\eta \simeq (N_A/N_B)^{\frac{1}{2}}$. Then, we find that

$$u_k^2 = \frac{S_B}{S_B - \eta^2 S_A} \quad , \quad u_k v_k = \frac{\eta(S_A S_B)^{\frac{1}{2}}}{S_B - \eta^2 S_A} \quad , \quad v_k^2 = \frac{\eta^2 S_A}{S_B - \eta^2 S_A} \tag{31}$$

To put the α-mode dispersion relation in a more understandable form we rewrite it as

$$\hbar\omega_\alpha = -\mu_{AA} + (\mu_{AA} + \mu_{BB})u_k^2 - (\mu_{AB} + \mu_{BA})u_k v_k$$

Now, from Equations 21 and 24,

$$\begin{aligned}\hbar\omega_\alpha^o &= -\mu_{AA}^o + (\mu_{AA}^o + \mu_{BB}^o)u_k^2 - (\mu_{AB}^o + \mu_{BA}^o)u_k v_k \\ &= g\mu_B H + Z'JS_{eff}\,\{\eta^2(N_B/N_A) - 1\}\end{aligned} \tag{32}$$

with $Z' = (N_B/N_A)^{\frac{1}{2}}\,\hat{z}$, $S_{eff} = \frac{N_A}{N_B}\left(\frac{S_A S_B}{S_A - \eta^2 S_B}\right)$

For small k, $\eta^2 \simeq (N_A/N_B)(1 + \frac{1}{3}a_{nn}^2 k^2)$, for a cubic lattice, where a_{nn} is the nearest neighbor distance. In this approximation the dispersion relation assumes the familiar ferromagnetic form given by

$$\hbar\omega_\alpha^o = g\mu_B H + \frac{1}{3} Z' J S_{eff} a_{nn}^2 k^2$$

with, for a spinel, $Z' = Z_A = 12$ and $a_{nn} = (\sqrt{11}/8)a$, where a is the lattice constant ($a \simeq 8.5$ Å).

The dipole-dipole terms can be treated analagously yielding

$$\hbar\omega_\alpha^d = \frac{N_A}{N_B} S_{eff}\Big(\{(S_B/S_A)K_{BB}^{(+,-)}(\vec{k}) - \eta(K_{BA}^{(+,-)}(\vec{k}) + K_{AB}^{(+,-)}(\vec{k})) + \eta^2(S_A/S_B)K_{AA}^{(+,-)}(\vec{k})\} - \frac{1}{2}\{(S_B/S_A)K_{BB}^{(z,z)}(0) - \eta(K_{BA}^{(z,z)}(0) + K_{AB}^{(z,z)}(0)) + \eta^2(S_A/S_B)K_{AA}^{(z,z)}(0)\}\Big) \quad ,(33)$$

where

$$K_{XY}^{(\mu,\nu)}(\vec{k}) = (N_X/N_Y)^{\frac{1}{2}} C_{XY}^{(\mu,\nu)}(\vec{k}) + (N_Y/N_X)^{\frac{1}{2}} C_{YX}^{(\mu,\nu)}(-\vec{k})$$

These dipole-wave sums can be directly evaluated for k = 0, and can be approximately evaluated for $k \neq 0$, assuming $kR > 10$, where R is the sample radius[5]. For example,

$$C_{XY}^{(z,z)}(0) = g^2\mu_B^2 \sum_{\delta_X}^{Y} \{R_{\delta_X}^2 - 3(R_{\delta_X}^z)^2\}/R_{\delta_X}^5$$

$$= - g^2\mu_B^2 \bar{N}_Y D^{(z,z)}(0) \quad , \quad \bar{N}_Y = N_Y/N_u$$

where $\bar{N}_Y$ is the number of Y-sublattice ions per unit cell and N_u is the number of unit cells, and

$$D^{(I,J)}(\vec{k}) = \bar{N}^{-1} \sum_{\ell}{}' (3r_\ell^I r_\ell^J - r_\ell^2\delta^{IJ}) r_\ell^{-5} \exp(i\vec{k}\cdot\vec{r}_\ell)$$

are the dipole-wave sums discussed by Keffer[5]. For k = 0, these sums give the Lorentz and demagnetizing fields

$$D^{IJ}(0) = L^{IJ} - N^I\delta^{IJ}$$

where $$L^{IJ} = \frac{4\pi}{3}\delta^{IJ} + \{D^{IJ}(0)\}_L$$

is the Lorentz factor with $\{D^{IJ}(0)\}_L$ the sum over all points on the interior of the Lorentz sphere. N^I is the demagnetizing factor along the Ith direction.

For $\vec{k} \neq 0$, $kR > 10$, the sum may be approximated by an integral[5] which for $\vec{k}$ not too large gives, with I, J = x,y,z

$$D^{IJ}(\vec{k}) \simeq L^{IJ} - 4\pi k^I k^J/k^2$$

An example of this is

$$K_{AA}^{(+,-)}(\vec{k}) = \frac{1}{4} g^2\mu_B^2 \sum_{\delta_A}^{A} \{2R_{\delta_A}^2 - 3R_{\delta_A}^{+} R_{\delta_A}^{-}\}/R_{\delta_A}^5 \tag{34}$$

$$\times \{\exp(i\vec{k}\cdot\vec{R}_{\delta_A}) + \exp(-i\vec{k}\cdot\vec{R}_{\delta_A})\}$$

$$= -\frac{1}{2} g^2\mu_B^2 \bar{N}_A\{L^{XX} + L^{YY} - 4\pi\sin^2\theta_{\vec{k}}\}$$

where $\theta_{\vec{k}}$ is the angle $\vec{k}$ makes with the z-axis.

Using these expressions we obtain the dipole-dipole part of the dispersion relation

$$\hbar\omega_\alpha^d = \frac{1}{2} g\mu_B\,(4\pi M^{\prime})\,\sin^2\theta_{\vec{k}} - g\mu_B\,N^z\,M^{\prime} \tag{35}$$

with

$$M^{\prime} = g(N_B/N_A)\{(S_B N_B - S_A N_A)^2/S_A N_A S_B N_B\}\mu_B S_{eff}\bar{N}_A \tag{36}$$

as the effective magnetization per unit volume.

Finally, then, the ferrimagnetic dispersion relation can be written as

$$\hbar\omega_\alpha = g\mu_B(H - N^z M^{\prime}) + Z^{\prime}JS_{eff}\{\eta^2(N_B/N_A) - 1\} + \frac{1}{2} g\mu_B(4\pi M^{\prime})\sin^2\theta_{\vec{k}} \quad , \tag{37}$$

The β-mode dispersion relation can be written down by inspection, ignoring dipole-dipole effects, giving

$$\begin{aligned}\hbar\omega_\beta^o &= \hbar\omega_\alpha^o - (\mu_{BB}^o - \mu_{AA}^o)\\ &= Z'J(S_B - (N_A/N_B)S_A) - g\mu_B H + Z'JS_{eff}\{\eta^2(N_B/N_A) - 1\}\end{aligned}$$

The first term, proportional to J, provides a large energy gap between the α- and β-modes. Thus, at low temperatures there will not be any appreciable number of β-mode magnons.

4.4 Higher order terms

There are two terms arising from higher order in the expansion of the total Hamiltonian in spin-wave operators which are of considerable importance in spin-wave relaxation processes at low temperatures. These higher order terms give rise to the second-order dipolar-induced two-magnon and the exchange-enhanced three-magnon processes.

4.4.a Three-magnon dipolar Hamiltonian

The first of these, the dipolar-induced process, arises from the $S^z S^\pm$ terms of the dipolar Hamiltonian of Equation 18. When expanded in terms of the spin-deviation operators a_k, b_k these terms give a three-magnon contribution to the Hamiltonian

$$\begin{aligned}\mathcal{H}_{dd}^{(3)} = -\sum_{k_1,k_2,k_3} \delta(\vec{k}_1 - \vec{k}_2 - \vec{k}_3) \Big[&(S_A/2N_A)^{\frac{1}{2}} \{\tfrac{1}{2} C_{AA}^{(z,-)}(0)\\ &+ K_{AA}^{(z,-)}(\vec{k}_2) - \tfrac{1}{2}(S_B/S_A)(N_B/N_A)^{\frac{1}{2}} K_{AB}^{(z,-)}(0)\} a_{k_1}^+ a_{k_2} a_{k_3}\\ &+ (2S_B/N_A)^{\frac{1}{2}} K_{AB}^{(z,-)}(-\vec{k}_3) a_{k_1}^+ a_{k_2} b_{k_3}^+ \quad - \end{aligned} \quad ,(38)$$

$$- (2S_A/N_B)^{\frac{1}{2}} K_{AB}^{(z,-)}(\vec{k}_3) b_{k_1} b^{+}_{k_2} a_{k_3} - (S_B/2N_B)^{\frac{1}{2}} \{\tfrac{1}{2} C_{BB}^{(z,-)}(0)$$

$$+ K_{BB}^{(z,-)}(\vec{k}_2) - \tfrac{1}{2} (S_A/S_B)(N_A/N_B)^{\frac{1}{2}} K_{AB}^{(z,-)}(0)\} b^{+}_{k_1} b^{+}_{k_2} b_{k_3} \Big)$$

$$+ \text{(complex conjugate)}$$

4.4.b Four-magnon exchange Hamiltonian

The second of these processes, the exchange-enhanced three-magnon process, results from the expansion of the exchange Hamiltonian to fourth order in spin-deviation operators. Then, to order (1/S),

$$\mathcal{H}^{(4)}_{ex} = -\frac{1}{8} J \sum_{\substack{k_1,k_2\\k_3,k_4}} \delta(\vec{k}_1 + \vec{k}_2 - \vec{k}_3 - \vec{k}_4)$$

$$\times \Big\{ 4(Z_A/N_B)\gamma^{A}_{-3-4}\, a^{+}_{k_1} a_{-k_2} b^{+}_{k_3} b_{-k_4} + 4(Z_B/N_A)\gamma^{B}_{-3-4}\, b^{+}_{k_1} b_{-k_2} a^{+}_{k_3} a_{-k_4}$$

$$+ Z_A(S_B/S_A N_A N_B)^{\frac{1}{2}} \gamma^{A}_{-4} (a^{+}_{k_1} a_{-k_2} a_{k_3} b_{-k_4} + a^{+}_{k_1} a^{+}_{k_2} a_{k_3} b^{+}_{k_4}) \qquad ,(39)$$

$$+ Z_B(S_A/S_B N_A N_B)^{\frac{1}{2}} (\gamma^{B}_{-2+3+4} a_{k_1} b^{+}_{k_2} b_{k_3} b_{k_4} + \gamma^{B}_{2-3-4} a^{+}_{k_1} b^{+}_{-k_2} b^{+}_{k_3} b_{-k_4})$$

$$+ Z_A(S_A N_A/S_B N_B^3)^{\frac{1}{2}} (\gamma^{A}_{1+2-3} b^{+}_{-k_1} b_{k_2} b_{-k_3} a_{k_4} + \gamma^{A}_{-1-2+3} b^{+}_{k_1} b^{+}_{k_2} b_{k_3} a^{+}_{k_4})$$

$$+ Z_B(S_B N_B/S_A N_A^3)^{\frac{1}{2}} (\gamma^{B}_{1}\, b_{k_1} a^{+}_{k_2} a_{k_3} a_{k_4} + \gamma^{B}_{1}\, b^{+}_{-k_1} a^{+}_{k_2} a^{+}_{-k_3} a_{k_4}) \Big\}$$

In addition, some four-magnon terms will arise from the six-magnon terms on commutating all creation operators to the left (since, $aa^{+} = a^{+}a + 1$). These terms are $\sim (1/S)^2$ however, and will be neglected here[19].

A more detailed discussion of these terms will be made in Chapter 3 in connection with the spin-lattice relaxation via spin-wave scattering.

5. Magnetocrystalline Anisotropy

The preceding discussion has introduced the concept of an anisotropy field due to dipolar interactions. The magnetic anisotropy describes the preference of the sample magnetization for a certain set of crystallographic directions (e.g., the [111] directions of $MnFe_2O_4$), and its reluctance to lie along other directions. This can be effectively described by an anisotropy energy which for cubic symmetry has the form[21]

$$F_K = K_1(\alpha_1^2\alpha_2^2 + \alpha_2^2\alpha_3^2 + \alpha_3^2\alpha_1^2) + K_2\alpha_1^2\alpha_2^2\alpha_3^2 + \cdots \tag{40}$$

where the α_i are the direction cosines locating the magnetization $\vec{M}_s$ with respect to the principal cubic axes. The energy of a magnetization $\vec{M}_s$ in a field $\vec{H}_K$ is $(\theta << \pi)$

$$E_K = -\vec{M}_s \cdot \vec{H}_K \simeq \frac{1}{2} M_s H_K \theta^2 \qquad (+\text{ constant}) \tag{41}$$

where θ is the angle between $\vec{M}_s$ and $\vec{H}_K$. In spherical polar coordinates the expression in Equation 40 becomes, approximately, $(\theta << \pi)$

$$\begin{aligned} F_K \simeq\ & K_1\{\theta^4 \sin^2\phi \cos^2\phi + (1 - \tfrac{1}{2}\theta^2)^2\,\theta^2\} \\ & + K_2\{\theta^4 \cos^2\phi \sin^2\phi (1 - \tfrac{1}{2}\theta^2)^2\} \simeq K_1\theta^2 \end{aligned} \tag{42}$$

Comparing these last two equations, where θ is the same angle in both, we find,

$$H_K \simeq 2K_1/M_s$$

Thus the effective anisotropy field H_K can be used to describe the crystalline anisotropy (from Eqn. 41 H_K is seen to be an effective field directed along the magnetically preferred direction).

Table 2 lists the preferred directions for the possible ranges of K_1 and K_2 in cubic crystals as well as values of F_K and H_K along these directions (from Smit and Wijn [12]).

Table 2: Magnetocrystalline anisotropy in cubic crystals

Direction	100	110	111
F_K	0	$\frac{1}{4}K_1$	$\frac{1}{3}K_1 + \frac{1}{27}K_2$
Preferred direction if	$K_1 \begin{cases} > 0 \\ > -\frac{1}{9}K_2 \end{cases}$	$0 > K_1 > -\frac{4}{9}K_2$	$K_1 \begin{cases} < -\frac{4}{9}K_2 \\ < -\frac{1}{9}K_2 \end{cases}$
H_K	$2K_1/M_s$	$\begin{cases} (100)\text{:} & -2K_1/M_s \\ (110)\text{:} & (K_1+K_2)/M_s \end{cases}$	$-(\frac{4}{3}K_1 + \frac{4}{9}K_2)/M_s$

From ferromagnetic resonance measurements[22] at T = 4.2 °K on a single crystal of $MnFe_2O_4$ the anisotropy constants were determined to be $K_1 \simeq -2.02 \times 10^5$ ergs/cc and $K_2 \simeq 0.34 \times 10^5$ ergs/cc , in good agreement with values reported elsewhere[23]. This corresponds to an effective anisotropy field

$$H_K = -\frac{2}{3}\left(\frac{2K_1}{M_s} + \frac{2}{3}\frac{K_2}{M_s}\right) \simeq 520 \text{ Oe.} \tag{44}$$

where $M_s = 560$ emu/cc is the saturation magnetization at T = 0 °K.

While the dipolar field as given in Equation 1 vanishes classically for sites of cubic symmetry, it has been shown[24,25] that the dipole-dipole interaction contributes to the anisotropy. In particular the off-diagonal terms in the dipole-dipole Hamiltonian of Equation 18 give a small contribution to the cubic anisotropy[25]. The main contribution to the magnetic anisotropy, however, in manganese ferrites appears to be from the interaction of the cations' ground state electron distribution with the crystal field, including the effects of the spin-orbit coupling, as discussed by Yosida and Tachiki[25]. In particular, the octahedral site Fe^{3+} and Mn^{3+} ions (especially for Mn-rich compositions) provide the largest contributions to the anisotropy[26].

The anisotropy constants K_1 and K_2 may exhibit very strong temperature dependences for some compositions and, at very low temperatures K_2 may become comparable to K_1[23].

6. Domain Walls

In the absence of an external magnetic field a ferromagnetic (or ferrimagnetic) material can exist in an unmagnetized state (i.e., no net magnetization). This is accomplished by the division of the sample volume into small magnetically saturated regions called domains whose moments are randomly distributed among the various preferred axes. The existence of domains was postulated by Weiss[13] in 1907 and has become an accepted and fundamental part of the physics of magnetic materials[27].

The domains are formed to minimize the total free energy of the system, consisting essentially of magnetostatic energy, due to uncompensated magnetic poles at the sample surface, and exchange energy. The individual domains are separated by narrow regions called domain walls in which the direction of the spin, as a function of position in the wall, rotates smoothly between the easy directions of the domains on either side of the wall. The width of these walls is determined by competition between exchange, anisotropy, and magnetostriction energies[27]. For the simple case of a 180° wall, neglecting magnetostriction, the exchange and anisotropy energies can be written as

$$\sigma_{ex} \approx k_B T_F / a' \delta_w \qquad \text{and} \qquad \sigma_K \approx \frac{1}{2} K \delta_w$$

where a' is the distance between nearest magnetic neighbors, K is the anisotropy constant, and δ_w is the domain wall width. Then,

$$\delta_w \approx (2 k_B T_F / a' K)^{\frac{1}{2}} \tag{45}$$

For manganese ferrite with $T_F = 600\ ^{\circ}K$, $K = 2 \times 10^5$ erg/cc , $a' \approx 3 \times 10^{-8}$ cm , this gives

$$\delta_w \approx 530\ \mathring{A} \approx 180 \times a'$$

When an external magnetic field is applied to the multidomain sample, those domains whose magnetizations lie most nearly parallel to the field will increase in size at the expense of those whose moments lie more antiparallel to the field. The domain walls then will move under the influence of the field until the increase in the sample magnetization is sufficient to set up a demagnetizing field $H_D = - N M$ large enough to cancel the effects of the applied field H_o. Thus, for external fields smaller than that required to effectively saturate the sample (remove all domain walls), the net internal magnetic field is $H_o - H_D = 0$ (except, as noted earlier, for microscopic fields such as the Lorentz and dipolar fields as well as the electronic hyperfine field, which are always present). Above the field H_s required for saturation the net internal field is $H_o - H_s$. The demagnetizing field determined by the demagnetization factor N is due to uncompensated surface poles, as discussed in Section 2.1. A magnetically saturated sample in an external field $H_o > H_s$ is equivalent to a single-domain sample in an external field $H_o - H_s$.

6.1 Equation of motion of a domain-wall

If we consider the example of a spherical sample of volume V which is divided into two domains by a single 180^o wall, we see from the preceeding discussion that if a magnetic field H_x is applied parallel to the wall, it responds by moving a distance z perpendicular to the wall such that the change in the net magnetization is $\Delta M = 2M_s Az/V$, where A is the wall area. The equation of motion of the wall is[28,29]

$$\mu(d^2z/dt^2) \;+\; \beta(dz/dt) \;+\; \alpha z \;=\; 2M_sH_x \;-\; \delta U \qquad (46)$$

where μ, the effective mass per unit area, β, the wall damping constant, and α, the stiffness constant, are given by[29]

$$\mu \;=\; 1/8\pi\gamma_e^2\delta_w \;, \qquad \alpha \;=\; 4M_s^2/\chi_o\ell \;, \qquad \beta \;=\; 2(\Delta H_{fmr})M_s/\delta_w(\gamma_e H_{res}) \;,(47)$$

Here, γ_e is the electronic gyromagnetic ratio , χ_o is the initial susceptibility, (ΔH_{fmr}) is the ferromagnetic resonance linewidth, $(\gamma_e H_{res})$ is the ferromagnetic resonance frequency, and ℓ is the wall length.

The expression on the right-hand side of Equation 46 is the pressure exerted on the wall; the first term is due to the applied field H_x and the second to the hyperfine interaction.

Neglecting the term in δU, the solution to Equation 46 is

$$z \;=\; 2M_sH_x\left[\frac{(\alpha - \mu\omega^2) - i\beta\omega}{(\alpha - \mu\omega^2)^2 + \beta^2\omega^2}\right]$$

The rf field acting on the nucleus is

$$H_1 \simeq H_N \frac{d\theta}{dz'} z \simeq H_N\left(\frac{\sin\theta}{\delta}\right) z \qquad \text{, for a } 180^o \text{ wall.}$$

Thus, there is an enhancement of the applied field H_x by a factor

$$\eta_1 = \left|\frac{H_1}{H_x}\right| = \frac{2H_N M_s \sin\theta}{\mu\delta\{(\omega_w^2 - \omega_N^2)^2 + (\beta/\mu)^2\omega_N^2\}^{\frac{1}{2}}} \tag{48}$$

where $\omega_w = (\alpha/\mu)^{\frac{1}{2}}$ is the domain-wall resonance frequency and ω_N is the nuclear resonance frequency.

In pulsed spin-echo experiments, after the rf field has been removed there will be a component of nuclear magnetization in the plane perpendicular to the nuclear hyperfine field (and therefore the electronic magnetization). In this case the second term on the right in Equation 46 becomes important. The energy density can be written as[28]

$$U = -(H_N/M) \int (\vec{M}\cdot\vec{m})\, dz'$$

where M is the sublattice electronic magnetization and m is the nuclear magnetization. Then there will be an effective pressure on the domain wall given by

$$-\frac{dU}{dz} = \left(\frac{H_N}{M}\right) \int \frac{d}{dz'} (\vec{M}\cdot\vec{m})\, dz' = \left(\frac{H_N}{M}\right) \int \frac{d\theta}{dz'} (\vec{M} \times \hat{z})\cdot\vec{m}\, dz'$$

$$\delta U = H_N \int \left(\frac{d\theta}{dz'}\right) m_\perp(z') dz' \tag{49}$$

where $\hat{z}$ is a unit vector in the z-direction. The solution to Equation 46 is now

$$z = H_N\langle m_\perp\rangle \frac{(\alpha - \mu\omega^2) - i\beta\omega}{(\alpha - \mu\omega^2)^2 + \beta^2\omega^2}$$

with $$\langle m_\perp\rangle = \frac{1}{\delta}\int m_\perp(z')\sin\theta\, dz' .$$

The oscillatory part of the total magnetization is

$$M' = 2M_s Az/V$$

and there is an enhancement of the nuclear magnetization by the factor

$$\eta_2 = \frac{M'}{\langle m_\perp \rangle} = 2H_N M_s \left(\frac{A\delta}{V}\right) \frac{1}{\mu\delta\{(\omega_w^2 - \omega_N^2)^2 + (\beta/\mu)^2\omega_N^2\}^{\frac{1}{2}}} \qquad (50)$$

Thus, when observing the nuclear resonance of nuclei within domain walls the signal will be doubly enhanced, once on application of the rf pulse, and again when the nuclear magnetization refocuses in the plane perpendicular to the hyperfine field.

For manganese ferrite, with $\chi_o \simeq .1$ emu/cm^{3}Oe , $M_s \simeq 560$ emu/cm^3 , $\ell \simeq .1$ cm , the constants in Equation 46 are

$$\alpha = 2.5 \times 10^7 \ \text{gm/cm}^2\text{sec}^2$$
$$\beta = 0.4 \ \text{gm/cm}^2\text{sec}$$
$$\mu = 2.6 \times 10^{-11} \ \text{gm/cm}^2$$

then,
$$\nu_w = \frac{\omega_w}{2\pi} \simeq 50 \text{ MHz}$$

Using values of $2\Delta H_{fmr} = 150$ Oe and $H_{res} = 2.3$ kOe,

$$\eta_1 \simeq 2 \times 10^5 \quad , \quad \eta_2 = \left(\frac{A\delta}{V}\right)\eta_1 \qquad (51)$$

The ratio ($A\delta/V$) is simply the ratio of domain wall volume to sample volume.

7. The Coupled Equations of Motion of the Magnetic Sublattices

To obtain the nuclear resonance condition for ^{55}Mn ions on the A-sites we solve the coupled sublattice equations of motion[30]

$$
\begin{aligned}
(d\vec{M}_A/dt) &= \gamma_e\{\vec{M}_A \times (\vec{H} - \lambda\vec{M}_B + \vec{H}_A - \alpha\vec{m})\} \\
(d\vec{M}_B/dt) &= \gamma_e\{\vec{M}_B \times (\vec{H} - \lambda\vec{M}_A + \vec{H}_B)\} \qquad (52) \\
(d\vec{m}/dt) &= \gamma_N\{\vec{m} \times (\vec{H} - \alpha\vec{M}_A)\}
\end{aligned}
$$

where $\vec{M}_{A,B}$ are the A,B sublattice electronic magnetizations, λ is the molecular field constant describing the A-B exchange interaction, γ_e and γ_N are the electronic and nuclear gyromagnetic ratios, $\alpha = |H_N/M_A^o|$, $\vec{H}_{A,B}$ are the A,B sublattice effective anisotropy fields, and $\vec{H}$ is the effective applied field (including demagnetizing effects). $\vec{m}$ is the A-sublattice nuclear magnetization. The effect of the B-site nuclei on the A-site resonance condition will be very small and can be neglected.

Transforming the M's and m to M^+, M^-, and m^+, m^-, these equations become

$$
\begin{aligned}
(\omega/\gamma_e)M_A^+ - (H - \lambda M_B^o - H_A - \alpha m^o)M_A^+ - \lambda M_B^o M_A^+ - \alpha m^+ M_A^o &= 0 \\
(\omega/\gamma_e)M_B^+ - (H + \lambda M_A^o + H_B)M_B^+ + \lambda M_B^o M_A^+ &= 0 \qquad (53) \\
(\omega/\gamma_N)m^+ - (H + \alpha M_A^o)m^+ + \alpha m^o M_A^+ &= 0
\end{aligned}
$$

assuming $M(t) = M^o e^{-i\omega t}$. The solution for low frequencies (neglecting terms like ω/γ_e) is

$$\omega_N = \gamma_N(H_o - H_D) + \gamma_N H_N \{1 - \eta'(m^o/M_A^o)\} \qquad (54)$$

where

$$\eta' = H_N/\{(H_o - H_D)(\beta - 1) + (\beta H_B + H_A) + \alpha m^o\} \qquad (55)$$

($\beta = M_B/M_A$). Here H has been replaced by $H_o - H_D$, the difference between the applied field and the demagnetizing field.

7.1 Single domain enhancement

The factor η' in Equations 54 and 55 is a result of the coupling of the electronic and nuclear magnetizations and is, in fact, the enhancement factor for nuclei not in domain walls. In general the rf field felt by the nucleus will be, with H_x applied perpendicular to H_N,

$$H_1 = H_x(H_N/H_{K'})$$

where $H_{K'}$ acts as an effective anisotropy field acting to prevent the "rocking" of H_N by the applied field H_x. For $H_{K'} = H_K = \beta H_B + H_A \simeq 1$ kOe, $H_o - H_D = 0$, $\beta = 1.9$, with (at $T \simeq 1.5\ ^oK$) $m^o \simeq 1$ Oe, $H_N = 560$ kOe,

$$\eta' \simeq 560$$

This enhancement occurs both as a response to an external rf field and as a response to an internally generated field, i.e., to the refocused nuclear magnetization.

7.2 Frequency pulling

Since the net nuclear magnetization varies with temperature as

$$m^o \simeq N(\gamma_N \hbar I)\left(\frac{I+1}{3}\right)\left(\frac{\gamma_N \hbar H_N}{kT}\right)$$

while M_A^o is nearly constant (for $T \lesssim 4.2\ ^oK$) the resonance frequency ω_N will be pulled to lower values as the temperature is lowered. This effect, known as frequency pulling[31], is very strong in some materials due to the low anisotropy. In manganese ferrites the effect is small but still visible[8,30]. Another effect of frequency pulling is illustrated in Figure 2-a where the resonance frequency for ^{55}Mn in a single crystal sample of $Ni_{.03}Mn_{.62}Fe_{2.36}O_4$ is plotted versus external field at $T = 1.5\ ^oK$.

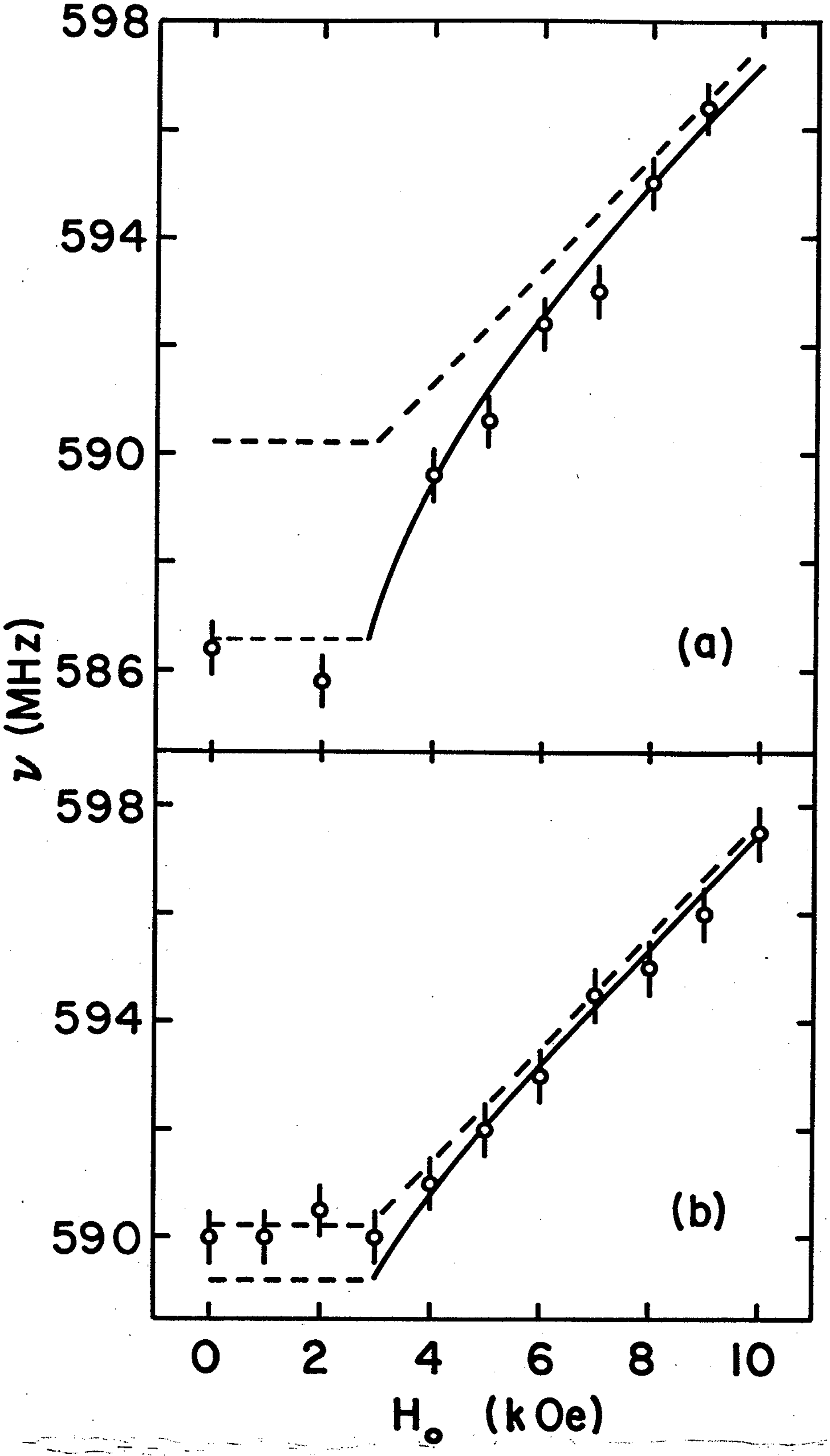

Figure 2. Frequency pulling, a) $T = 1.5\ ^{o}K$, b) $T = 4.2\ ^{o}K$.

The dashed line has a slope of $\gamma_{Mn} = 1.055 \times 10^{3}$ (sec Oe)$^{-1}$ and an $H_o - H_D = 0$ value of $\gamma_{Mn} \times 559.5$ kOe. The solid curve is the resonance frequency calculated from Equations 54 and 55 using $H_K = 0.7$ kOe. Figure 2.b is for the spectrum at 4.2 ^oK. The solid curve in this case is the calculated resonance frequency using the same hyperfine field as in part (a) of the figure but with $H_K = 1.0$ kOe.

When the enhancement factor η' is very large, an external rf field can become so strong that it destroys the resonance condition[31]. This is especially true in pulsed NMR where the rf fields are already very strong, and it may be impossible to observe the resonance unless an external static field large enough to significantly weaken the enhancement factor is applied.

8. Free Precession of Nuclear Moments

The free precession[32] techniques in magnetic resonance, since they involve the response of the magnetic system to a number of rf pulses, allow the observation of the precessing magnetization (about the static magnetic field) in the absence of continuous external driving fields, and, therefore, are ideally suited for the study of relaxation effects and the interactions which cause them.

8.1 Free induction decay and spin echoes

In the vector model of pulsed resonance[32,33], viewed in a reference frame rotating at the Larmor precessional frequency ω_L, an rf field of frequency $\omega_o = \omega_L$ and strength H_1^x applied perpendicular to the static magnetic field H^z (and the net equilibrium nuclear magnetization), will exert a torque on the nuclear magnetization ($\vec{H}_1 \times \vec{m}$) and will rotate it in the plane perpendicular to H_1^x . If the rf field is left on for a time δt such that $\gamma_N H_1^x \delta t = \pi/2$, the nuclear magnetization will lie along the y-direction when the pulse is removed. In the laboratory frame this will produce a rotating field in the plane perpendicular to the static field. This rotating field can be detected by a coil or cavity and gives the familiar free induction decay (fid). If the individual nuclear spins have slightly different Larmor frequencies ($\omega_i - \omega_L << \omega_L$) this free induction signal will decrease in intensity due to the gradual loss of phase coherence in the total spin system.

If at a time τ later a second rf pulse is applied along the same direction in the rotating frame the components of the individual nuclear moments perpendicular to H_2^x will again experience a torque and will be rotated out of the plane. If this second pulse has a length δt such that $\gamma_N H_2^x \delta t = \pi$, these components will have been effectively reflected through the x-axis. Then, due to the spread in Larmor frequencies, the individual moments will regain their phase coherence temporarily at a time τ following the application of the second pulse. This results in a net moment along the -y direction in the rotating frame, which can again be detected as a rotating field in the laboratory frame. This is the two-pulse spin-echo experiment described by Hahn[32] ($\pi/2 - \pi/2$ sequence) and by Carr-Purcell[33] ($\pi/2 - \pi$ sequence) , and has been the primary tool in this study of the nuclear magnetic resonance in manganese ferrites.

8.2 Relaxation processes--longitudinal and transverse

Due to interactions between nuclear spins and between the spins and their surroundings the free precession signals (fid and spin echo) do not

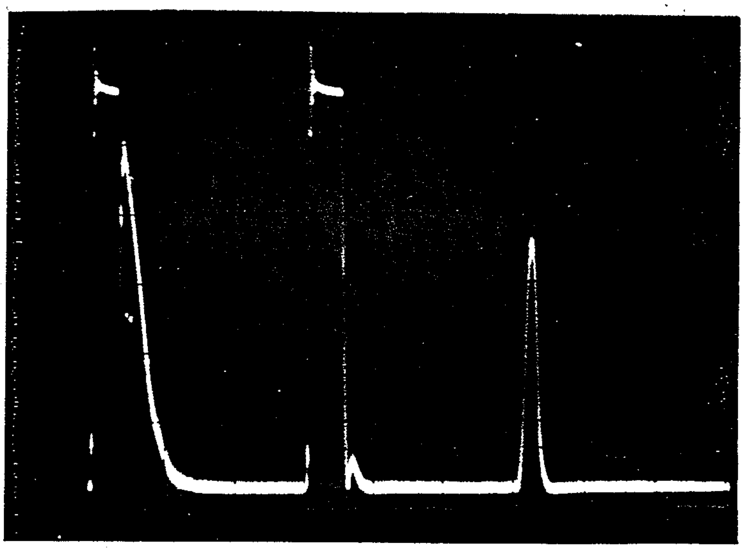

Figure 3. Free induction decay and spin echo in $MnFe_2O_4$. T = 4.2 °K.

persist indefinitely. There are two basic types of relaxation possible: the longitudinal processes which bring the magnetization out of the x-y plane and back along the z-axis, and transverse processes which involve the destruction of phase coherence of the moments rotating in the x-y plane. The longitudinal and transverse relaxation rates are usually described in terms of characteristic relaxation times T_1 and T_2 respectively.

If the time between the two rf pulses is varied the spin-echo amplitude will vary due to relaxation processes, as shown in Figure 4-a. The data for this figure were taken at 1.45 °K in an external field of H_o = 8.0 kOe. The clearly exponential behaviour of the spin-echo decay implies that the relaxation can be well described by a single relaxation time. This relaxation time can, however, represent the sum of several relaxation processes--of both longitudinal and transverse type. The spin-echo amplitude for this simple two-pulse experiment can be written as

$$A(2\tau) = A(\tau = 0)\exp(-2\tau/T) \qquad (56)$$

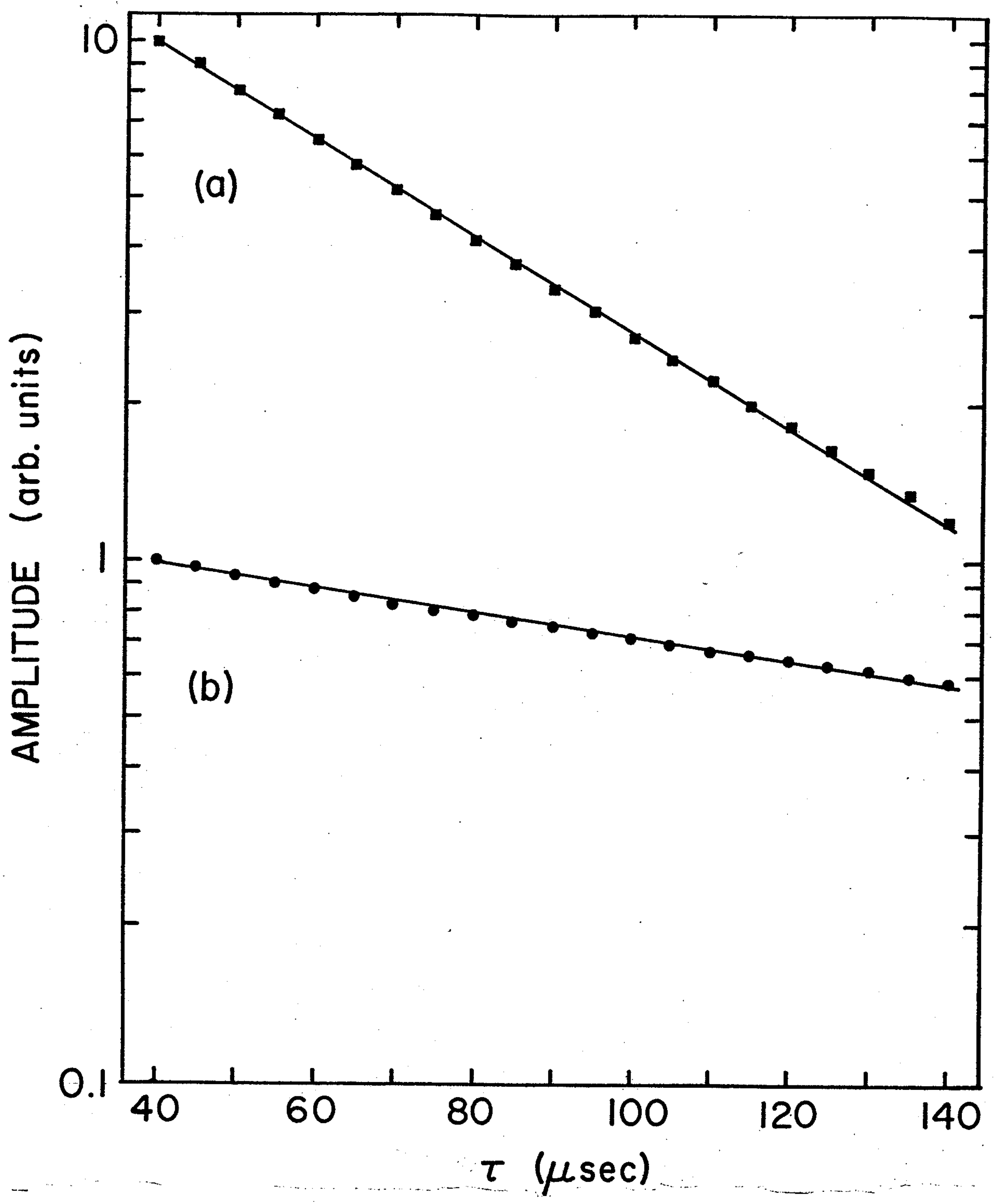

Figure 4. Spin echo decay envelopes at T = 1.45 °K in H_o = 8 kOe; a) two-pulse echo, b) three-pulse stimulated echo.

where T includes effects from all different relaxation processes.

To separate T_1 processes from T_2 processes various techniques have been devised[32,33,34] using larger numbers of pulses. A simple technique to determine T_1 independent of T_2 , consists in applying a third rf pulse (length corresponding to a rotation of $\frac{\pi}{2}$) at a time τ_2 after the second pulse. Under these conditions several spin-echoes appear, as shown in Figure 5. The echo occurring at a time $t = \tau_1 + \tau_2$ is of particular interest since it's amplitude as a function of τ_1 and τ_2 is given (in the absence of diffusion effects) by

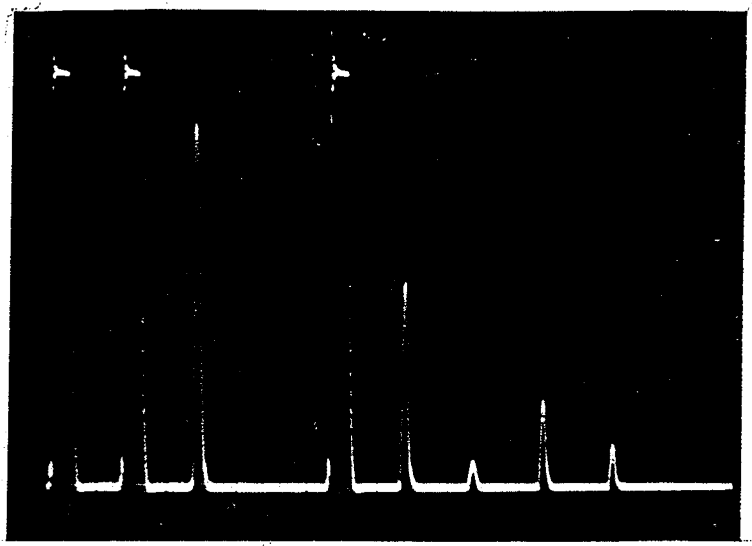

Figure 5. Response to three rf pulses showing stimulated echo and secondary echoes.

$$A'(\tau_1 + \tau_2) = A_o' \exp\{-\tau_1(\frac{1}{T_1} + \frac{2}{T_2})\} \times \exp(-\tau_2/T_1) \qquad ,(57)$$

Then, if τ_1 is held constant while τ_2 is varied the plot of echo amplitude versus τ_2 gives the longitudinal relaxation time T_1 , as illustrated in Figure 4-b. The transverse relaxation rate can be obtained from $(1/T_2) = (1/T) - (1/T_1)$.

9. Inhomogeneous Broadening--Instrumental Considerations

In a case where spin diffusion (whether actual particle diffusion or spectral diffusion) and relaxation effects can be neglected during the rf pulses and during the fid or spin-echo, if the resonance line is narrower than the bandwidth of the rf pulse the free induction and spin-echo can be viewed as the Fourier transform of the resonance line[35]. In ordered magnetic materials, however, the resonance is strongly broadened by sample inhomogeneities and is usually much broader than the rf pulse bandwidth. Thus, the echo and fid will reflect the frequency spectrum of the pulse rather than that of the actual nuclear resonance spectrum. To obtain information about the entire spectrum then we must sample it as a function of frequency in a step by step fashion. Figure 6 shows a spectrum obtained in this manner. The pulse bandwidth is $\sim 1/\delta t \simeq 0.5$ MHz, while the resonance line's half-width at half-maximum is $\delta \simeq 3$ MHz.

Such strong inhomogeneous broadening creates some special instrumental problems. First, the pulse spectrometer must be a variable frequency type (sometimes over a very broad range) and one must insure that the rf pulse amplitude and receiver sensitivity remain constant over the entire spectrum. Second, because of the large hyperfine fields and subsequent high resonant frequencies, the rf wavelengths are of the order of meters and uhf techniques should be used. Third, since the enhancement factor for nuclei in domain walls is a function of the nucleus' position in the wall, the tuning conditions (for a $\pi/2$ or π pulse) will change with the positions in the wall being sampled at a given frequency.

In the case of ^{55}Mn resonance at the A-sites in $MnFe_2O_4$ these problems are not so severe as they are in other cases (e.g., ^{55}Mn resonance

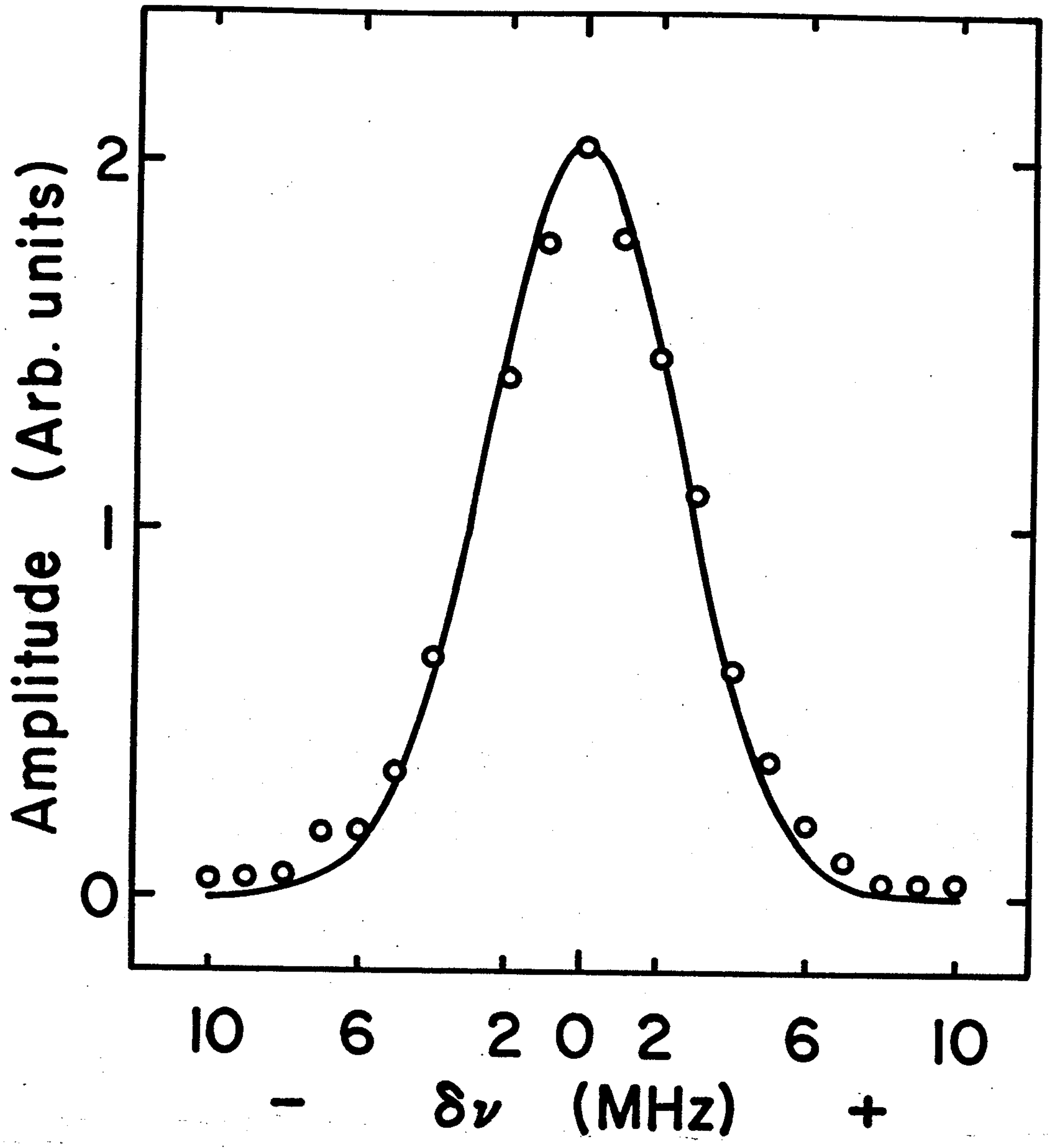

Figure 6. Spectrum extrapolated to $\tau = 0.0$ at T = 1.5 °K in H_o = 3.0 kOe for a single crystal of $Ni_{0.03}Mn_{0.62}Fe_{2.36}O_4$.

for nuclei at the B-sites), since the linewidth is ∿ 3 MHz while the resonance frequency is ≈ 600 MHz ($f/\Delta f \approx 200$). RF pulse power output is assumed constant over this range while receiver sensitivity is easily calibrated using an rf pulse of known amplitude (obtained from an rf signal generator). To minimize cable reflections, and since maximum power transfer was not a consideration, the rf cables were made long (> 10 meters) to approximate an infinite transmission line. For more critical applications, variable stub stretchers should be utilized.

The enhancement mechanisms discussed earlier depend both on the amount of nuclear magnetization at the particular frequency being sampled and on the applied magnetic field. Thus, the condition for optimum pulse widths will be a function of frequency and field. For each new frequency and field the pulse width must be readjusted. This should help to cancel any frequency variation of pulse amplitude since, in the vector model, a change in H_1^x may be compensated for by a change in pulse width.

Because of the strong enhancement of the applied rf field it is never clear that the pulses form a true ($\pi/2$, π) pair. Very large turning angles are possible[36] for strong pulses, particularly for nuclei within domain walls. The very large enhancement factors for nuclei in domain walls (compared to the enhancement for nuclei in domains) introduces a severe experimental difficulty since it is impossible to satisfy the ($\pi/2$, π) condition for both nuclei within domain walls and domains simultaneously. Thus, as the proportion of domain wall nuclei contributing to the signal changes with frequency, coupled with the changing enhancement factor, the tuning conditions (pulse widths) sometimes change drastically introducing considerable experimental uncertainty. At higher values of external field the situation is considerably simplified since then the domain walls have been almost entirely removed and the sample is a single domain. At low fields, however, several experimental runs were necessary before reproducible results were obtained, and it was found that the situation was much improved at low rf pulse powers. For this reason, and to insure a well-shaped pulse from the pulsed oscillator, a rather low pulse amplitude was used throughout, being only large enough to allow good signal to noise ratio throughout the frequency, field, and temperature ranges of interest. Even so, it is expected that a large part of the difficulty in the interpretation of the spectra at low fields is due to this problem (see the discussion in Chapter IV).

Two types of resonant cavities were used in these experiments, one which was inserted into the cryostat and allowed the sample to be rotated about an axis perpendicular to the external field, and the other which was outside the dewar. Both are coaxial cavities whose resonant frequencies

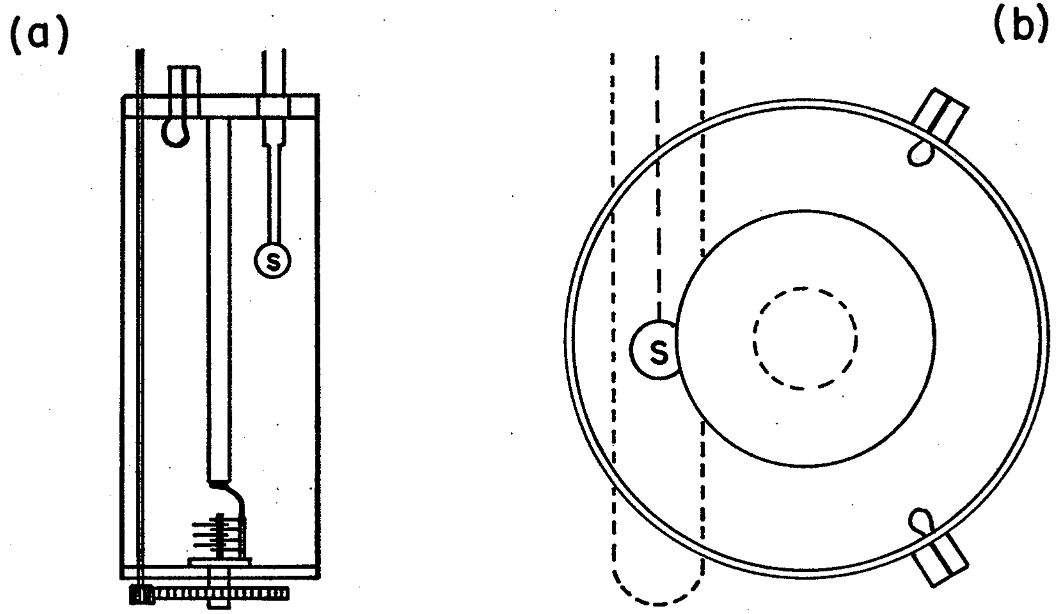

Figure 7. The cavities used in the pulsed NMR experiments. a) side view of cavity placed inside cryostat, b) front view of external cavity showing cryostat tip inserted. S is sample.

are varied by adjusting a capacitance at one end. The in-dewar cavity is illustrated in Figure 7-a where the capacitor at the bottom is a 15 pf trimmer. The external cavity, illustrated in Figure 7-b, uses a brass disc fastened to the top of the central post, and the cavity front, which screws into the cavity on very fine threads, to form the variable capacitance. This latter configuration was very successful because there is no rf current flowing across the points where the cavity front makes contact with the body of the cavity. The tip of the dewar containing the sample was inserted into the cavity as shown in the figure.

In both of these cavities the rf magnetic field is in a mode cylindrically symmetric with respect to the axis of the cavity. The rf pulse is applied to a single loop of wire as shown in the figure, and the signal is detected by a similar loop on the opposite side of the cavity.

Figure 8 is a block diagram of the system for measuring the spectra when the echo decay envelope is nearly exponential (used for spectra taken on the $Ni_{.03}Mn_{.62}Fe_{2.36}O_4$ sample). The exponential generator uses an

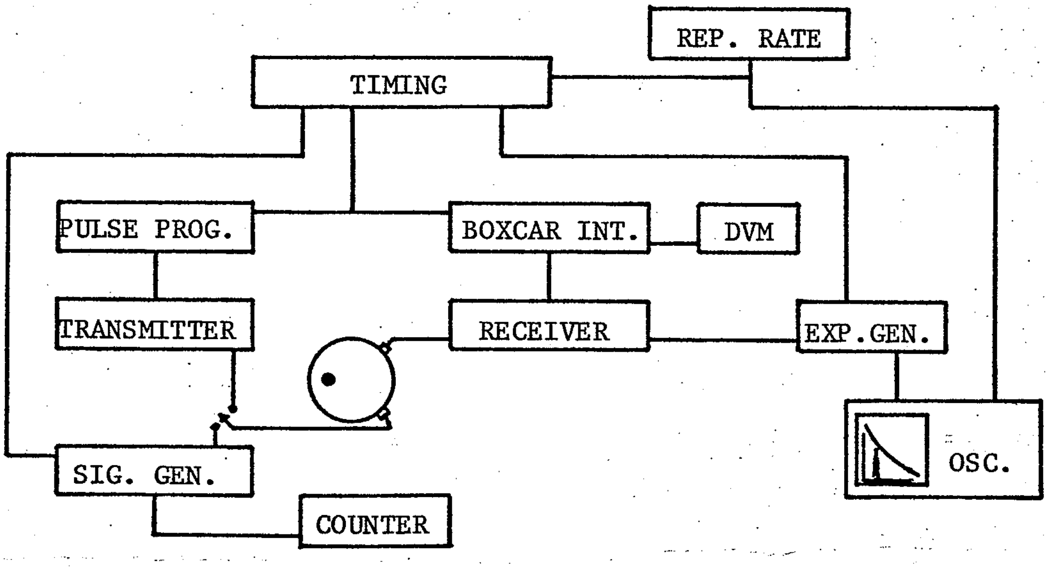

Figure 8. Block diagram of spectrometer system for comparing echo decay envelope to an exponential of known time constant.

R-C circuit to generate an exponential of known time constant to which the echo amplitude is compared while varying the time between rf pulses. The receiver is calibrated using the pulse modulated rf signal generator whose output is applied at the transmitter side of the cavity. The signal generator's output voltage is selected and fixed throughout the experiment so that its output pulse will not saturate the receiver even at those parts of the spectrum where the receiver gain is the highest (i.e., far from resonance). The gate of the boxcar integrator is placed at the position ($t \simeq 2\tau$) of the echo maximum and has a width ($\simeq$ 20 nanoseconds) which is much less than the width of the echo. The signal generator output pulse is timed to occur at the same position as the echo so that the boxcar integrator and the digital voltmeter can be used to measure the receiver gain as well as the echo amplitude, depending on the position of the switch to the cavity. By measuring the decay time, echo amplitude, and receiver gain as a function of frequency the resonance spectrum is obtained. The spectrum shown in Figure 6 was obtained in this manner.

As discussed earlier, for low values of external field, domain walls exist in sufficient quantity that the echo will consist of two components with different amplitudes and relaxation times. In this case the echo decay envelope will not appear exponential. For this condition the system described by the block diagram in Figure 9 was used. Here the triggers for the two rf pulses as well as the box-car's gate positioning pulse are derived from a square wave whose frequency is varied by applying a ramp voltage to the VCG input of the square wave generator. In this way the separation between pulses can be continuously varied over a range of > 100 μsec, and the boxcar gate position automatically tracks the echo position (at 2τ). The area of the square wave is proportional to the

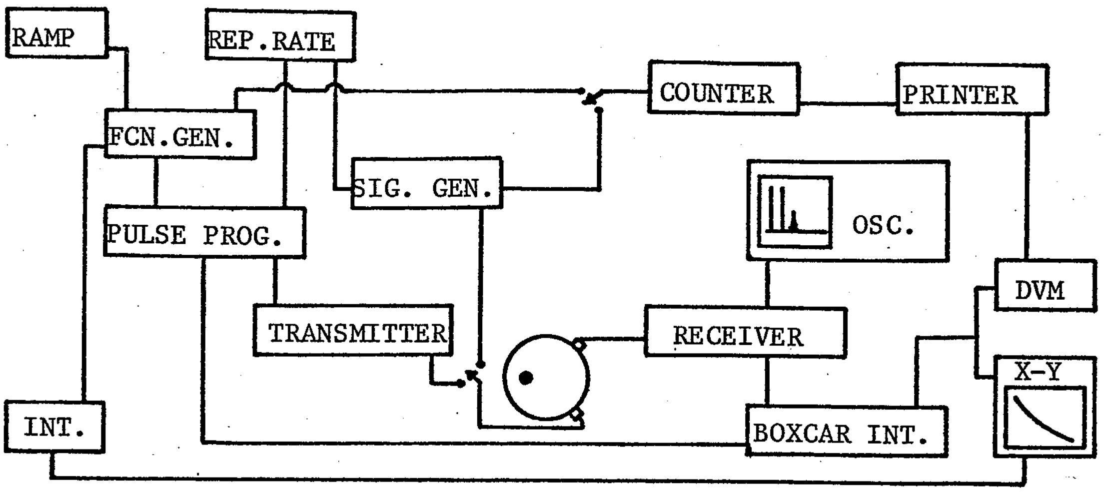

Figure 9. Block diagram of spectrometer system used in the case of non-exponential decay.

period of the square wave, thus, the output of the square-wave integrator is applied in analog form to the x-axis of an x-y recorder and in digital form to the digital printer. The boxcar output is similarly applied to the output units and a continuous record of echo amplitude versus time between pulses is obtained. This, together with receiver gain, is sufficient to obtain the complete spectrum when repeated over the entire frequency range. The spectra taken on the $MnFe_2O_4$ single crystal sphere were done in this way.

CHAPTER II

The Suhl-Nakamura Interaction and the Formation of Multiple Echoes

When there is a high density of nuclear spins in a material, whether liquid[37], solid[38], metal[39], or magnetically ordered[40,41], there exists an effective nuclear spin-spin interaction which may be of either pseudo-dipolar or pseudo-exchange form[38,42]. This interaction proceeds through a partial polarization of the electronic states by the electron-nucleus interaction, and its form may be obtained through a second-order perturbation treatment of the electronic energy levels with the electron-nucleus interaction as the perturbing Hamiltonian. In liquids the interaction is restricted to a single molecule while in insulating solids near neighbors may interact. In metals the perturbation sets up a localized spin-density wave which extends over many atomic distances ($\mathcal{H}_{eff} \sim \cos(2k_F R)/R^3$), and in magnetic materials, due to the strong exchange and hyperfine interactions, the effective spin-spin interaction ($\mathcal{H}_{eff} \sim R^{-1}\exp(-\alpha R)$) can have a very long range and, therefore, a strong effect.

1. The Hyperfine Interaction--Spin-Wave Expansion

At low temperatures, where the spin-wave theory outlined in Chapter I can be effectively applied, the hyperfine interaction (Equation I.3) for the isotropic case (applicable to the A-site ions) can be written as

$$\mathcal{H}_{hf} = \frac{1}{2} A \sum_{n}^{A} (I_n^+ S_n^- + I_n^- S_n^+) + A \sum_{n}^{A} I_n^z S_n^z \qquad (1)$$

with $A = -g_N\mu_N\vec{H}_{hf}\cdot\vec{S}/(\vec{S}\cdot\vec{S})$, where S is the A-site electronic spin. Then, the Holstein-Primakoff transformations allow the hyperfine interaction to be written in terms of the spin-wave operators defined in Chapter I. Up to third order in spin-wave operators the hyperfine interaction may be written as

$$\mathcal{H}_{hf} = \mathcal{H}_{hf}^{(0)} + \mathcal{H}_{hf}^{(1)} + \mathcal{H}_{hf}^{(2)} + \mathcal{H}_{hf}^{(3)} \qquad (2)$$

where,

$$\mathcal{H}_{hf}^{(0)} = -AS_A \sum_n I_n^z \qquad (3)$$

is the zero-magnon term representing an energy shift due to the net z-polarization of the nuclear spin system. The one-magnon term,

$$\mathcal{H}_{hf}^{(1)} = \frac{1}{2} A(2S_A)^{\frac{1}{2}} \sum_k (I_k^+ a_k + I_k^- a_k^+) \qquad (4)$$

gives rise to the effective spin-spin interaction when treated as a perturbation. Here the nuclear spin operators $I_n^{\pm}$ have been transformed to

$$I_k^{\pm} = (1/\sqrt{N_A}) \sum_n I_n^{\pm} \exp(\pm i\vec{k}\cdot\vec{r}_n)$$

The two-magnon term is

$$\mathcal{H}_{hf}^{(2)} = (A/N_A) \sum_n \sum_{k_1,k_2} I_n^z \exp\{-i(\vec{k}_1 - \vec{k}_2)\cdot\vec{r}_n\} a_{k_1}^+ a_{k_2} \qquad (5)$$

while the three-magnon term is written as

$$\mathcal{H}_{hf}^{(3)} = -\frac{1}{2} A(2S_A)^{\frac{1}{2}}(1/4N_A^{3/2}S_A) \sum_n \sum_{k_1,k_2,k_3} \Big(I_n^+ \exp\{-i(\vec{k}_1 - \vec{k}_2 - \vec{k}_3)\cdot\vec{r}_n\}$$
$$\times\, a_{k_1}^+ a_{k_2} a_{k_3} + I_n^- \exp\{-i(\vec{k}_1 + \vec{k}_2 - \vec{k}_3)\cdot\vec{r}_n\}\, a_{k_1}^+ a_{k_2}^+ a_{k_3}\Big) \qquad (6)$$

These higher order terms (Equations 5 and 6) will be of considerable importance in relation to the spin-wave relaxation processes to be discussed in Chapter III.

The one, two, and three-magnon expressions in Equations 4, 5, and 6 when written in terms of the magnon normal-mode operators α_k , β_k become

$$\mathcal{H}^{(1)}_{hf} = \frac{1}{2} A(2S_A)^{\frac{1}{2}} \sum_k \left(I^-_k(-v_k\alpha_k + u_k\beta^+_k) + I^+_k(-v_k\alpha^+_k + u_k\beta_k)\right) \qquad ,(7)$$

$$\begin{aligned}\mathcal{H}^{(2)}_{hf} = (A/N_A) \sum_n \sum_{k_1,k_2} I^z_n \exp\{i(\vec{k}_1 - \vec{k}_2)\cdot\vec{r}_n\} \\ \times \left(v_{k_1}v_{k_2}\alpha_{k_1}\alpha^+_{k_2} - u_{k_1}v_{k_2}\beta^+_{k_1}\alpha^+_{k_2}\right. \\ \left. - v_{k_1}u_{k_2}\alpha_{k_1}\beta_{k_2} + u_{k_1}u_{k_2}\beta^+_{k_1}\beta_{k_2}\right)\end{aligned} \qquad ,(8)$$

$$\begin{aligned}\mathcal{H}^{(3)}_{hf} = -(2S_A)^{\frac{1}{2}}(A/8N_A^{3/2}S_A) \sum_n \sum_{k_1,k_2,k_3} \Big(\exp\{-i(\vec{k}_1 + \vec{k}_2 - \vec{k}_3)\cdot\vec{r}_n\} I^-_n \\ \times \left(-v_1v_2v_3\alpha_1\alpha_2\alpha^+_3 + u_1v_2v_3\beta^+_1\alpha_2\alpha^+_3 + v_1u_2v_3\alpha_1\beta^+_2\alpha^+_3 + v_1v_2u_3\alpha_1\alpha_2\beta_3\right. \\ \left. - v_1u_2u_3\alpha_1\beta^+_2\beta_3 - u_1v_2u_3\beta^+_1\alpha_2\beta_3 - u_1u_2v_3\beta^+_1\beta^+_2\alpha^+_3 + u_1u_2u_3\beta^+_1\beta^+_2\beta_3\right) + \\ \exp\{i(\vec{k}_1 + \vec{k}_2 - \vec{k}_3)\cdot\vec{r}_n\} I^+_n \left(-v_1v_2v_3\alpha^+_1\alpha^+_2\alpha_3 + u_1v_2v_3\beta_1\alpha^+_2\alpha_3 + v_1u_2v_3\alpha^+_1\beta_2\alpha_3\right. \\ + v_1v_2u_3\alpha^+_1\alpha^+_2\beta^+_3 - v_1u_2u_3\alpha^+_1\beta_2\beta^+_3 - u_1v_2u_3\beta_1\alpha^+_2\beta^+_3 - u_1u_2v_3\beta_1\beta_2\alpha_3 \\ \left. + u_1u_2u_3\beta_1\beta_2\beta^+_3 \right)\Big)\end{aligned} \qquad ,(9)$$

In these expressions, $\alpha_i = \alpha_{k_i}$, $v_i = v_{k_i}$, etc., and

$$a_k = - v_k\alpha^+_k + u_k\beta_k$$

as given in Equation I.26. The transformation coefficients are

$$u_k^2 = \frac{S_B}{S_B - \eta^2 S_A} \quad , \qquad v_k^2 = \frac{\eta^2 S_A}{S_B - \eta^2 S_A}$$
$$\eta = \frac{\hat{z}\, N_A}{\tfrac{1}{2}\{N_A Z_A \gamma_k^A + N_B Z_B \gamma_k^B\}} \tag{10}$$

Equations 8 and 9 will be discussed further in Chapter III.

2. Second-order Effective Nuclear Spin-Spin Interaction

2.1 Perturbation expansion

The second-order shift in the energy levels, using the usual perturbation expansion with the one-magnon term of Equation 7 as the perturbing Hamiltonian, is given by

$$\Delta E = - \sum_k \frac{<0|\mathcal{H}_{hf}^{(1)}|k><k|\mathcal{H}_{hf}^{(1)}|0>}{E_k - E_o} \tag{11}$$

where the state $|k>$ is the state with one spin-wave (either α or β) of wave vector $\vec{k}$ and $|0>$ is the state with no spin-waves. Since the magnon dispersion relation has two branches (Equation I.28) the one-magnon hyperfine interaction is written

$$\mathcal{H}_{hf}^{(1)} = \mathcal{H}_{\alpha}^{(1)} + \mathcal{H}_{\beta}^{(1)}$$
$$\mathcal{H}_{\alpha}^{(1)} = - \frac{1}{2} A(2S_A)^{\frac{1}{2}} \sum_k \{I_k^+ v_k \alpha_k^+ + I_k^- v_k \alpha_k\} \tag{12}$$
$$\mathcal{H}_{\beta}^{(1)} = + \frac{1}{2} A(2S_A)^{\frac{1}{2}} \sum_k \{I_k^+ u_k \beta_k + I_k u_k \beta_k^+\}$$

and the energy shift becomes

$$\Delta E = - \sum_k \left[\frac{<0|\mathcal{H}_\alpha^{(1)}|k><k|\mathcal{H}_\alpha^{(1)}|0>}{\hbar\omega_\alpha} + \frac{<0|\mathcal{H}_\beta^{(1)}|k><k|\mathcal{H}_\beta^{(1)}|0>}{\hbar\omega_\beta} \right] \tag{13}$$

$$= \Delta E_\alpha + \Delta E_\beta$$

Then, since $\alpha_k|0> = 0$, $\beta_k^+|0> = |k>$, etc., the energy shifts can be written as

$$\Delta E_\alpha = - \frac{1}{2} A^2 S_A \sum_k \left(\frac{I_k^- I_k^+}{\hbar\omega_\alpha} \right) v_k^2$$

$$\Delta E_\beta = - \frac{1}{2} A^2 S_A \sum_k \left(\frac{I_k^+ I_k^-}{\hbar\omega_\beta} \right) u_k^2 \tag{14}$$

Since the gap between the α and β branches of the spin-wave spectrum is quite large for ferrimagnets, the energy denominator $\hbar\omega_\beta$ is large and ΔE_β may be neglected, giving $\Delta E \simeq \Delta E_\alpha$. Thus, the form of the Suhl-Nakamura effective spin-spin interaction for ferrimagnets is the same as that for ferromagnets[40].

2.2 Asymptotic form of the range function

Transforming the expression in Equation 14 for ΔE_α back to the nuclear spin operators $I_n^\pm$, the effective nuclear spin-spin interaction takes the form

$$\mathcal{H}_{S-N} = - \frac{1}{2} A^2 S_A \sum_{i \neq j} \{ (1/N_A) \sum_k \left(\frac{v_k^2}{\hbar\omega_\alpha} \right) \exp\{i\vec{k}\cdot(\vec{r}_i - \vec{r}_j)\} \; I_j^- I_i^+ \} \tag{15}$$

omitting from the summation self-energy terms where a magnon is emitted and then reabsorbed by the same nucleus. The expression

$$B_{ij} = (A^2 S_A / N_A) \sum_k \left(\frac{v_k^2}{\hbar\omega_\alpha} \right) \exp\{i\vec{k}\cdot(\vec{r}_i - \vec{r}_j)\} \tag{16}$$

is called the Suhl-Nakamura range function. The α-mode dispersion relation is, for $MnFe_2O_4$,

$$\hbar\omega_\alpha = g\mu_B H' + 4JS_{eff}a^2k^2(11/64) \qquad (17)$$

where $$S_{eff} = \frac{N_A}{N_B}\left(\frac{S_AS_B}{S_B - \eta^2 S_A}\right) \simeq \frac{1}{2}\left(\frac{S_AS_B}{S_B - \frac{1}{2}S_A}\right)$$

The sum over $\vec{k}$ in Equation 16 can be replaced by an integral in the long wavelength approximation. Then, with

$$\sum_k \left(\frac{v_k^2}{\hbar\omega_\alpha}\right) e^{i\vec{k}\cdot\vec{r}_{ij}} \simeq (S_{eff}/S_B) \sum_k \left(\frac{e^{ikr\cos\theta_{ij}}}{c + dk^2}\right)$$

since $v_k^2 \simeq \frac{1}{2} S_A/(S_B - \frac{1}{2} S_A)$, (which amounts to neglecting a term like $g\mu_B H'k^2$ compared to $g\mu_B H_{ex}k^2$), the range function, on transforming to an integral, becomes

$$B_{ij} = A^2S_A(S_{eff}/S_B)(\hat{a}/2\pi)^3 \int_0^{2\pi} d\phi \int_{-1}^{1} d\cos\theta \int_0^\infty dk\, k^2 \left(\frac{e^{ikr\cos\theta}}{c + dk^2}\right) \qquad ,(18)$$

$$= A^2S_A(S_{eff}/S_B)(\hat{a}^3/(2\pi)^2)(1/2dr)\ \mathrm{Im}\left(\int_{-\infty}^{\infty} dz\, \frac{ze^{iz}}{c/d + z^2}\right)$$

$$= A^2S_A(S_{eff}/S_B)(\hat{a}^3/4\pi d)(1/r)\exp\{-(c/d)^{\frac{1}{2}}r\}$$

Then, as a function of the effective internal field H' (including externally applied fields, anisotropy and demagnetizing fields) and the exchange energy $\hbar\omega_e$, where $\hat{a}^3$ is the volume per A-site ion,

$$B_{ij} = \left(\frac{2A^2S_A}{z\hbar\omega_e}\right)\left(\frac{S_{eff}}{S_B}\right)(1/\overline{N}_A)\ f(r_{ij})$$

where z is the number of A-site nearest magnetic neighbors and $\overline{N}_A$ is the number of A-site ions per unit cell, $\hbar\omega_e = 4JS_{eff}(11/64)$, and the function $f(r_{ij})$ is given by

$$f(r_{ij}) = \frac{1}{4\pi\alpha} \frac{a}{r} \exp\{-(g\mu_B H'/\hbar\omega_e)^{\frac{1}{2}} (r/a)\} \qquad (19)$$

with the constant $\alpha = (2/z) = 1/6$.

In Figures 1-a,b the asymptotic range function is plotted as a function of distance (r/a_{nn}) and as a function of the effective field H'. The effective range of the interaction , R, is defined as the distance where $(r/a\ \ ) = R = (g\mu_B H'/\hbar\omega_e)^{-\frac{1}{2}}$. For the values $\hbar\omega_e = 1.29 \times 10^{-15}$ ergs and H'= 1.0 kOe, the range is $R = 21.4 \times a_{nn} = 76$ Å .

Even though the interaction would appear to be quite weak due to its second order nature, its very long range makes it the strongest internuclear interaction in these materials and it provides the most effective nuclear magnetic relaxation channel at low temperatures.

The Suhl-Nakamura Hamiltonian of Equation 15 describes an interaction between the transverse (I^+, I^-) components of the nuclear spin; therefore, when there are a large number of nuclear spins in the x-y plane, as is the case in the usual pulsed NMR experiments, the spins will interact strongly. The result of this interaction, other than the transverse relaxation to be discussed in Chapter III, is an effective magnetic field at one nucleus due to the x, y components of the spin of another nucleus. This effect will be discussed in connection with the formation of multiple echoes after a brief discussion of the density matrix treatment of pulsed nuclear resonance.

3. Density Matrix Treatment of Pulsed Resonance

The density matrix formalism provides a straightforward and powerful method of calculating the response of the nuclear spin system to an external excitation[43,44]. Given a general state of the system ψ which is a linear superposition of the orthonormal eigenstates u_m of the Hamiltonian

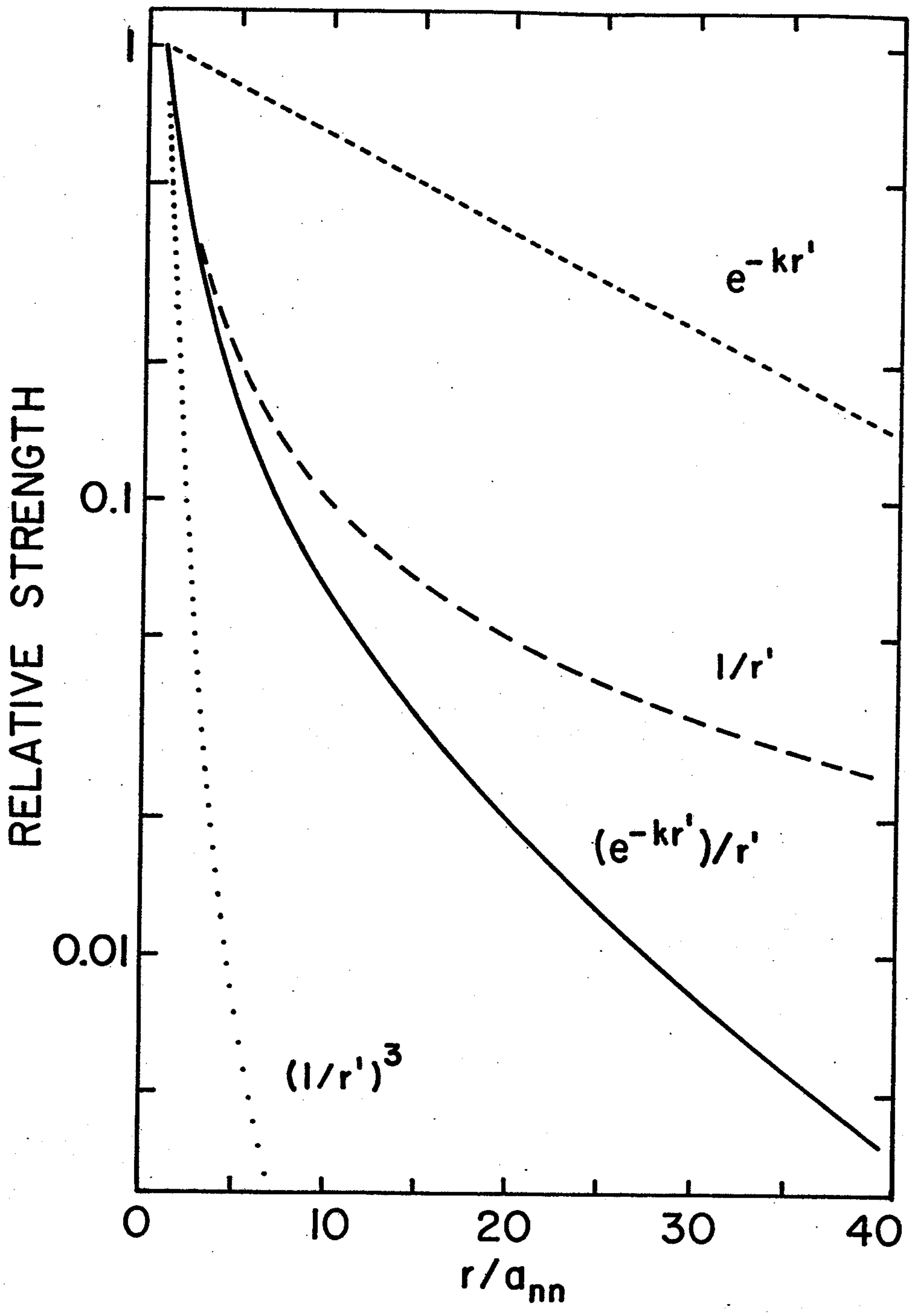

Figure 1a. Distance dependence of Suhl-Nakamura asymptotic range function compared to other range functions. $r' = r/a_{nn}$, $k = 4.6 \times 10^{-2}$

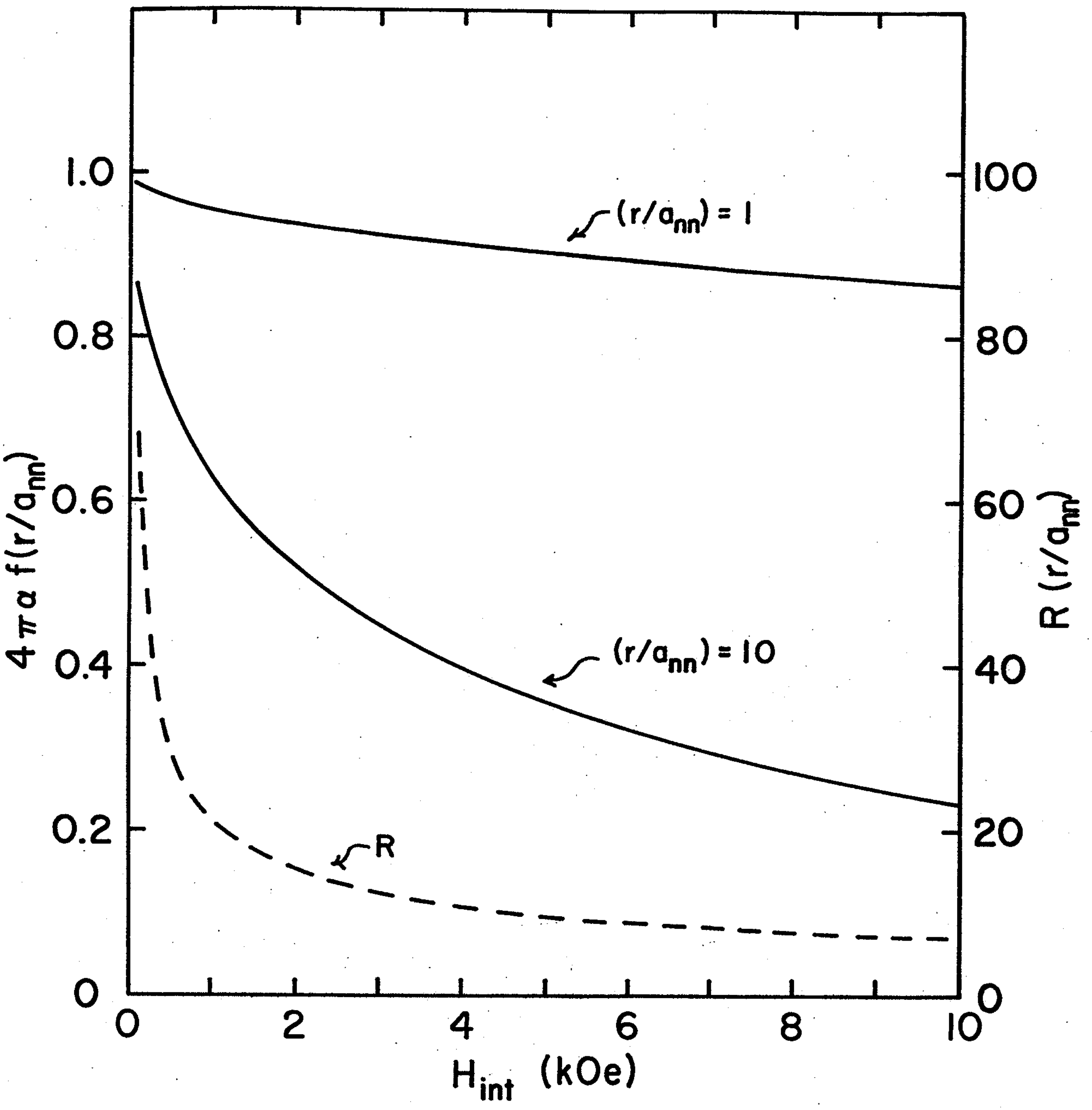

Figure 1b. Field dependence of Suhl-Nakamura asymptotic range function and effective range R for $\hbar\omega_e = 1.32 \times 10^{-15}$

the expectation value of an operator M_z in the state ψ is

$$\langle M_z \rangle = (\psi^*, M_z\psi) = \sum_{n,m} a_n^* a_m \langle u_n | M_z | u_m \rangle = \sum_{n,m} \langle m|P|n\rangle\langle n|M_z|m\rangle \quad ,(20)$$

where $\langle m|P|n\rangle = a_m a_n^*$ defines an operator P. From Equation 20 we have that the average value of M_z is

$$\langle M_z \rangle = \sum_m \langle m|PM_z|m\rangle$$

The density operator ρ is defined as the ensemble average[43] of matrix elements of P

$$\langle m|\rho|n\rangle = \overline{a_m a_n^*} = \overline{\langle m|P|n\rangle}$$

Then, in general, the expectation value of any operator T is

$$\langle T\rangle = \mathrm{Tr}(\rho T) = \sum_m \langle m|\rho T|m\rangle \quad (21)$$

From the Schrödinger equation for the state ψ

$$(-\hbar/i)(\partial\psi/\partial t) = \mathcal{H}\psi = (-\hbar/i)\sum_n (\partial a_n/\partial t)|u_n\rangle$$

with Hamiltonian $\mathcal{H}$, the density matrix ρ can be seen to satisfy the equation

$$d\rho/dt = (i/\hbar)\left[\rho , \mathcal{H}\right] \quad (22)$$

with solution, if $\mathcal{H}$ is not a function of t,

$$\rho(t) = \exp(-i\mathcal{H}t/\hbar)\ \rho(0)\ \exp(\ i\mathcal{H}t/\hbar) \quad (23)$$

where the t = 0 matrix elements can be defined by the Boltzmann factor and therefore,

$$\rho(0) = \exp(-\mathcal{H}_o/k_BT)/\left(\sum_n \exp(-iE_n/k_BT)\right) \quad (24)$$

where $\mathcal{H}|n\rangle = E_n|n\rangle$. For the equilibrium density matrix in the absence of external rf fields

$$\rho(0) \;\alpha\; \exp\{\, \hbar(\omega_o I_z + aI_z^2)/k_B T \,\}$$

in the presence of Zeeman ($\hbar\omega_o I_z$) and quadrupole (aI_z^2) Hamiltonians. In the high temperature approximation $k_B T >> \hbar(\omega_o I_z + aI_z^2)$, valid for all but the very lowest temperatures ($\sim 10^{-3}$ °K),

$$\rho(0) \sim 1 + (\hbar\omega_o I_z/k_B T) \qquad (25)$$

if $\hbar a I_z^2 << \hbar\omega_o I_z$. The constant term in this expression can be neglected since it will not affect any of the calculated properties.

If $\mathcal{H} = \mathcal{H}_o + \mathcal{H}_1$, where $\mathcal{H}_1$ is a function of time, then the equation of motion becomes

$$d\rho^*/dt = (i/\hbar)\left[\rho^*, \mathcal{H}_1^*(t)\right] \qquad (27)$$

where $\rho(t) = \exp(-i\mathcal{H}_o t/\hbar)\ \rho^*(t)\ \exp(i\mathcal{H}_o t/\hbar)$

and $\mathcal{H}_1^*(t) = \exp(i\mathcal{H}_o t/\hbar)\ \mathcal{H}_1(t)\ \exp(-i\mathcal{H}_o t/\hbar)$

Then the time development of $\rho^*(t)$ can be solved by iteration[42] yielding, to second order in $\mathcal{H}_1^*(t)$,

$$d\rho^*(t)/dt = (i/\hbar)\left[\rho^*(0), \mathcal{H}_1^*(t)\right] + (i/\hbar)^2 \int_0^t \left[\left[\rho^*(0), \mathcal{H}_1^*(t)\right], \mathcal{H}_1^*(t)\right] dt' \qquad (28)$$

This approach is very useful in cases where there is a fluctuating internal field, etc.[42]

3.1 Form of the time development operators

In the case where $\mathcal{H}$ is time-independent the time development operators can be evaluated from the knowledge of the Hamiltonian. In the case of a

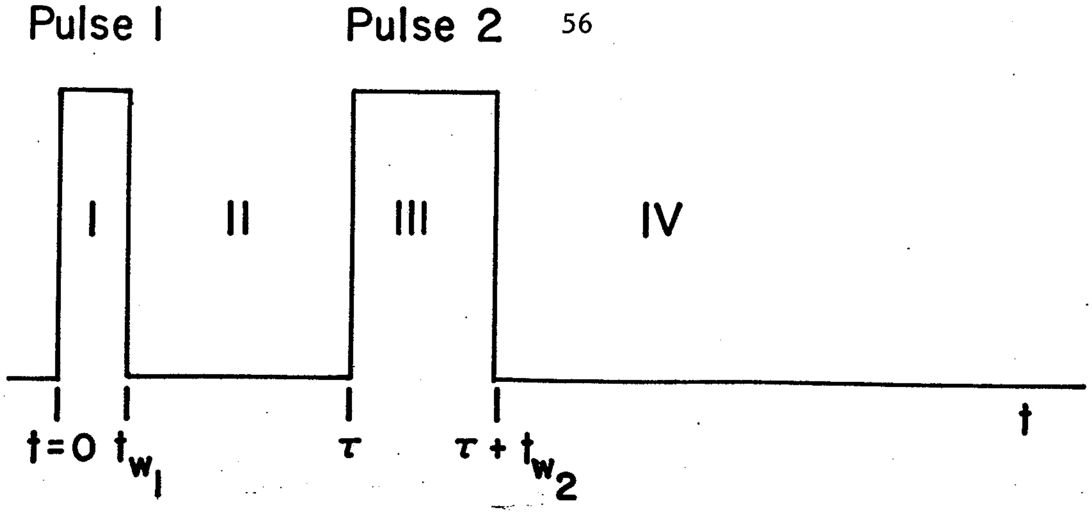

Figure 2. Division of time axis in a two pulse experiment.

two pulse NMR experiment, time can be divided as shown in Figure 2. Before $t = 0$ the spin system is in equilibrium described by the density matrix $\rho(0)$. In region I in the figure, during the first pulse (of length t_{w_1} and strength $H_1 = \omega_1/\gamma$), the Hamiltonian, in the frame rotating about the z-axis at a frequency ω' equal to the frequency of the applied rf pulse, is given by

$$\mathcal{H}_I = \hbar(\omega_o - \omega')I_z + \hbar a\, I_z^2 + \hbar\omega_1 I_y$$

if the pulse is applied along the y-axis in the rotating frame. Then, with $\Delta\omega = \omega_o - \omega'$, the time development operator in the first region is

$$U_I = \exp\{-i(\Delta\omega\, I_z + \omega_1 I_y + a\, I_z^2)\, t_{w_1}\} \qquad (29)$$

and, $\rho_2 = U_I\, \rho_1\, U_I^{-1}$

is the density matrix immediately following the first rf pulse, where $\rho_1 = \hbar\Delta\omega\, I_z$ is the $t = 0$ density matrix in the rotating frame.

From the expansion

$$U(t) = \exp(-i\mathcal{H}t/\hbar) = \sum_{n=0} \frac{(-i)^n}{n!} \mathcal{H}^n t^n$$

and since $\langle m|\mathcal{H}|m'\rangle = (-1)^{m-m'}\langle m'|\mathcal{H}|m\rangle$ and $\langle -m|\mathcal{H}|-m'\rangle = \langle m'|\mathcal{H}|m\rangle$

whenever $\mathcal{H} \sim$ any of the spin angular momentum operators, by induction, if

$$\langle m|\mathcal{H}^k|m'\rangle = (-1)^{m-m'}\langle m'|\mathcal{H}^k|m\rangle$$

and

$$\langle -m|\mathcal{H}^k|-m'\rangle = \langle m'|\mathcal{H}^k|m\rangle$$

then for k + 1, $\mathcal{H}^{k+1} = \frac{1}{2}(\mathcal{H}^k\mathcal{H} + \mathcal{H}\mathcal{H}^k)$

$$\langle m|\mathcal{H}^{k+1}|m'\rangle = (-1)^{m-m'}\langle m'|\tfrac{1}{2}(\mathcal{H}\mathcal{H}^k + \mathcal{H}^k\mathcal{H})|m\rangle$$

and

$$\langle -m|\mathcal{H}^{k+1}|-m'\rangle = \langle m'|\tfrac{1}{2}(\mathcal{H}\mathcal{H}^k + \mathcal{H}^k\mathcal{H})|m\rangle$$

Thus, in general the operators have the form (shown here for I = 5/2)

$$U = \begin{pmatrix} A & B & C & D & E & F \\ -B & G & H & I & J & E \\ C & -H & K & L & I & D \\ -D & I & -L & K & H & C \\ E & -J & I & -H & G & B \\ -F & E & -D & C & -B & A \end{pmatrix} \qquad (30)$$

and they have only 12 distinct elements.

In region I, during the first pulse, for nuclei with Larmor frequencies ω_o such that $\omega_o - \omega' \ll \omega_1$, and assuming that the quadrupole coupling constant a is small, the first time development operator is given by

$$U_I = \exp(-i\omega_1 t_{w_1} I_y) \qquad (31)$$

which represents a rotation[17] about the y-axis through an angle $\omega_1 t_{w_1}$. If the quadrupole coupling constant a is not small compared to ω_1, the operators can be evaluated iteratively using the identity[44]

$$\exp(\beta A)\ \exp(-\beta(A+B)) = 1 - \int_0^\beta d\lambda\ \exp(\lambda A)\ B\ \exp(-\lambda(A+B))$$

for the two cases $a < \omega_1$, and $a > \omega_1$. The matrices will still have the form of Equation 30. For the nuclei at the tetrahedral sites in $MnFe_2O_4$, there should be no quadrupole splitting and the quadrupole coupling constant a may be neglected. The expressions for the observed signal to be evaluated in this section will be valid in the presence of quadrupole splitting since these expressions only require that the operators have the form of Equation 30.

At a time $t > t_{w_1}$, i.e., in region II in Figure 2, the density matrix is given by

$$\begin{aligned}\rho_3(t) &= U_{II}\rho_2(t_{w_1})U_{II}^{-1} = U_{II}^{(1)}U_{II}^{(2)}\rho_2(U_{II}^{(2)})^{-1}(U_{II}^{(1)})^{-1} \\ &= U_{II}^{(1)}\rho_2'\,(U_{II}^{(1)})^{-1}\end{aligned} \quad ,(32)$$

where,

$$U_{II} = U_{II}^{(1)}U_{II}^{(2)} = \exp\{-i\Delta\omega(t - t_{w_1})I_z\}\,\exp\{-ia(t - t_{w_1})I_z^2\} \quad ,(33)$$

since $[I_z, I_z^2] = 0$, and the matrix elements of this operator may be immediately evaluated.

During the time interval immediately following the first pulse the spin system is not in equilibrium and the Hamiltonian used in the time-development operator in Equation 33 should contain the terms describing the relaxation of the spin system towards equilibrium. These terms include the Suhl-Nakamura and dipole-dipole interactions, but if their main effect is to cause relaxation, they may be described by a relaxation time T such that the transverse magnetization at a time t following a single rf pulse is given by

$$S_3^*(t) = c_n\, e^{-t/T}\, \mathrm{Tr}(I^+\rho_3) \quad (34)$$

where ρ_3 is given by Equation 32, and c_n is a normalization constant.

3.2 The free induction decay and spin echoes

From the form of the time development operator given in Equation 33 the transverse magnetization, in the rotating frame, following a single rf pulse can be rewritten as

$$S_3^*(t) \;=\; c_n\, e^{-t/T} \exp(ia_3)\, \mathrm{Tr}(I^+\rho_2') \tag{35}$$

where $a_3 = \Delta\omega(t - t_{w_1})$. The trace in this equation can be easily evaluated once the matrix elements of U_I have been determined.

To obtain an expression for the free induction decay we must average Equation 35 over the distribution $g(\omega_s)$ of spins excited by the rf pulse. The function $g(\omega_s)$ will be the product of the lineshape function $f(\omega_o)$ of the inhomogeneously broadened resonance and the rf pulse shape function $h(\omega_s)$. The observed spectrum will then be the convolution[45] of the two functions $f(\omega_o)$ and $h(\omega_s)$ while the free induction decay and spin echoes at a given spectrometer frequency ω_s will have a shape determined by the product function $g(\omega_s)$. Taking the average over $g'(\omega_o') = g(\omega_s+\omega_o')$ and transforming back to the laboratory frame, the free induction decay will be proportional to

$$S_3(t) \;=\; \exp\{i\omega_s(t-t_{w_1})\} \int_{-\infty}^{\infty} d\omega_o'\, g'(\omega_o') \exp\{i\omega_o'(t-t_{w_1})\} \\ \times\, \mathrm{Tr}(I^+\rho_2)\, \exp(-t/T)\, c_n \tag{36}$$

Since the functions $f(\omega_o)$ and $h(\omega_s)$, while they may both be symmetric about their central frequencies, have in general different shapes and different central frequencies, the free induction and spin-echo shape function will, in the case of strong inhomogeneous broadening (when the spread in Larmor frequencies in the sample is much greater than the pulse bandwidth, $\delta\omega_o >> \delta\omega_s$), change on varying the spectrometer frequency ω_s through the spectrum described by $f(\omega_o)$.

Defining the shape function by

$$G(t) = \int d\omega_o' \exp(i\omega_o' t) g(\omega_s + \omega_o') \tag{37}$$

the signal following one pulse is

$$S_3(t) = \exp\{i\omega_s(t-t_{w_1})\} \operatorname{Tr}(I^+\rho_2) G(t-t_{w_1}) \exp(-t/T) c_n \tag{38}$$

The signal will thus have a frequency ω_s and, for a symmetric $g(\omega_s)$ (i.e., at $\omega_s = \omega_{oo}$), will have a maximum at $t-t_{w_1} = 0$.

If, after allowing the spin system to develop according to Equation 32 until a time $t = \tau_1$, a second rf pulse, of strength ω_2/γ and length t_{w_2}, is applied, the operator U_{III} describing this pulse will be of the same form as U_I in Equation 31, namely,

$$U_{III} = \exp(-i\omega_2 t_{w_2} I_z) \tag{39}$$

assuming that both pulses are applied along the same direction in the rotating frame (for the case of an incoherent pulse spectrometer with all pulses applied at the same point in the cavity this is always true, however, for coherent pulse spectrometers if the phase of the two rf pulses is shifted, a transformation such as that applied in the discussion of Section 4.3 to the case of the effective refocusing pulse due to the first echo must be employed). Again, the more general form given for U_I in Equation 29 may be used for U_{III}. The matrix elements of the density operator during the second pulse are

$$(\rho_4)_{ij} = (U_{III}\rho_3 U_{III}^{-1})_{ij} = \sum_k \sum_l (U_{III})_{ik}(U_{III})^*_{jl}(\rho_2')_{kl}\exp(i(k-1)a_3) \qquad ,(40)$$

Then,

$$\mathrm{Tr}(I^+\rho_4) = \sum_n \sum_m (I^+)_{nm}(\rho_4)_{nm} = \sum_{r=0} M_r^{(3)} \exp(ria_3) \qquad ,(41)$$

$$(r=k-1)$$

where

$$M_r^{(3)} = \sum_{i=1}^{2I} \sigma_i \sum_k{}' (U_{III})_{i+1,k}(U_{III})^*_{i,k-r}(\rho_2')_{k,k-r} \qquad ,(42)$$

with $\sigma_i = (I^+)_{i,i+1}$, and the sum Σ_k' is over k such that $k-r \geq 1$, $k \leq 2I+1$

Following the second pulse,

$$\rho_5 = U_{IV}\rho_4 U_{IV}^{-1}$$

with $$U_{IV} = \exp\{-i(\Delta\omega I_z + a\, I_z^2)(t-\tau_1-t_{w_2})\} = U_{IV}^{(1)} U_{IV}^{(2)} \qquad (43)$$

and the response of the spin system will be given by

$$\mathrm{Tr}(I^+\rho_5) = \exp(ia_5)\ \mathrm{Tr}(I^+\rho_4') \qquad (44)$$

where $a_5 = \Delta\omega(t-\tau_1-t_{w_2})$ and $\rho_4' = U_{IV}^{(2)}\rho_4 U_{IV}^{(2)}$, similar to the definition of ρ_2' . The transverse magnetization and the signal in the laboratory frame are then given by

$$S_{(5)}(t) = c_n' \sum_{r=0}^{2I} \exp(i\omega_s(a_5 + ra_3))\ M_r^{(3)}\ G\left(\frac{a_5 + ra_3}{\Delta\omega}\right) e^{-t/T}\ \eta^2(H_{ext}) \qquad ,(45)$$

with $M_r^{(3)}$ given by Equation 42 and G(t) defined in Equation 37. The factor $\eta^2(H_{ext})$ is included to give the field dependence of echo amplitude due to the enhancement mechanisms[46] discussed in Chapter I, Sections 6 and 7. In the case where the quadrupole constant $a \neq 0$, the $\mathrm{Tr}(I^+\rho_4')$ will contain terms which depend on time (like e^{iat}) .

These modulation terms[44] do not change the form of G(t) since they do not enter the averaging process.

From Equation 45 it can be seen that in general 2I echoes can be observed, occurring at times $(a_5 + ra_3)/\Delta\omega$. These echoes may occur as a result of a quadrupole interaction by the introduction into the operators U_I and U_{III} of non-zero elements more than one position off the diagonal[44] or by a generalized excitation condition wherein the rf pulses do not represent pure rotations.

For pure rotations in the absence of a quadrupole interaction, the expression in Equation 45 is non-zero only for times near

$$t = \tau_1 + t_{w_2}$$

and

$$t = 2\tau_1 + t_{w_2} - t_{w_1} \qquad (46)$$

These mark the occurrence of the free induction decay and first spin-echo following the second pulse.

4. Multiple Echoes

Multiple spin echoes have been observed in various materials and several explanations have been applied to the different cases[44,47-51]. As shown above for nuclei with $I > \frac{1}{2}$ quadrupole effects can cause as many as 2I echoes following a two pulse excitation[44,47,49]. Also, external processes[48] requiring the active participation of the resonant cavity can cause a refocusing of the spin and consequently, multiple echoes.

4.1 Observation of multiple echoes in manganese ferrites[50]

In manganese ferrites, as illustrated in Figure 3, the application

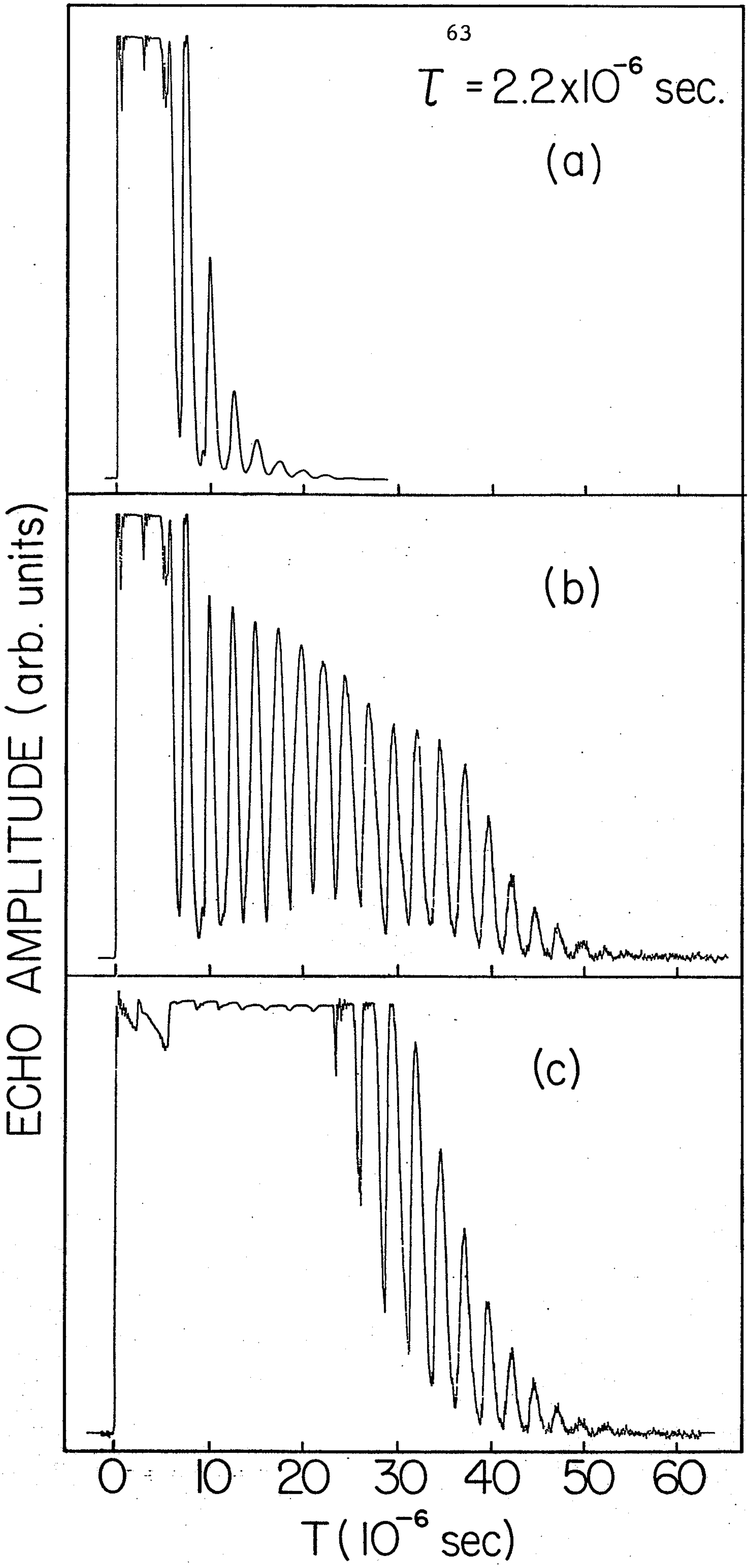

Figure 3. Response of spin system to two rf pulses at T = 1.6 °K, H_o = 0.0 kOe, and ν = 587 MHz. a) minimum receiver gain, b) varying gain to exhibit the echoes clearly, c) maximum gain.

of two rf pulses results in a very large number of spin echoes[50,51]. The number of echoes observed increases rapidly on lowering the temperature of the sample from 4.2 to 1.5 ^{o}K due to the increase in relaxation times at lower temperatures. At 1.5 ^{o}K more than 20 spin echoes are observed, while from Equation 45 above, for generalized excitation conditions or with quadrupole interactions, only $2I = 5$ echoes are expected. From Figure 3-a it can be seen that the envelope of the multiple echoes is exponential with a decay time of $\sim$ 4 μsec at $\nu = 587$ MHz[50].

In Figure 4 this decay rate is plotted as a function of frequency, showing that the refocusing mechanism, whatever its origin, is most efficient at the resonance frequency ($\nu_{oo} \simeq 587$ MHz) of the nuclear spin system. This characteristic frequency dependence suggests that a transverse spin-spin interaction, such as the Suhl-Nakamura interaction, is responsible for the refocusing.

4.2 Stimulation by nuclear spin-spin interaction

The formation of multiple echoes in the present case can be easily visualized if one considers the reaction of a single spin j' to the partial polarization of the rest of the spin system. During the formation of the first echo, spin j' will feel the net nuclear magnetization in the rotating frame. Since this magnetization represents an internal field, nucleus j' will respond to this field in much the same way that it would respond to the application of an rf pulse along the direction of echo formation. The reaction of the spin system will be to refocus again at a time $\Delta t \simeq \tau$ after the first echo. This process then continues with ever decreasing amplitude resulting in the multiple refocusing of the spin system.

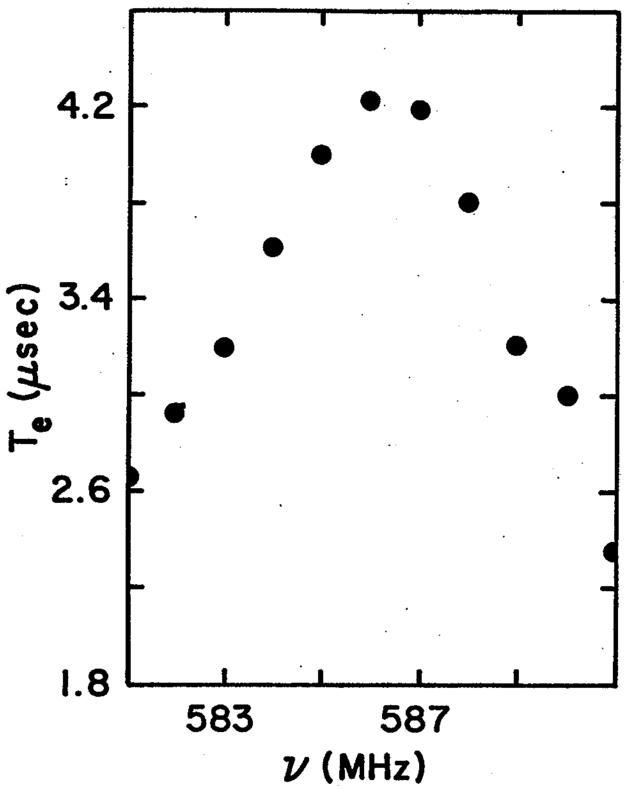

Figure 4. Characteristic time of multiple echo envelope versus frequency.

What is necessary in this process is an interaction between nuclei of sufficient strength to allow repetitive refocusing. The dipole-dipole interaction with its r^{-3} dependence is too weak, but the long-range nature of the Suhl-Nakamura interaction makes it sufficient for multiple echo formation when there is a large abundance of identical spins.

From Equations 14 and 19 the interaction between the transverse components of a spin j' and the rest of the spin system can be written as

$$\mathcal{H}^{j'}_{S-N} = -\,C \sum_{j}{}' f(r_{jj'})(I_j^+ I_{j'}^- + I_j^- I_{j'}^+) \tag{47}$$

where the sum Σ_j' is over $j \neq j'$. This interaction can be visualized as an interaction between a magnetic field H_{S-N} and a magnetic moment $\hbar\gamma I_{j'}$. The Hamiltonian can be written as

$$\mathcal{H}^{j'}_{S-N} = -\,C \left(\Big(\sum_{j}{}' f(r_{jj'})\, I_j^+ \Big) I_{j'}^- \;+\; \Big(\sum_{j}{}' f(r_{jj'})\, I_j^- \Big) I_{j'}^+ \right) \tag{48}$$

and, when the spin system is in equilibrium, $\Sigma_j\ f(r_{jj'}) I_j^{\pm} = 0$. Following the application of a $\pi/2$ pulse and a π pulse at a time τ_1 later, both along the y-axis, the magnetization in the x-y plane is no longer zero and, therefore, the sums above do not vanish and there will be an interaction between the spins. At a time $t = 2\tau_1 + t_{w_2} - t_{w_1}$ the components of spin in the x-y plane will refocus along the negative x-axis. At this time, neglecting relaxation, $I_j^+ = I_j^x = I_j^-$, and

$$\mathcal{H}^{j'}_{S-N} = -\,2C \Big(\sum_{j} f(r_{jj'})\, I_j^x \Big)(I_{j'}^- + I_{j'}^+) \tag{49}$$

or, writing the effective field H_{S-N} as

$$H_{S-N} = (\omega_{S-N}/\gamma) = -4(C/\hbar)\ \Sigma_j\ f(r_{jj'}) I_j^x$$

the interaction takes the form

$$\mathcal{H}_{S-N} = H_{S-N}\,(\hbar\gamma\, I^x_{j'}) = \hbar\omega_{S-N}\, I^x_{j'}$$

In general, if $g_e(t)$ is the function describing the x-component of nuclear magnetization, i.e., the echo shape function,

$$\mathcal{H}_{S-N} = \hbar\, g_e(t)\, \omega^{max}_{S-N}\, I^x_{j'}$$

and the time development operator following the second pulse will be of the form

$$U_{IV} = \exp\{-i(\Delta\omega\, I_z + a\, I_z^2)(t - \tau_1 - t_{w_2}) - ig_e(t)\omega^{max}_{S-N}\, I^x_{j'}\} \qquad ,(51)$$

The function $g_e(t)$ has a maximum at $t = 2\tau_1 + t_{w_2} - t_{w_1}$ and is zero for times far from this value. Thus, the spin system sees an effective pulse along the direction of formation of the first echo, in this case, the negative x-axis. This pulse is due to the Suhl-Nakamura interaction and causes the refocusing of the spin-system to form a second echo and is partly responsible for the formation of a third echo.

An upper bound on the strength of this pulse can be estimated from the observed transverse relaxation time assuming that the Suhl-Nakamura interaction is the primary relaxation channel. Then,

$$E_{S-N}\, T_{S-N} \sim \hbar \qquad \text{or} \qquad \omega_{S-N}\, T_{S-N} \sim 1$$

and, for $T_{S-N} \simeq 25$ μsec at $T = 4.2\ ^oK$, $\omega_{S-N} \simeq 4 \times 10^4\ (\text{sec})^{-1}$. If the echo shape function $g_e(t)$ is assumed to be a Gaussian with amplitude h, replacing it by a rectangular pulse of height h with the same area as $g_e(t)$ gives for the turning angle of the effective pulse at $t = 2\tau_1 + t_{w_2} - t_{w_1}$ with $\delta_e \simeq 2.8 \times 10^{-7}$ sec (the half-width at half-maximum of the echo) $\omega_{S-N}^{max}\, h\, \delta_e \sqrt{(\pi/2\ln 2)}\; \eta \simeq \eta h \cdot 2.4 \times 10^{-2}$ radians (52)

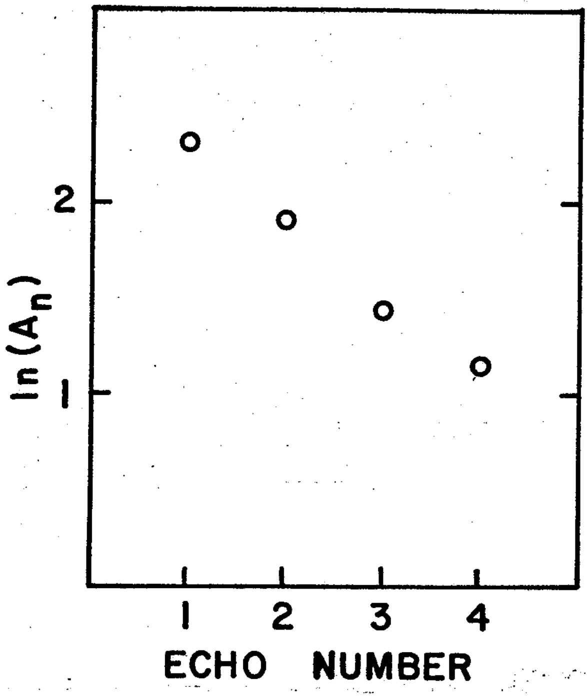

Figure 5. Logarithm of echo amplitude versus echo number at T=1.5 ^{o}K, H= 0.0 kOe, and ν=587 MHz.

The factor η is the enhancement factor as discussed in Sections I.6 and I.7 , which for the single-domain or saturated sample case is ∿ 500 . The height of the echo, h, depends on the absolute magnitude of the refocused magnetization and is difficult to estimate directly. However, the data shown in Figure 5 showing the t = 0 amplitudes of the first four echoes suggest that the effective pulse must be strong enough to provide a rotation of nearly π radians about the x-axis, since each echo is ∿ 2/3 the amplitude of the preceding echo. Recall that while the second echo is due solely to the refocusing by the first echo, the third and fourth (and higher) echoes have contributions from more than one source. Thus,

$$\eta h \cdot 2.4 \times 10^{-2} \simeq 12h \lesssim \pi$$

giving a value of h $\lesssim$ 1 as expected since the value for ω_{S-N} determined from the relaxation time should provide a good estimate of the strength of the interaction (with h = 1). The data in Table 1 , taken in H_{ext}= 0 at T = 1.5 ^{o}K show quite clearly the frequency dependence expected for a refocusing mechanism depending on the number of spins in the x-y plane, i.e., a transverse spin-spin interaction, as the first echo is far less

Table 1. Frequency dependence of multiple echoes at $T = 1.5\ ^{o}K$ in $H = 0$. A_n and T_n are the amplitudes and relaxation times of the nth echo.

ν(MHz)	T_e(μsec)	Echo #	T_n(μsec)	A_n^o(arb. units)	A_{n+1}/A_n
581.0	2.65	1	140.	0.257	0.25
		2	70.0	0.064	0.22
		3	57.5	0.014	0.21
		4	57.5	0.003	
583.0	3.20	1	100.	0.440	0.35
		2	45.0	0.153	0.32
		3	40.0	0.049	0.37
		4	32.5	0.018	
585.0	4.00	1	40.0	0.816	0.50
		2	24.0	0.405	0.46
		3	22.0	0.187	0.58
		4	17.0	0.108	
587.0	4.20	1	26.0	1.000	0.67
		2	14.0	0.668	0.62
		3	12.0	0.415	0.75
		4	10.0	0.312	
589.0	3.20	1	26.0	0.552	0.53
		2	13.0	0.292	0.49
		3	11.0	0.143	0.81
		4	8.0	0.116	
591.0	2.40	1	45.0	0.210	0.26
		2	24.0	0.054	0.31
		3	16.0	0.017	0.35
		4	12.0	0.006	

effective in refocusing the spins at frequencies far from the central frequency of $\nu = 587$ MHz. (The frequency dependence of the relaxation time will be discussed in Chapters III and IV.)

In this connection it should be noted that near 587 MHz the pulse tuning conditions (pulse widths) required to maximize the first echo are different from those required to maximize the second echo and that for some tuning conditions the third echo is larger than the second echo. These effects are due to the extreme strength of the refocusing mechanism, i.e., the first echo when maximized is apparently equivalent to a pulse whose width is greater than π radians, thus the decrease in second echo amplitude on increasing the first echo.

4.3 Density matrix calculation for the effective pulse[51]

Continuing the discussion of Section II.3 by treating the first echo as an rf pulse occurring along the x-axis at a time $t = 2\tau_1 + t_{w_1} - t_{w_1} = \tau_1 + \tau_2$, of strength ω_e and length $t_{w_e} = \delta_e\sqrt{(\pi/2\ln 2)}$. Neglecting $\Delta\omega$ and a during the first echo, the operator describing this effective pulse is

$$U_V = D_z(\pi/2)\exp(-i\omega_e t_{w_e} I'_y)\, D_z(-\pi/2) = D_z(\pi/2)\,\Theta\, D_z(-\pi/2) \qquad (53)$$

representing a rotation through an angle $\omega_e t_{w_e}$ about the negative x-axis, where the $D_z(\pm\pi/2)$ are rotations of $\pm\pi/2$ radians about the z-axis. The density matrix during this pulse is

$$\rho_6 = U_V \rho_5 U_V^{-1}$$

with $$(U_V)_{jk} = \exp(-i(k-j))\,\Theta_{jk}$$

Then the response of the spin system to this effective pulse is given by

$$\mathrm{Tr}(I^{+}\rho_6) = \sum_{r=-2I}^{2I} \sum_{s=-2I}^{2I} M^{(4)}_{r,s} \exp(sia_5) \exp(ria_3) \qquad ,(54)$$

where as before $a_3 = \Delta\omega(t-t_{w_1})$, $a_5 = \Delta\omega(t-\tau_1-t_{w_2})$, also,

$$M^{(4)}_{+|r|,s} = \sum_{p=1}^{2I+1-|r|} \delta_{p,p+|r|} \sum_{\ell} (U_{III})_{p+|r|,\ell+s} (U_{III})^{*}_{p,\ell} (\rho_2)_{\ell+s,\ell} \qquad ,(55)$$

and

$$M_{-|r|,s} = \sum_{p=1}^{2I+1-|r|} \delta_{p+|r|,p} \sum_{\ell} (U_{III})_{p,\ell+s} (U_{III})^{*}_{p+|r|,\ell} (\rho_2)_{\ell+s,\ell} \qquad ,(56)$$

with $\delta_{ij} = \sum_{k=1}^{2I} \sigma_k \Theta_{k+1,j} \Theta^{*}_{k,i}$

and, as before, $\sigma_k = (I^{+})_{k,k+1}$.

Then following the first echo, at time t, with $\tau_2 = \tau_1 + t_{w_2} - t_{w_1} - \frac{1}{2}t_{w_e}$, the time development operator is

$$U_{VI} = \exp\{-i\Delta\omega(t-\tau_1-\tau_2-t_{w_e})I_z\} \exp\{-ia(t-\tau_1-\tau_2-t_{w_e})I_z^2\} \qquad ,(57)$$

$$= U^{(1)}_{VI}\, U^{(2)}_{VI} = \exp(-ia_7 I_z)\, U^{(2)}_{VI}$$

and, defining $\rho_6' = U^{(2)}_{VI} \rho_6 (U^{(2)}_{VI})^{-1}$

then, $\rho_7 = U^{(1)}_{VI} \rho_6' (U^{(1)}_{VI})^{-1}$

and $\mathrm{Tr}(I^{+}\rho_7) = \exp(ia_7)\, \mathrm{Tr}(I^{+}\rho_6')$,(58)

Finally, the observed signal following two external pulses and the first echo will be proportional to

$$S^{(7)}(t) = c_n' \sum_{r=-2I}^{2I} \sum_{s=-2I}^{2I} M^{(4)}_{r,s} \exp\{i\omega_s(a_7+sa_5+ra_3)\}\, G\left(\frac{a_7+sa_5+ra_3}{\Delta\omega}\right) e^{-t/T} \eta^2 \qquad ,(59)$$

The factor $\eta^2(H_{ext})$ is again included to give the field dependence of echo amplitudes due to enhancement mechanisms. However, due to the dependence of the effective strength of this pulse (given by ω_e), on the amplitude of the first echo, and to the inclusion of the enhancement factor η in Equation 52 for the turning angle of the effective pulse, the second echo amplitude should decrease more strongly with field than the first echo. Figure 6 shows the amplitude of the first two echoes as a function of the effective internal magnetic field $H' = 1/\eta$ for the two temperatures $T = 1.5$ and 4.2 $^{\circ}$K. As expected the first echo's amplitude goes roughly as $(1/H')^2$ while the second echo's amplitude varies more nearly like $(1/H')^3$. The higher echoes (echoes 3, 4, etc.) will have more complicated behaviour with field, all falling off more rapidly than $(1/H')^2$.

The expression in Equation 59 for the signal following the first echo can also be applied to the case of a third external pulse applied at a time τ_2 following the second pulse. This method can be applied to the calculation of the spin-system's response to an arbitrary number of rf pulses applied along any axes if transformations such as that used with U_V above are applied.

In general the expression in Equation 59 allows the formation of a large number of echoes, however, the assumption of pure rotations and no quadrupole interaction reduces these allowed echoes to only two, occurring for times

$$t = 2\tau_1 + \tau_2 - t_{w_1} + t_{w_e}$$

and

$$t = 2\tau_1 + 2\tau_2 - t_{w_2} - t_{w_1} + t_{w_e}$$

These are the second and third echoes, respectively. As mentioned earlier, the third echo, which appears here due to the refocusing of the spin system by the first echo, will also receive a contribution due to the refocus-

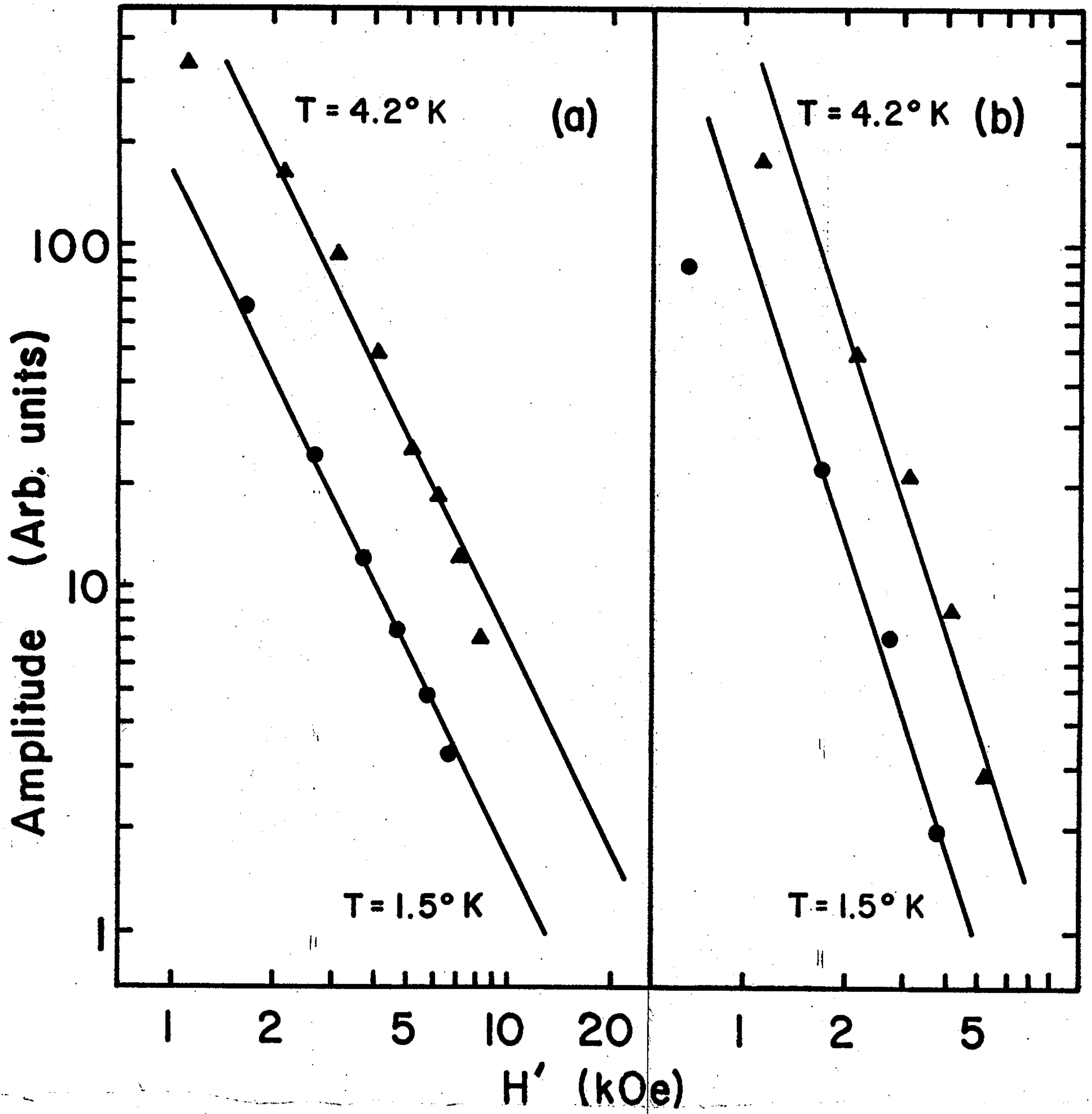

Figure 6. Signal amplitude versus effective internal field, a) first echo, b) second echo.

ing effect of the second echo, and in general all higher numbered echoes will have such multiple contributors. This should explain why the ratios of echo amplitudes (A_{n+1}/A_n) shown in Table 1 do not appear to decrease for higher numbered echoes.

In conclusion it should be mentioned that any material with a large concentration of identical nuclear moments which undergo a strong spin-spin coupling can exhibit the multiple echo phenomenon, for example ^{59}Co resonance in cobalt powders exhibits a similar sequence of echoes in both the fcc and hexagonal cobalt phases. The relaxation processes described in the next chapter will provide further verification of this model of multiple echo formation.

CHAPTER III

Relaxation Processes in Magnetically Ordered Systems

One of the most interesting and informative aspects of magnetic resonance is the process of relaxation. The free precession or pulse techniques discussed in Chapter I are ideally suited to the study of relaxation since they allow, after the initial pulse excitation, the direct observation of the spin system's approach to equilibrium. The form and strength of the various interactions responsible for the relaxation of the spin system can be determined by measuring the relaxation rate over a suitable range of the experimentally controlled variables, such as temperature, frequency, and external magnetic field.

1.1 The approach to equilibrium

The relaxation processes allowing the spin-system to come to equilibrium can be conveniently classified as either spin-lattice or spin-spin processes. In magnetic insulators at low temperatures electronic spin-wave scattering processes provide the most effective spin-lattice mechanism while the nuclear spin-spin relaxation is a result of the nuclear dipole-dipole and the Suhl-Nakamura interactions. The dipole-dipole interaction must be further separated into its transverse (mutual spin flip) and longitudinal parts, while the Suhl-Nakamura interaction is basically transverse (for high density of identical nuclei).

Basically, the experimental measurement, as discussed in Chapter I, of the relaxation times consists of a measurement of echo amplitude as a function of rf pulse separation in a two pulse experiment. The echo decay envelope if exponential, as it is for the Mn^{2+} resonance in $MnFe_2O_4$ at high fields, can be described by a single relaxation rate ($1/T_{tot}$) which is the sum of the relaxation rates due to each of the different spin interactions. The temperature, frequency, and field dependences of the various interactions make it possible to separate and identify the individual contributions to the total decay rate.

The spin system's approach to equilibrium can be most easily visualized by considering a simple pulse experiment in which a $\pi/2$ pulse is applied perpendicular to the z-axis (the axis of quantization). This pulse rotates a significant part of the nuclear magnetization into the x-y plane. Transverse relaxation then corresponds to a loss of phase coherence of the precessing spins in the plane while longitudinal relaxation corresponds to the return of the nuclear magnetization to the z-axis. The energy absorbed by the spins during the rf pulse must eventually be absorbed by the lattice--in the present case via spin-wave relaxation processes.

1.2 Line broadening

The width of a nuclear resonance line can be due either to homogeneous broadening by interactions between spins or to inhomogeneous broadening by sample inhomogeneities, such as the broad distribution of hyperfine fields common to magnetic materials, or inhomogeneous external fields. Homogeneous broadening is a result of the interactions responsible for the spin relaxation, and the relaxation rate characteristic of a given interaction is a measure of its contribution to the total linewidth. Thus, in the absence of inhomogeneous broadening, the resonance linewidth is given by $\delta\omega \sim 1/T_{tot}$. In the presence of inhomogeneous broadening[52], however, the linewidth does not reflect the relaxation effects and other methods, such as the free precession techniques, must be used to measure the relaxation rate. The extreme inhomogeneous broadening in magnetic materials permits the measurement of the frequency dependence of the relaxation rate and, therefore, simplifies the identification of the interactions responsible.

The contributions of the various interactions to the homogeneous linewidth and the relaxation rate can be calculated, at least in principle, by the method of moments[53-55], as outlined in Appendix I, and in the next section.

1.3 The method of moments

The moments of the spectral distribution function in principle give all the information necessary for complete determination of the resonance lineshape. However, higher order moments become increasingly difficult to evaluate and, in practice, one must be satisfied in most cases with the first two even moments, M_2 and M_4 (although the sixth moment for the dipole-dipole interaction has been calculated[56,57]). The second moment of the homogeneously broadened resonance line, where $\mathcal{H}'$ is the Hamiltonian describing the interaction responsible for the line broadening, is given by

$$M_2 = -\operatorname{Tr}\{[\mathcal{H}', I_x]^2\} / \operatorname{Tr}\{I_x^2\} \qquad (1)$$

and the fourth moment is

$$M_4 = \operatorname{Tr}\{[\mathcal{H}', [\mathcal{H}', I_x]]^2\} / \operatorname{Tr}\{I_x^2\} \qquad (2)$$

where I_x is the x-component of the nuclear spin. If the lineshape function $f(\omega)$ is a Gaussian, the half-width at half-maximum is given by

$$\delta = \sqrt{2\ln 2}\; M_2^{\frac{1}{2}} \tag{3}$$

while for a cut-off Lorentzian

$$\delta = \frac{1}{6}\pi\sqrt{3}\;(M_2^2/M_4)^{\frac{1}{2}}\,M_2^{\frac{1}{2}} \tag{4}$$

Thus, the ratio (M_2^2/M_4) will indicate which lineshape is more nearly correct (see Appendix I for a more detailed discussion of the moment method). In the next section the moments of the longitudinal part of the dipole-dipole interaction will be discussed, while the treatment of the Suhl-Nakamura and the transverse dipole-dipole interactions will be presented in Section 3.

2. Longitudinal Dipole-Dipole Relaxation

The total dipole-dipole Hamiltonian for the interaction between two nuclei labeled 1 and 2 (from Equations I.18, 19) can be written in the form[58,59] (using the notation of reference 58)

$$\mathcal{H}_{dd} = \frac{\gamma_1\gamma_2\hbar}{r_{12}^3}\{A + B + C + D + E + F\} \tag{5}$$

with

$$\begin{aligned}
A &= I_1^z I_2^z (1 - 3\cos^2\theta)\\
B &= -\frac{1}{4}\{I_1^+I_2^- + I_1^-I_2^+\}(1 - 3\cos^2\theta)\\
C &= -\frac{3}{2}\{I_1^+I_2^z + I_1^zI_2^+\}\sin\theta\cos\theta e^{-i\phi}\\
D &= -\frac{3}{2}\{I_1^-I_2^z + I_1^zI_2^-\}\sin\theta\cos\theta e^{i\phi} \qquad (6)\\
E &= -\frac{3}{4}\; I^+I^+ \sin^2\theta e^{-2i\phi}
\end{aligned}$$

$$F = -\frac{3}{4} I_1^- I_2^- \sin^2\theta e^{2i\phi}$$

where r_{12} , θ, ϕ are the usual spherical polar coordinates, r_{12} joining nuclei 1 and 2.

The term A represents the longitudinal interaction between the two nuclei (not necessarily identical), while the B term is the transverse or spin-flip part of the dipole-dipole interaction which is effective only for nuclei whose Larmor frequencies are close together (within an energy ~ the dipole-dipole interaction energy). Thus, the B term is an interaction between what can be called identical nuclei, much like the Suhl-Nakamura interaction, and will be considered in the next section. The remaining terms, C – F , do not conserve energy in zeroth order and will not be considered in the moment analysis. These terms however can be of importance when considering higher order processes, in particular, spin-wave scattering, and will be discussed in this connection in Section 4. (See reference 59 for a discussion of the physical significance of these terms.)

The second moment of the longitudinal part of $\mathcal{H}_{dd}$ is the sum of two contributions, from like nuclei and from unlike nuclei. In the present case this means first a contribution from the Mn^{2+} nuclei on the A-sites and secondly, contributions from $^{57}Fe^{3+}$ ions on the A- and B-sites as well as Mn^{3+} nuclei on the B-sites. Since we are dealing only with term A in this section, all of these contributions to the second moment have the same form. The commutator $[\mathcal{H}', I_x]$ in Equation 1 is, summing over j,k

$$\begin{aligned} [\mathcal{H}', I_x] &= \gamma_1\gamma_2\hbar \sum_{j<k} \frac{1}{r_{jk}^3} (1 - 3\cos^2\theta_{jk}) \left[I_j^z I_k^z, \sum_{\ell} I_\ell^x\right] \\ &= i\gamma_1\gamma_2\hbar \sum_{j<k} \left(\frac{1 - 3\cos^2\theta_{jk}}{r_{jk}^3}\right) (I_j^z I_k^y + I_k^z I_j^y) \end{aligned} \qquad (7)$$

and the second moment for nuclei of type 1[54] interacting with nuclei of type 2 is given by

$$M_2(1,2) = \frac{1}{3}\gamma_1^2\gamma_2^2\, I_2(I_2+1)\,\hbar^2 \sum_k{}' \left(\frac{1-3\cos^2\theta_{jk}}{r_{jk}^3}\right)^2 \qquad (8)$$

where the sum Σ_k' is over nuclei of type 2 . Then, the total longitudinal second moment can be written

$$M_2 = M_2(\mathrm{Mn}^A,\mathrm{Mn}^A) + M_2(\mathrm{Mn}^A,\mathrm{Fe}^A) + M_2(\mathrm{Mn}^A,\mathrm{Mn}^B) + M_2(\mathrm{Mn}^A,\mathrm{Fe}^B) = M_2^A + M_2^B$$

the superscripts A, B signifying the sublattice the nuclei belong to. The separate sublattice contributions are

$$M_2^A = \frac{1}{3}\gamma_{\mathrm{Mn}}^2\hbar^2\left(C_{\mathrm{Mn}}^A\gamma_{\mathrm{Mn}}^2(35/4) + C_{\mathrm{Fe}}^A\gamma_{\mathrm{Fe}}^2(3/4)\right)\sum_k^A\{(1-3\cos^2\theta_{jk})/r_{jk}^3\}^2$$

$$,(9)$$

and

$$M_2^B = \frac{1}{3}\gamma_{\mathrm{Mn}}^2\hbar^2\left(C_{\mathrm{Mn}}^B\gamma_{\mathrm{Mn}}^2(35/4) + C_{\mathrm{Fe}}^B\gamma_{\mathrm{Fe}}^2(3/4)\right)\sum_k^B\{(1-3\cos^2\theta_{jk})/r_{jk}^3\}^2$$

where now the sums are over all nuclei on the individual sublattices and $C_{\mathrm{Mn}}^{A,B}$ is the manganese concentration on the A, B sublattice while $C_{\mathrm{Fe}}^{A,B}$ is the ^{57}Fe concentration on the respective sublattices. These sums may be easily carried out on a computer since, because of the $(1/r^3)^2$ behaviour, they converge quite rapidly. The results for $\mathrm{MnFe_2O_4}$ are

$$M_2^A = 2.31\times10^7 \quad (\mathrm{sec})^{-2}, \quad M_2^B = 0.57\times10^7 \quad (\mathrm{sec})^{-2}$$

$$M_2 = 2.88\times10^7 \quad (\mathrm{sec})^{-2}$$

This total second moment, assuming a Gaussian lineshape, corresponds to a relaxation rate

$$1/T_{d\ell} = \sqrt{2\ln 2}\; M_2^{\frac{1}{2}} \approx 6.32\times10^3 \quad (\mathrm{sec})^{-1} \qquad (10)$$

or $$T_{d\ell} \approx 158 \quad \mu\text{sec}$$

For a more nearly Lorentzian lineshape, the fourth moment must be calculated and used as in Equation 4, and the resonance linewidth will appear narrower than that estimated from the second moment alone. Thus, the result in Equation 10 is an upper limit on the linewidth due to the longitudinal dipole-dipole interaction and the value of $T_{d\ell}$ given is the lower bound for the relaxation time. Since this time is already much longer than the total relaxation time observed near resonance, over the entire field and temperature range, it will be sufficient to neglect the contribution of this interaction to the total relaxation rate except in including it as a frequency independent background relaxation process whose magnitude can be obtained from the experimental data. Because of this the fourth moment need not be calculated.

A proper treatment of the dipole-dipole relaxation processes requires the calculation of the second and fourth moments of the total dipole-dipole Hamiltonian including the frequency dependent behaviour of the transverse part of the interaction[60]. In fact, the Suhl-Nakamura and dipole-dipole interactions should also be treated at the same time to avoid dropping the cross terms since, e.g.,

$$M_2^{tot} = M_2^{S-N} + M_2^{dd} - 2\,\frac{\mathrm{Tr}\{[\mathcal{H}_{S-N}, I_x][\mathcal{H}_{dd}, I_x]\}}{\mathrm{Tr}\{I_x^2\}} \tag{11}$$

These points will be discussed further in the next section.

3. Suhl-Nakamura and Transverse Dipole-Dipole Relaxation

The Suhl-Nakamura interaction

$$\mathcal{H}_{S-N} = -\frac{1}{2} A^2 S_A \sum_{j\neq j'} B_{jj'}(I_j^+ I_{j'}^- + I_j^- I_{j'}^+) \tag{12}$$

and the transverse dipole-dipole interaction

$$\mathcal{H}_{td} = \gamma^2\hbar \sum_{j\neq j'} d_{jj'} (I_j^+ I_{j'}^- + I_j^- I_{j'}^+) \qquad (13)$$

have the same general form and can be treated in the same manner, except as outlined at the end of the last section. The second and fourth moments of this "spin-flip" form of interaction have been calculated, for the case of a strictly homogeneously broadened line, by Van Vleck[53]. The second moment, where $V_{jj'}$ can be either $-\frac{1}{2} A^2 S_A B_{jj'}$ or $\gamma^2\hbar\, d_{jj'}$ is

$$M_2^h = \frac{1}{3} I(I+1) \sum_{j'}{}' V_{jj'}^2 \qquad (14)$$

where the sum is over spins $j' \neq j$ and the superscript h identifies this as the second moment of the homogeneously broadened line. The prime on the summation symbol is to indicate that for spin-flip terms the sums are over identical nuclei only. In the case of an inhomogeneously broadened line the definition of "identical" spins must be modified[61] to include all those identical nuclei whose Larmor frequencies, ω_i and ω_j for nuclei i and j , are such that $|(\omega_i - \omega_j)| < |V_{ij}|$. For strong inhomogeneous broadening, $\delta >> (M_2^{S-N})^{\frac{1}{2}}$, where δ is the half-width of the resonance line, the probability that spin j has a Larmor frequency within $|V_{ij}|$ of ω_i is $g(\omega_i)|V_{ij}|$. Figure 1 illustrates the essential features of this model. Here, the fraction of spins within $\pm\Delta$ of ω_j is approximately $g(\omega_j)\cdot\Delta$. Thus, if the homogeneous Suhl-Nakamura linewidth, Δ , is much less than the inhomogeneous linewidth, δ , $|B_{jk}|\Delta \sim 1$ and only spins with Larmor frequencies such that $|\omega_j - \omega_k| \lesssim |B_{jk}|$ can interact. Then in sums of the form

$$\sum_{j,k}{}' B_{jk}^2 = N \sum_k{}' B_{jk}^2$$

the final sum, over k, should be weighted by the probability that nuclei j and k can interact. Thus, in calculating the second moment in Equation 14, one makes the replacement

$$\sum_j{}' V_{ij}^2 \rightarrow \sum_j{}' V_{ij}^2 \, V_{ij} \, g(\omega_i)$$

For the Suhl-Nakamura interaction

$$M_2^i = \frac{1}{3} I(I + 1) g(\omega) (\tfrac{1}{2} A^2 S_A)^3 \sum_j B_{ij}^3 \quad ,(15)$$

since B_{ij} is non-negative , here the i superscript indicates that this is for an inhomogeneously broadened line.

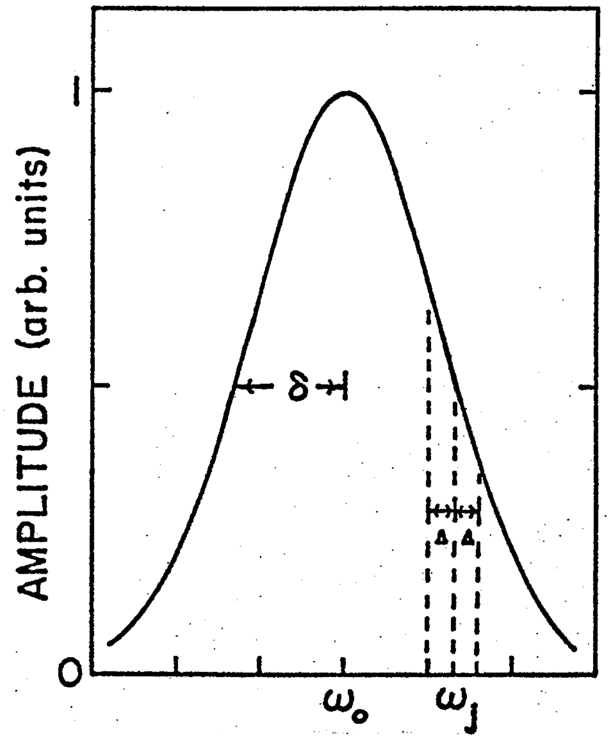

Figure 1. Inhomogeneously broadened resonance line with half-width δ compared to S-N interaction strength Δ .

The dipole-dipole interaction can be treated similarly, however, because it is composed of two parts which behave differently, the Hamiltonian is written as

$$\begin{aligned} \mathcal{H}_{dd} &= \mathcal{H}_{\ell d} + \mathcal{H}_{td} \\ &= \gamma^2 \hbar \sum_{j \neq} \sum_k d_{jk} I_j^z I_k^z + \frac{1}{2} \gamma^2 \hbar \sum_{j \neq} \sum_k d'_{jk} (I_j^z I_k^z - \vec{I}_j \cdot \vec{I}_k) \end{aligned} \qquad (16)$$

where d'_{jk} has the same form as d_{jk} , the prime indicating that the interaction is between like nuclei. Then, since

$$\mathrm{Tr}\{[\mathcal{H}_{dd}, I_x]^2\} = \mathrm{Tr}\{[\mathcal{H}_{\ell d}, I_x]^2\} + \mathrm{Tr}\{[\mathcal{H}_{td}, I_x]^2\} + 2\mathrm{Tr}\{[\mathcal{H}_{\ell d}, I_x][\mathcal{H}_{td}, I_x]\}$$

the second moment of the dipole-dipole interaction can be written as

$$M_2^i = \frac{1}{3} I(I+1) \sum_k d_{jk}^2 + \frac{1}{12} I(I+1) \sum_k d'^2_{jk} + \frac{1}{3} I(I+1) \sum_k d_{jk} d'_{jk} \qquad ,(17)$$

where the sums are over all $k \neq j$, while d'_{jk} indicates that for nucleus j only those k nuclei within the range $|\omega_j - \omega_k| \leq |d_{jk}|$ will interact. In the limiting cases of unlike spin broadening (strictly longitudinal coupling) and strictly homogeneous broadening, Equation 17 gives the expected results[54]. Again, since the probability that spin k has Larmor frequency ω_k within this range is $|d_{jk}| g(\omega_j)$, the total second moment is given by

$$\begin{aligned} M_2^i &= \frac{1}{3} I(I+1) \sum_k d_{jk}^2 + \frac{1}{12} I(I+1)\ g(\omega) \sum_k d_{jk}^2 |d_{jk}| \\ &\qquad + \frac{1}{3} I(I+1)\ g(\omega) \sum_k d_{jk}^2 |d_{jk}| \qquad (18) \\ &= M_2^\ell + \frac{5}{12} I(I+1)\ g(\omega) \sum_k d_{jk}^2 |d_{jk}| \end{aligned}$$

where M_2^ℓ is the longitudinal second moment discussed in the previous section.

As mentioned earlier, the Suhl-Nakamura and dipole-dipole contributions to the total second moment should not be treated separately. However, in the present case the Suhl-Nakamura relaxation is far stronger near resonance than the dipole-dipole relaxation is, while far from resonance, only the longitudinal dipole-dipole term needs to be retained.

The treatment of the fourth moment is considerably more involved. For an interaction of the form $B_{jk}(I_j^+ I_k^- + I_j^- I_k^+)$ the normal fourth moment, in the absence of inhomogeneous broadening is [61,62]

$$M_4^h = \{\tfrac{1}{3}\, I(I+1)\}^2 \{5(\sum_k{}' B_{jk}^2)^2 - 2 \sum_{k,\ell}{}'' B_{jk}^2 B_{k\ell} B_{\ell j} + 3 \sum_k{}' B_{jk}^4 \left(1 - \frac{1}{2I(I+1)}\right)\} \tag{19}$$

where Σ_k' is the sum over $k \neq j$, and $\Sigma_{k,\ell}''$ is a double sum with $j \neq k$, and $k \neq \ell$. The fourth moment for the total dipole-dipole interaction $(\mathcal{H}_{d\ell} + \mathcal{H}_{dt})$ is[63,54] , in the absence of inhomogeneous broadening

$$M_4^h = \{\tfrac{1}{3}\, I(I+1)\}^2 \{3(\sum_k{}' d_{jk}^2)^2 - \frac{1}{3} \sum_{k,\ell}{}'' d_{k\ell}^2 (d_{jk} - d_{j\ell})^2 - \frac{1}{5}\left(8 + \frac{3}{2I(I+1)}\right) \sum_k{}' d_{jk}^4\} \tag{20}$$

where there is assumed to be only one spin species (for the case of two spin species, see Van Vleck[53] and Abragam[54]). In the presence of strong inhomogeneous broadening, the expression for the fourth moment given in Equation 19 must be modified to include only those nuclei within the bandwidth $\pm|B_{jk}|$. Since

$$(\sum_k{}' B_{jk}^2)^2 = \sum_{k,\ell}{}'' B_{jk}^2 B_{j\ell}^2 + \sum_k{}' B_{jk}^4 \tag{21}$$

transforming to the inhomogeneous model[61]

$$\sum_k{}' B_{jk}^4 \rightarrow g(\omega) \sum_k{}' B_{jk}^5 \tag{22}$$

$$\sum_{k,\ell}{}'' B_{jk}^2 B_{j\ell}^2 \rightarrow (g(\omega))^2 \sum_{k,\ell}{}'' B_{jk}^3 B_{j\ell}^3 = (g(\omega))^2 \{(\sum_k{}' B_{jk}^3)^2 - \sum_k{}' B_{jk}^6\} \tag{23}$$

yields

$$(\sum_k{}' B_{jk}^2)^2 \rightarrow (g(\omega))^2 (\sum_k{}' B_{jk}^3)^2 + g(\omega) \sum_k{}' B_{jk}^5 - (g(\omega))^2 \sum_k{}' B_{jk}^6 \quad ,(24)$$

Similarly,

$$\sum_{k,\ell}'' B^2_{jk} B_{k\ell} B_{\ell j} \rightarrow (g(\omega))^2 \sum_{k,\ell}'' B^2_{jk} B^2_{k\ell} B^2_{\ell j} \tag{25}$$

Thus, the fourth moment is now given by

$$M^i_4(\omega) = \{\tfrac{1}{3} I(I+1)\}^2 \Big\{5\big[g(\omega) \sum_k{}' B^3_{jk}\big]^2 - 2\, g^2(\omega) \sum_{k,\ell}'' B^2_{jk} B^2_{k\ell} B^2_{\ell j} - 5\, g^2(\omega) \sum_k{}' B^6_{jk} + g(\omega) \Big(8 - \frac{3}{2I(I+1)}\Big) \sum_k{}' B^5_{jk}\Big\} \quad ,(26)$$

The ratio M^i_4/M^{i2}_2 is

$$\frac{M^i_4}{(M^i_2)^2} = 5 - 2 \frac{\sum''_{k,\ell} B^2_{jk} B^2_{k\ell} B^2_{\ell j}}{(\sum'_k B^2_{jk})^2} + \frac{1}{g(\omega)} \Big(8 - \frac{3}{2I(I+1)}\Big) \frac{\sum'_k B^5_{jk}}{(\sum'_k B^3_{jk})^2}$$

$$= \Gamma + \Big(\frac{1}{g(\omega)}\Big) \Big(8 - \frac{3}{2I(I+1)}\Big) \frac{\sum'_k B^5_{jk}}{(\sum'_k B^3_{jk})^2} \quad ,(27)$$

where $-1 < \Gamma < 5$ [61]. Then, neglecting Γ in the limit of strong inhomogeneous broadening $(M^i_4 >> (M^i_2)^2)$, the Suhl-Nakamura relaxation rate is

$$\Big(\frac{1}{T}\Big)_{S-N} = \frac{1}{6} \pi\sqrt{3}\, g(\omega) \{\tfrac{1}{3} I(I+1)\}^{\frac{1}{2}} \left[\frac{(\sum'_k B^3_{jk})^{3/2}}{(\sum'_k B^5_{jk})^{1/2}}\right] \Big\{8 - \frac{3}{2I(I+1)}\Big\}^{-\frac{1}{2}} \quad ,(28)$$

The transverse part of the dipole-dipole interaction will give an identical expression with B_{jk} representing $\mathcal{H}_{dt}$. Hone, et al.[61] included the total dipole-dipole interaction under the assumption of interactions only between nuclei with $|\omega_j - \omega_k| \leqslant |d_{jk}|$, finding an expression, analagous to the above, giving

$$\left(\frac{1}{T}\right)_{dd} = \frac{1}{6}\pi\sqrt{3}\, g(\omega)\{\frac{1}{3} I(I+1)\}^{\frac{1}{2}} \left[\frac{(\sum_{k} |d_{jk}|^3)^{3/2}}{(\sum_{k} |d_{jk}|^5)^{1/2}}\right] \{1.4 - \frac{0.3}{I(I+1)}\}^{-\frac{1}{2}} \quad ,(29)$$

This equation is at best useful only as an order of magnitude estimate of the strength of the dipole-dipole relaxation rate. A more useful expression, derived by Barak, et al.[60] is obtained if one writes an effective dipole-dipole interaction as

$$\mathcal{H}^{eff}_{dd} = \sum_{j<k} d_{jk}\{\frac{2}{3} I^z_j I^z_k - C(\frac{1}{6} I^+_j I^-_k + \frac{1}{6} I^-_j I^+_k)\} \quad ,(30)$$

where C is the average fraction of spins which interact via the spin-flip terms. This gives

$$M^C_2 = \left(\frac{2 + C}{3}\right)^2 M^{dd}_2 \quad (31)$$

where M^{dd}_2 is the normal dipole-dipole second moment, and, for the fourth moment,

$$M^C_4 = 3(M^C_2)^2 - \{ \frac{C}{3N} \left(\frac{4-C}{3}\right)\left(\frac{2+C}{3}\right)^2 \sum''_{j,k,\ell} d^2_{jk}(d_{k\ell} - d_{j\ell})^2$$

$$+ \frac{1}{5}\left(\frac{2+C}{3}\right)^2 \{8\left(\frac{1+2C}{3}\right) + \frac{3}{2I(I+1)}\left(\frac{8 - 4C + 5C^2}{9}\right)\} \quad (32)$$

$$\times \sum_{j,k} d^4_{jk}\} \{\frac{1}{3} I(I+1)\}^2$$

where the constant C depends on frequency. In the limit as C → 1 this reduces to the usual expression for M^h_4 . When C = 0 , this expression gives the fourth moment for longitudinal dipole coupling only. In the presence of more than one nuclear spin species, as with ^{57}Fe and ^{55}Mn^{A,B} in $MnFe_2O_4$, this expression must again be modified[53]. This, unfortunately, has not been carried out. For manganese ferrites, however, the estimates for the strengths of the dipole-dipole and Suhl-Nakamura relaxation rates suggest that such a detailed calculation is not necessary. Section 5 discusses the agreement of these relaxation rate calculations with the relaxation time data showing that the model of a frequency dependent Suhl-Nakamura relaxation rate superimposed on a frequency independent background rate is sufficient to explain the observations.

4. Spin-Wave Scattering Processes

The energy absorbed by the nuclear spin system in a nuclear magnetic resonance experiment must eventually be channeled to the lattice via spin-lattice relaxation processes. In ordered magnetic materials the most efficient spin-lattice relaxation mechanism is the scattering of electronic spin-waves via the hyperfine interaction. In Chapter II the hyperfine interaction for Mn^{2+} nuclei on the A-sites was expanded to third order in spin-deviation creation and annihilation operators

$$\begin{aligned}
\mathcal{H}_{hf} = & - AS_A \sum_n I_n^z + \frac{1}{2} A(2S_A)^{\frac{1}{2}} \sum_k (I_k^+ a_k + I_k^- a_k^+) \\
& + \frac{A}{N_A} \sum_n \sum_{k_1,k_2} I_n^z \exp\{i(\vec{k}_1 - \vec{k}_2)\cdot\vec{r}_n\}\, a_{k_1}^+ a_{k_2} \\
& - \frac{1}{2} A(2S_A)^{\frac{1}{2}} \left(\frac{1}{4N_A^{3/2} S_A}\right) \sum_n \sum_{k_1,k_2,k_3} \{ I_n^+ \exp\{i(\vec{k}_1 + \vec{k}_2 - \vec{k}_3)\cdot\vec{r}_n\} \\
& \times a_{k_1} a_{k_2} a_{k_3}^+ + I_n^- \exp\{-i(\vec{k}_1 + \vec{k}_2 - \vec{k}_3)\cdot\vec{r}_n\}\, a_{k_1}^+ a_{k_2}^+ a_{k_3} \}
\end{aligned} \tag{33}$$

where A is the isotropic hyperfine coupling constant and

$$I_k^{\pm} = (N_A)^{-\frac{1}{2}} \sum_n I_n^{\pm} \exp(\pm i\vec{k}\cdot\vec{r}_n)$$

From the form of this expansion one expects, for the nth order term in the expansion, relaxation processes involving the scattering of n spin-waves, subject to the restrictions of conservation of energy and spin angular momentum.

The zero-magnon term can be ignored in a discussion of relaxation processes, while the one-magnon term corresponds to the processes illustrated in Figure 2, where a nuclear spin-flip, designated by the symbol $\otimes$, is accompanied by the absorbtion, or emission, of an electronic spin wave. This "direct" process can be neglected because of the large difference between the energy required to create a spin wave and that necessary to flip a nuclear spin ($\hbar\omega_{\vec{k}} \gg \hbar\omega_L$, ω_L the nuclear Larmor frequency).

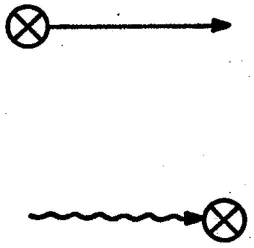

Figure 2. The direct spin-wave process. $\otimes$ represents a nuclear spin-flip, while the arrows represent the magnons.

The two-magnon term in the expansion corresponds to a scattering process in which a spin-wave of wave vector $\vec{k}_1$ is annihilated, a nuclear spin is flipped, and a spin-wave of wave vector $\vec{k}_2$ is created. This Raman scattering process is energetically allowed, ($\hbar\omega_{\vec{k}_1} - \hbar\omega_{\vec{k}_2} = \hbar\omega_L$) however, since spin angular momentum cannot be conserved in a system where the electronic and nuclear spin quantization axes are colinear (for the case of an isotropic hyperfine interaction)[64], for the A-site ^{55}Mn resonance in $MnFe_2O_4$ this process is forbidden and may be neglected.

The three-magnon term in the expansion of the hyperfine interaction, corresponding to a process of the type illustrated in Figure 4, describes a process where both energy and angular momentum can be conserved, $\hbar\omega_{\vec{k}_1} - \hbar\omega_{\vec{k}_2} - \hbar\omega_{\vec{k}_3} = \hbar\omega_L$. This is the lowest order term which can contribute to the spin-lattice relaxation in this system.

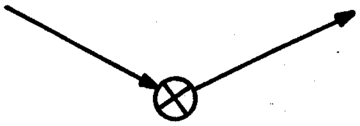

Figure 3. Raman scattering process.

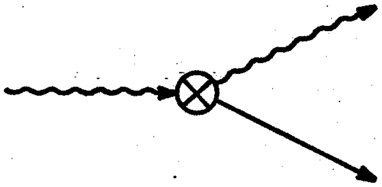

Figure 4. Three-magnon scattering.

4.1 Three-magnon relaxation

The three-magnon term in the expansion of the hyperfine interaction is given in terms of the spin-wave normal mode operators α_k^+ , α_k , β_k^+ , β_k where

$$\alpha_k = v_k a_k^+ + u_k b_k$$

and

$$\beta_k = u_k a_k + v_k b_k^+$$

as given in Equation II-9. This Hamiltonian includes many processes of the type shown in Figure 4 , several of which are not allowed; for example, the terms requiring the simultaneous creation (or annihilation) of all three magnons. The different allowed processes are illustrated in Figure 5 where the wiggly arrows correspond to β-mode magnons and the straight arrows to α-mode magnons, while at the vertex of each process there occurs a nuclear spin flip. Thus, there are only four three-magnon processes which conserve both energy and angular momentum[65].

With these restrictions the three-magnon Hamiltonian reduces to

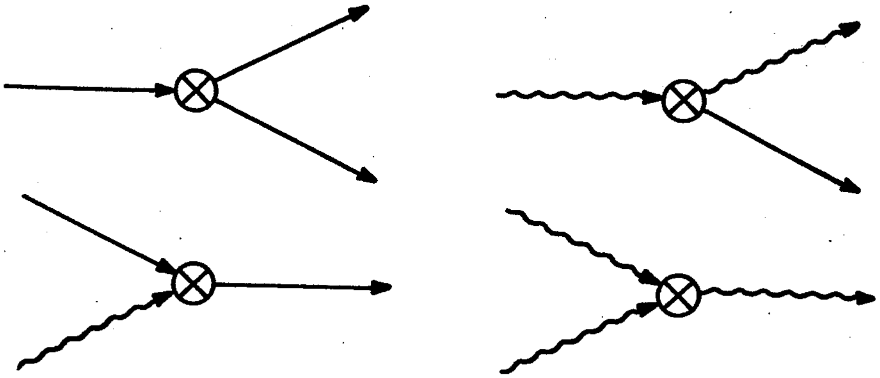

Figure 5. The allowed three-magnon processes

$$\begin{aligned}
\mathcal{H}^{(3)} &= (2S_A)^{\frac{1}{2}}\left(\frac{A}{8N_A^{3/2}S_A}\right)\sum_n \sum_{k_1,k_2,k_3} \exp\{i(\vec{k}_1 + \vec{k}_2 - \vec{k}_3)\cdot\vec{r}_n\} \\
&\quad \times I_n^+ \{-v_1v_2v_3\alpha_1^+\alpha_2^+\alpha_3 + u_1v_2v_3\beta_1\alpha_2^+\alpha_3 + v_1u_2v_3\alpha_1^+\beta_2\alpha_3 \\
&\quad - v_1u_2u_3\alpha_1^+\beta_2\beta_3^+ - u_1v_2u_3\beta_1\alpha_2^+\beta_3^+ + u_1u_2u_3\beta_1\beta_2\beta_3^+\} \\
&= (2S_A)^{\frac{1}{2}}\left(\frac{A}{8N_A^{3/2}S_A}\right)\sum_n \sum_{k_1,k_2,k_3} \exp\{i(\vec{k}_1 + \vec{k}_2 - \vec{k}_3)\cdot\vec{r}_n\} \\
&\quad \times I_n^+ \{-v_1v_2v_3\alpha_1^+\alpha_2^+\alpha_3 + 2\,u_1v_2v_3\beta_1\alpha_2^+\alpha_3 - 2\,v_1u_2u_3\alpha_1^+\beta_2\beta_3^+ \\
&\quad + u_1u_2u_3\beta_1\beta_2\beta_3^+\}
\end{aligned} \tag{35}$$

This perturbing Hamiltonian induces transitions between nuclear spin states causing the relaxation of the nuclear magnetization towards its equilibrium value. The probability of inducing a transition from a state with nuclear azimuthal quantum number m to one with quantum number m+1 is

$$W = \left(\frac{2\pi}{\hbar}\right) \sum_f |\langle f|\mathcal{H}^{(3)}|i\rangle|^2\, \delta(E_f - E_i) \tag{36}$$

and the relaxation rate for this process is

$$\left(\frac{1}{T}\right)_{3m} = 2W/(I-m)(I+m+1) \tag{37}$$

yielding finally as the total three-magnon relaxation rate

$$\begin{aligned}\left(\frac{1}{T}\right)_{3m} = \left(\frac{2\pi}{\hbar}\right)\left(\frac{A^2}{16N_A^3S_A}\right) \sum_{k_1,k_2,k_3} &\{(v_1v_2v_3)^2(n^{\alpha}_{k_1}+1)(n^{\alpha}_{k_2}+1)n^{\alpha}_{k_3} \\ &+ 4(u_1v_2v_3)^2 n^{\beta}_{k_1}(n^{\alpha}_{k_2}+1)n^{\alpha}_{k_3} + 4(v_1u_2u_3)^2(n^{\alpha}_{k_1}+1)n^{\beta}_{k_2}(n^{\beta}_{k_3}+1) \\ &+ (u_1u_2u_3)^2 n^{\beta}_{k_1}n^{\beta}_{k_2}(n^{\beta}_{k_3}+1)\}\ \delta(\hbar\omega_3 - \hbar\omega_2 - \hbar\omega_1)\end{aligned} \tag{38}$$

where, $n^{\alpha}_{k} = \dfrac{1}{\exp(\beta\hbar\omega^{\alpha}_{\vec{k}}) - 1}$, $n^{\beta}_{k} = \dfrac{1}{\exp(\beta\hbar\omega^{\beta}_{\vec{k}}) - 1}$

At low temperatures, since the ferrimagnetic optical or β-mode spin-wave branch of the spectrum is at much higher energy than the α-mode branch, it may be assumed that $n^{\beta}_{k} \simeq 0$. This leaves the first term in Equation 38, which is identical to the result obtained for a ferromagnet[64,66]. Thus, the relaxation rate is given by

$$\begin{aligned}\left(\frac{1}{T}\right)_{3m} = \left(\frac{2\pi}{\hbar}\right)\left(\frac{A^2}{16N_A^3S_A}\right) \sum_{k_1,k_2,k_3} &(v_1v_2v_3)^2\ (n^{\alpha}_{k_1}+1)(n^{\alpha}_{k_2}+1)n^{\alpha}_{k_3} \\ &\times\ \delta(\hbar\omega_{k_3} - \hbar\omega_{k_2} - \hbar\omega_{k_1})\end{aligned} \tag{39}$$

The triple sum in this expression can be transformed into a triple integral, yielding in the small-k approximation with $v_i \simeq \frac{1}{2} S_A/(S_B - \frac{1}{2} S_A)$,

$$\left(\frac{1}{T}\right)_{3m} = \left(\frac{2\pi}{\hbar}\right)\left(\frac{A^2}{16N_A^3S_A}\right)\left(\frac{\frac{1}{2}S_A}{S_B - \frac{1}{2}S_A}\right)^3 \quad \times$$

$$\times \int\int\int \frac{\nu(E_1)\,dE_1}{e^{\beta E_1}-1}\left(\frac{\nu(E_2)\,dE_2}{e^{\beta E_2}-1}\right)\frac{\nu(E_3)\,dE_3}{e^{\beta E_3}-1}\; e^{\beta(E_1+E_2)}\;\delta(E_3-E_2-E_1) \tag{40}$$

where $\nu(E)$ is the density of states at energy E. Then, using the transformations

$$x_i = (E_i/kT) = x_o + (\hbar\omega_e/kT)k_1^2 a^2$$

$$x_o = (g\mu_B H'/kT) \qquad , \qquad \hbar\omega_e = 2JS_{eff}(11/32)$$

the relaxation time is given, in the small-k and low temperature approximation, by

$$\left(\frac{1}{T}\right)_{3m} = \frac{2\pi}{\hbar}\left(\frac{A^2}{16S_A\hbar\omega_e}\right)\left(\frac{\tfrac{1}{2}S_A}{S_B-\tfrac{1}{2}S_A}\right)^3\left(\frac{1}{4\pi^2}\right)^3\left(\frac{1}{N_A}\right)^3\left(\frac{kT}{\hbar\omega_e}\right)^{7/2} I_{3m} \qquad ,(41)$$

The integral in this expression

$$I_{3m} = \int_{x_0}^{\infty}\int_{x_0}^{\infty} dx_1\,dx_2\left(\frac{(x_1-x_0)^{\frac{1}{2}}(x_2-x_0)^{\frac{1}{2}}(x_1+x_2-x_0)^{\frac{1}{2}}\,e^{x_1+x_2}}{(e^{x_1}-1)\,(e^{x_2}-1)\,(e^{x_1+x_2}-1)}\right) \qquad ,(42)$$

is, for $g\mu_B H' << kT$, independent of temperature and field and has a value of ∿ 7.6 [64,66].

Thus, the three-magnon scattering process provides a relaxation mechanism with a $T^{7/2}$ temperature dependence. The only difference between this result for a ferrimagnet and that for a ferromagnet[64] is in the factor $(\tfrac{1}{2}S_A/(S_B - \tfrac{1}{2}S_A))^3$.

4.2 Exchange enhancement of the three-magnon process

The presence of the four-magnon scattering terms in the spin-wave expansion of the exchange Hamiltonian, as discussed in Chapter I, Section 4.4-b , leads to a second order relaxation process[64,65,67] as illustrated in Figure 6, where, for those processes on the left in

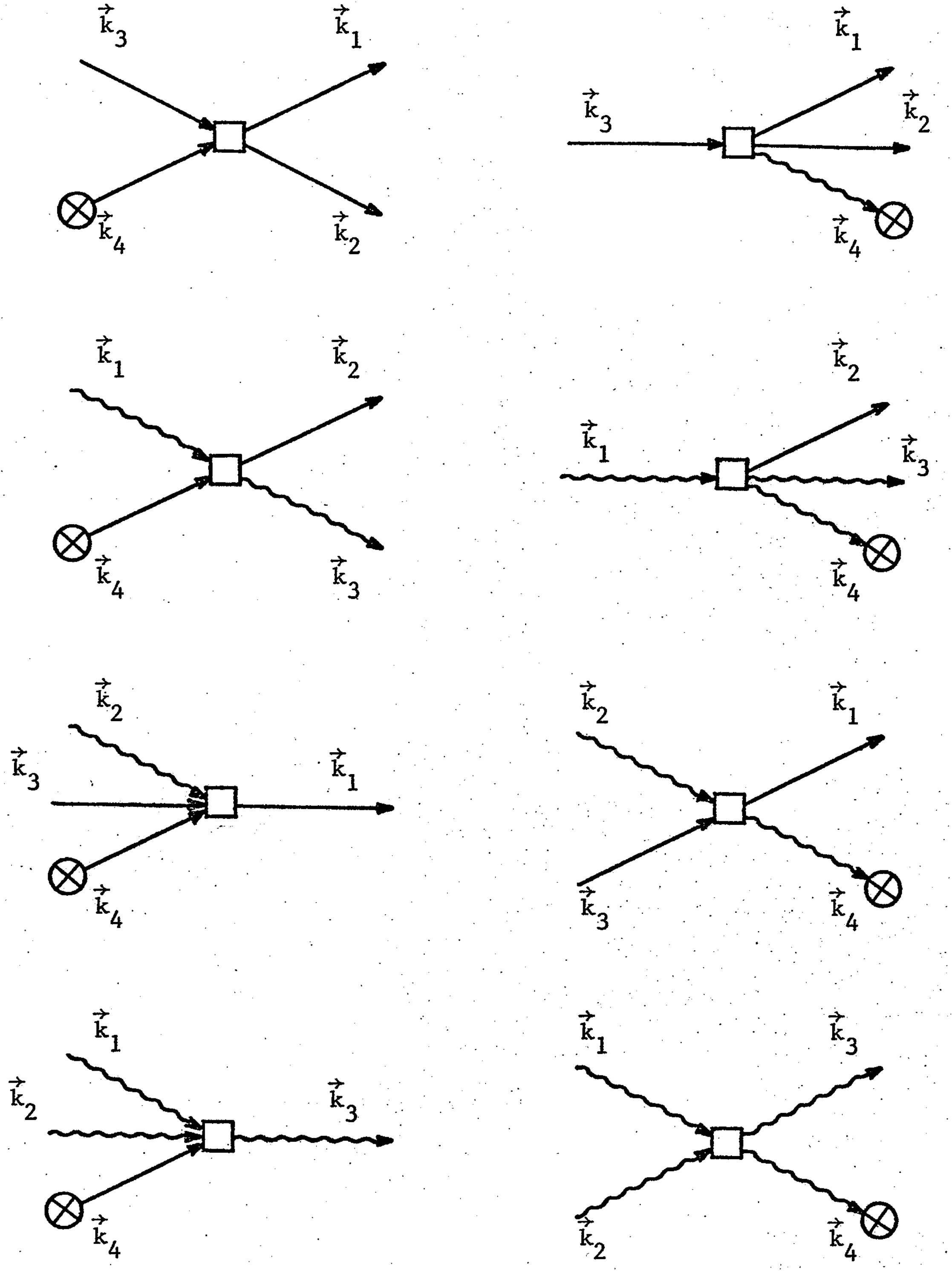

Figure 6. The four-magnon exchange scattering processes. k_4 represents a virtual magnon emitted or absorbed by the nucleus.

the figure, a virtual magnon is created by a nuclear spin-flip which then interacts with the electronic magnons via this four-magnon term, or, for the processes on the right side of the figure, the electronic magnons interact with each other producing, in the final state, one or two magnons plus a virtual magnon which is then absorbed by a nucleus, producing a nuclear spin flip. The initial and final electronic states can be seen to be identical to those for the three-magnon scattering processes illustrated in Figure 5. Thus, these terms must be included in an evaluation of the total three-magnon relaxation process.

The four-magnon terms in the exchange Hamiltonian are given in Equation I.39 (to order 1/S) . These terms, together with the one-magnon term in the expansion of the hyperfine interaction, given in Equation II.7 , combine to give, in a second order perturbation treatment, an effective three-magnon term such that [64,68]

$$<f|\mathcal{H}_{eff}|i> = \frac{<f|\mathcal{H}^{(4)}_{ex}|v><v|\mathcal{H}^{(1)}_{hf}|i>}{-E_{v\pm AS}} \tag{43}$$

where $|f>$ is the final state, $|i>$ the initial state, and $|v>$ is the intermediate state involving the virtual magnon, and $E_{v\pm AS}$ is the energy of the virtual magnon ($\hbar\omega_{\vec{k}_4}$) $\pm AS$ (the spin-flip energy). $AS << \hbar\omega_{\vec{k}_4}$ due to the large energy gap in the spin wave spectrum, and may be neglected.

To obtain the form of this effective interaction explicitly, recalling that only those terms involving only the α_k's need to be retained since $n^{\beta}_{k} \simeq 0$, the one-magnon term in the hyperfine interaction is written

$$\mathcal{H}^{(1)}_{hf} = -\frac{1}{2}A(2S_A)^{\frac{1}{2}} \sum_{k_4} (I^{+}_{k_4} v_{k_4} \alpha^{+}_{k_4} + I^{-}_{k_4} v_{k_4} \alpha_{k_4}) \quad ,(44)$$

where $\vec{k}_4$ is taken to be the wave-vector of the virtual magnon. Similarly, in transforming the four-magnon exchange Hamiltonian in terms of its normal mode operators α_k , β_k only the terms in the α_k's need to be retained. Then, substituting $a_k = -v_k\alpha_k^+$ and $b_k = u_k\alpha_k$ into Equation I.39, the four-magnon exchange scattering Hamiltonian becomes

$$
\begin{aligned}
\mathcal{H}_{ex}^{(4)} = & -\frac{1}{8} J \sum_{k_1,k_2,k_3,k_4} \delta(\vec{k}_1 + \vec{k}_2 - \vec{k}_3 - \vec{k}_4) \\
& X \; \{4(Z_A/N_B)\gamma^A_{-3-4}\, v_1v_2u_3u_4\alpha_1\alpha^+_{-2}\alpha^+_3\alpha_{-4} + 4(Z_B/N_A)\gamma^B_{3+4}u_1u_2v_3v_4\alpha^+_{-1}\alpha_2\alpha_{-3}\alpha^+_4 \\
& - Z_A(S_B/S_AN_AN_B)^{\frac{1}{2}}\gamma^A_{-4}\{v_1v_2v_3u_4\alpha_1\alpha^+_{-2}\alpha^+_3\alpha_{-4} + v_1v_2v_3u_4\alpha_1\alpha_2\alpha^+_3\alpha^+_4\} \\
& - Z_B(S_A/S_BN_AN_B)^{\frac{1}{2}}\{\gamma^B_{-2+3+4}v_1u_2u_3u_4\alpha^+_1\alpha^+_2\alpha_3\alpha_4 + \gamma^B_{2-3-4}v_1u_2u_3u_4\alpha_1\alpha^+_{-2}\alpha^+_3\alpha_{-4}\} \\
& - Z_A(S_AN_A/S_BN_B^3)^{\frac{1}{2}}\{\gamma^A_{1+2-3}u_1u_2u_3v_4\alpha^+_{-1}\alpha_2\alpha_{-3}\alpha^+_4 \qquad\qquad (45) \\
& \qquad\qquad + \gamma^A_{-1-2+3}u_1u_2u_3v_4\alpha^+_1\alpha^+_2\alpha_3\alpha_4\} \\
& - Z_B(S_BN_B/S_AN_A^3)^{\frac{1}{2}}\gamma^B_1\;\{u_1v_2v_3v_4\alpha_1\alpha_2\alpha^+_3\alpha^+_4 + u_1v_2v_3v_4\alpha^+_{-1}\alpha_2\alpha_{-3}\alpha^+_4\}\;\}
\end{aligned}
$$

where v_1 , α_3 are short for v_{k_1}, α_{k_3} , and $v_{-k} = v_k$, $u_{-k} = u_k$. By interchanging indices on a particular term this expression can be reduced to the following, where for small k, $u_k = u$, $v_k = v$,

$$
\mathcal{H}_{ex}^{(4)} = -\frac{1}{8} J\,(u^2v^2) \sum_{k_1,k_2,k_3,k_4} \delta(\vec{k}_1 + \vec{k}_2 - \vec{k}_3 - \vec{k}_4)\alpha^+_1\alpha^+_2\alpha_3\alpha_4 \quad \Phi^{(1,2)}_{(3,4)} \qquad ,(46)
$$

where the k-dependent function $\Phi^{(1,2)}_{(3,4)}$ is given by

$$
\Phi^{(1,2)}_{(3,4)} = 4\gamma^A_{-1+4}(Z_A/N_B) - \gamma^A_4\, Z_A(S_AN_A/S_BN_B^3)^{\frac{1}{2}}\,(u/v) -
$$

$$
\begin{aligned}
&- \gamma_3^B Z_B (S_A/S_B N_A N_B)^{1/2}(u/v) \quad + \quad 4\gamma_{2-3}^B (Z_B/N_A) \quad - \quad \gamma_{-2}^A Z_A (S_A N_A/S_B N_B^3)^{1/2}(u/v) \\
&- \gamma_{-1}^B Z_B (S_B N_B/S_A N_A^3)^{1/2}(v/u) \quad - \quad \gamma_{-1}^A Z_A (S_B/S_A N_A N_B)^{1/2}(v/u) \\
&- \gamma_4^B Z_B (S_B N_B/S_A N_A^3)^{1/2}(v/u) \quad - \quad \gamma_{-1}^B Z_B (S_A/S_B N_A N_B)^{1/2}(u/v) \qquad (47) \\
&- \gamma_4^A Z_A (S_A N_A/S_B N_B^3)^{1/2}(u/v)
\end{aligned}
$$

Then, to include those processes which are indistinguishable from the above[69], i.e., those described by $\Phi_{(3,4)}^{(2,1)}$, $\Phi_{(4,3)}^{(1,2)}$, and $\Phi_{(4,3)}^{(2,1)}$, the Hamiltonian is written as

$$
\begin{aligned}
\mathcal{H}_{ex}^{(4)} = -\frac{1}{32} J\, v^2 u^2 \sum_{k_1,k_2,k_3,k_4} \delta(\vec{k}_1 + \vec{k}_2 - \vec{k}_3 - \vec{k}_4)\alpha_1^+ \alpha_2^+ \alpha_3 \alpha_4 \\
\times \left\{\Phi_{(3,4)}^{(1,2)} + \Phi_{(3,4)}^{(2,1)} + \Phi_{(4,3)}^{(1,2)} + \Phi_{(4,3)}^{(2,1)}\right\} \qquad (48)
\end{aligned}
$$

or,

$$
\mathcal{H}_{ex}^{(4)} = -\frac{1}{32} J\, u^2 v^2 \sum_{k_1,k_2,k_3,k_4} \delta(\vec{k}_1 + \vec{k}_2 - \vec{k}_3 - \vec{k}_4)\ \alpha_1^+ \alpha_2^+ \alpha_3 \alpha_4\ K_{(3,4)}^{(1,2)} \qquad ,(49)
$$

where, since $v/u = \eta(S_A/S_B)^{1/2}$ and $\gamma_{-k} = \gamma_k$

$$
\begin{aligned}
K_{(3,4)}^{(1,2)} \;=\; & 4(\gamma_{-1+4}^A + \gamma_{-1+3}^A + \gamma_{-2+4}^A + \gamma_{-2+3}^A)(Z_A/N_B) \\
& + 4(\gamma_{2-3}^B + \gamma_{2-4}^B + \gamma_{1-3}^B + \gamma_{1-4}^B)(Z_B/N_A) \\
& - \eta\Big((\gamma_1^A + \gamma_2^A + \gamma_3^A + \gamma_4^A) Z_A\{(N_A/N_B^3)^{1/2} + 1/(N_A N_B)^{1/2}\} \qquad (50) \\
& + (\gamma_1^B + \gamma_2^B + \gamma_3^B + \gamma_4^B) Z_B\{(N_B/N_A)^{1/2} + 1/(N_A N_B)^{1/2}\}\Big)
\end{aligned}
$$

In the case where $Z_A = Z_B$, $N_A = N_B$, and $\gamma_k^A = \gamma_k^B$, this expression reduces to the usual form given for the ferromagnetic case, for small k, by

$$\mathcal{H}^{(4)'}_{ex} = (Ja_{nn}^2/2N) \sum_{k_1,k_2,k_3,k_4} \alpha_1^+\alpha_2^+\alpha_3\alpha_4 \; (\vec{k}_1\cdot\vec{k}_2 + \vec{k}_3\cdot\vec{k}_4) \; \delta(\vec{k}_1+\vec{k}_2-\vec{k}_3-\vec{k}_4) \qquad ,(51)$$

By inserting the one-magnon hyperfine Hamiltonian of Equation 44, and the four-magnon exchange scattering Hamiltonian given in Equation 49, into Equation 43 one obtains the effective three-magnon Hamiltonian

$$\begin{aligned}\mathcal{H}^{(3)'}_{eff} = -\frac{A}{8SN_A}(2S/N_A)^{\frac{1}{2}} \sum_{n} \sum_{k_1,k_2,k_3} I_n^+ \exp\{i(\vec{k}_1+\vec{k}_2-\vec{k}_3)\cdot\vec{r}_n\} \; \alpha_1^+\alpha_2^+\alpha_3 \\ X \left\{\frac{(1/8)SJu^2v^3N_A K^{(1,2)}_{(3,3-1-2)}}{\hbar(\omega_{\vec{k}_3} - \omega_{\vec{k}_1} - \omega_{\vec{k}_2})}\right\}\end{aligned} \qquad (52)$$

where the conservation of linear momentum, represented by the δ-function in Equation 49 has been used, and the spin-flip energy (AS) has been neglected. This may be combined with the direct three-magnon process Hamiltonian to give

$$\begin{aligned}\mathcal{H}^{(3)}_{eff} = \frac{A}{8SN_A}(2S/N_A)^{\frac{1}{2}} \sum_{n} \sum_{k_1,k_2,k_3} I_n^+ \exp\{i(\vec{k}_1+\vec{k}_2-\vec{k}_3)\cdot\vec{r}_n\} \; v^3 \; \alpha_1^+\alpha_2^+\alpha_3 \\ X \{1 - M(\vec{k}_1,\vec{k}_2,\vec{k}_3)\}\end{aligned} \qquad (53)$$

The relaxation rate due to this total three-magnon process is then calculated by the same method as used in obtaining Equation 41. The factor $M(\vec{k}_1,\vec{k}_2,\vec{k}_3)$, when reduced to a form--such as that corresponding to the special case of identical sublattices given in Equation 51--involving the scalar products of the wave-vectors, can be replaced by a suitable angular average leaving what amounts to an effective enhancement of the three-magnon process. In the case of ferromagnets[64] this enhancement to the relaxation rate is ∿ 8 while in antiferromagnets[64,68] an enhancement of ∿ 2 - 4 is expected. Thus, in the present ferrimagnetic case, an enhancement of a similar magnitude is expected. The calculation has not been carried out due to the complexity of the angular function involved, and also because the three-magnon process is not expected to be the most effective spin-wave relaxation process at very low temperatures.

The presence of the spin-wave energies in the denominator of the expression in Equation 52 introduce a field-dependence into the exchange enhancement process. Thus, there is expected to be a decrease in the effective three-magnon relaxation rate as the applied field is increased. Comparison with the data is left for Section 5 following the discussion of the dipolar induced two-magnon process in the next section.

4.3 Dipolar induced two-magnon process

As discussed in Section 4.1 the Raman or two-magnon scattering process is forbidden in colinear, isotropic spin systems by conservation of angular momentum. However, the terms such as $S^zS^{\pm}$ in the dipolar Hamiltonian, since they do not commute with S^z, need not conserve angular momentum and, therefore, in second order, allow a relaxation process wherein a nuclear spin emits or absorbs a virtual magnon which is scattered by two real magnons via the three-magnon terms in $S^zS^{\pm}$ given in Equation I.38. These terms ($S^zS^{\pm}$) connect states whose z-component of angular momentum differ by one unit, thus, the scattering processes which are allowed in a two sublattice system are those shown in Figure 7.

The virtual spin-wave involved in each of these diagrams is either created or destroyed, accompanying a nuclear spin-flip, by the one-magnon term in the hyperfine interaction just as in the case of the exchange-enhanced process discussed in the preceding section. As before, because of the large energy gap separating the two branches of the magnon spectrum

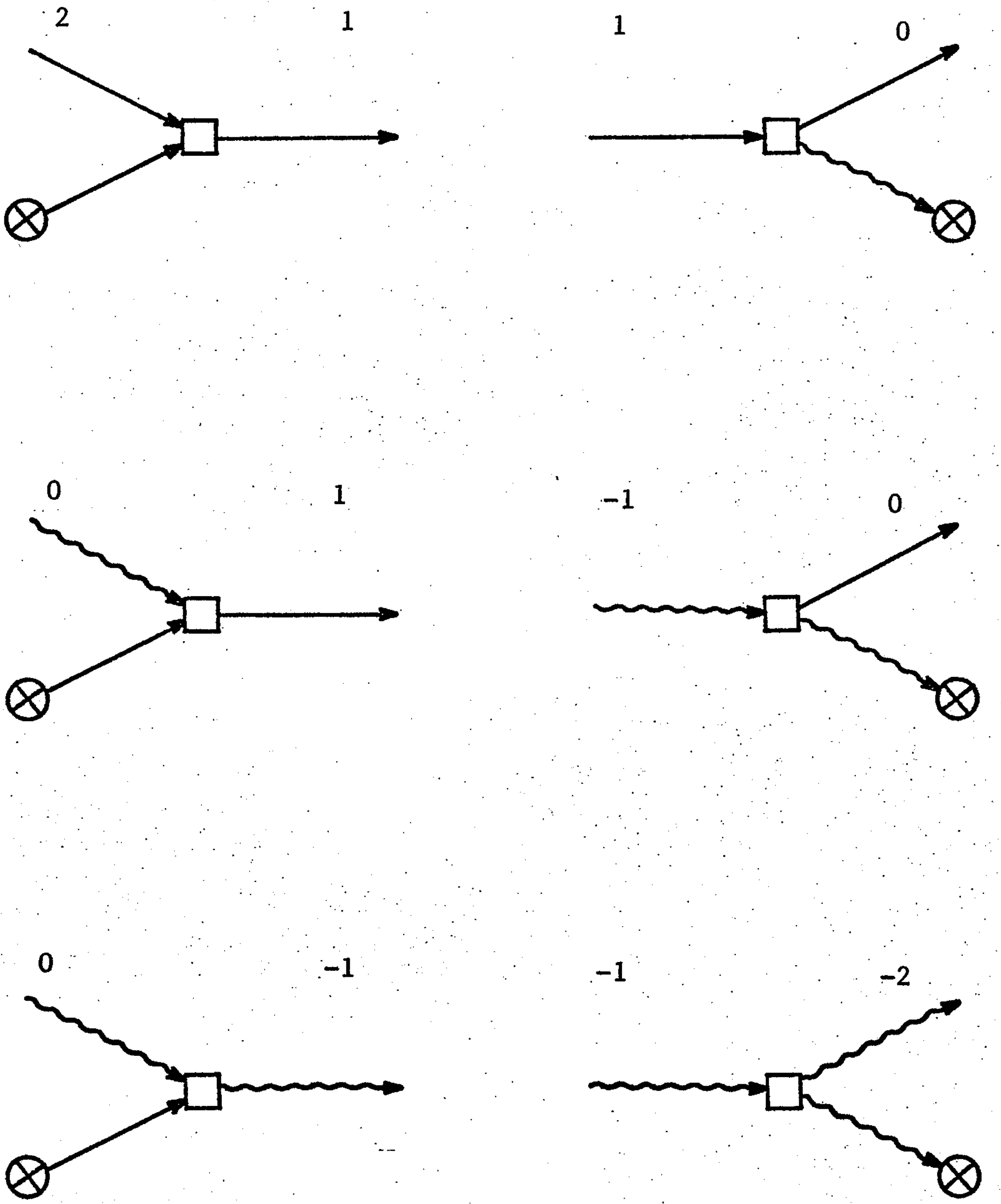

Figure 7. The dipolar-induced two-magnon processes. The numbers above each diagram refer to the z-component of angular momentum of each configuration.

in a ferrimagnet, we need to consider only the process described by the first diagram in Figure 7, that involving only α-mode magnons.

On transforming the Hamiltonian of Equation I.38 to normal mode operators α , β with $a_k = -v_k\alpha_k^+$ and $b_k = u_k\alpha_k$, the three-magnon term in the dipolar Hamiltonian becomes

$$\begin{aligned}\mathcal{H}_{dd}^{(3)} = -\sum_{k_1,k_2,k_3} \delta(\vec{k}_1+\vec{k}_2-\vec{k}_3)\ \Big\{(S_A/2N_A)^{\frac{1}{2}}\ \{\tfrac{1}{2}\,C_{A,A}^{(z,+)}(0) + K_{A,A}^{(z,+)}(\vec{k}_1) \\ -\tfrac{1}{2}(S_B/S_A)(N_B/N_A)^{\frac{1}{2}}\,K_{A,B}^{(z,+)}(0)\}(-v_1v_2v_3) + (S_B/2N_A)^{\frac{1}{2}}\,K_{A,B}^{(z,+)}(\vec{k}_1)(v_1v_2u_3) \\ + (S_A/2N_B)^{\frac{1}{2}}\,K_{A,B}^{(z,+)}(-\vec{k}_1)(u_1u_2v_3) - (S_B/2N_B)^{\frac{1}{2}}\ \{\tfrac{1}{2}\,C_{B,B}^{(z,+)}(0) \\ + K_{B,B}^{(z,+)}(\vec{k}_1) - \tfrac{1}{2}(S_A/S_B)(N_A/N_B)^{\frac{1}{2}}\,K_{A,B}^{(z,+)}(0)\}(u_1u_2u_3)\Big\}\ \alpha_1\alpha_2\alpha_3^+ \\ + \text{(complex conjugate)} \\ = -\sum_{k_1,k_2,k_3} \delta(\vec{k}_1+\vec{k}_2-\vec{k}_3)\ F(\vec{k}_1)\ \alpha_1\alpha_2\alpha_3^+ \quad + \text{ c.c.}\end{aligned} \quad ,(54)$$

In this expression the factor $F(\vec{k}_1)$ is a function only of $\vec{k}_1$, since for small k_i , $u_1 = u_2 = u_3$, $v_1 = v_2 = v_3$. Since this interaction arises from the $S^zS^\pm$ terms in the dipole-dipole Hamiltonian, $F(\vec{k}) \propto k^zk^\pm/k^2$, as discussed in Section I.4.3 . A term which is independent of k, due to the $K_B^{(z,+)}(0)$ terms, which is $\sim \Sigma_\delta\ R_\delta^zR_\delta^-/R_\delta^5$, vanishes in the case of a spinel lattice due to the cubic A-site symmetry and the trigonal axis symmetry of the B-sites.

Then, following the same procedure as used for the exchange-enhancement process, with

$$<f|\mathcal{H}_{eff}^{(2)}|i> \;=\; \frac{<f|\mathcal{H}_{dd}^{(3)}|v><v|\mathcal{H}_{hf}^{(1)}|i>}{-\hbar\omega_{\vec{k}_v}}$$

the effective two-magnon Hamiltonian is given by, (with $S' = (N_B/N_A)S_{eff}$)

$$\mathcal{H}_{eff}^{(2)} = -\frac{1}{2}\,Au^2v^2\; g\mu_B(4\pi M'/V)(S_A/S')\;\sum_n I_n^+ \sum_{k,k'} \exp\{i(\vec{k}' - \vec{k})\cdot\vec{r}_n\}$$

$$\times\;\left(\frac{k^+k^z}{k^2} + \frac{(k' - k)^+(k' - k)^z}{(\vec{k}' - \vec{k})\cdot(\vec{k}' - \vec{k})}\right)\left(\frac{1}{E(\vec{k}' - \vec{k})}\right)\alpha_k\alpha_{k'}^+ \tag{55}$$

where $M' = g\mu_B S'\bar{N}_A\{(N_BS_B - N_AS_A)^2/N_AS_AN_BS_B\}$, as derived in Chapter I, and $E(\vec{k})$ is the spin-wave energy. The case where magnons $\vec{k}_1$ and $\vec{k}_2$, in Equation 54, have been interchanged, has been explicitly included.

The relaxation rate is given by

$$(1/T_1)_{2m} = \frac{\pi}{\hbar}\,(v^2)^2\,\{Ag\mu_B(4\pi M'/V)\}^2\;\sum_f\;|<f|\left(\sum_{k',k}\right.$$

$$\left.\times\;\left(\frac{k^+k^z}{k^2} + \frac{(k' - k)^+(k' - k)^z}{(\vec{k}' - \vec{k})\;\;(\vec{k}' - \vec{k})}\right)\frac{\alpha_k\alpha_{k'}^+}{E(\vec{k}' - \vec{k})}\right)|i>|^2\;\delta(E_f - E_i) \tag{56}$$

$$= \frac{\pi}{\hbar}\,(v^2)^2\,\{Ag\mu_B(4\pi M'/V)\}^2\sum_{k',k}\left(\frac{k^+k^z}{k^2} + \right.$$

$$\left.\frac{(k' - k)^+(k' - k)^z}{(\vec{k}' - \vec{k})\cdot(\vec{k}' - \vec{k})}\right)^2\left(\frac{1}{E(\vec{k}' - \vec{k})}\right)^2 n_k^\alpha(n_{k'}^\alpha + 1)\;\delta(E_f - E_i)$$

The sums may be replaced by integrals in the usual manner giving, for the angular part, the integral Φ

$$\Phi = \int\!\!\int\!\!\int\!\!\int\left(\frac{k^+k^z}{k^2} + \frac{(k' - k)^+(k' - k)^z}{(\vec{k}' - \vec{k})\cdot(\vec{k}' - \vec{k})}\right)^2\left(\frac{1}{E(\vec{k}' - \vec{k})}\right)^2 d\cos\theta\; d\phi\; d\cos\theta'\; d\phi'$$

$$\approx \left(\frac{1}{g\mu_B H}\right)^2\int\!\!\int\!\!\int\!\!\int\left(\frac{k^+k^z}{k^2} + \frac{(k' - k)^+(k' - k)^z}{(\vec{k}' - \vec{k})\cdot(\vec{k}' - \vec{k})}\right)^2 \quad\times$$

$$\text{X} \quad \{1 - \frac{4\alpha^2 k^2}{g\mu_B H}\} \, d\cos\theta \; d\phi \; d\cos\theta' \; d\phi' \qquad (57)$$

since $E(\vec{k}' - \vec{k}) = g\mu_B H + \alpha^2(\vec{k}' - \vec{k})^2 \simeq g\mu_B H + 2\alpha^2 k^2(1 - \cos\gamma)$, where γ , the angle between wavevectors $\vec{k}$ and $\vec{k}'$, is small. With this approximation, to second order in γ ,

$$\Phi = \frac{32\pi^2}{15} \qquad (+ O(\gamma^4))$$

Then, the relaxation is given by

$$(1/T_1)_{2m} = \frac{16}{15}\,\frac{(v^2)^2}{2\pi}\,(Ag\mu_B M')^2(1/g\mu_B H)^2(1/\bar{N}_A)^2$$

$$\text{X} \int\!\!\int k^2 dk \; k'^2 dk' \; n_k^\alpha(n_{k'}^\alpha + 1) \; \delta(E_{k'} - E_k) \qquad (58)$$

$$= (A^2/\hbar^2\omega_e)(g\mu_B M'/\bar{N}_A\hbar\omega_e)^2(v^2)^2 \, \frac{2}{15\pi} \left(\frac{kT}{g\mu_B H}\right)^2 \log\left(\frac{\exp(g\mu_B H/kT)}{\exp(g\mu_B H/kT) - 1} \right)$$

This approximate expression exhibits explicitly the roughly $\sim (T/H)^2$ behaviour obtained graphically by Beeman and Pincus[64].

The dipolar-induced two-magnon process and the exchange enhanced three-magnon process are the two most effective spin-wave relaxation mechanisms when the direct and Raman processes are forbidden. The characteristic temperature dependences of these two processes suggest that at very low temperatures the two-magnon process will be the stronger of the two, while at higher temperatures, the three-magnon process should dominate. The comparison of the calculated relaxation rates to the experimental values is deferred till Chapter IV since these background relaxation rates could not be measured until a method for the separation of domain and domain-wall components of the signal was devised.

5. Frequency Dependent Relaxation--Comparison with Data--Relaxation of Multiple Echoes

As shown in Section 3, the Suhl-Nakamura relaxation rate shows a strong frequency dependence such that $(1/T_2)_{S-N} \alpha\ g(\nu)$, where $g(\nu)$ is the inhomogeneously broadened lineshape function. The very strong inhomogeneous broadening in manganese ferrite, resulting in a half-width at half-maximum of ~ 1 MHz, allows the direct measurement of this frequency dependent relaxation. Figure 8 gives an illustration of this effect in a single crystal sample[70] of roughly ellipsoidal shape, of $Ni_{.03}Mn_{.62}Fe_{2.36}O_4$. These relaxation times were measured by comparing the echo decay envelope to an exponential of known time constant. The open circles are for data taken at $T = 4.2\ ^{o}K$ in an external field of $H_{ext} = 3$ kOe, sufficient to effectively saturate this sample, while the solid circles are from data taken at 77 ^{o}K in the same external field. The error bars for the lower temperature data, and the size of the circles for the 77 ^{o}K data represent an estimated error of $\sim$ 10%.

The straightforward calculation of the Suhl-Nakamura relaxation time using Equation 28 gives a value which is considerably larger than that measured, suggesting that the asymptotic range function has underestimated the true range function by a factor of $\sim 2 - 3$. The asymptotic range function is good for $r/a_{nn} >> 1$. Thus, the short-wavelength (large k) contribution may be underestimated[60], particularly in cases such as this with a large number of near neighbor identical nuclei (a spinel A-site has 12 next-nearest neighbor A-sites). Then, using the value of exchange energy, $\hbar\omega_e = 6 \times 10^{-16}$ ergs, obtained from the spin-wave relaxation time calculation for the two-magnon process (for a $MnFe_2O_4$ crystal, discussed in Chapter IV, Section 3.2) and, at $T = 4.2\ ^{o}K$, $H_K = 1.0$ kOe, $H_N = 559.5$ kOe, and with a frequency in-

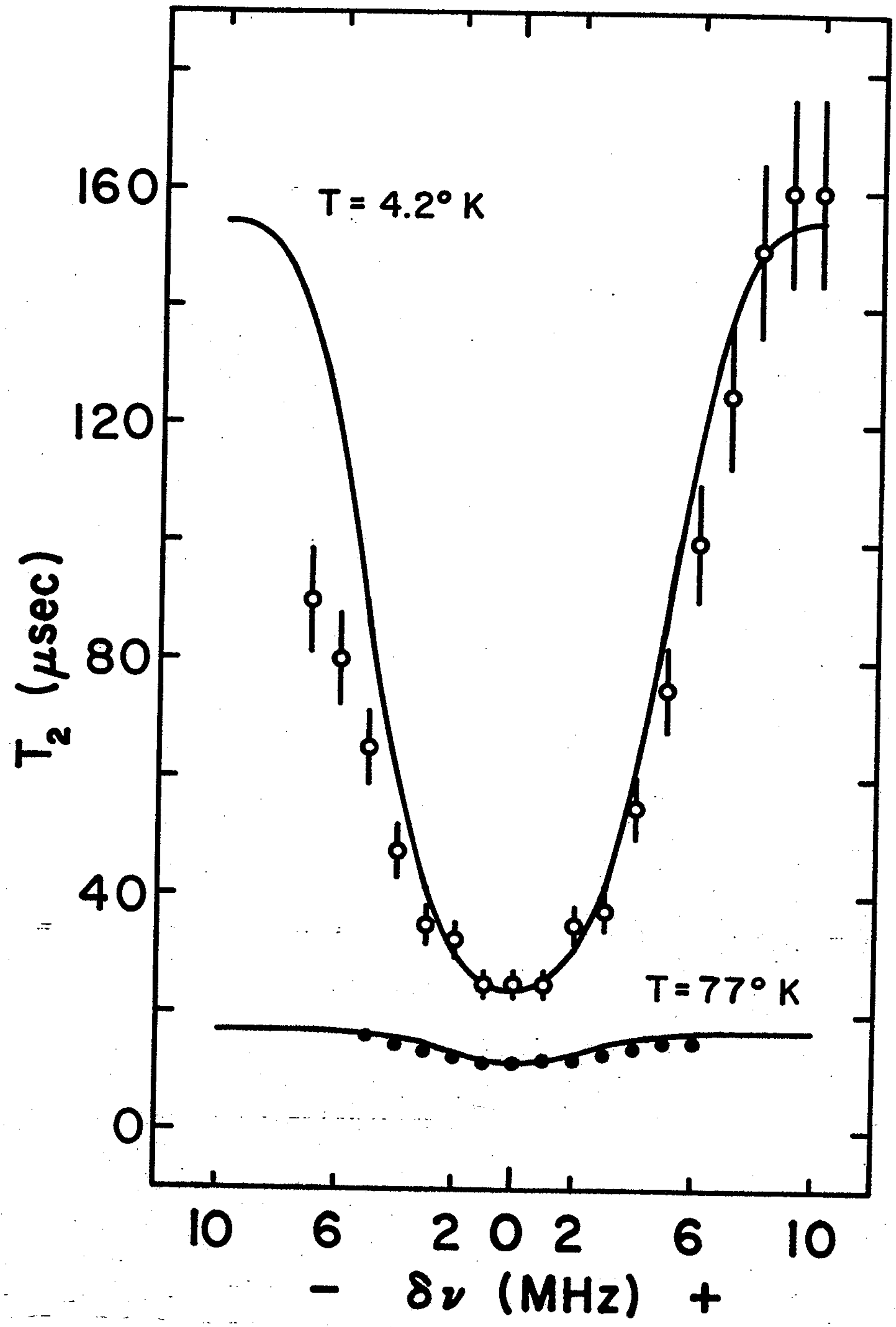

Figure 8. Frequency dependent relaxation in $Ni_{0.03}Mn_{0.62}Fe_{2.36}O_4$

dependent background relaxation time of ∿ 155 μsec, the asymptotic range function, when multiplied by a factor of ∿ 2.06, gives a reasonably good fit to the data, as shown by the upper solid curve in the figure. The fit to the T = 77 ^{o}K data uses H_K = 1.5 kOe, H_N = 555.4 kOe, and a background relaxation time of ∿ 17 μsec, all other parameters remaining the same, and is shown by the lower curve in the figure. (The necessity of including this numerical factor in the range function points out an error in the calculation of the Suhl-Nakamura relaxation times in reference 51.) A more precise calculation of the range function should yield results more in agreement with experiment, however, the relatively complex lattice structure makes this difficult. The procedure used here is felt to be justifiable since the expression, Equation 28, for the Suhl-Nakamura relaxation time, shows a characteristic field dependence due to the form of the range function, while the transverse part of the dipole-dipole relaxation, which exhibits a frequency dependence much like that of the Suhl-Nakamura relaxation, is independent of field. Figure 9 shows the total relaxation time at the central (or resonance) frequency as a function of external magnetic field, for the same sample as discussed above, at T = 1.5 and 4.2 ^{o}K. The solid curves are the calculated relaxation times at resonance using the same parameters as used in fitting the data in Figure 8 except that at T = 1.5 ^{o}K the background relaxation time and the anisotropy field were taken to be ∿ 250 μsec and 0.7 kOe, respectively. This field dependence completes the identification of the spin-spin relaxation as being primarily due to the Suhl-Nakamura interaction. The transverse dipole-dipole interaction, since it is field independent, should become more important at higher fields, since the Suhl-Nakamura interaction is becoming less effective, and the total relaxation time at resonance is expected to increase less rapidly with field than calculated assuming Suhl-Nakamura relaxation alone.

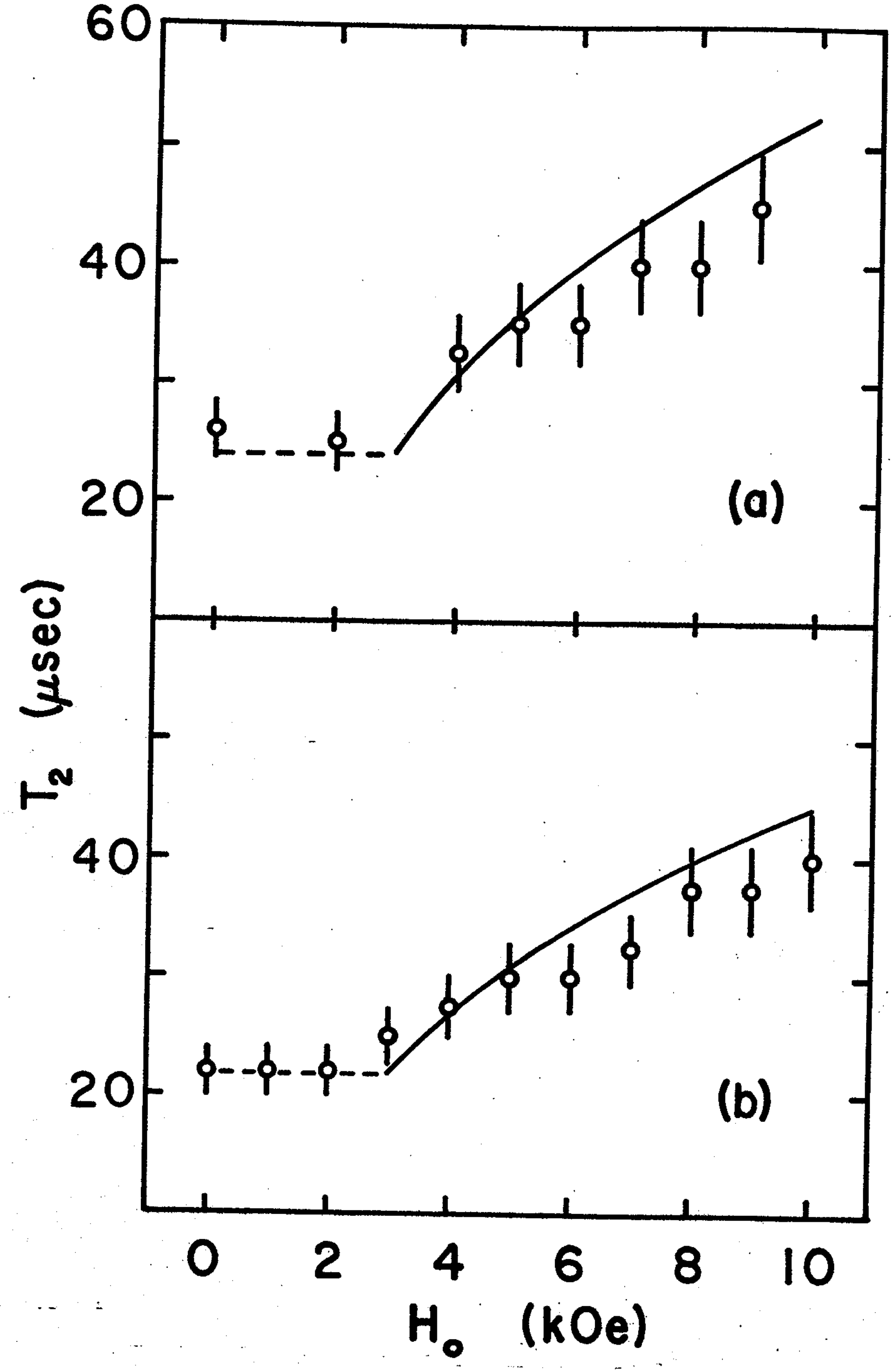

Figure 9. Field dependence of total relaxation time at resonance.

The multiple echoes observed in manganese ferrites, and discussed in Chapter II, exhibit the same frequency and field dependences as the first echo does. The open circles in Figure 10 are the relaxation times for the $Ni_{.03}Mn_{.62}Fe_{2.36}O_4$ sample at T = 1.5 ^oK, corresponding to the decay envelope of the first echo. The solid curve for this case again is the calculated relaxation time, assuming a background relaxation time of ∿ 250 μsec. The solid circles in this figure are the decay times of the second echo's decay envelope, at the same temperature. The calculated curve in this case was obtained by a computer calculation based on the density matrix method discussed in Chapter II, where the first echo (i.e., the effective third pulse) was allowed to decrease in amplitude, with pulse separation τ , as $\exp(-2\tau/T_2)$. This naturally leads to the more rapid decay with τ of the higher order echoes. There are no adjustable parameters in calculating the second echo relaxation time, the observed first echo minimum $T_2 \simeq 33$ μsec predicts straightforwardly a second echo minimum $T_2 \simeq 20$ μsec, as shown in the figure.

Figure 11 shows the frequency dependence of the amplitudes and relaxation times for the first four echoes in a field H_{ext} = 0.0 kOe at T = 1.5 ^oK. The echo amplitudes show the same lineshape and linewidth for each of the echoes, and the relaxation times show the same behaviour, as expected. It is interesting to note, however, that echoes 2-4 have maxima at $\nu \simeq 588$ MHz while echo 1 has its maximum at $\nu \simeq 586.5$ MHz. This seems to suggest that the first echo has some domain-wall component (since the domain-wall signal occurs at a frequency slightly below that of the domain component), while the higher echoes do not. In Figure 12, which is similar to Figure 11 but for H_{ext} = 4.0 kOe, sufficient to effectively saturate the sample, all of the echoes have maxima at

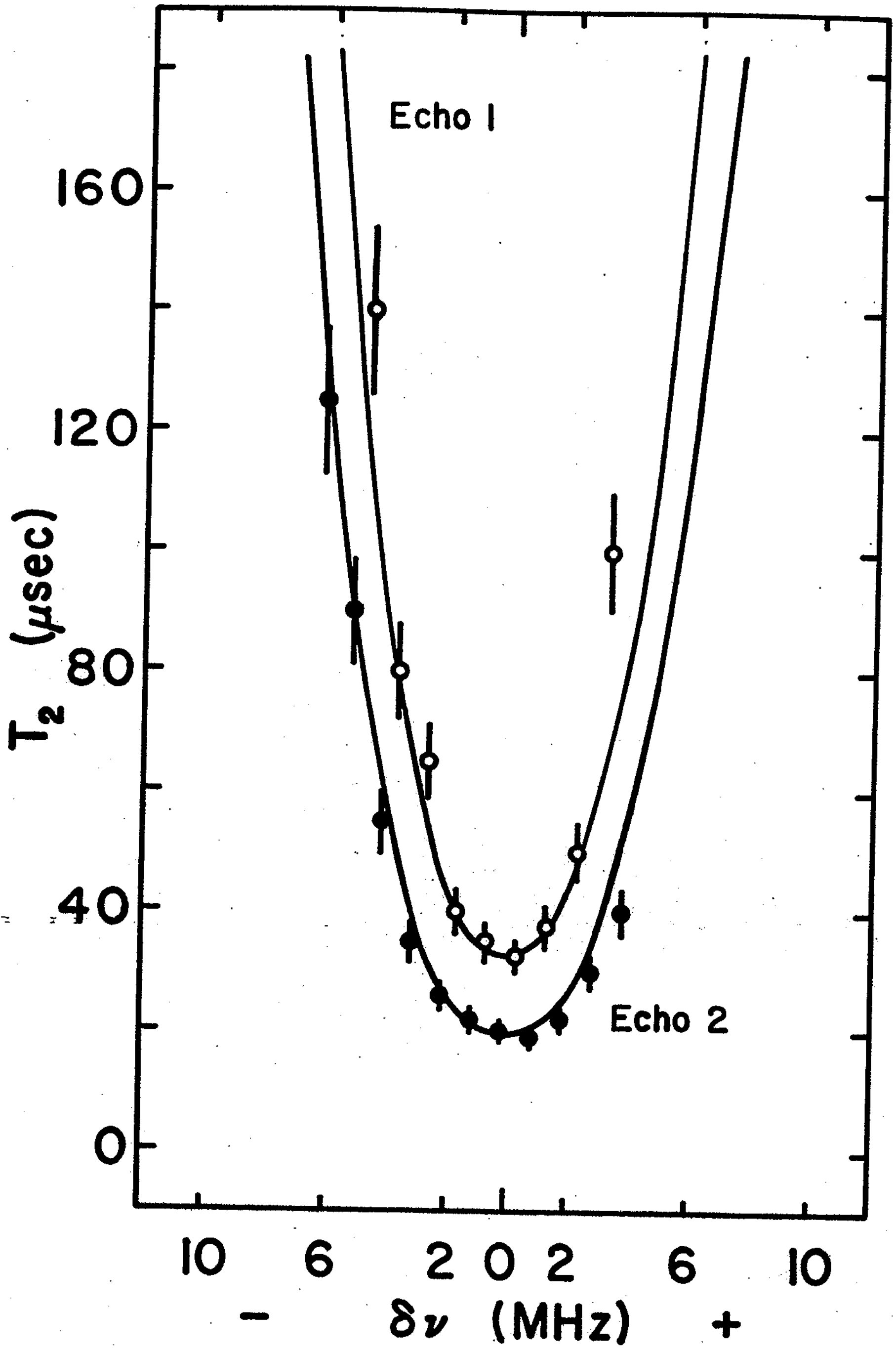

Figure 10. Frequency dependent relaxation of first two echoes at T = 1.5 °K.

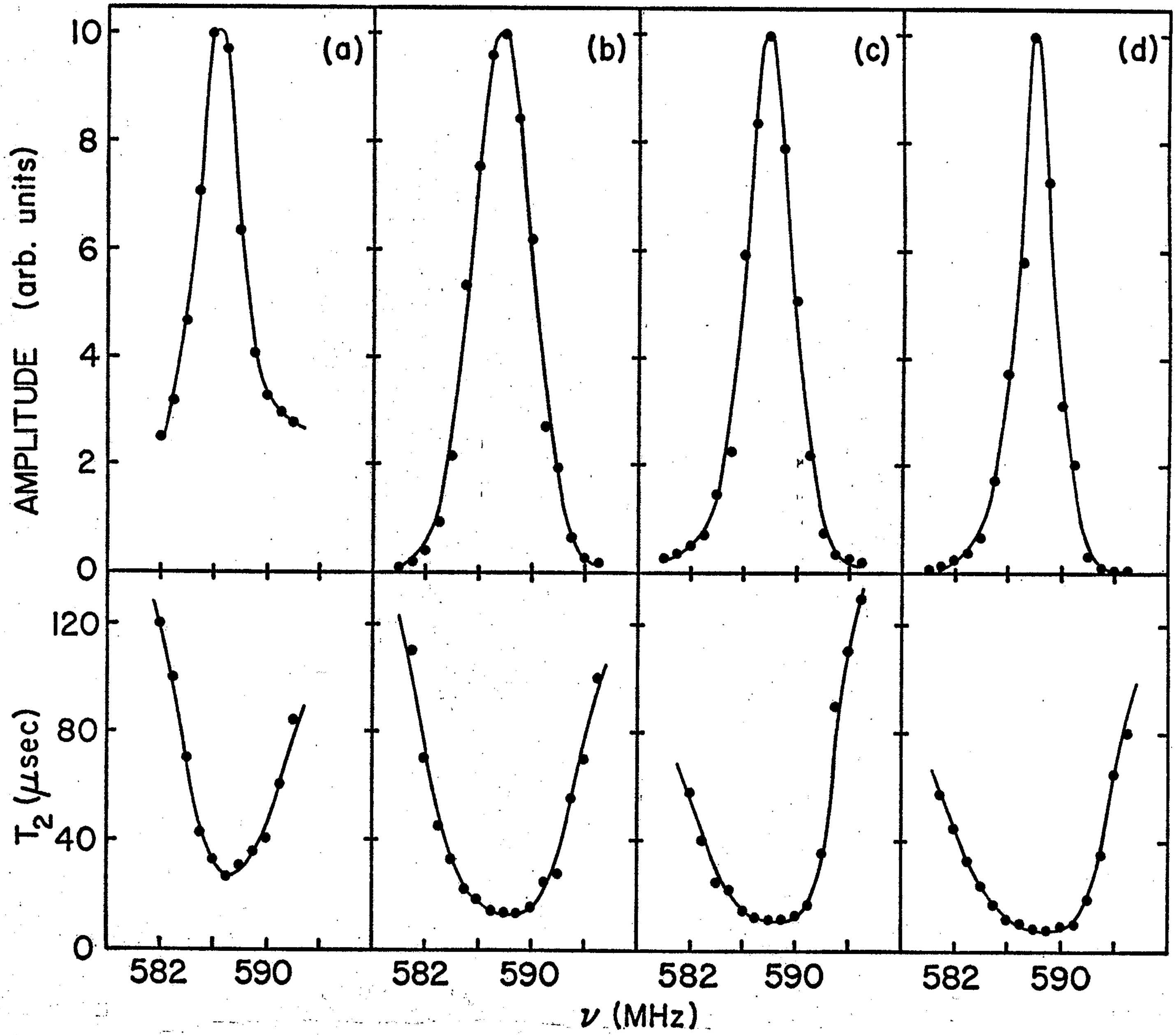

Figure 11. Echo amplitude extrapolated to $\tau = 0$ and relaxation time versus frequency for the first four echoes at $T = 1.5\ {}^{o}K$ in $H_o = 0$ kOe. a) first echo, b) second echo, c) third echo, d) fourth echo.

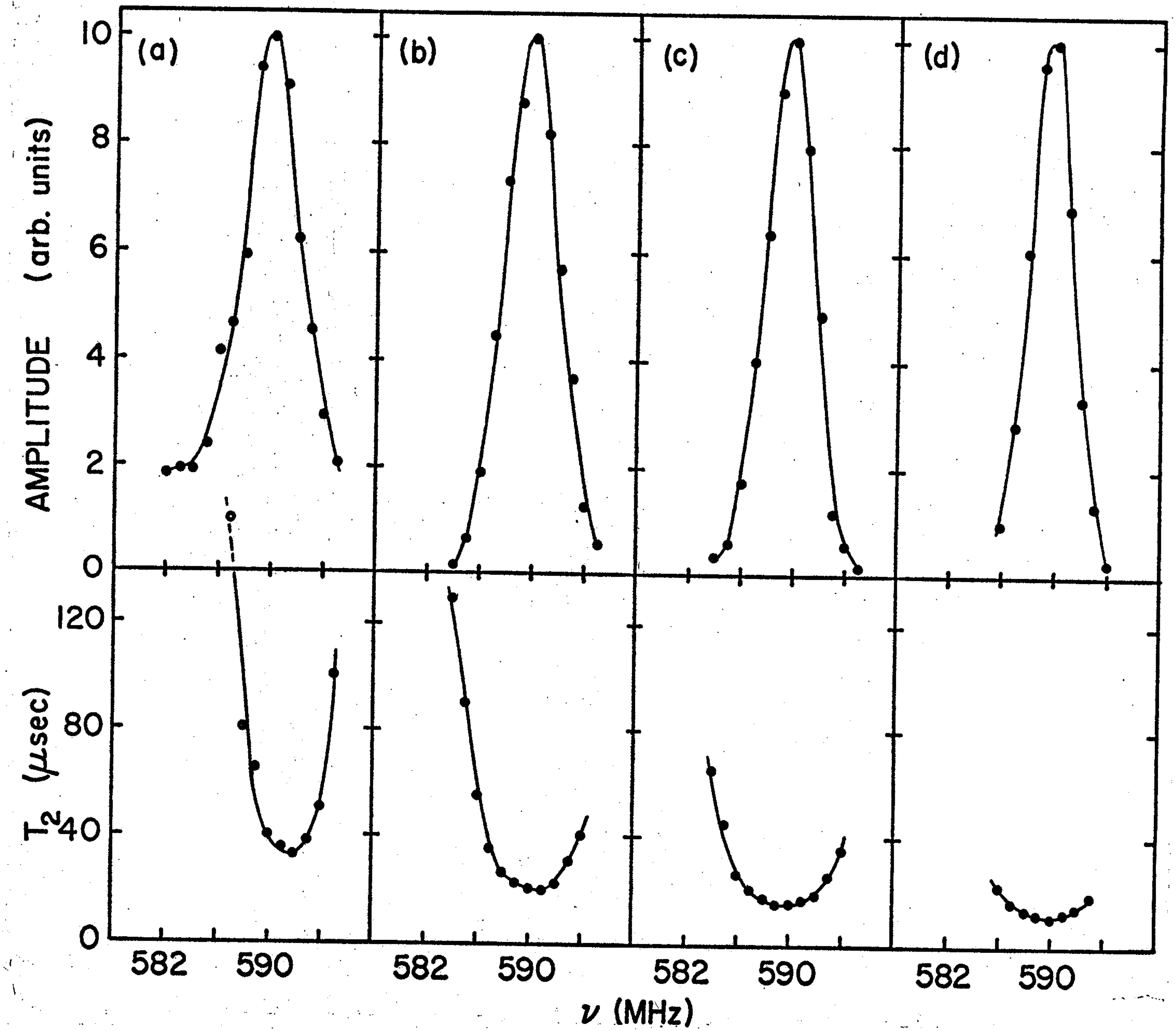

Figure 12. Echo amplitude extrapolated to $\tau = 0$ and relaxation time versus frequency for the first four echoes at $T = 1.5$ °K in $H_o = 4$ kOe. a) first echo, b) second echo, c) third echo, d) fourth echo.

ν = 590 MHz. Thus, it appears that either the domain-wall component does not contribute to the formation of multiple echoes, or that the relaxation time of the domain-wall component's contribution to higher echoes is so much shorter than that of the domain signal's contribution that it is effectively unobservable. It will be seen in Chapter IV that the domain-wall component of the first echo does have a considerably shorter relaxation time.

The higher numbered echoes will also exhibit a field dependence like that of the first echo. The measured values of the second echo relaxation time as a function of H_{ext} are compared with the values calculated, in the same manner as the frequency dependence of the second echo relaxation time, at T = 1.5 ^{o}K, in Figure 13-a, and at T = 4.2 ^{o}K, in Figure 13-b. The calculated values do not quite follow the measured times, particularly at the lower temperature. The third echo relaxation time at these same temperatures are plotted against external field in Figures 14-a,b. The solid curves are the relaxation times calculated neglecting the refocusing effects of the second echo, thus the agreement is not expected to be very good.

The generation and relaxation of multiple echoes, as well as the more basic resonance and relaxation data for the first echo, particularly the frequency and field dependences of the relaxation time, appear to be well explained by the Suhl-Nakamura spin-spin interaction, at least in the single-domain or saturated region. The background relaxation process, which is strongly temperature dependent and therefore likely due to spin-wave scattering, requires a more detailed study to identify the particular mechanism, and will be discussed in the next chapter. In the multi-domain region, however, the nuclei within

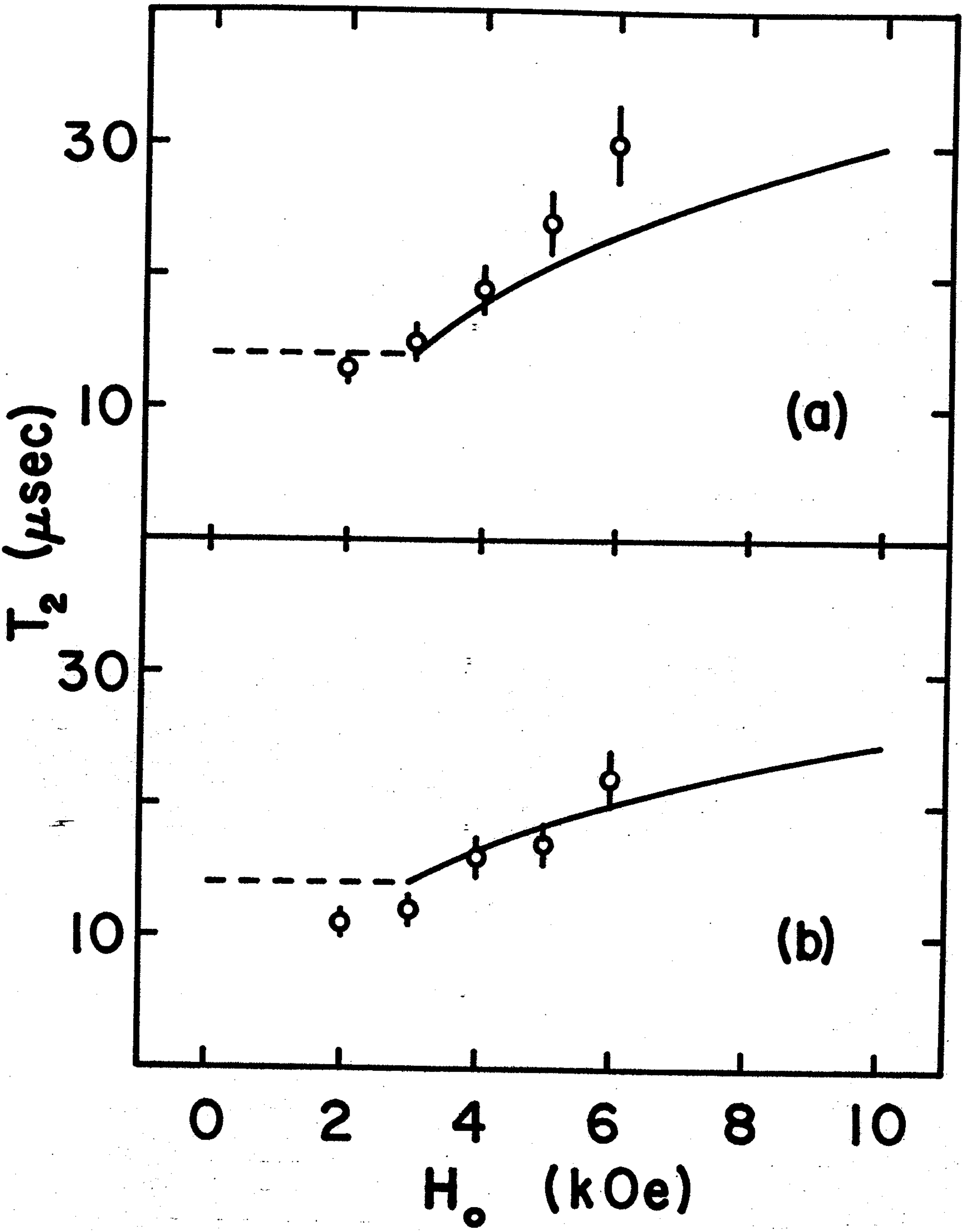

Figure 13. Field dependence of total relaxation time at resonance of the second echo. a) T = 1.5 °K, b) T = 4.2 °K.

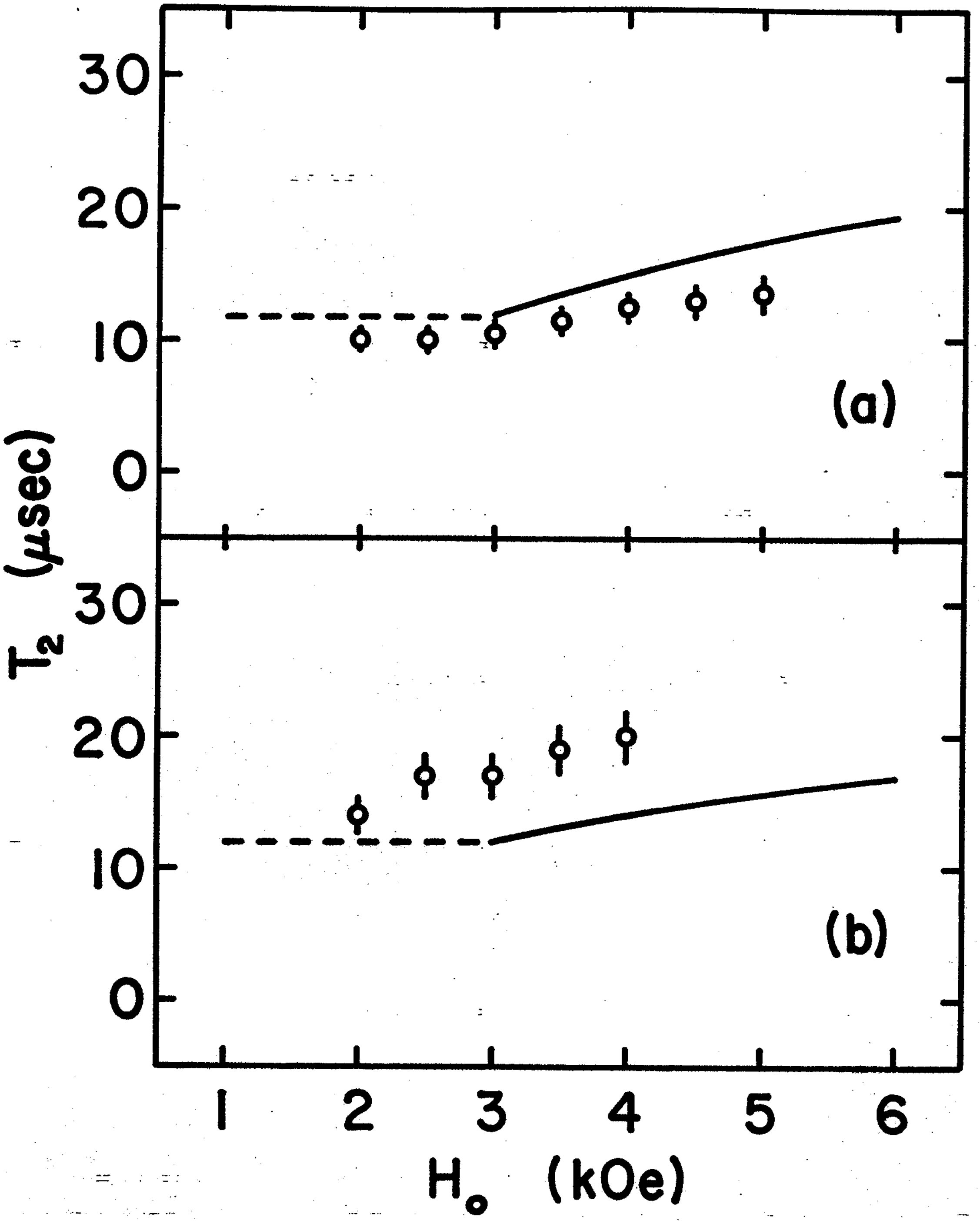

Figure 14. Field dependence of total relaxation time at resonance of the third echo. a) T = 1.5 °K, b) T = 4.2 °K.

domain walls are expected to give a large contribution to the signal, due to the large enhancement factor (see Chapter I), and the spectrum should consist of two overlapping resonance lines.

6. The Multi-Domain Spectra

The spectrum in Figure 15-a was taken at 4.2 ^{o}K in zero field on the $Ni_{0.03}Mn_{0.62}Fe_{1.36}O_4$ crystal, and shows some indication of the presence of two components to the signal for this sample. The spectra in Figure 15-b,c , taken at the same temperature and field as that in part a of the figure, are for polycrystalline samples of $Mn_xFe_{3-x}O_4$ with x = 0.8 and 1.0 respectively. These spectra show more clearly the two component nature of the signal. In particular, the x = 1.0 spectrum in Figure 15-c shows two clear maxima while the relaxation time data gives an indication of the presence of two minima (the echo decay envelopes are quite non-exponential for some frequencies).

Figure 16-a, on the other hand, shows the echo decay envelope of the x = 1.0 sample in zero field at 586 MHz and T = 1.47 ^{o}K. The solid curve is the best fit assuming a single relaxation time, and the decay is quite obviously non-exponential. An obvious explanation for a non-exponential echo decay, in this case, is the presence of two independently relaxing resonance lines. Figure 16-b shows the data of Figure 16-a replotted and fit to the function $A_1\exp(-2\tau/T_1) + A_2\exp(-2\tau/T_2)$, where the subscripts on the A's and T's refer to the two signal components. The fit to this function is quite good, suggesting that the echo does consist of two independently relaxing components. However, spectral diffusion[32,71-73] can also lead to non-exponential decay, in particular, the echo is expected to decay as $\exp(-\kappa\tau^2)$ or $\exp(-\kappa\tau^3)$

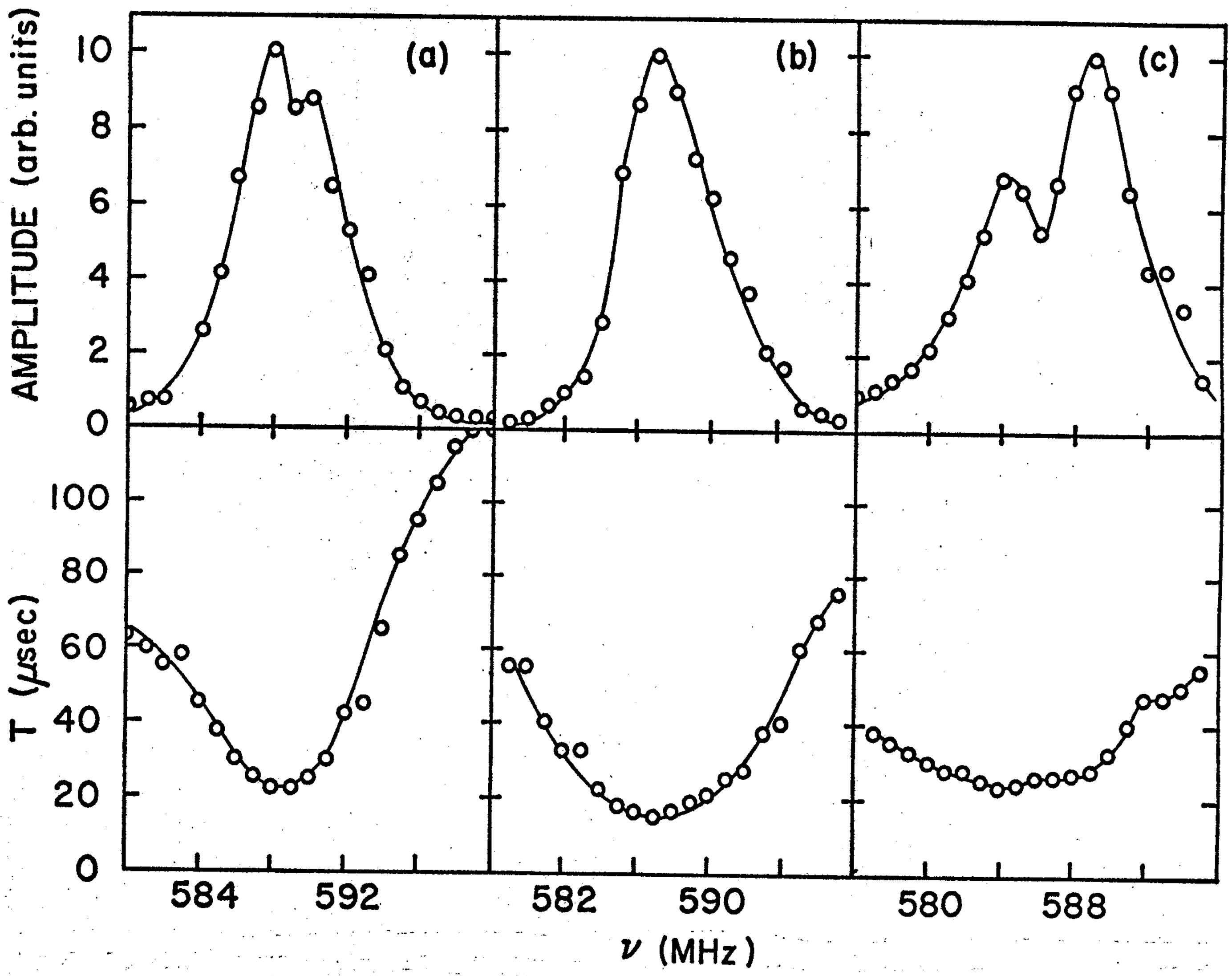

Figure 15. Echo amplitude extrapolated to $\tau = 0$ and relaxation time versus frequency at $T = 4.2$ °K. a) $Ni_{0.03}Mn_{0.62}Fe_{2.36}O_4$ single crystal, b) polycrystalline $Mn_{0.8}Fe_{2.2}O_4$, c) polycrystalline $Mn_{1.0}Fe_{2.0}O_4$.

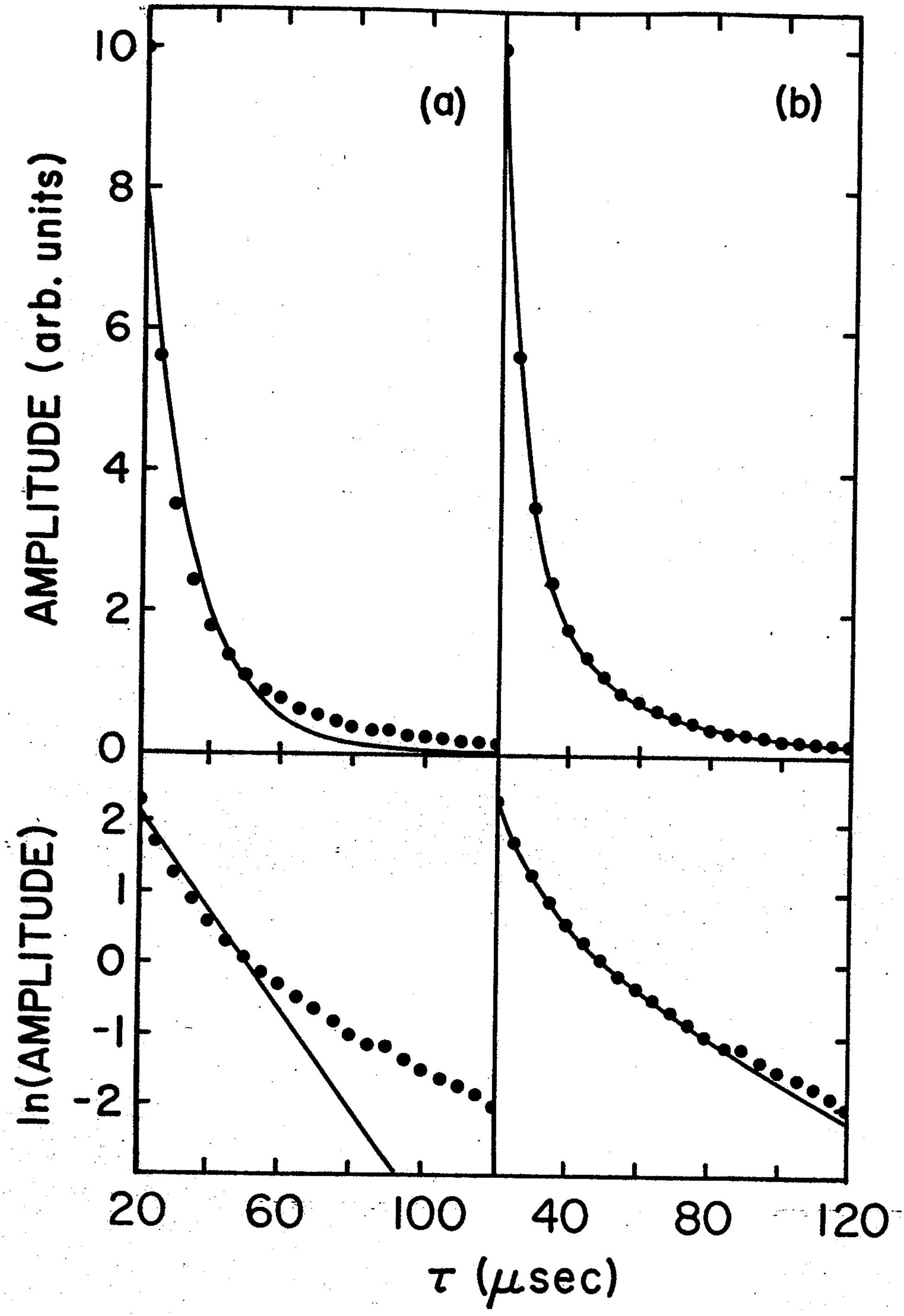

Figure 16. Echo amplitude and ln(echo amplitude) versus at $T = 1.47$ °K, $\nu = 586$ MHz, and $H_o = 0.0$ kOe. a) fit to a single exponential, b) fit to the sum of two exponentials.

for Lorentzian and Gaussian diffusion processes, respectively. Neither of these decay functions, nor the product of both of them, when multiplied by exp(-t/T) give a reasonable fit to the data. Thus, although spectral diffusion cannot be ruled out completely (see Chapter IV for a further discussion of spectral diffusion), it cannot be measured by the decay of the two-pulse echo.

When a magnetic field large enough to saturate the sample is applied, the signal from domain walls should vanish (since the walls themselves have been removed) and the echo decay envelope should be a simple exponential. Figure 17 shows the echo decay for a single crystal sphere of $MnFe_2O_4$ at 4.2 ^oK in external fields of H_{ext} = 2.0 kOe, for the lower curve, and H_{ext} = 7.0 kOe for the upper curve, at frequencies corresponding to maximum overlap of domain and domain-wall signal components at the different values of field[74]. The effect is as expected and demonstrates that the observed echo decay can be analyzed in a two component model. The separation of the two components would appear to be the straightforward procedure of doing a least squares fit to a set of decay curves such as those in Figures 16-17 for all frequencies to obtain two complete spectra together with their frequency dependent relaxation times. The result of such a procedure is shown in Figure 18 which is a plot of the parameters obtained from a least squares fit to the sum of two exponentials versus frequency. In the central region, the region of maximum overlap of the two components, the corresponding parameters of the two signal components do not differ by very much and cannot be uniquely determined or identified. Thus, a more careful analysis is required, one which considers the entire set of echo decay envelopes at once. This can be ac-

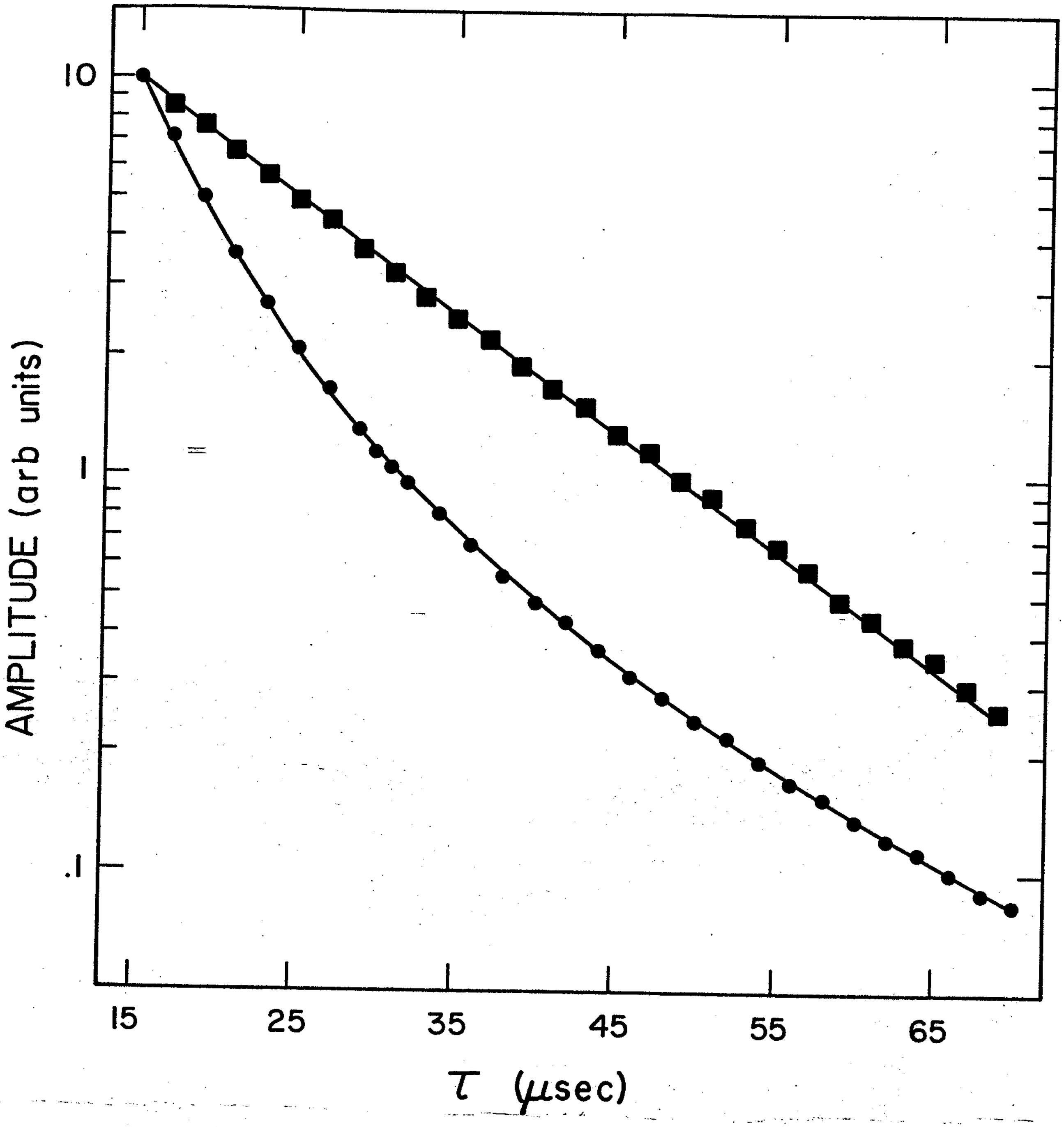

Figure 17. Echo amplitude versus τ at T = 4.2 °K. The lower curve is a least squares fit to the data points taken in H_o = 2.0 kOe at ν = 590 MHz, assuming two independently relaxing exponentials. The upper curve is the least squares fit, assuming a single exponential, to the data at H_o = 7.0 kOe and ν = 594 MHz.

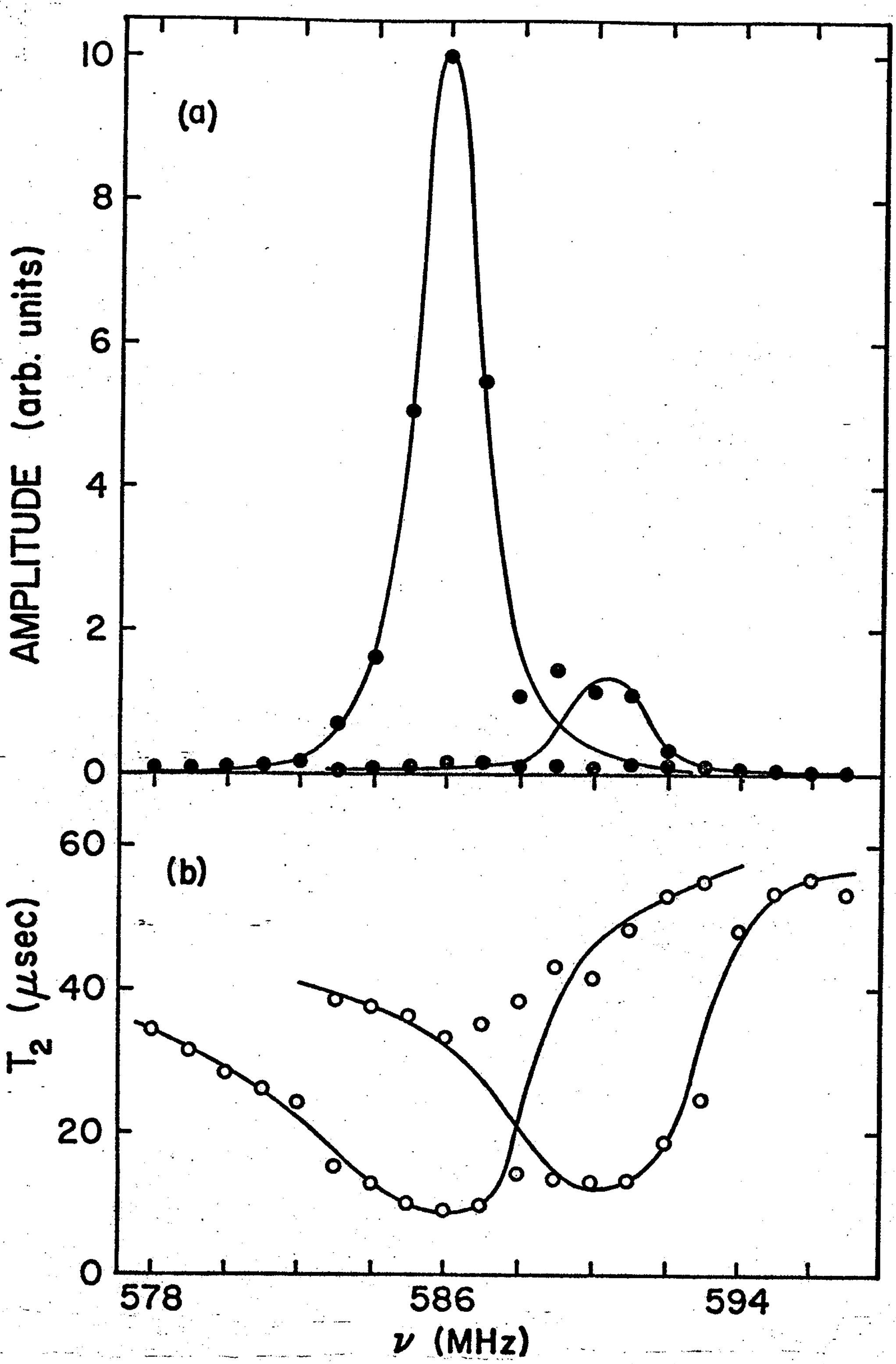

Figure 18. Amplitudes and relaxation times, obtained from a least squares fit of the echo decay envelopes to the sum of two exponentials, plotted versus frequency at T = 4.2 °K and H_o = 0.0 kOe on a single crystal sphere of $MnFe_2O_4$.

complished by doing a least-squares fit in two variables, frequency and time between rf pulses, as described in the next chapter.

CHAPTER IV

Spectra from Domain Walls and Domains

In the absence of any external magnetic field, there are two types of ^{55}Mn nuclei occupying the A-sites in $MnFe_2O_4$--those within domain walls and those within the bulk of the sample, i.e., within the domains. As pointed out in Chapter I and again in Chapter III, because of these two different environments, the nuclear magnetic resonance signal in the multi-domain or non-saturated region consists of two independent components which differ only slightly in resonance frequency and which have comparable amplitudes. These two signal components may exhibit different lineshapes and linewidths due to the structure of the domain walls, and different relaxation behaviour due to the differing local magnetic environments. (All of the spectra discussed in this chapter were taken on an 8 mm diameter single crystal sphere of $MnFe_2O_4$.[75])

Because of the large linewidths (> 1 MHz) and the relatively small separation between these two components ($\sim$ 2.5 MHz) there is significant overlap of the two signal components, as discussed in the last section of Chapter III. Figure 1-a shows the unrelaxed spectrum (calculated for pulse separation $\tau = 0.0$ from measured parameters) at $T = 1.45\ ^{o}K$ in an applied field of $H_{ext} = 3.0$ kOe. The solid curve is the sum of the two dashed curves which correspond to the domain-wall signal, centered at 584.2 MHz, and the domain signal, centered at 586.7 MHz. Figure 1-b shows plots of the total relaxation times of the two components with corresponding central frequencies.

1. Separation of the Two Signal Components

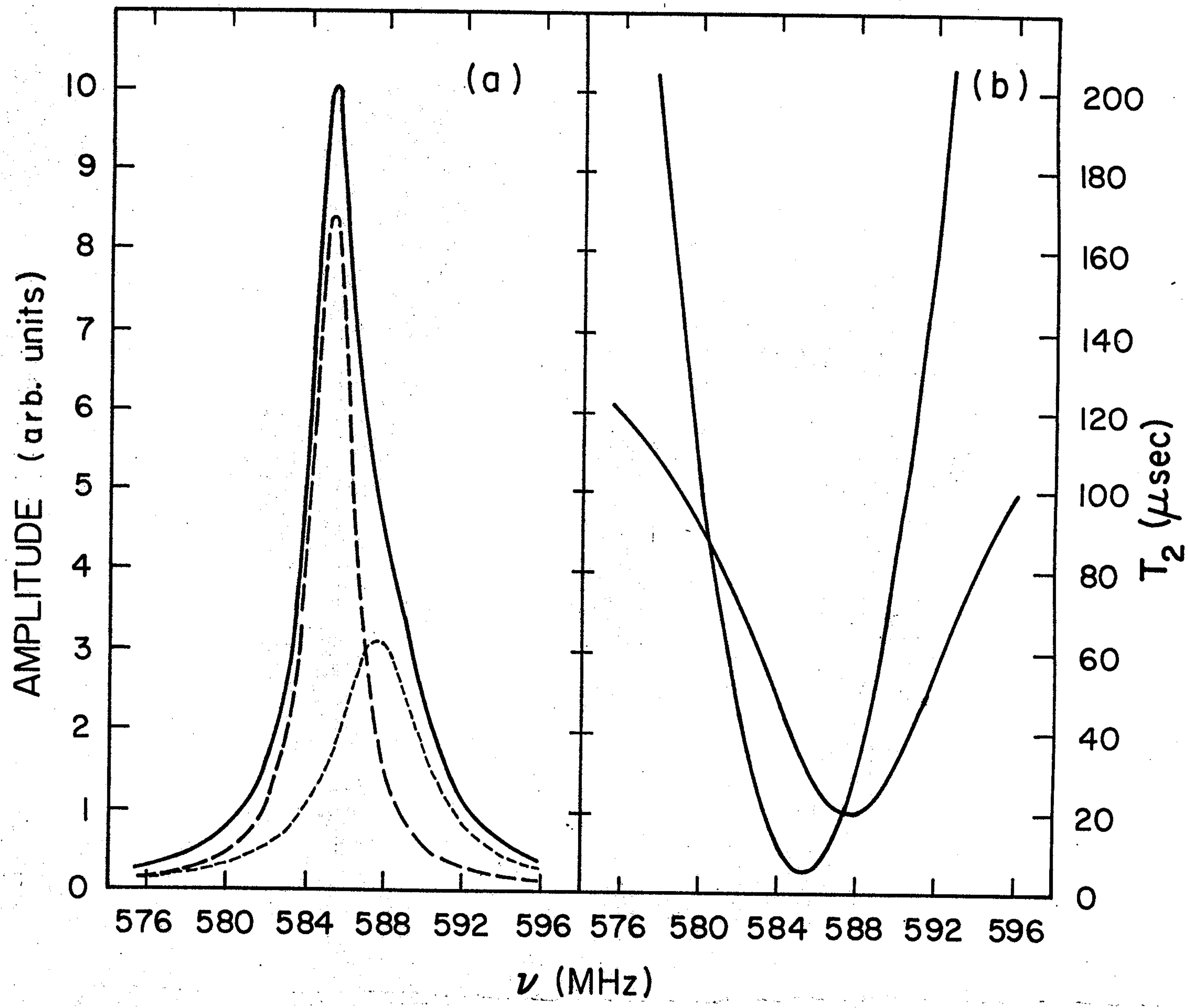

Figure 1. Spectrum at T = 1.45 °K in H_o = 3.0 kOe. a) solid curve is the spectrum at τ = 0 , dashed curves show the domain-wall (lower frequency) and domain (upper frequency) components, b) total relaxation times of the two components.

By considering a set of partially relaxed spin-echo spectra (or equivalently a set of echo-decay curves), taken over a range of pulse separations sufficient to determine the relaxation times, and fitting them collectively to a function of the two independent variables τ, pulse separation, and ν, rf pulse frequency, giving the echo amplitude as

$$F(\nu,\tau) = A_1(\nu)\exp(-2\tau/T_1(\nu)) + A_2(\nu)\exp(-2\tau/T_2(\nu)) \quad ,(1)$$

the two signal components can be studied individually. The parameters $A_i(\nu)$ and $T_i(\nu)$ are now functions of frequency. If the domain-wall signal's lineshape is described by a function $g_w(\nu - \nu_{10})$ and the domain signal's lineshape by $g_d(\nu - \nu_{20})$, then

$$A_1(\nu) = A_{10}g_w(\nu - \nu_{10}) \quad , \quad A_2(\nu) = A_{20}g_d(\nu - \nu_{20})$$

where ν_{10} and ν_{20} are the wall and domain nuclear resonance frequencies and A_{10} and A_{20} are the resonant amplitudes of the two components. Both signal components exhibit a linewidth of the order of a few megahertz due to local inhomogeneous broadening. Thus, the lineshape of the domain component will be determined by the distribution of hyperfine fields in the bulk of the sample. The domain-wall component will, in addition, exhibit broadening due to the wall structure. This, and the variation of the enhancement factor with position in the wall[8,28,76] may lead to a different lineshape for the domain-wall component of the signal. The most appropriate lineshapes, assumed to be either Gaussian or Lorentzian, will be determined from the data, and in all cases, the parameter δ describing the linewidth will be defined as the half-width at half-maximum.

The frequency dependence of the relaxation time $T_1(\nu)$ and $T_2(\nu)$ can be readily determined from the form of the interactions responsible for the relaxation. These interactions are: i) the Suhl-Nakamura interaction which results in a relaxation rate $(1/T)_{S-N} \propto g(\nu - \nu_{10})$, ii) the dipole-dipole interaction whose transverse part has the same form as the Suhl-Nakamura interaction and whose longitudinal part provides a frequency independent background contribution to the relaxation, and iii) spin-wave scattering processes which are frequency independent but strongly temperature dependent. Thus, the data, consisting of a collection of partially relaxed spectra, are fit to the function

$$F(\nu,\tau) = A_{10}g_w(\nu - \nu_{10}) \exp\left[-2\tau\left(\frac{1}{T_{B_w}} + \frac{g_w(\nu - \nu_{10})}{T_{10}}\right)\right] + A_{20}g_d(\nu - \nu_{20}) \exp\left[-2\tau \left(\frac{1}{T_{B_d}} + \frac{g_d(\nu - \nu_{20})}{T_{20}}\right)\right] \qquad (2)$$

using a non-linear least-squares procedure[77] based on the Marquardt technique of non-linear optimization[78] which returns the values of the two sets of parameters $(A_o, \nu_o, T_B, T_o, \delta)_{w,d}$ describing the two components of the signal.

To obtain the best values of these ten parameters the data should be collected over as wide a frequency range and over as wide a range of τ as possible. For practical reasons a frequency range of about 20 MHz and a pulse separation range of from 30 to 130 μsec (except for the spectra at $T = 1.45\ ^{o}K$ where τ ranged from 40 to 140 μsec) were chosen. The frequency range was covered in 1 MHz steps except near the center of the range where the steps were 0.5 MHz. The pulse separation was varied continuously with readings taken after each 5 μsec increment. The range of τ covered represents a change in echo position of 200 μsec which is sufficient to determine most of the relaxation times observed over the temperature range of 1.45 to 4.2 ^{o}K. The experimental apparatus used is illustrated in Chapter

I, Figure I-9, and is described in the discussion there.

2. Spectra at 1.45 ^{o}K

The basic features of the nuclear magnetic resonance signal in $MnFe_2O_4$ are: i) the presence of two resonance lines, one originating from domain walls the other from the bulk domains, of comparable amplitudes and separated in frequency by an amount roughly of the order of the linewidth of either of the two components, ii) each of these lines is characterized by strongly frequency dependent relaxation, as described in Chapter III, which at 1.45 ^{o}K can lead to a change in relaxation time of from perhaps several hundred μsec in the wings to less than about 10 μsec near resonance, iii) the linewidth of the domain component of the signal, since it is considered to be due to sample inhomogeneities, is expected to be independent of applied field and temperature, while the linewidth of the domain-wall component should include effects due to the structure of the wall itself as well as the characteristic sample inhomogeneous broadening and hence is expected to be broader than that of the bulk domain component, (since the domain wall structure may change with field, the domain-wall linewidth may also change with applied field), iv) as the field is increased the domain walls should gradually disappear leaving, at high fields, only a single resonance line.

To begin the analysis of the spectra it seems reasonable to consider first the spectra at high fields, since here only one line is present, and determine any parameters expected to be field independent, in particular the linewidth, and more generally the lineshape, of the domain component.

2.1 Lineshape of the two components

The spectrum shown in Figures 2-a,b was taken in $H_{ext} = 8.0$ kOe, which is considerably above the field required to remove most domain walls. The experimental points, represented in the figure by darkened circles, show the frequency dependence of the echo amplitude for a pulse separation $\tau = 40$ μsec. The spectrum at this field value is nearly symmetric about the frequency $\nu = 592.1$ MHz, and the notch at the center of the spectrum is due to the frequency dependent relaxation. The solid curve in Figure 2-a represents the best fit to the function in Equation 2 assuming a Gaussian lineshape for the domain component of the signal, represented by the finely dashed line in the figure, and a Lorentzian lineshape for the domain-wall component, given by the coarsly dashed line. In Figure 2-b the solid curve is the best fit assuming a Lorentzian lineshape for both signal components, that due to domains being again represented by the finely dashed line and that due to domain walls by the coarsly dashed line.

While the domain-wall component of the signal is required here to explain the slight asymmetry of the spectrum, it will be neglected because of its small amplitude and, since it arises from walls which must be tightly pinned to lattice imperfections, etc., the parameters returned by the fitting procedure are not expected to be truly representative of the domain-wall nuclear resonance.

This figure illustrates quite clearly that the lineshape of the domain component is somewhere between the Gaussian and Lorentzian, being nearly Lorentzian at the center of the line and tending toward the Gaussian shape in the wings. At lower fields the departure of the Lorentzian

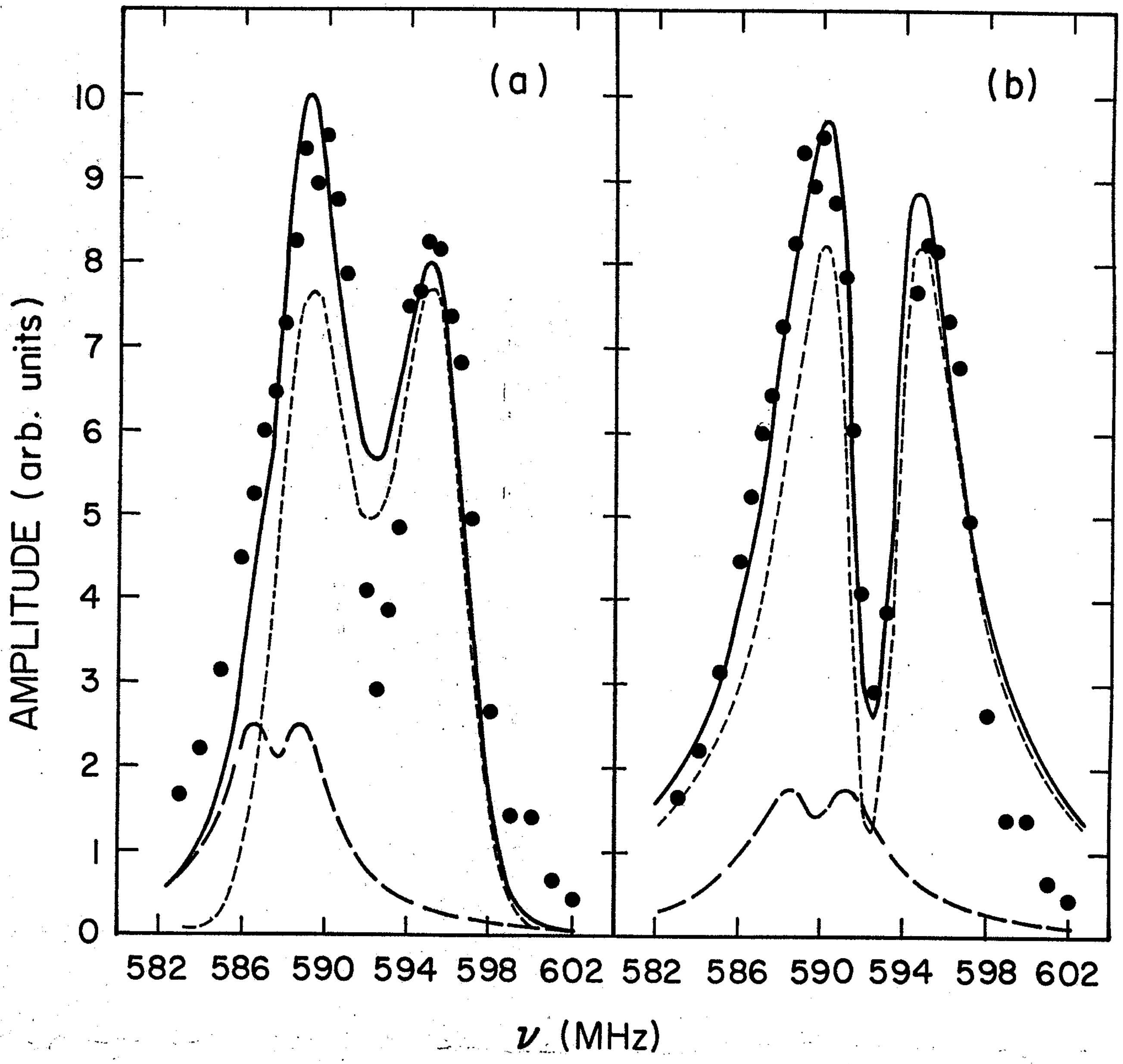

Figure 2. Spectrum at T = 1.45 °K in H_o = 8.0 kOe for τ = 40 μsec. a) solid curve is the fit to the data assuming a Lorentzian domain-wall lineshape and a Gaussian domain lineshape, b) solid curve gives the fit obtained assuming a Lorentzian lineshape for both components.

curve from the data in the wings becomes particularly objectionable since it overlaps too much of that portion of the signal which is due to the domain-wall nuclei. Thus, while at $H_{ext} = 8.0$ kOe the Lorentzian lineshape for the domain line yields a variance which is slightly better than that given by a Gaussian, the use of a Gaussian lineshape for the domain line and a Lorentzian for the domain-wall line results in a greatly improved fit at lower fields. This is illustrated in Figure 3 which shows the spectrum in zero field. The fit in Figure 3-a assumes that both components are described by Gaussian lineshapes leading to considerable difficulty on the low frequency side of the spectrum. Figure 3-b shows the fit to the same data assuming two Lorentzian shaped components, also leading to some difficulty on the low frequency side, as well as on the high frequency side. The assumption of a Lorentzian domain-wall lineshape and a Gaussian domain lineshape leads to a much improved fit, as shown in Figure 3-c. The values of the parameters obtained from these three attempts to fit this spectrum are listed in Table I for comparison, as are the parameters obtained from the three fits to the $H_{ext} = 5.0$ kOe spectrum.

It appears that neither a Gaussian nor a Lorentzian lineshape can adequately describe either of the signal components. The best results so far obtained have assumed a Lorentzian domain-wall component lineshape and a Gaussian domain component lineshape. All the data have been fit under this assumption and there will be a further comparison made in the discussion of the spectra in the intermediate field region. From the high field spectra the linewidth of the domain component was determined to be $\delta = 2.63$ MHz (half-width at half-maximum).

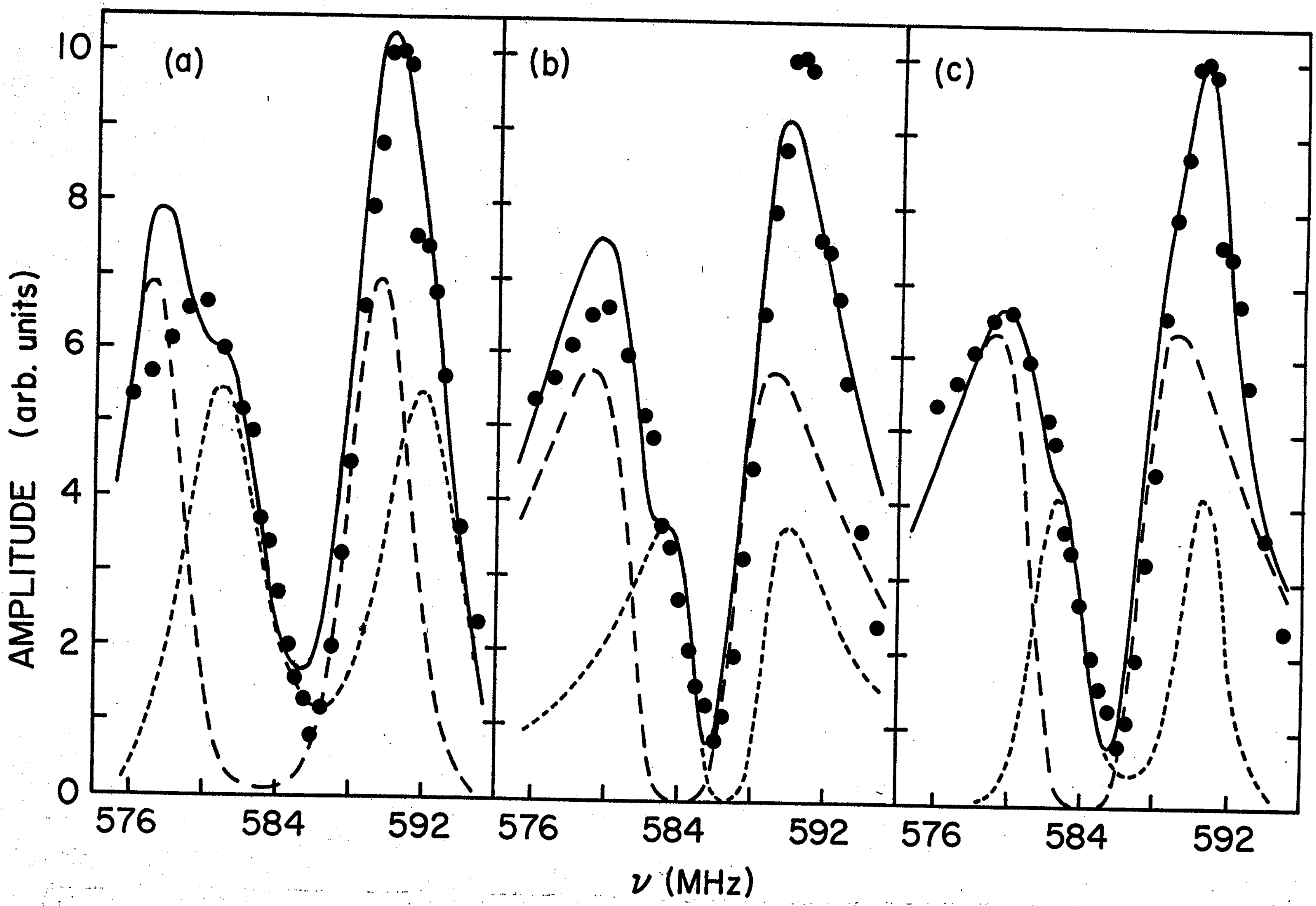

Figure 3. Spectrum at T = 1.45 °K in H_o = 0.0 kOe for τ = 40 μsec. Solid curve is the best fit assuming a) two Gaussian lineshapes, b) two Lorentzian lineshapes, c) a Lorentzian domain-wall lineshape and a Gaussian domain lineshape.

Table 1. T = 1.45 ^{o}K spectra at H_o = 0.0 kOe and H_o = 5.0 kOe.

H_o(kOe)	line-shapes	A_{10}	T_{10}	ν_{10}	δ_1	T_{B_1}	A_{20}	T_{20}	ν_{20}	δ_2	T_{B_2}
0.0	G-G	404.2	11.28	583.3	3.66	-----	179.4	20.51	586.4	3.87	363.0
	L-L	542.4	6.98	584.1	1.53	-----	410.9	9.57	586.7	1.24	160.0
	L-G	862.4	4.87	584.2	1.262	-----	254.2	16.52	586.7	2.626	183.2
5.0	G-G	194.0	10.72	586.7	3.22	-----	127.3	34.66	589.4	3.34	252.8
	L-L	131.9	10.16	586.9	1.53	-----	403.5	16.30	589.6	1.24	131.3
	L-G	304.8	6.31	587.6	1.262	-----	167.0	30.58	589.6	2.626	173.2

2.2 Field dependence of the spectra

The H_{ext} = 0.0 kOe spectrum shown in Figure 3 exhibits the asymmetric or two-component nature of the low field spectra. Due to the multi-domain character of the sample all of the spectra at fields too low to saturate the sample are expected to be very similar. The relative amplitudes of the two components are expected to change with field as some of the domain walls are being removed; and the domain-wall component's lineshape may change slightly due to some change in domain-wall structure or in domain-wall enhancement factor at intermediate values of field.

The spectrum at H_{ext} = 3.0 kOe is shown in Figures 4-a,b,c for pulse separations τ = 40, 50, 60 μsec, illustrating the frequency dependent relaxation effects. Although from magnetization measurements the sample reaches magnetic saturation ($M(H) \sim .9\ M_s$) at $H_{ext} \sim$ 2 - 3 kOe, the spectrum at 3.0 kOe is not very different from that at 0.0 kOe. Thus there are still significant numbers of domain walls in the sample. As before, the solid curves in the figure represent the best fit to the entire spectrum which consists of a set of 21 partially relaxed spectra such as those shown in this figure (for values of τ from 40 to 140 μsec). The finely dashed curves represent, as usual, the Gaussian domain component and the coarsly dashed curves the Lorentzian domain-wall component of the signal. Figure 1, which is the calculated unrelaxed spectrum (τ = 0.0) using the parameters obtained from the fit to the data represented in Figure 4, and this figure present a clear illustration of the strongly frequency dependent relaxation effects characteristic of this material.

As the field is further increased to 5.0 kOe, the domain-wall component becomes significantly weaker, as shown in Figure 5. Parts a, b,

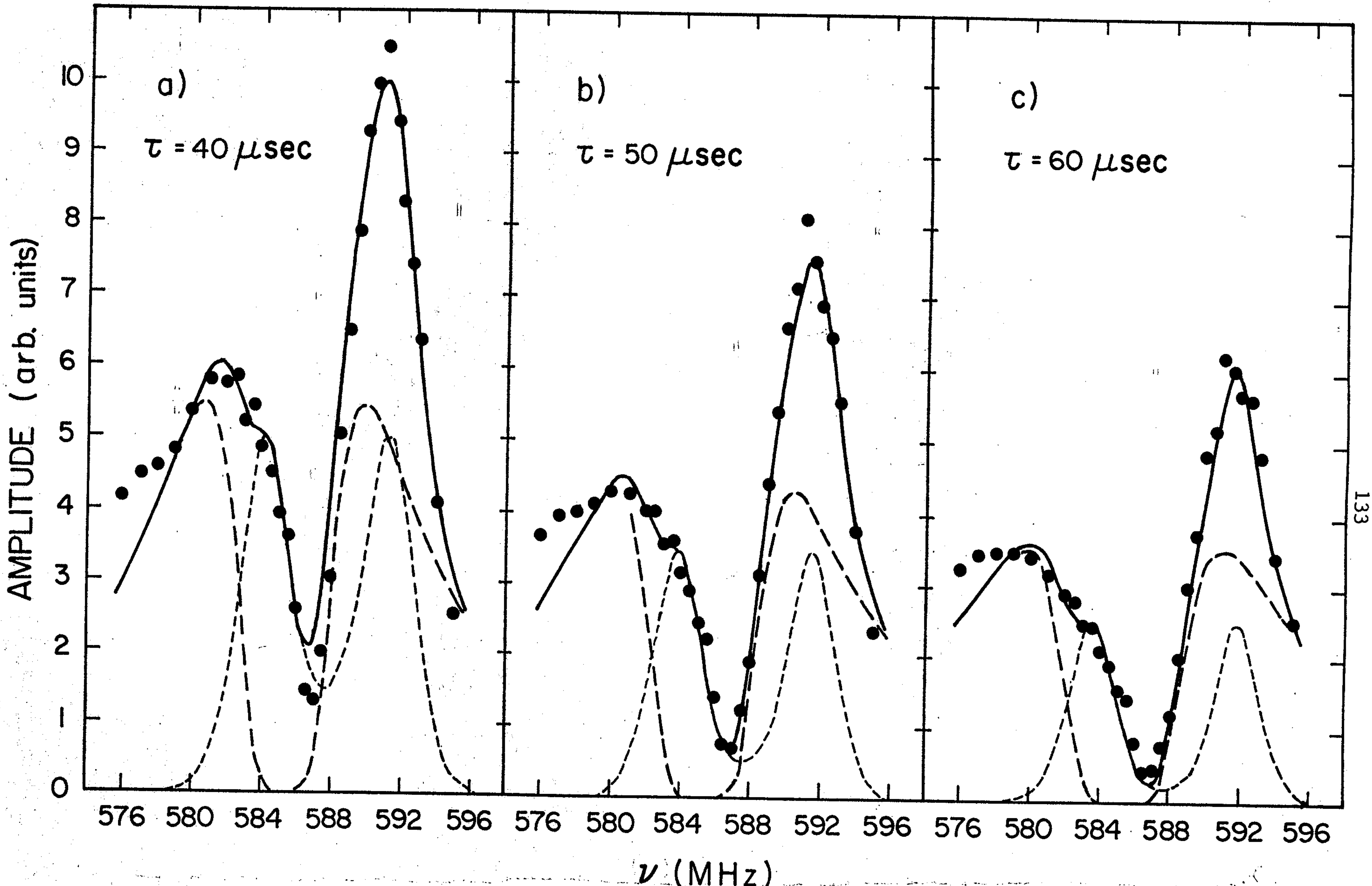

Figure 4. Partially relaxed spectra at T = 1.45 °K in H_o = 3.0 kOe, solid curves give the fit using a Lorentzian domain-wall lineshape and a Gaussian domain lineshape. a) τ = 40 μsec, b) τ = 50 μsec, c) τ = 60 μsec.

and c of this figure show the same spectrum fit, as the $H_{ext} = 0.0$ kOe spectrum of Figure 3, in three ways : a) two Gaussian lineshapes, b) two Lorentzian lineshapes, and c) a Lorentzian domain-wall lineshape and a Gaussian domain lineshape. Again the fit in case c) is significantly better than that of the other two cases.

Even at this relatively high value of external field there still remain a large number of domain walls in the sample, indicating that these walls must be loosely pinned to sample imperfections (only loosely pinned because, as shown in Figure 2, at $H_{ext} = 8.0$ kOe nearly all of the domain-walls have been removed leaving only the strongly pinned walls). The nature of the domain-walls in this intermediate field region will be discussed further when the field dependence of the spectral parameters is discussed.

There is some indication that the domain-wall component's linewidth changes slightly in the intermediate field region, $2 < H_{ext} < 8$ kOe, however, the data do not conclusively show this since, in the central region of this component, i.e., in that part of the line most sensitively dependent on the linewidth, the signal due to the domain walls has almost completely relaxed due to the short relaxation times, and accurate determination of the linewidth is not possible. To study this effect carefully would require that data be taken for as short a time τ between pulses as possible. The minimum pulse separation was changed from the value of 40 μsec used for the $T = 1.45\ {}^{o}K$ spectra to 30 μsec for the higher temperature spectra discussed later. However, since the value of the total relaxation time at resonance of the domain-wall signal component is $\sim$ 4 - 6 μsec, a minimum pulse separation of $\sim$ 10 μsec or less would be desirable. There are instrumental difficulties in doing this however, in

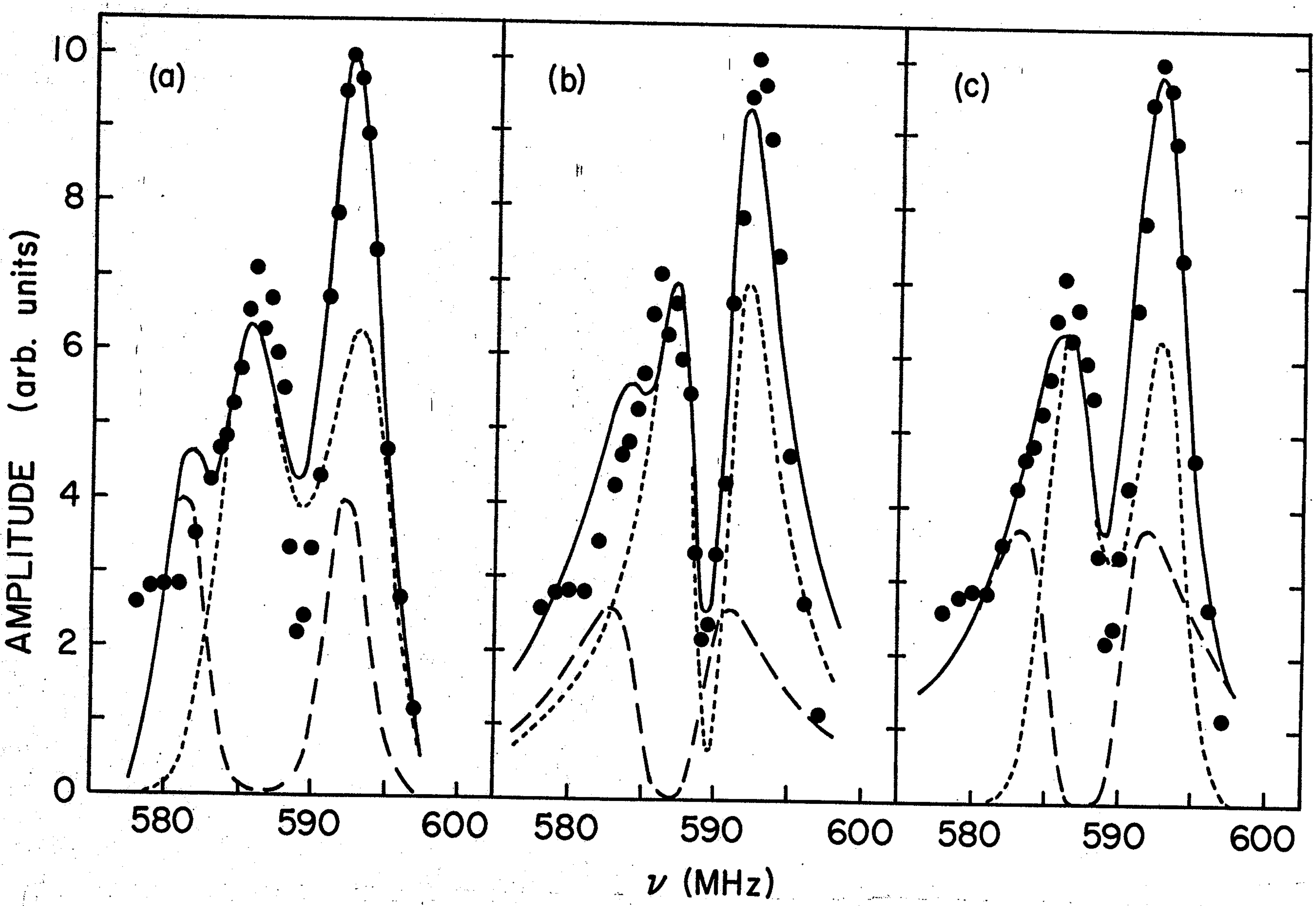

Figure 5. Spectrum at T = 1.45 °K in H_o = 5.0 kOe for τ = 40 μsec. Solid curve is the best fit assuming a) two Gaussian lineshapes, b) two Lorentzian lineshapes, c) a Lorentzian domain-wall lineshape and a Gaussian domain lineshape.

particular, for pulse separations less than ∼20 μsec, the length of the second pulse is affected by the presence of the first pulse (since the pulsed oscillator has not fully recovered), and the technique of continuously sweeping the pulse separation cannot be used. This data could be collected in a point by point scan of τ ; however, the amount of data required makes this very time consuming.

Figure 6-a is a plot of amplitude at resonance ($\tau = 0.0$) vs H_{ext}. The open circles are domain-wall signal amplitudes and the dark circles are domain signal amplitudes. The percentage contribution to the total signal at $\tau = 0.0$ (from the areas of the signal components) goes from about 70% domain-wall : 30% domain, at $H_{ext} = 0.0$ kOe, to about 45% domain-wall : 55% domain, at $H_{ext} = 6.0$ kOe (see Table 2). The relative weights of the two components in the observed partially relaxed spectra is, of course, quite different due to the different relaxation behaviour. Thus, for fields above ∿ 7 kOe, the domain-wall component is very difficult to observe.

Magnetic saturation occurs in these materials (manganese ferrites) near $H_{ext} \sim$ 3 kOe (from magnetization measurements). The peak in the amplitudes occurring at $H_{ext} = 2$ kOe, for the domain-wall case, may be due to an increase in domain-wall mobility, and therefore in enhancement factor, due to the displacement by the field from its $H_{ext} = 0$ equilibrium position (which may be determined by lattice imperfections). In the domain case this amplitude peak is probably due to the preference, in the field, for domains with moments parallel to the field over the other possible orientations, since these domains will see the largest effective rf field the signal will be a maximum when the largest number of domains are of this type.

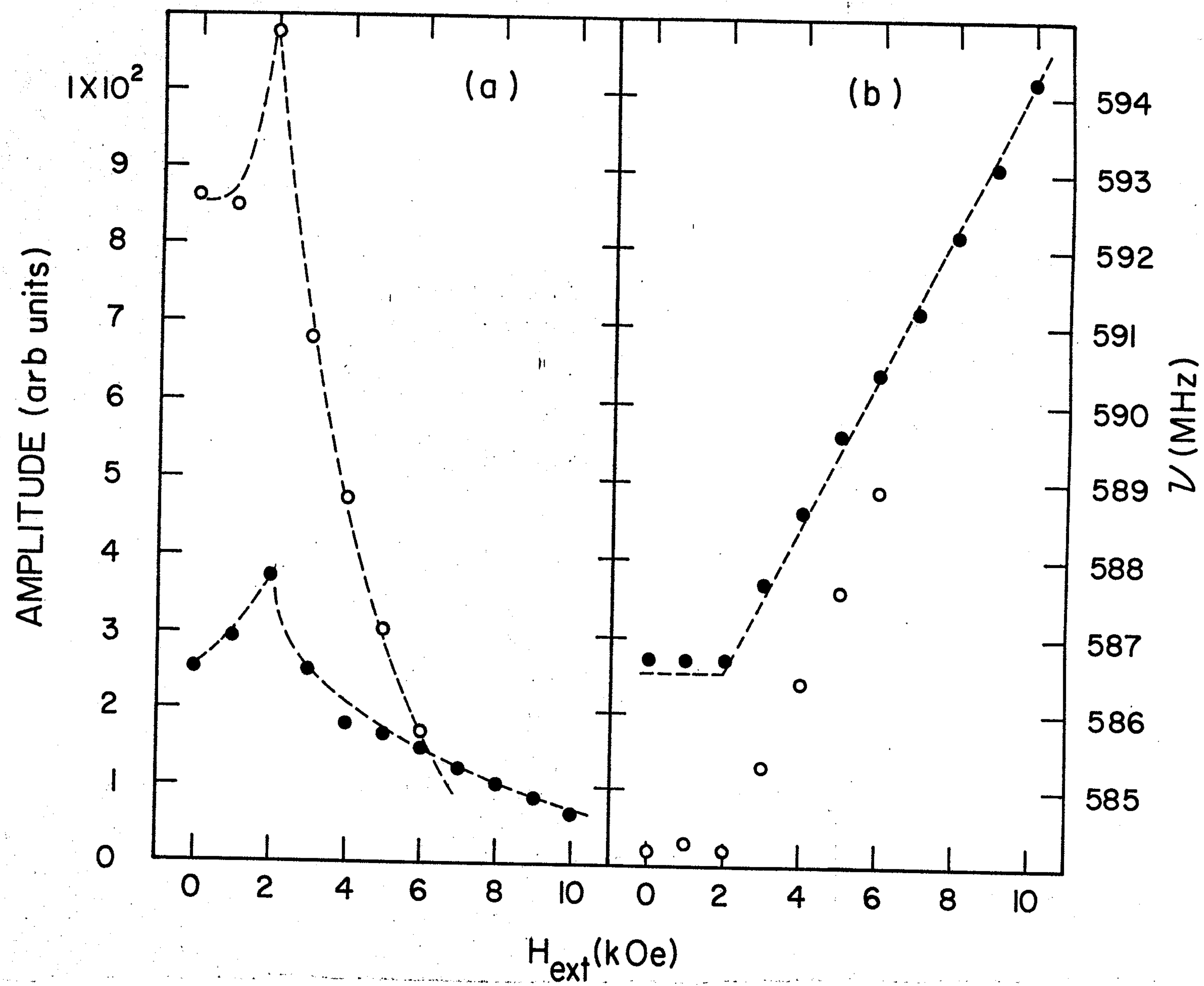

Figure 6. a) Amplitudes of the two components versus H_{ext}, b) resonant frequencies of the two components versus field. For T = 1.45 ^{o}K; open circles refer to the domain-wall component, dark circles to the domain component.

Table 2. Spectra at T = 1.45 °K

H_{ext}(kOe)	A_o(arb. units)	T_{10}(μS)	ν_{10}(MHz)	δ_1(MHz)	T_{B_w}(μS)	B_o(arb. units)	T_{20}(μS)	ν_{20}(MHz)	δ_2(MHz)*	T_{B_d}(μS)
0.0	862.4 (70.6%)	4.868	584.2	1.262*	-----	254.2 (29.4%)	16.52	586.7	2.626	183.2
1.0	849.0 (70.7%)	4.913	584.3	1.262*	-----	293.2 (29.3%)	16.61	586.7	2.626	145.7
2.0	1075.0 (67.2%)	4.485	584.2	1.262*	-----	372.8 (32.8%)	16.37	586.7	2.626	131.1
3.0	680.0 (65.6%)	5.675	585.3	1.262*	-----	251.8 (34.4%)	22.98	587.7	2.626	159.8
4.0	473.8 (64.7%)	5.929	586.4	1.262*	-----	182.3 (35.3%)	27.02	588.6	2.626	188.4
5.0	304.8 (56.4%)	6.309	587.6	1.262*	-----	167.0 (43.6%)	30.58	589.6	2.626	173.2
6.0	172.7 (44.7%)	6.864	588.9	1.262*	-----	150.5 (55.3%)	33.99	590.4	2.626	177.4
7.0	146.4	5.570	590.0	1.262*	-----	124.9	35.41	591.2	2.626	223.0
8.0	18.58	45.93	587.7	1.262*	-----	103.6	35.30	592.2	2.626	240.8
9.0	9.09	81.91	591.8	5.459	-----	84.30	34.80	593.1	2.626	185.6
10.0	9.27	81.23	592.8	4.983	-----	64.14	37.00	594.2	2.626	197.4

*held constant

Above H_{ext} = 2 kOe the amplitudes of the two components decrease rapidly, the domain-wall component's amplitude decreasing more rapidly because the walls are being physically removed from the sample, and the domain signal amplitude decreasing because of the $\eta \sim 1/H_{eff}$ behaviour of the enhancement factor η. For fields above H_{ext} = 6 kOe any domain walls remaining must be strongly pinned and are then essentially small regions of high local anisotropy which can only be expected to produce a very broad, weak, and poorly behaved contribution to the total signal, which will make the high-field spectra somewhat difficult to fit and interpret.

In a perfect magnetic material there should exist a critical value of H_{ext} above which all domain walls will have been removed and below which the demagnetizing field (for a sphere $H_D = -4\pi\vec{M}/3$, where $\vec{M}$ is the sample magnetization) exactly cancels the applied field. In Figure 6-b, which is a plot of the resonance frequency of the two components vs H_{ext} (open circles for domain-walls, dark circles for domains), it can be seen that H_{ext} has no effect below 2 kOe. Above this value the domain component's resonant frequency increases with applied field along the dotted line which has a slope of $\gamma_{Mn} = 1.055 \times 10^3$ Hz/Oe, while in the intermediate region, i.e., in the region where the demagnetizing field cannot cancel the applied field but where the sample is not completely saturated, the domain-wall component's resonance frequency increases with field at a rate which is slightly faster than that given by γ_{Mn}, possibly due to frequency pulling effects, or to the possibility that the domain walls are being straightened out by the field, tending to make them more like the domain regions, and less like domain walls.

The negative shift of ∼ 2.5 MHz in the resonance of the domain-wall line relative to the frequency of the domain line may be a result of the non-colinear nature of the domain wall[79]. The electronic contribution to the hyperfine field (the hyperfine field here is viewed as the total microscopic field felt by the nucleus, with the exception of externally applied fields) could be affected through the decreased strength of the exchange between what are now non-colinear spins, however, the angle between spins of nearest or next-nearest magnetic neighbors is extremely small since next-nearest neighbor distances are ∼ 3 Å while the domain wall width is ∼ 530 Å . If the domain-wall nuclear hyperfine field fluctuates with time, the time-averaged field at the nucleus could quite possibly be decreased enough to explain this shift. Further evidence for fluctuating hyperfine fields in the domain walls will be discussed in the next section in connection with the temperature dependent background relaxation rate.

The behaviour of the domain resonance frequency with field suggests that the bulk of the sample is nearly saturated for $H_{ext} > 2$ kOe with at most some small regions surrounded by loosely pinned domain walls. The increase in domain-wall nuclear resonance frequency with field for $H_{ext} > 2$ kOe implies that the external field is penetrating the remaining domain walls to some extent and that perhaps the walls are being "straightened out" by the field rather than being pushed out through the surface of the sample.

As a final point in the discussion of the field dependent behaviour at 1.45 °K, Figure 7 shows the minimum value (i.e., the value at resonance) of the frequency dependent part of the relaxation time plotted vs applied field. The solid circles are, as usual, for the domain reson-

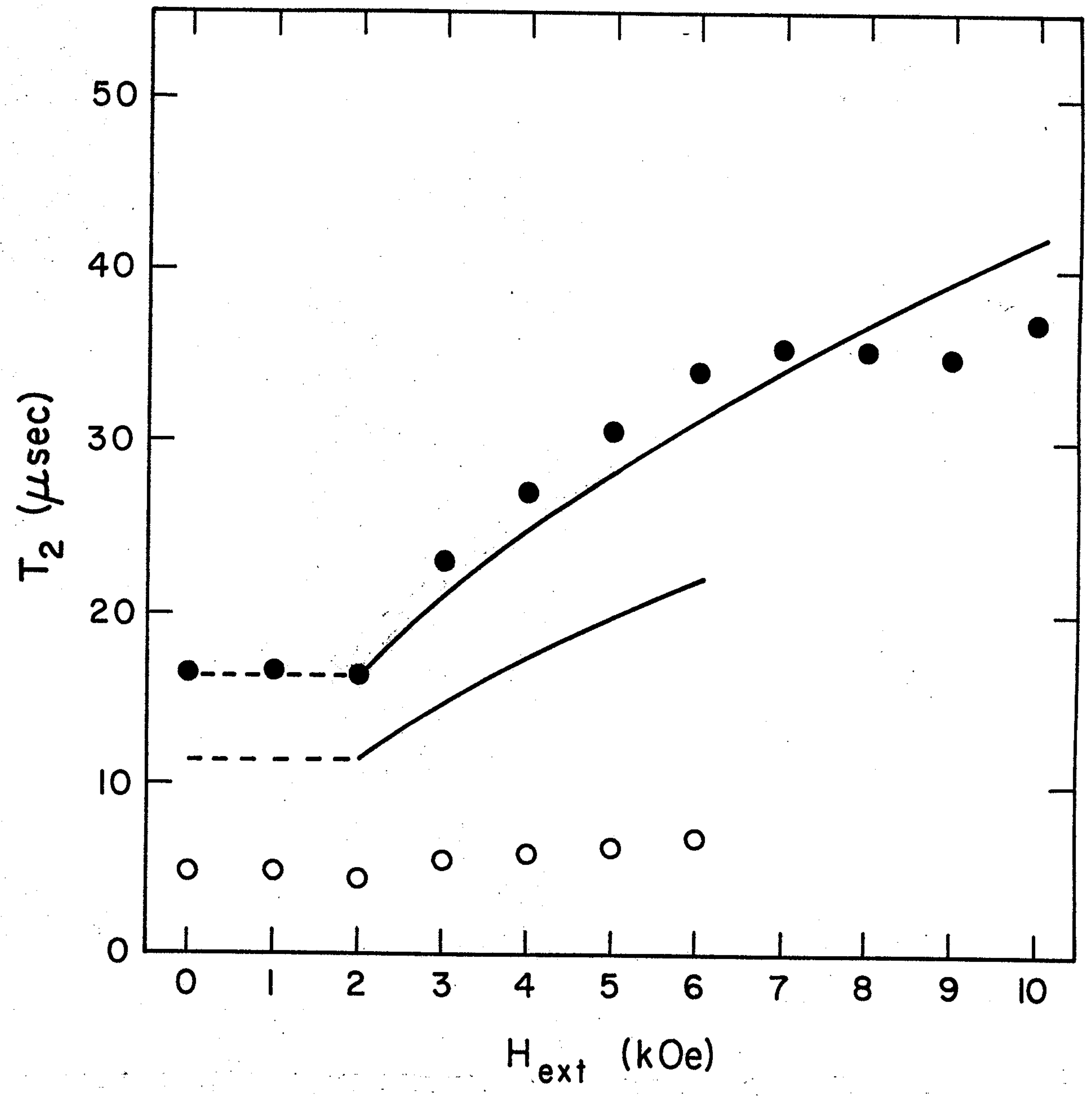

Figure 7. Minimum value of frequency dependent relaxation times versus H_{ext}. Open circles refer to the domain-wall component, closed circles to the domain component. The solid curve is the calculated Suhl-Nakamura relaxation time.

ance while the open circles refer to the domain wall signal. The solid lines are the relaxation times calculated as a function of the field using Equation III-28, with the Suhl-Nakamura range function given in Equation II-19 (multiplied by a factor of 2.06, as discussed in Chapter III, Section 5), with anisotropy field $H_K = 1.0$ kOe, using $\hbar\omega_e = 6.0 \times 10^{-16}$ ergs (determined from the fit of the two-magnon spin-wave relaxation times to the domain-wall component's background relaxation time), and a hyperfine field of $H_{hf} = 559.5$ kOe determined from the data in Figure 6-b. The difference in the T_{S-N} vs H_{ext} curves calculated for the two signal components is a result only of the different normalization factors of the Gaussian and Lorentzian lineshapes assumed to describe the two components. This results in a numerical factor of $G(\nu_0)/L(\nu_0) = \sqrt{\pi \ln 2}\,(\delta_w/\delta_d)$. The fact that this factor does not account for the entire difference in the observed relaxation times suggests that the anisotropy field and the exchange field within the wall are different from the values of these fields in the bulk domains.

The inflection in the domain component relaxation time data of Figure 7 is a result of the difficulty in describing the domain-wall contribution to the total signal for intermediate values of field, and should not be considered to be of physical origin. The relaxation time parameters obtained in the least squares fitting process are correlated, and any difficulty in determining the domain-wall component's parameters will result in some uncertainty in the domain component's parameters. Again, the observed relaxation time may not rise as rapidly with field as calculated from the Suhl-Nakamura interaction alone due to the dipole-dipole contribution.

The relaxation time for domain-wall nuclei increases with applied field indicating again that the external field is penetrating the wall rather than merely displacing it.

To summarize the field dependent behaviour it is best to divide the range of fields discussed into three regions: i) $H_{ext} \leq 2$ kOe, ii) $2 < H_{ext} < 8$ kOe, and iii) $H_{ext} \geq 8$ kOe. In region i) the applied field is not strong enough to saturate the sample and the resonance frequencies and relaxation times are constant while the amplitudes increase to a maximum at $H_{ext} = 2$ kOe. In the intermediate region, region ii), the sample is essentiallly saturated in that the demagnetizing field can no longer completely cancel the effects of the external field, but large numbers of domain walls are still present in the sample. The properties of the domain contribution to the signal are quite straightforward while the field dependence of the resonance frequency and relaxation time of the domain-wall signal suggest that the walls are pinned in the sample and are penetrated by the external field, also, there is some evidence, though not conclusive, that the domain-wall component's linewidth changes slightly with field in this region. Finally, in region iii), the high field region, only strongly pinned domain walls remain, giving a broad, weak, ill-behaved background superimposed on a still strong domain nuclear resonance signal which has a lineshape assumed to be Gaussian but tending more towards a Lorentzian near the center of the line.

Table 2 gives a summary of the parameters used to fit the spectra at 1.45 ^{o}K. The only parameters that have not been discussed are the background relaxation times for the two components. These are termed "background" relaxation times because the processes responsible for them are frequency independent: the spin-wave scattering processes and the longitudinal part of the dipole-dipole interaction. An important point to notice is that the domain-wall background relaxation time T_{B_w} is very large (at $H_{ext} = 3.0$ kOe it was determined, from this data, to be $\sim$ 3400 μsec, however, this data, since it covers a range of only 200 μsec, cannot adequately determine such long relaxation times), while that for domains has an average value at 1.45 °K of T_{B_d} = 182 μsec. This difference will be the subject of a large part of the discussion of the next section. The domain component's background relaxation time does not show any obvious field dependence in this data. A larger range of fields and a more accurate measure of these times is required for an accurate field dependence study of this relaxation time. This will be discussed to some extent with reference to the spin-wave relaxation processes in the next section.

3. Temperature Dependence--1.45 → 4.2 °K

As the temperature is varied over the range of 1.45 to 4.2 °K there occur some significant changes in the observed spectra. These changes are expected to be due to the strong temperature dependence of the spin-wave scattering processes, as discussed in Chapter III, Section 4, and to the temperature dependence of the magneto-crystalline anisotropy[80], described here by an effective anisotropy field H_K. The temperature dependence of the anisotropy is very sample dependent and in the absence of any detailed anisotropy measurements on this particular crystal is not very well defined. However, from the measurements[80] on stoichiometric manganese ferrites, the anisotropy for this composition is not expected to exhibit any strong temperature dependence.

Spectra were taken at temperatures 1.45, 1.75, 1.91, 2.10, 2.51, 3.28, and 4.2 °K in fields of 3.0 and 8.0 kOe. The spectra taken in H_{ext} = 8.0 kOe were used primarily as an aid in fitting the spectra at the lower value of field rather than in an attempt to determine field dependence of the parameters at these temperatures. The sample was in thermal equilibrium with the liquid helium bath whose temperature was maintained at the preset value by controlling the pumping rate with a manostat which held the pressure constant to within ∿ .2% of its nominal value over the period of the experiment.

3.1 The shape of the spectra

The only parameter expected to remain constant over this temperature range is δ_d , the linewidth of the domain component of the signal, which depends only on the microscopic sample inhomogeneities. T_{10} and T_{20} , the resonance values of the frequency dependent relaxation times, can change over this temperature range only through a change in anisotropy field H_K , since the Suhl-Nakamura range function goes as $\exp\{-\{(H + H_K)/H_{ex}\}^{\frac{1}{2}}r/a\}$. The dipole-dipole contribution to the relaxation is temperature independent, thus, any change in T_{10} or T_{20} must be due to a change in H_K. However, for $H_K > \sim 1$ kOe, these relaxation times are not very sensitive functions of H_K , thus, they do not provide a very good measure of the changes in H_K.

Figures 8-a,b,c show the spectrum at 1.75 °K in H_{ext} = 3.0 kOe for pulse separations τ = 30, 40, 50 μsec, respectively. Comparing Figures 4-a,b with Figures 8-b,c it is apparent that there has been little change in the overall shape of the spectrum on going from T = 1.45 to 1.75 °K. The fit to the 30 → 130 μsec spectrum at 1.75 °K , however, gives shorter values for T_{10} and T_{20} than those obtained from the fit to the 40 → 140 μsec spectrum at 1.45 °K. This difference, at least for T_{10} , is probably due to the different time bases of the spectra, illustrating the need to cover as wide a range of τ values as possible to accurately deter-

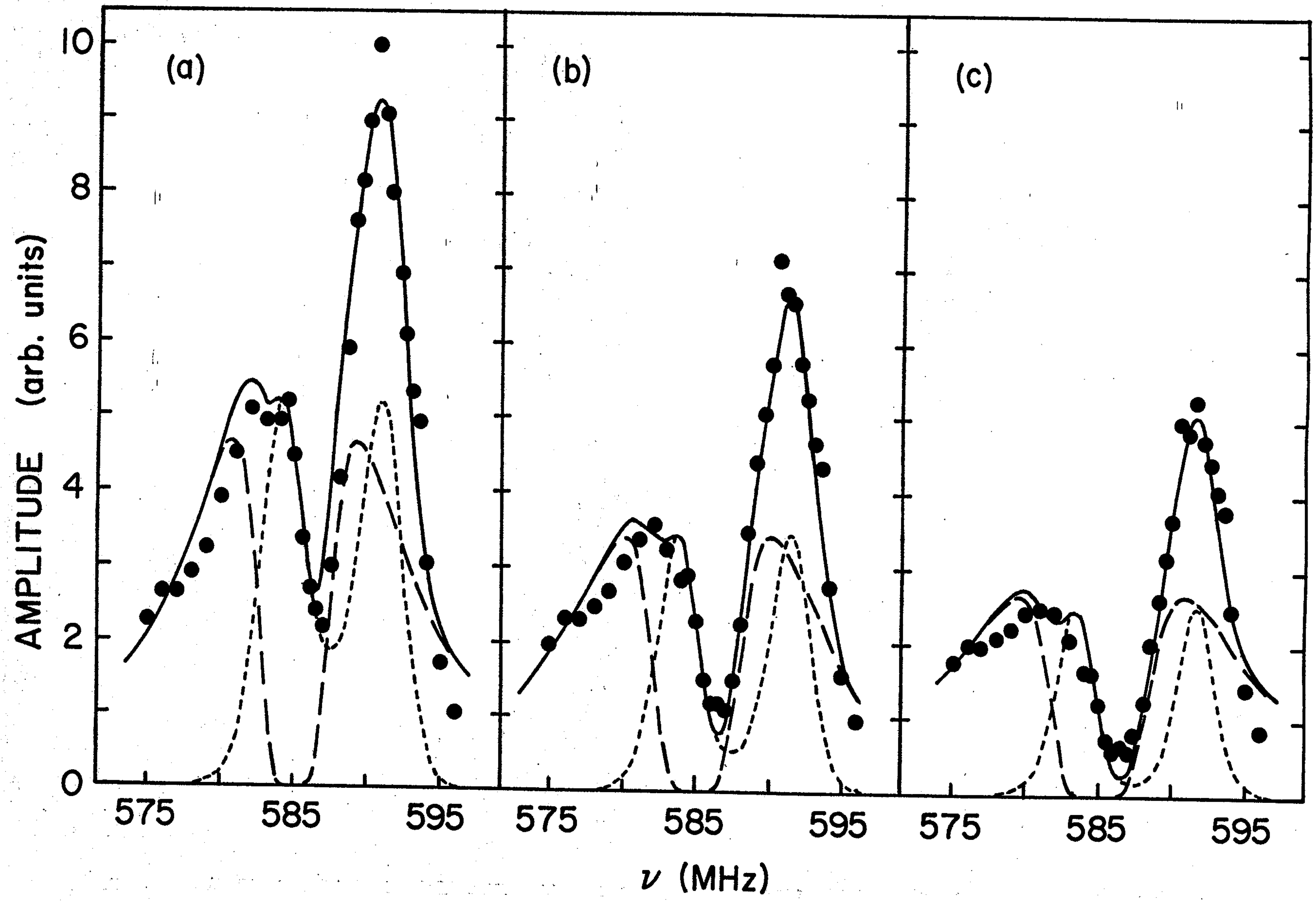

Figure 8. Partially relaxed spectra at T = 1.75 °K in H_o = 3.0 kOe for a) τ = 30 μsec, b) τ = 40 μsec, c) τ = 50 μsec. The solid curves are the best fit to the entire set of partially relaxed spectra for τ from 30 to 130 μsec.

Table 3. Temperature dependence of the spectral parameters at $H_{ext} = 3.0$ kOe.

$T(^{o}K)$	A_o(arb. units)	T_{10}(μS)	ν_{10}(MHz)	δ_1(MHz)	T_{B_w} (μS)	B_o(arb. units)	T_{20}(μS)	ν_{20}(MHz)	δ_2(MHz)	T_{B_d} (μS)
1.45	680.0	5.675	585.3	1.262*	34348.	251.8	22.98	587.7	2.626*	159.8
1.75	293.8	4.793	585.0	1.262*	1843.	108.4	18.77	587.5	2.626*	206.7
(40-130)	303.7	5.104	584.9	1.262*	1843.*	112.4	18.68	587.6	2.626*	195.2
1.92	142.6	4.797	584.9	1.262*	1455.	61.44	19.79	587.4	2.626*	151.6
2.10	176.8	4.881	584.7	1.262*	501.1	79.03	18.54	587.4	2.626*	167.5
2.51	255.7	3.434	584.1	1.262*	257.4	70.88	17.65	586.9	2.626*	130.6
3.28	171.0	3.200	584.0	1.262*	152.9	38.88	23.12	587.4	2.626*	73.46
4.2 a)	64.32	4.63	586.5	1.189	85.7	26.57	61.18	588.9	2.626*	55.47
b)	66.41	4.541	586.3	0.874	125.0	57.51	30.00*	588.9	2.008	55.00

* held constant

mine the parameters. Doing a fit to the 1.75 °K spectrum using only the data from the range 40 → 130 μsec gives parameters more nearly in agreement with those obtained from the 1.45 °K spectrum.

A_{10} and A_{20} , the amplitudes of the two components, are expected to vary with temperature through the variation of the enhancement factor η given, for the single domain case, by

$$\eta = H_N/\{(H_{ext} - H_D)(\beta - 1) + H_K + \alpha m^o\}$$
$$\alpha = |H_N/M_A^o| \quad , \quad \beta = M_B^o/M_A^o \simeq 1.9 \tag{3}$$

as derived in Chapter I. αm^o is small at these temperatures (∿ 1 Oe), and for low fields where H_D cancels H_{ext} , $\eta \simeq H_N/H_K$. The amplitudes at 4.2 °K are ∿ 5 - 10 times smaller than those at 1.45 °K. Thus, since $A \propto \eta^2$, an increase in H_K by a factor of ∿ 2 - 3 at 4.2 °K (above its value at 1.45 °K) would explain this difference in amplitude. However, as shown in the first column of Table 3, which is a summary of the parameters of the spectra taken over this temperature range, the amplitudes do not change very smoothly. This may be partly due to the fact that different spectra were taken over a long period of time during which the sample was thermally cycled (room temperature to liquid helium) many times and during which the spectrometer was used for other purposes. Thus, the experimental conditions were probably not identical in all cases. There is however, a definite change in amplitudes on lowering the temperature.

The amplitudes, as shown above, change through variation in the enhancement factor which in the single domain case is directly related to the anisotropy field. The domain-wall enhancement factor, as discussed in Chapter I, Section 6, is considerably more complex, but as seen in the table, must account for roughly a factor of 5 change in domain-wall component amplitude.

Finally, it should be noted that the values obtained for the amplitudes are very sensitively dependent on the assumed linewidth and lineshape and that there are again correlations between the parameters used to fit the spectra. These factors will be discussed later in connection with what appears to be a fundamental change in the nature of the domain-wall component of the signal.

The resonance frequencies ν_{10} and ν_{20} are expected to vary through changes in H_K according to the relation, Equation I-54, describing frequency pulling

$$\nu_0 = \gamma_N(H_{ext} - H_D) + \gamma_N H_D(1 - \eta(m^o/M_A^o)) \qquad (4)$$

where $\gamma_N = 1.055 \times 10^3$ (Oe-sec)$^{-1}$ is the ^{55}Mn gyromagnetic ratio. Since, according to the preceding discussion of signal amplitudes, η should be increasing on lowering the temperature and since the ratio m^o/M_A^o should also increase with decreasing temperature, the resonance frequencies are expected to decrease slightly on lowering the temperature.

At 1.45 ^{o}K where, according to the Boltzmann factor, the nuclear spin system is $\sim$ 2% polarized, the ratio $m^o/M_A^o \simeq 8.6 \times 10^{-6}$. At 4.2 ^{o}K, this ratio is $\sim 3.0 \times 10^{-6}$. Thus, at 1.45 ^{o}K an enhancement factor of 100 would result in a frequency shift of $\sim$ 0.6 MHz, while at 4.2 ^{o}K it would be $\sim$ 0.2 MHz. Similarly, an enhancement factor of 1000 would give frequency shifts of $\sim$ 6 MHz at 1.45 ^{o}K and $\sim$ 2 MHz at 4.2 ^{o}K. From Tables 1 and 3, and Figure 6-b, there appears to be less than about one MHz of frequency pulling over the entire field and temperature ranges for the domain component, suggesting that the enhancement factor for the domain nuclei is of the order of a few hundred, while from the ν_{10} vs H_{ext} plot in Figure 6-b, there may be slightly stronger frequency pulling for domain-wall nuclei, suggesting a slightly stronger enhancement factor, but not nearly as strong as expected from the discussion of the domain wall enhancement factor in Chapter I. The difficulty in fitting the spectrum in H_{ext} = 3.0 kOe at 4.2 ^{o}K prevents any accurate determination of the size of frequency pulling effects at this stage. The indications are that the decrease in domain wall resonance frequency on going from 4.2 to 1.45 ^{o}K is about 1 MHz, which is roughly the same size as the decrease in domain resonance frequency over this temperature range.

Some of the difficulty in reconciling the observed frequency pulling with the expected size of the domain wall enhancement factor is related to the fact that the domain wall enhancement factor, given by Equation I-48, is a function of the position of the nucleus in the wall. Thus, in the presence of frequency pulling, the domain-wall lineshape will be distorted since regions of high enhancement factor will be shifted more than those of low enhancement factor. This effect may also be connected with the difficulty in interpreting the spectra for temperatures between 4.2 and 2.51 ^{o}K. Since the exact nature of the domain-wall signal at the upper end of this temperature range is uncertain, little more can be said about the weak frequency pulling observed in this sample. The data for the single crystal of $Ni_{0.03}Mn_{0.62}Fe_{2.36}O_4$, shown in Figure I-2, exhibit the frequency pulling effect much more clearly.

In studying the low-field spectra, where there are two components to the signal, it becomes apparent that, in doing a least-squares fit, the sharp drop (see e.g., Figures 4 and 8) in echo amplitude on the high frequency side of the spectrum pushes the domain-wall component fitting function, assumed to be Lorentzian and thus very broad in the wings, to lower frequencies where, because of the more gradual decrease with frequency in echo amplitude on the lower frequency side, the Lorentzian wings pay a smaller penalty in σ^2(the variance, minimized by the fitting procedure). To compensate for this, the Gaussian domain line fitting function, which is actually too weak in the wings, is pulled to higher frequencies by the fitting procedure. Thus, whenever both signal components are present there appears to be a repulsion of the two components strictly due to the error in the fitting process due to the deviation of the fitting functions from the true lineshapes. This effect could mask some small frequency pulling, although the expected change of a megahertz or more should easily overcome this problem.

Figures 9-1a,b show the H = 3.0 kOe spectra at temperatures T = 1.91 and 2.10 ^{o}K, respectively. These spectra have the same general shape as those in the same external field at lower temperatures, and the parameters used to fit these spectra are very nearly the same as those which fit the 1.45 and 1.75 ^{o}K spectra, as given in Table 3. Further, as shown in Figures 10-a,b,c which show the H = 8.0 kOe spectrum at 2.10 ^{o}K for pulse separations τ = 30, 40, 50 μsec, respectively, the higher field spectra retain their relatively simple shape (compare with the H = 8 kOe spectrum at 1.45 ^{o}K shown in Figure 2).

At higher temperatures, however, the low field spectrum begins to change shape, as shown in Figure 11-a, illustrating the T = 2.51 ^{o}K spectrum in H_{ext} = 3.0 kOe. The low frequency side of the spectrum appears flattened, making it impossible to fit the spectrum, with the same accuracy as those at lower temperatures, with two symmetric lines. The spectrum for

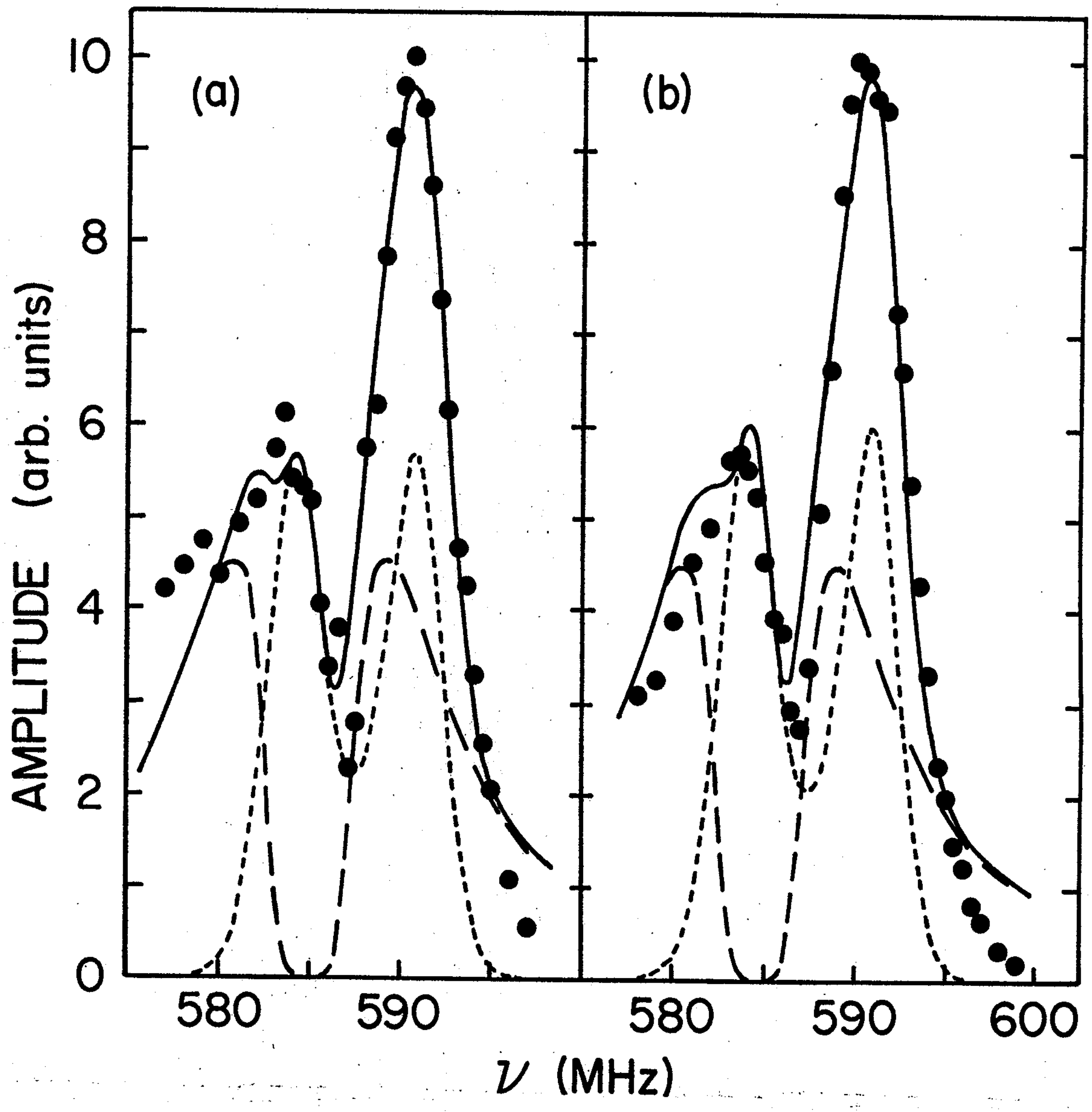

Figure 9. H_o = 3.0 kOe spectra for τ = 30 μsec at a) T = 1.91 °K, b) T = 2.10 °K. Solid curves are the fit to the spectra, and the dashed curves show the two components of the signal.

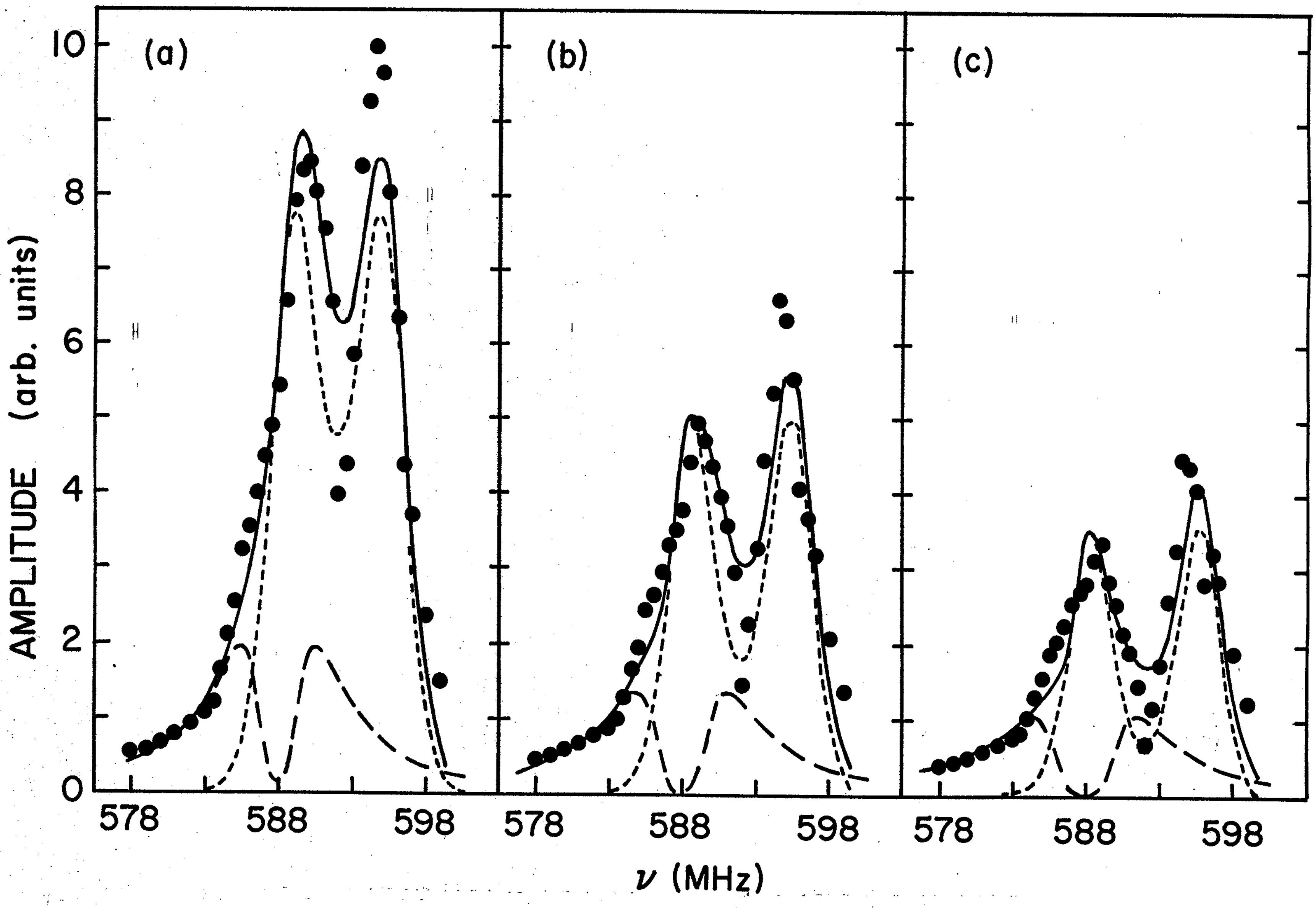

Figure 10. Partially relaxed spectra at T = 2.10 °K in H_o = 8.0 kOe for a) τ = 30 μsec, b) τ = 40 μsec, c) τ = 50 μsec. Solid curves show the fit to the entire set of partially relaxed spectra.

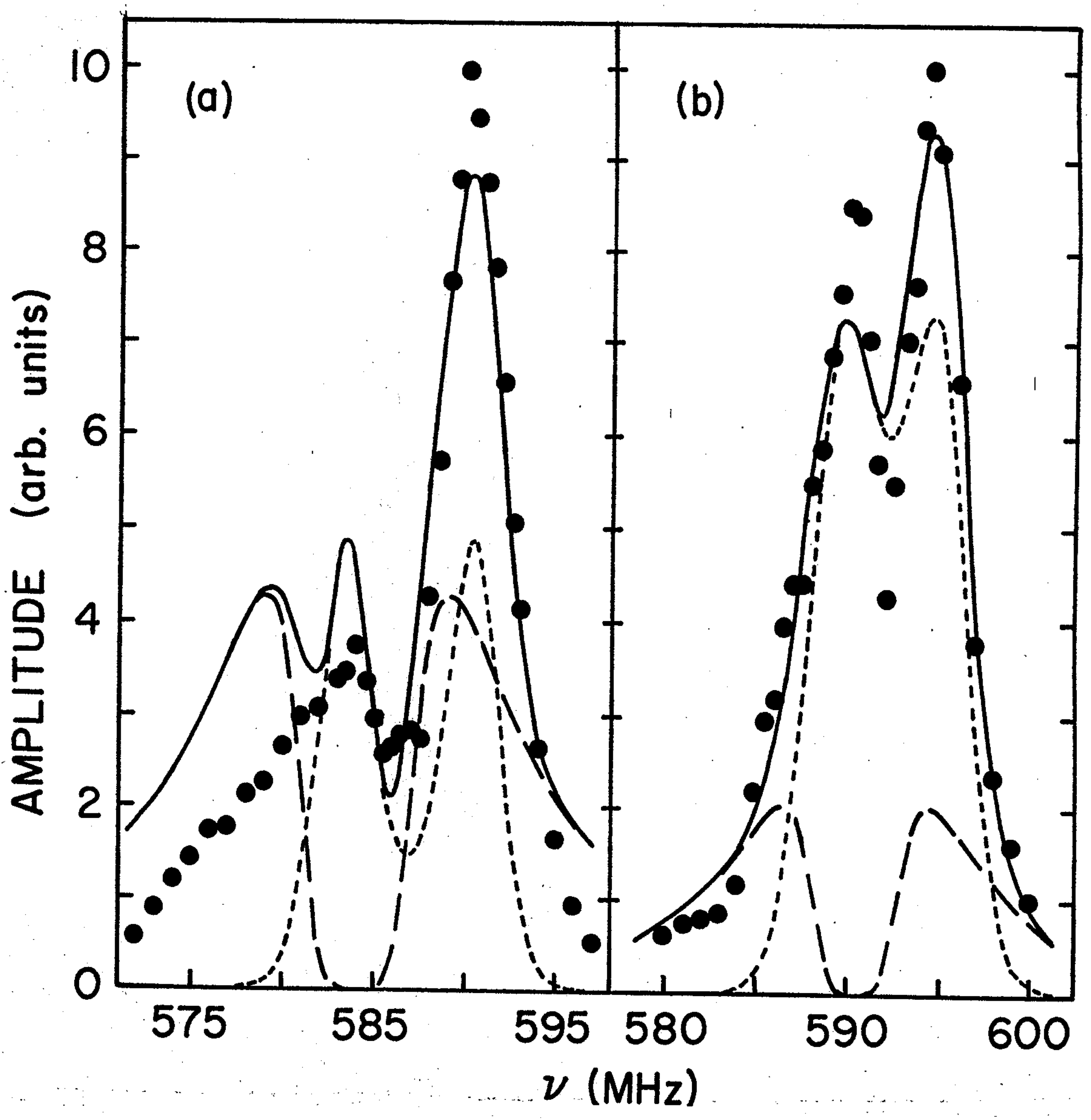

Figure 11. Spectra at T = 2.51 °K for τ = 30 μsec. a) H_o = 3.0 kOe, b) H_o = 8.0 kOe. Solid curves are the fits to the spectra.

H_{ext} = 8.0 kOe at this temperature, shown in Figure 11-b, is very similar to all of the spectra at corresponding fields at lower temperatures. At T = 3.28 ^{O}K the spectrum at the lower value of field is even more distorted, as shown in Figure 12-a, while the higher field spectrum at this temperature, shown in Figure 12-b, is still well behaved. Thus, it appears that the domain-wall component is changing in some way on raising the temperature, making the spectra quite difficult to interpret. The domain component of the spectrum appears to remain the same throughout the temperature range however. Table 4 summarizes the H_{ext} = 8.0 kOe data for the entire temperature range, showing little change in the domain component parameters.

The intermediate to high field spectra at 4.2 ^{O}K are illustrated in Figures 13-a,b,c for H_{ext} = 8.0, 6.0, 5.0 kOe, respectively. The spectrum at H_{ext} = 8.0 kOe is quite similar to those for this field at lower temperatures, although there is a bit more scatter in the data, especially for larger values of pulse separation. This spectrum can still be fit fairly well with the usual 8 kOe parameter values, as shown in Table 4. At H_{ext} = 6.0 kOe, the spectrum still seems fairly well-behaved while at 5 kOe, there is an indication of some difficulty in the appearance of an extra peak in the τ = 30 μsec spectrum shown in this figure. At H_{ext} = 3.0 kOe the spectrum shown in Figure 14 has acquired a very different shape which is difficult to interpret within the framework of the model of two symmetric overlapping lines. Figure 14-a shows an attempt to fit this spectrum assuming linewidths δ_1 = 1.189 MHz and δ_2 = 2.626 MHz, while Figure 14-b is the fit obtained allowing these linewidths to vary, yielding δ_1 = 0.874 MHz and δ_2 = 2.008 MHz. The parameters for these two attempts at fitting this spectrum are given in Table 3 with the labels a)

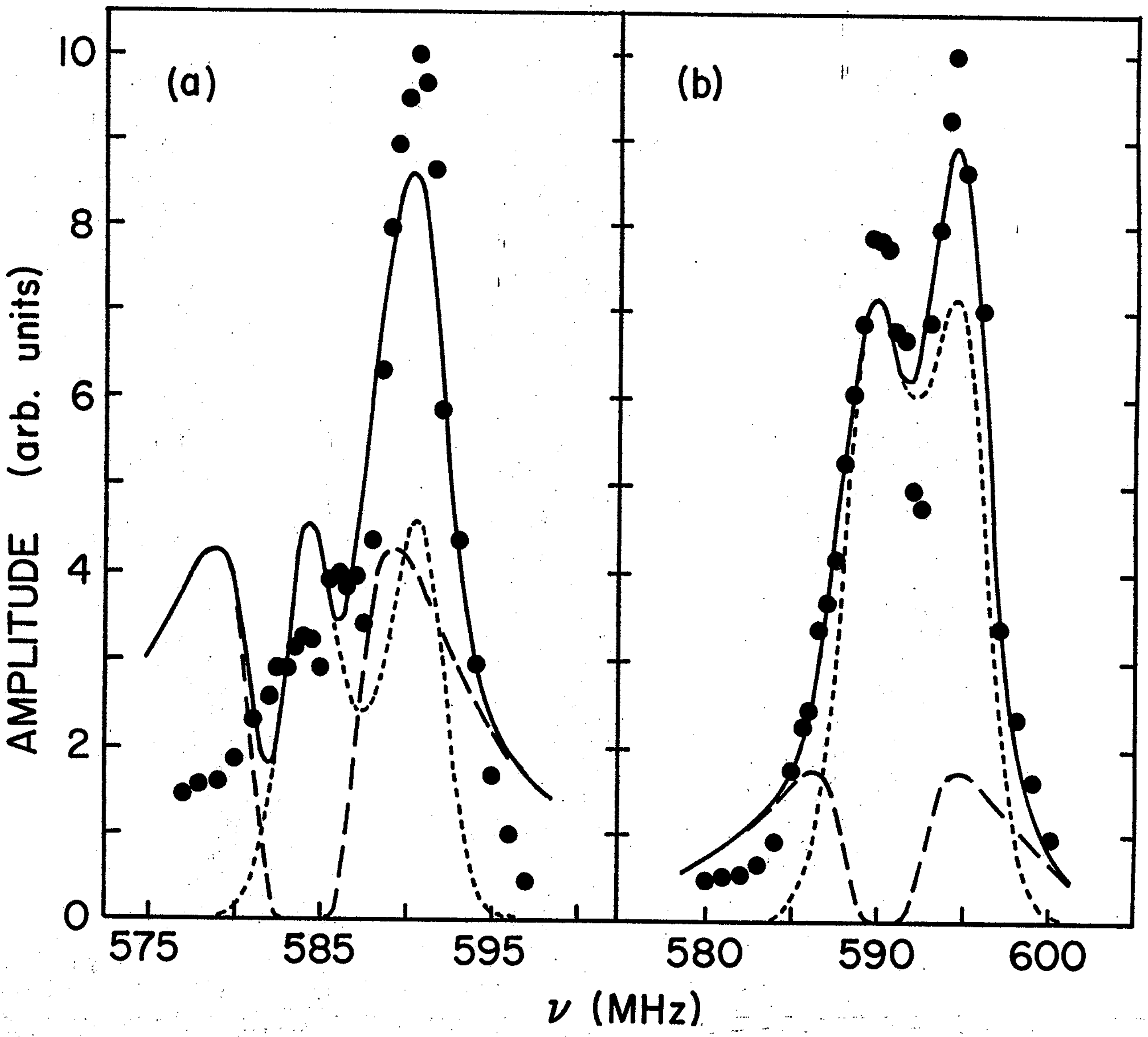

Figure 12. Spectra at T = 3.28 °K for τ = 30 μsec with a) H_o = 3.0 kOe, b) H_o = 8.0 kOe. Solid curves are the fits to the spectra.

Table 4. Temperature dependence of spectral parameters in H_o = 8.0 kOe.

T	A_1	T_{10}	ν_{10}	δ_1	T_{B_1}	A_2	T_{20}	ν_{20}	δ_2*	T_{B_2}
1.45	18.58	45.93	587.7	1.262*	-----	103.6	35.30	592.2	2.626	240.8
1.75	12.93	25.80	587.9	1.201	-----	43.86	26.83	592.1	2.626	300.1
1.91	3.380	31.75	587.9	4.655	-----	21.03	25.36	591.8	2.626	222.6
2.10	15.76	11.27	587.9	1.25	500.0*	35.28	25.61	591.9	2.626	166.4
2.51	30.25	4.89	590.4	1.189	519.2	22.25	34.15	592.1	2.626	128.7
3.28	24.61	4.51	590.4	1.189*	126.0	15.48	35.09	592.1	2.626	91.85
4.2	20.92	5.06	590.6	1.189*	98.35	19.79	46.65	592.5	2.626	55.25

*held constant.

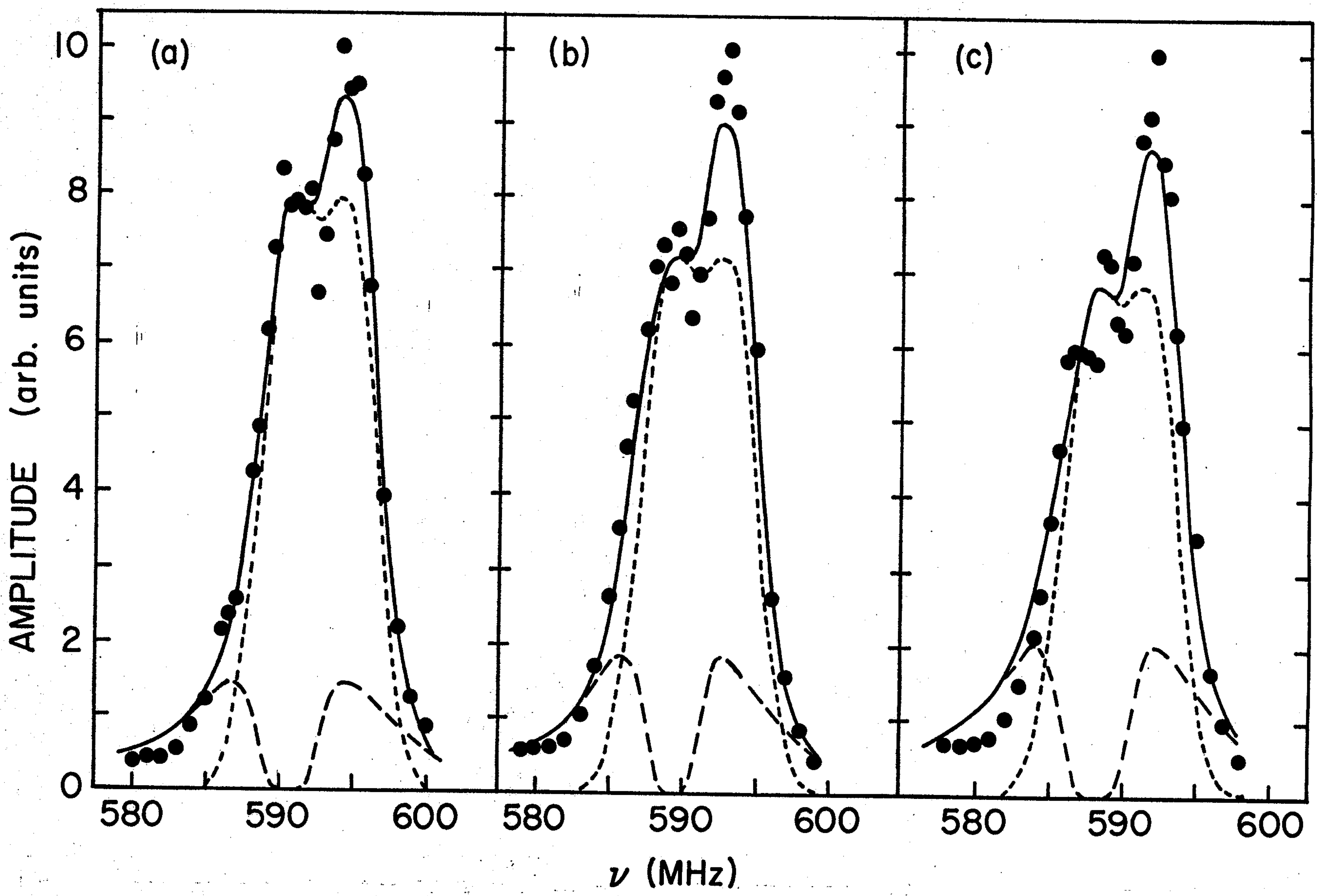

Figure 13. T = 4.2 °K spectra for τ = 30 μsec with a) H_o = 8.0 kOe, b) H_o = 6.0 kOe, c) H_o = 5.0 kOe. Solid curves are the fits to the spectra.

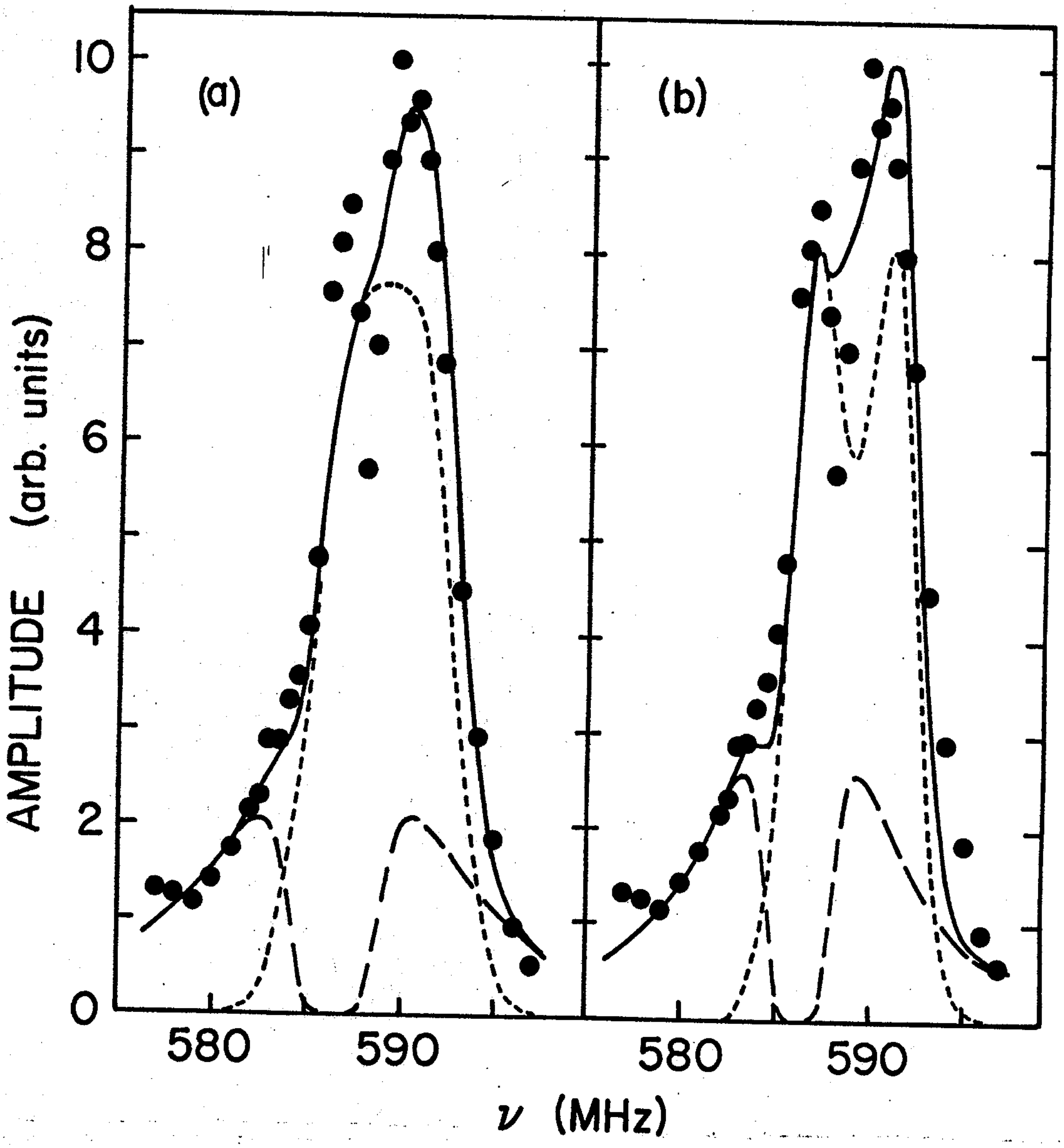

Figure 14. Spectrum at T = 4.2 °K in H_o = 3.0 kOe for τ = 30 μsec. Solid curves give the fit to the spectrum with a) δ_1 = 1.189 MHz and δ_2 = 2.626 MHz, b) δ_1 = 0.874 MHz and δ_2 = 2.008 MHz.

and b) to identify them with this figure. Notice also that the values of T_{10} and T_{20} do not agree with those obtained at other temperatures.

Before proceeding to the discussion of the temperature dependent background relaxation it seems appropriate to summarize the main features of the data. The temperature range covered, from 1.45 to 4.2 °K, should be divided into two regions, above and below 2.10 °K. In the lower temperature region the spectra are well described by the two component model. The amplitudes of both components of the signal appear to decrease with increasing temperature in this range, probably due to changes in the enhancement factors. The linewidths and frequencies of the two components, as well as T_{10} and T_{20}, can be considered to be roughly constant over this part of the temperature range. In the higher temperature region, above 2.10 °K, the spectrum at $H_{ext} = 3.0$ kOe becomes increasingly difficult to interpret as the temperature is raised, while at $H_{ext} = 8.0$ kOe the spectrum remains fairly well behaved and well described by the model throughout the entire temperature range. Thus, it appears that the domain-wall component of the signal is changing with temperature. Above 2.1 °K the spectra at 8.0 kOe fit better with $\delta_1 = 1.189$ MHz than with the value of $\delta_1 = 1.262$ MHz used for lower temperatures. The 3 kOe spectra, in the higher temperature region, look (to the eye) as though a narrower domain-wall line might improve the fit. However, attempts to force the computer to fit these spectra with a narrower line were not successful. Finally, the unexpectedly weak frequency pulling of both components (being of roughly the same magnitude) may be related to the difficulty in fitting the higher temperature spectra.

In Section 4 there will be a further discussion of the low field spectra at 4.2 °K on the oriented crystal in an attempt to clear up some of the difficulties discussed here. In this context it will be shown that the spectra at H_{ext} = 2.0 kOe are considerably easier to analyze since the sample appears to saturate more easily at 4.2 ^{o}K than at 1.45 ^{o}K with the result that at H_{ext} = 3.0 kOe at 4.2 ^{o}K the domain-wall signal has become quite weak.

3.2 Temperature dependent background relaxation

One effect which is quite clearly visible from the spectra taken over this temperature range is the temperature dependence of the background relaxation rate, as shown in Figures 15-a,b for the domain and domain-wall components. There is considerable scatter in the values obtained for these background relaxation rates due to the difficulty in extracting these relatively small contributions to the relaxation in the presence of the strong frequency-dependent relaxation processes. However, there is definitely an observable change both in the data for the $MnFe_2O_4$ single crystal sphere, as shown in Table 3, and in the data for the $Ni_{0.03}Mn_{0.62}Fe_{2.36}O_4$ crystal, discussed in Chapter III with reference to the frequency dependent relaxation processes. Also, as is clearly evident in Figure 15, there is a great difference in the behaviour of the background relaxation rates of the two components, that for the domain component apparently tending toward the constant value of $(1/T_c) = 4.67 \times 10^3$ $(sec)^{-1}$, as shown by the dashed line in the figure, while the domain-wall component's background rate drops steadily with decreasing temperature. By subtracting $(1/T_c)$ from each of the domain component values, shown by the solid circles, the values given by the triangles are seen to follow a temperature dependence very similar to that of the domain-walls'.

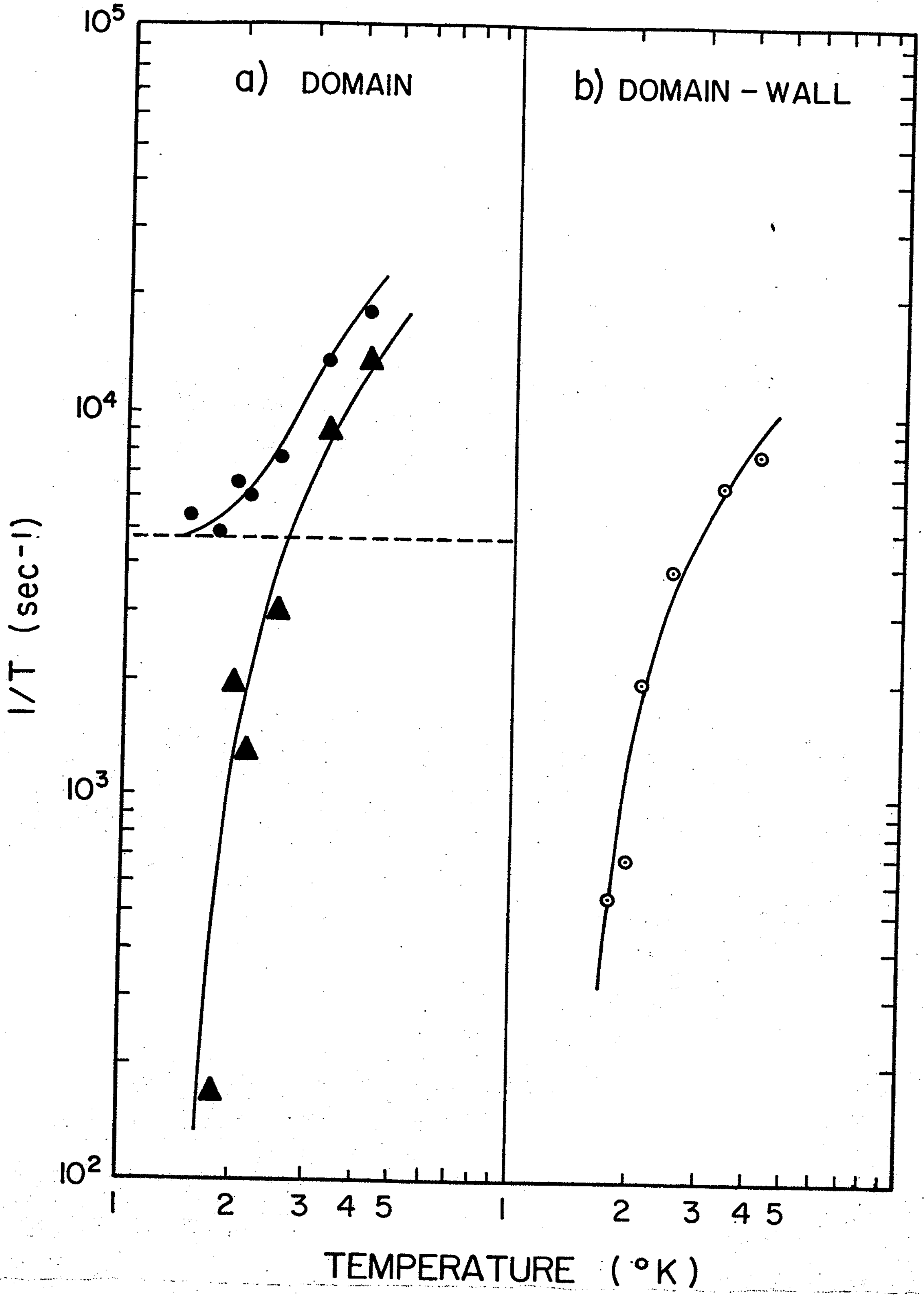

Figure 15. Temperature dependence of the background relaxation rate in H_{ext} = 3.0 kOe, a) the solid circles give the measured relaxation rate of the domain component while the triangles show the values obtained when $1/T_C = 4.67 \times 10^3$, shown as the dashed line, is subtracted from each point b) the open circles give the background relaxation rate of the domain-wall component.

The magnitude of T_c is comparable to the value of $T_{\ell d}$, the longitudinal dipole-dipole relaxation time, obtained from the calculated second moment of $\mathcal{H}_{\ell d}$, in Chapter III. This suggests that somehow the longitudinal dipole-dipole interaction is ineffective in relaxing the domain-wall component. The transverse part, $\mathcal{H}_{td}$, may or may not be affected, it is difficult to tell since its relaxation rate exhibits the same frequency dependence as $1/T_{S-N}$, the relaxation rate due to the Suhl-Nakamura interaction, which is still very strong for domain-wall nuclei.

It appears then that the contribution of the longitudinal part of the dipole-dipole interaction to the homogeneous linewidth of the domain-wall component has been strongly narrowed. The mechanism for this narrowing effect is unclear but may be one of the following: i) spectral-diffusion within the domain walls, ii) thermal fluctuations of the domain walls, or iii) fluctuations of the domain-wall hyperfine field. The direct identification of the narrowing mechanism is made more difficult by the presence of the two independently relaxing components to the signal.

In the usual theory of motional narrowing[81] one considers a total Hamiltonian of the form

$$\mathcal{H} = \mathcal{H}_o + \mathcal{H}_p + \mathcal{H}_m \qquad (4)$$

where, for example, $\mathcal{H}_o$ is the Zeeman interaction which determines the position of the resonance lines in the spectrum, $\mathcal{H}_p$ is the perturbing interaction responsible for the broadening of these lines, and $\mathcal{H}_m$ is some motional Hamiltonian which may narrow the broadening due to $\mathcal{H}_p$ by introducing a time dependence (e.g., a random frequency modulation) to $\mathcal{H}_p$. To use the results of this theory, the following conditions must be met

$$[\mathcal{H}_m, I_x] = 0 \quad , \quad [\mathcal{H}_m, \mathcal{H}_p] \neq 0 \quad , \quad [\mathcal{H}_m, \mathcal{H}_o] = 0 \tag{5}$$

These commutation relations simply state that, to apply the motional narrowing theory as developed, $\mathcal{H}_m$ must have no direct effect on the spectrum, it cannot affect the radiation emitted or absorbed by the system, its only effect being to modulate $\mathcal{H}_p$.

In the present case, the total Hamiltonian is of the form

$$\mathcal{H} = \mathcal{H}_I^z + \mathcal{H}_S^z + \mathcal{H}_{II} + \mathcal{H}_{IS} + \mathcal{H}_{SS} \tag{6}$$

where $\mathcal{H}_I^z$ and $\mathcal{H}_S^z$ are the nuclear and electronic Zeeman Hamiltonians, $\mathcal{H}_{II}$ represents all of the nuclear spin-spin interactions (Suhl-Nakamura as well as transverse and longitudinal dipole-dipole), $\mathcal{H}_{IS}$ is the hyperfine interaction $(A\vec{I}\cdot\vec{S})$, and $\mathcal{H}_{SS}$ is the electronic exchange interaction.

$\mathcal{H}_{SS}$ commutes with I_x and all of the other terms in the total Hamiltonian except $\mathcal{H}_{IS}$. Thus the electronic exchange Hamiltonian can, and does, narrow the contribution of the hyperfine interaction to the nuclear resonance linewidth. Because of the great strength of the exchange interaction, any direct contribution of the hyperfine interaction to the linewidth may be neglected. The exchange interaction may be neglected, however, when considering the broadening due to $\mathcal{H}_{II}$, since it can have no effect on this contribution to the linewidth[82].

Since $\mathcal{H}_{IS}$ does not commute with $\mathcal{H}_{II}$, fluctuations in the hyperfine interaction, as may be described by a fluctuating hyperfine field, may be expected to affect the broadening due to $\mathcal{H}_{II}$. However, $\mathcal{H}_{IS}$ does not commute with I_x and a straightforward application of the prescription for motional narrowing as outlined in Equations 4 and 5 is not possible. However, a rough physical argument can give some insight into the effects produced by a fluctuating hyperfine field.

The z-component of the hyperfine interaction can be written in conjunction with the nuclear Zeeman interaction as

$$\begin{aligned}\mathcal{H} &= \mathcal{H}_I^z + AI_z\langle S_z\rangle + AI_z(S_z(t) - \langle S_z\rangle) \\ &= \hbar\gamma(H_o + H'_{hf}) + \hbar\gamma h(t) \qquad (7) \\ &= \mathcal{H}_I'^z + \mathcal{H}'_{IS}\end{aligned}$$

The hyperfine field H'_{hf} is the mean value of the hyperfine field in the presence of fluctuations in the field and will have a magnitude somewhat smaller than the maximum hyperfine field--the field in the absence of any fluctuations. There will be a distribution of hyperfine fields, centered at H'_{hf}, with a width $\sim (1/\tau_c)$, where τ_c is the characteristic time describing the fluctuations. The contribution of this fluctuating hyperfine field to the linewidth would be expected to be very large if not for the very strong narrowing due to the electronic exchange interaction, as mentioned earlier. There is expected to be a static broadening, due to the expected distribution of hyperfine fields, given by $(1/\tau_c)$, however, for correlation times $\tau_c \gtrsim 10$ μsec, this additional broadening would not be visible in the presence of the strong inhomogeneous broadening ($\sim$ 1 - 2 MHz) characteristic of these magnetic materials.

For the purposes of this discussion the correlation function for the fluctuating field h(t) in Equation 7 may be assumed bo be of the form[83]

$$G(\tau) = \langle h_o^2\rangle \exp(-\tau/\tau_c) \qquad (8)$$

Then, for $\tau_c \gg \tau_L$, where τ_L is the period of the Larmor precession, the shift in Zeeman energy $\Delta\mathcal{H}^z = \hbar\delta\omega_o$ due to the fluctuations is given by

$$G(\tau_L) \approx G(0) = \langle h_o^2 \rangle \sim \hbar\delta\omega_o \qquad (9)$$

the magnetic energy of the fluctuating field[83].

The broadening of the resonance line due to nuclear spin-spin interactions is the result of two types of interactions: the transverse interactions (dipole-dipole and Suhl-Nakamura) and the longitudinal dipole-dipole interaction. The contributions to the linewidth are $(1/T_t)$ and $(1/T_\ell)$ and for $T_t \approx 5$ μsec, and $T_\ell \approx 200$ μsec, as in the present case, result in a line much like that illustrated in Figure 16 showing two Gaussian lines with corresponding widths (the ratio of the linewidths in the figure is 10 rather than the 40 obtained from the relaxation times given above, thus the actual difference is even greater than suggested by the figure). For a correlation time such that $5 << \tau_c << 200$ μsec, one might expect the broadening due to the longitudinal relaxation to be severly narrowed, while that due to the transverse interaction to be relatively unchanged since the criterion for moational narrowing is, roughly, that $\overline{(\Delta\omega^2)}^{\frac{1}{2}}\tau_c << 1$.

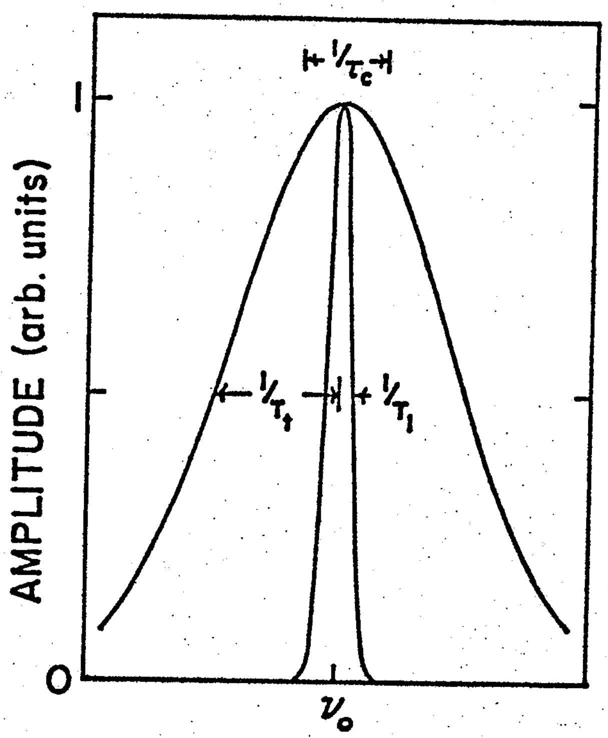

Figure 16. Contributions to the linewidth compared to $1/\tau_c$.

Each nucleus within a domain-wall feels the fluctuations in its hyperfine field resulting in fluctuations in its Zeeman energy or in its

Larmor precessional frequency. Since the hyperfine field at each nucleus fluctuates independently from that at neighboring nuclei, any interactions between nuclei will be randomly frequency modulated, resulting in a decreased effectiveness in the interaction, as in the usual motional narrowing situation. The transverse interaction, even though it requires mutual spin flips between nuclei, and therefore, energy conservation, is so strong (especially in the case of the Suhl-Nakamura interaction) that the fluctuations in nuclear Zeeman energy are too small to affect the mutual exchange of energy, i.e., $\Delta E_t \tau_c << h$, where ΔE_t is the transverse interaction energy.

If the observed shift of ∿ 2.5 MHz in the domain-wall nuclear resonance frequency from that of nuclei in domains is due to hyperfine field fluctuations, as in Equation 9, then in order for these fluctuations to be responsible for the apparent narrowing of the longitudinal dipole-dipole relaxation, it is expected that, on a time scale defined by $T_\ell = 200$ μsec,

$$G(\tau = 200\ \mu\text{sec}) = \langle h_o^2 \rangle \exp(-200/\tau_c) \sim \hbar(2\pi/T_\ell) = (h/200)$$

or

$$\exp(-200/\tau_c) \sim (1/200)/\delta\nu_o \simeq 2 \times 10^{-3} \qquad (10)$$

giving

$$\tau_c \simeq 32\ \mu\text{sec}$$

as the correlation time. This fits nicely within the limits $200 >> \tau_c >> 5$ μsec , necessary for the narrowing of the longitudinal dipolar linewidth but not of the transverse linewidth.

This rough physical picture indicates that a static frequency shift is compatible with a narrowing of the longitudinal portion of the resonance linewidth. The estimate of the correlation time is very insensitive to the magnitude of the frequency shift, however. The physical process responsible for the fluctuations is still uncertain. If this process is thermally activated there will of course be a temperature dependence in the correlation time, however, further speculation on this subject is not warranted at this time. A more detailed study of the frequency independent relaxation is required before any further analysis can be attempted.

The temperature dependent part of the background relaxation rates of both signal components, shown in Figure 15, is expected to be due to spin-wave scattering processes, in particular the three-magnon exchange enhanced process and the dipolar induced two-magnon processes discussed in Chapter III, Section 4.

The three-magnon relaxation rate, from Equation III-41, is

$$(1/T)_{3m} = m(2\pi/\hbar)\,\frac{A^2}{16S_A\hbar\omega_e}\left(\frac{S_A/2}{S_B - S_A/2}\right)^3(1/4\bar{N}_A\pi^2)^3(7.6)(kT/\hbar\omega_e)^{7/2} \quad ,(11)$$

where m is the effective enhancement of the process due to the four-magnon exchange scattering ($m \sim 8$) and the factor of 7.6 is due to an integral which, for $g\mu_B H << kT$, is only slightly dependent on H and T, the field and temperature. Using the value $\hbar\omega_e = 1.3 \times 10^{-15}$ ergs corresponding to an exchange field $H_{ex} = 2.6 \times 10^6$ Oe as determined from $T_F \sim 600$ °K, the three magnon relaxation rate is given by

$$(1/T)_{3m} = m(1.8 \times 10^{-5})\; T^{7/2}$$

which at T = 4.2 °K gives $(1/T)_{3m} \approx 2.2 \times 10^{-2}\,\mathrm{sec}^{-1}$, which is far too small to account for the measured relaxation rate.

The two-magnon relaxation rate, from Equation II-58 is

$$(1/T)_{2m} = \left(\frac{S_A/2}{S_B - S_A/2}\right)^2(2/15\pi)\,\frac{A^2}{\hbar^2\omega_e}\left(\frac{g\mu_B M'}{\hbar\omega_e}\right)^2\left(\frac{kT}{g\mu_B H}\right)^2(1/\bar{N}_A^2)\ln\left(\frac{\exp(g\mu_B H/kT)}{\exp(g\mu_B H/kT) - 1}\right)$$

$$= \left(\frac{S_A/2}{S_B - S_A/2}\right)^2\frac{A^2}{\hbar^2\omega_e}\left(\frac{g\mu_B M'}{\bar{N}_A\hbar\omega_e}\right)^2 F(kT/g\mu_B H) \quad ,(12)$$

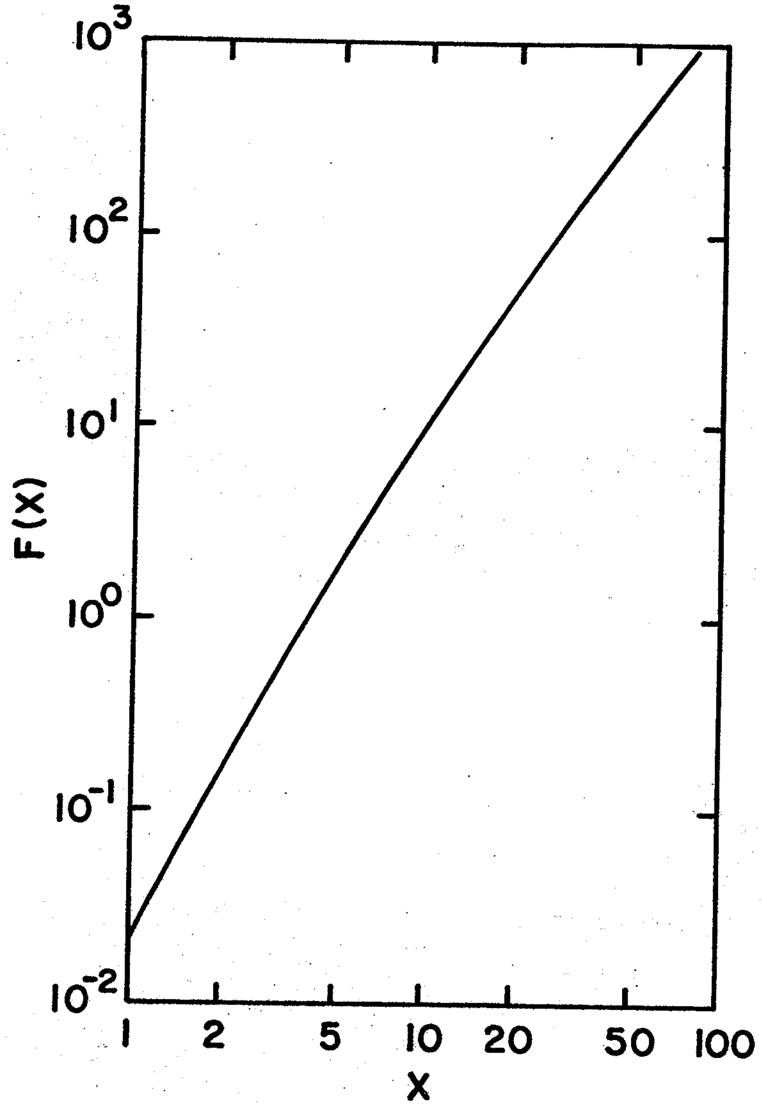

Figure 17. Two-magnon relaxation function F(x) versus x.

where the function

$$F(kT/g\mu_B H) \;=\; (2/15\pi)(kT/g\mu_B H)^2 \ln\left(\frac{\exp(g\mu_B H/kT)}{\exp(g\mu_B H/kT) - 1}\right) \qquad (13)$$

is plotted in Figure 17. Thus, the two-magnon relaxation rate is given by

$$(1/T)_{2m} = 0.852 \times F(kT/g\mu_B H)$$

using M' = 560 emu/cc. For $H = H_K \simeq 500$ Oe, and T = 4.2 °K, (using the same value of $\hbar\omega_e$ as for Eqn. 11),

$$(1/T)_{2m} = 7.79 \times 10^2 \text{ sec}^{-1}$$

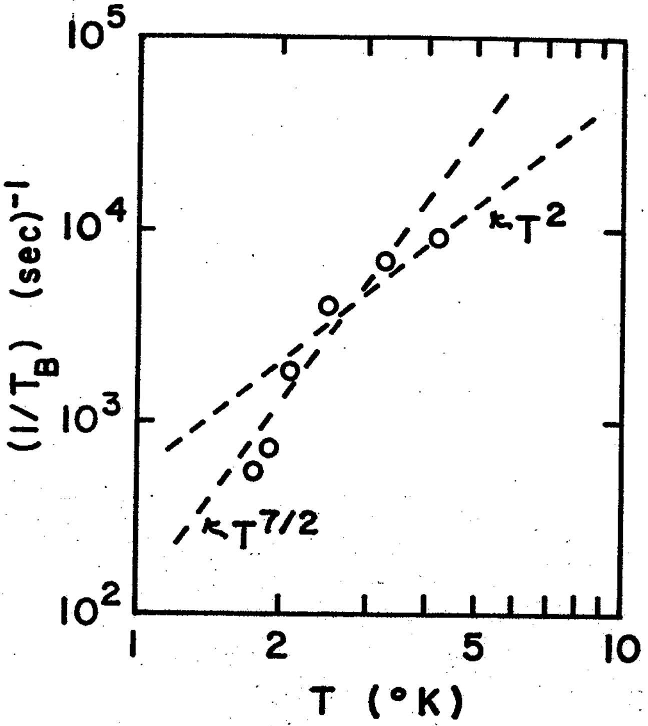

Figure 18. Comparison of domain-wall background relaxation rate to temperature dependences of spin-wave relaxation processes.

This value corresponds within an order of magnitude to the measured relaxation rate for the domain-wall component. The agreement is almost within the considerable experimental error, however, decreasing $\hbar\omega_e$ by roughly a factor of two so that $\hbar\omega_e = 6.0 \times 10^{-16}$ ergs, gives the measured value at T = 4.2 °K. Figure 18 compares the calculated relaxation rates with the domain-wall component's relaxation rate over the temperature range of 4.2 to 1.45 ^{o}K, here the two-magnon relaxation rate is assumed to vary as (T^2) while the three-magnon relaxation rate goes as ($T^{7/2}$), these are shown by the dashed lines in the figure. The measured values do not follow either line very closely, and appear to follow a temperature dependence which is a mixture of these two. More data is required, however, before a detailed comparison between experiment and theory can be made. Each of the two most prominent spin-wave processes (these two- and three-magnon processes) exhibit a characteristic field dependence which will help identify which is responsible for the relaxation if the data is taken over a wide enough range of fields. This will require going to fields considerably higher than 10 kOe. The domain component of the signal is still very strong at 10 kOe, and should allow measurements to be made up to as high as 25 kOe, if the field is available.

It can be mentioned that if the spin-wave relaxation processes responsible for the observed relaxation are the same for both nuclei within the domain walls and those in the domains, the somewhat weaker exchange and anisotropy fields expected for domain-wall nuclei (as pointed out in the discussion of the frequency dependent Suhl-Nakamura relaxation time in Section 2 of this chapter) should lead to domain-wall relaxation-rates somewhat larger than those of the domain nuclei. Also, the non-colinear arrangement of spins in the domain-wall may permit the occurrence of the direct Raman process, resulting in stronger domain-wall relaxation. The background relaxation rates of the two signal components seem to be roughly equal, however, and more detailed as well as more accurate measurements are required to resolve these points.

This concludes the discussion of a large part of the experimental data. It seems appropriate at this point to review briefly the major features of the observed spectra. These spectra are from a randomly oriented single crystal sphere of $MnFe_2O_4$, covering a temperature range of from 1.45 to 4.2 ^oK, in externally applied fields of from 0 to 10 kOe. The A-site ^{55}Mn nuclear magnetic resonance occurs under these conditions at a frequency of $\sim$ 590 MHz due to the strong electronic hyperfine field at the nucleus. The low field spectra contain two components, one from nuclei in domain-walls which have a hyperfine field of $\sim$ 558 kOe, the other from nuclei in the bulk domains with a hyperfine field of $\sim$ 560 kOe. The lineshapes of these two components are of an intermediate character with the domain-wall component's lineshape tending more towards a Lorentzian while the domain component's lineshape is more nearly Gaussian. The linewidths of the two components are comparable (half-widths at half-maximum given by, $\delta_w = 1.262$ MHz assuming a Lorentzian domain-wall line, and $\delta_d = 2.626$ MHz for a Gaussian domain line) and are of the same order of magnitude as the difference in the resonance frequencies of the two components ($\nu_{d_o} - \nu_{w_o} \approx 2.5$ MHz, at $T = 1.45$ ^oK), resulting in considerable overlap of the two resonance lines. There is a conspicuous absence of the strong frequency pulling effects expected for the domain-wall component in that both components exhibit roughly the same amount of frequency pulling (of less than $\sim$ 2 MHz over the temperature and field ranges). The data for the $Ni_{0.03}Mn_{0.62}Fe_{2.36}O_4$ crystal, discussed in Chapters II and III, show indications of stronger frequency pulling for the domain component, but the domain-wall component was not studied in this crystal. A further distinction between the two crystals is the persistence of the domain-wall component up to fields as high as $\sim$ 7 kOe in the $MnFe_2O_4$ sample, whereas, in the previous sample, the spectrum was well described by a single domain line at fields as low as $\sim$ 3 kOe.

The relaxation processes are dominated by the Suhl-Nakamura interaction which gives a frequency dependent relaxation time in good agreement with the data. The dipole-dipole interaction provides two additional relaxation processes; one which exhibits the same frequency dependence as the Suhl-Nakamura interaction and is due to the transverse part of the dipole-dipole interaction, and the other, due to the longitudinal part, which is frequency and temperature independent. For nuclei in domain-walls the longitudinal dipole-dipole mechanism appears to be strongly narrowed, probably by fluctuations in the hyperfine field, while the domain component's low temperature frequency-independent relaxation rate is in good agreement with the second moment of the longitudinal dipole-dipole interaction. Both signal components exhibit a strongly temperature dependent background relaxation rate which is at least in order of magnitude agreement with the calculated dipolar-induced two-magnon process. Finally, there remains the unresolved problem of the apparent change in the nature of the domain-wall component for temperatures above $\sim 2.1\ ^{\circ}K$. This last point will be discussed in the next section as part of the discussion of the spectra observed on the oriented crystal.

4. Effects of Crystal Orientation on the Spectrum at $T = 4.2\ ^{\circ}K$

The spectra observed at $4.2\ ^{\circ}K$, shown in Figures 14 and 15, and discussed in Section 3.1, were very difficult to fit using the model of two symmetric resonance lines of widths $\delta_1 = 1.262$ MHz and $\delta_2 = 2.626$ MHz. For this reason, additional spectra were taken in external fields of $H_{ext} = 2.0$ and 3.0 kOe (insufficient to saturate the sample) on the oriented crystal. The sample was mounted on a plexiglas rod with its axis along the crystallographic [110] direction of the sample. Thus, by rotating the sample about this axis the external field (or rf field) could be directed along the ⟨100⟩, ⟨110⟩, and ⟨111⟩ directions, all of which lie in the (110) plane. In these spectra the rf field was applied parallel to the external magnetic field allowing the observation of the spectra from a different point of view. For very low fields this geometry is essentially the same as the configuration normally used where the rf field is perpendicular to H_o, since the sample's internal field remains zero. However, because of the crystalline anisotropy, the sample saturates much more quickly along the [111] direction than, for example, along the [100] direction. Figure 19-a illustrates this effect very clearly, showing the echo amplitude (extrapolated to $\tau = 0$) as a function of angle measured with respect to the ⟨100⟩ direction in the (110) plane. The frequency of 586 MHz was chosen so that only the domain component of the signal was observable (as illustrated in Figure 14 the domain-wall component is essentially totally relaxed at this frequency over the pulse separation range (30 - 130 μsec) used in the measurements). Along the [100] direction the applied field of $H_o = 2$ kOe is not nearly strong enough to saturate the sample and the domain signal is quite strong since the individual domains are still randomly aligned with their magnetization axes along the various ⟨111⟩ directions. In this configuration the rf field makes an angle of $\sim 35^{o}$ with the ⟨111⟩ directions, allowing considerable enhancement of the rf field by the rocking motion of the electronic magnetization. When the crystal is rotated into a position where $\vec{H}_o$ and $\vec{h}_{rf}$ are parallel to the ⟨111⟩ direction, the sample is much closer to saturation in $H_o = 2$ kOe. Thus the rf field is now parallel to the direction of magnetization of most of the crystalline volume, and since there is little rf field enhancement for this configuration, the signal is very

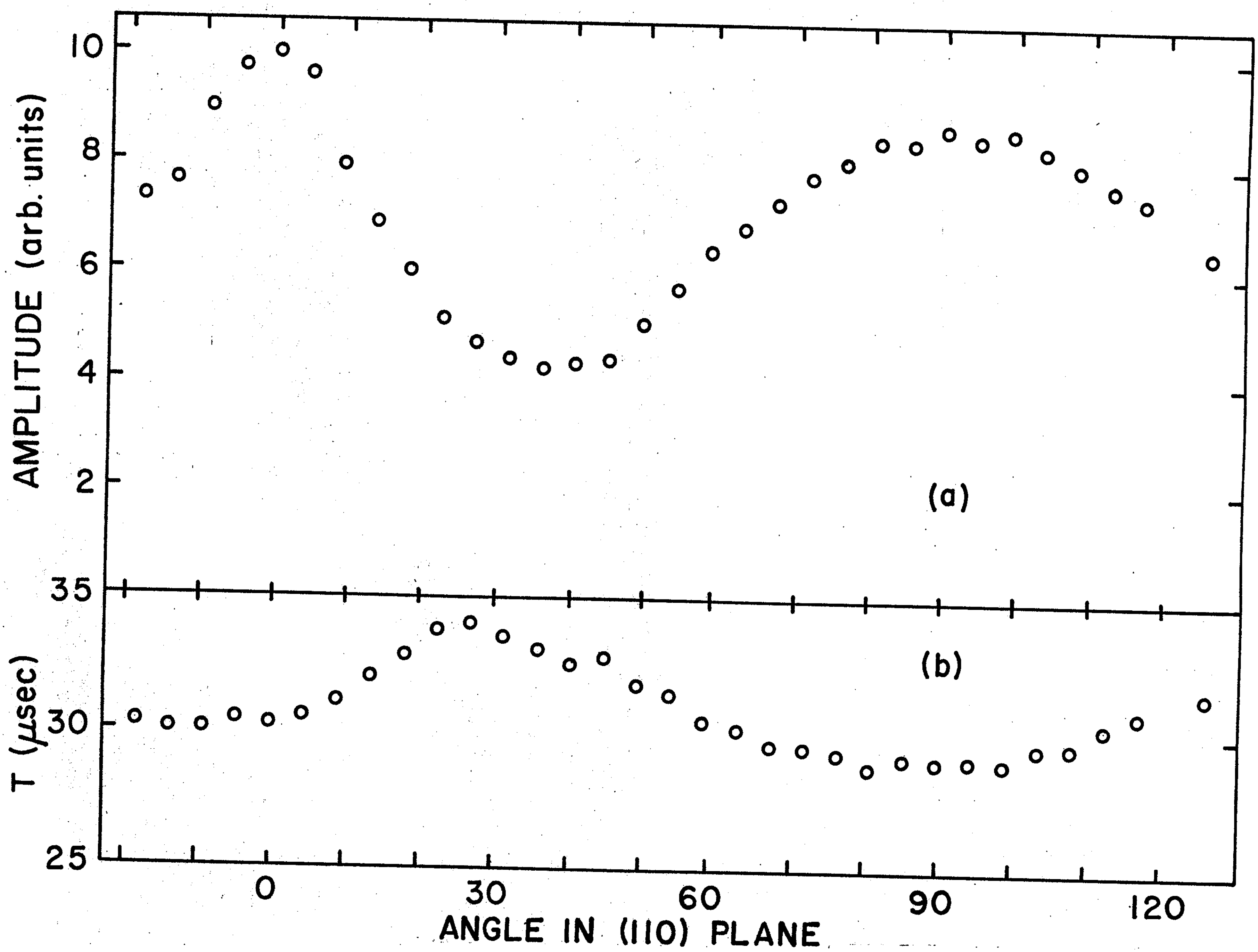

Figure 19. Angular dependence of a) $\tau = 0$ amplitude, and b) relaxation time. $T = 4.2$ °K, $H_o = 2.0$ kOe, and $\nu = 586$ MHz.

weak. The [110] direction is an intermediate case. Here the sample is somewhat easier to saturate than along the [100] direction and significant regions of the sample will have their magnetization along the field direction, reducing the signal to some extent.

Figure 19-b shows the relaxation time of the echo in part (a) of the figure. There appears to be some very small angular dependence which may be due either to a small admixture of domain-wall component for some angles (the echo decay envelope is well described by a single exponential for all angles, however) or to a slight anisotropy in the hyperfine field resulting in the angular variation via the frequency dependent part of the relaxation time. There is also the possibility of introducing some Raman scattering spin-wave relaxation when the applied field is applied along a direction other than the magnetization axis (<111>).

Complete spectra were taken for $\vec{H}_o$ and $\vec{h}_{rf}$ along the <100>, <110>, and <111> directions, covering the same frequency and pulse separation ranges as before although this time the echo amplitude was sampled for every $\tau = 2$ μsec increment in pulse spacing over the 30 to 130 μsec range, providing somewhat improved statistics for determining the relaxation times. The spectra at $H_o = 2$ kOe are very similar in shape for each of these directions, and are shown in Figures 20-a,b,c. In particular they all show the sharp notch at ∿ 588 MHz. This notch is difficult to fit with a Gaussian domain line, however, as discussed in Section 1, the improvement available in this part of the spectrum by using a Lorentzian lineshape will not compensate for the deviation in the wings which would result.

The parameters obtained in fitting these $H_o = 2$ kOe spectra are listed in Table 5. The amplitudes for a given component of the spectrum for

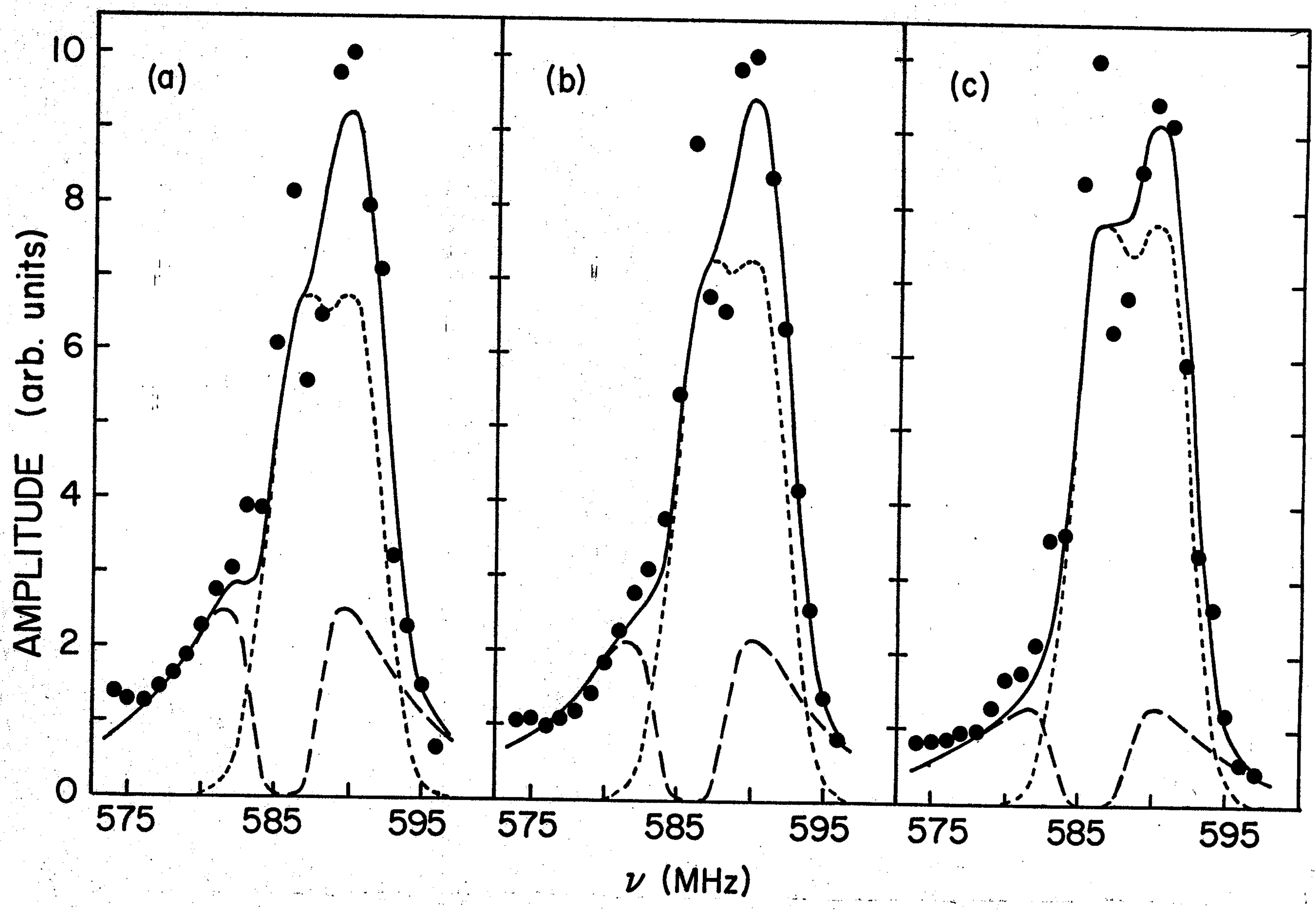

Figure 20. Spectra at T = 4.2 °K in H_o = 2.0 kOe with H_o along a) <100>, b) <110>, and c) <111> directions.

Table 5. Spectra at $T = 4.2\ ^{o}K$ in $H_o = 2$ kOe

Dir. of H_o	A_1	T_{10}	ν_{10}	δ_1	T_{B_1}	%	A_2	T_{20}	ν_{20}	δ_2	T_{B_2}	%
100	128.3	5.056	585.6	1.262	89.73	65	48.50	48.47	588.3	2.626	61.77	35
110	163.0	4.879	585.8	1.262	101.6	58	83.74	49.79	588.4	2.626	58.53	42
111	53.02	4.421	585.7	1.262	137.4	35	70.69	42.52	588.3	2.626	51.47	65

Table 6. Spectra at $T = 4.2\ ^{o}K$ in $H_o = 3$ kOe

Dir. of H_o	A_1	T_{10}	ν_{10}	δ_1	T_{B_1}	%	A_2	T_{20}	ν_{20}	δ_2	T_{B_2}	%
100	44.13	7.801	587.7	1.262	85.43	47	35.00	175.0	590.4	2.626	44.64	53
110	34.22	7.284	586.8	1.262	50.77	81	5.754	49.79	588.4	2.626	59.01	19
111	12.38	6.781	586.9	1.262	56.05	74	3.137	68.91	589.2	2.626	47.60	26

the three different orientations are not related to each other (such data may be more easily and more accurately obtained as in Figure 19). The relative percentages of the two components, as shown in the table are significant, however, showing the rapid removal of domain-wall volume.

The other parameters show only small changes with orientation. The resonance frequencies are well defined and still separated from each other by ∿ 2.6 MHz. The values of the resonance frequencies are ∿ 1.5 MHz higher than the corresponding values measured at $T = 1.45\ ^{o}K$ (see Table 2). This shift in both resonance frequencies is very probably due to frequency pulling, as might have been inferred from the data in Table 3 had the $H_o = 3$ kOe spectra not been so difficult to fit. These $H_o = 2$ kOe spectra are fairly easy to interpret compared to those obtained in a 3 kOe field. There is still some difficulty with determining the relaxation times though, due to the very fast background relaxation process.

The domain-wall relaxation time T_{10} is rather well defined since it is more than an order of magnitude shorter than the corresponding background relaxation time T_{B_1}. For the domain component, however, T_{20} and T_{B_2} are of comparable magnitudes and separating them is very difficult. The values given for T_{20} in Table 5 are much higher than those found at lower temperatures. How much of this is due to an increase in anisotropy (resulting in an increase in the Suhl-Nakamura relaxation time) and how much is due to the difficulty in fitting the spectrum, is uncertain.

The spectra in $H_o = 3.0$ kOe, shown in Figure 21, change noticeably with orientation and are quite difficult to fit. The parameters obtained are given in Table 6. The most noticeable difference between the spectra is the apparent upward shift in resonant frequency of both components for the <100> orientation. The value of T_{20} is anomalously long here, perhaps

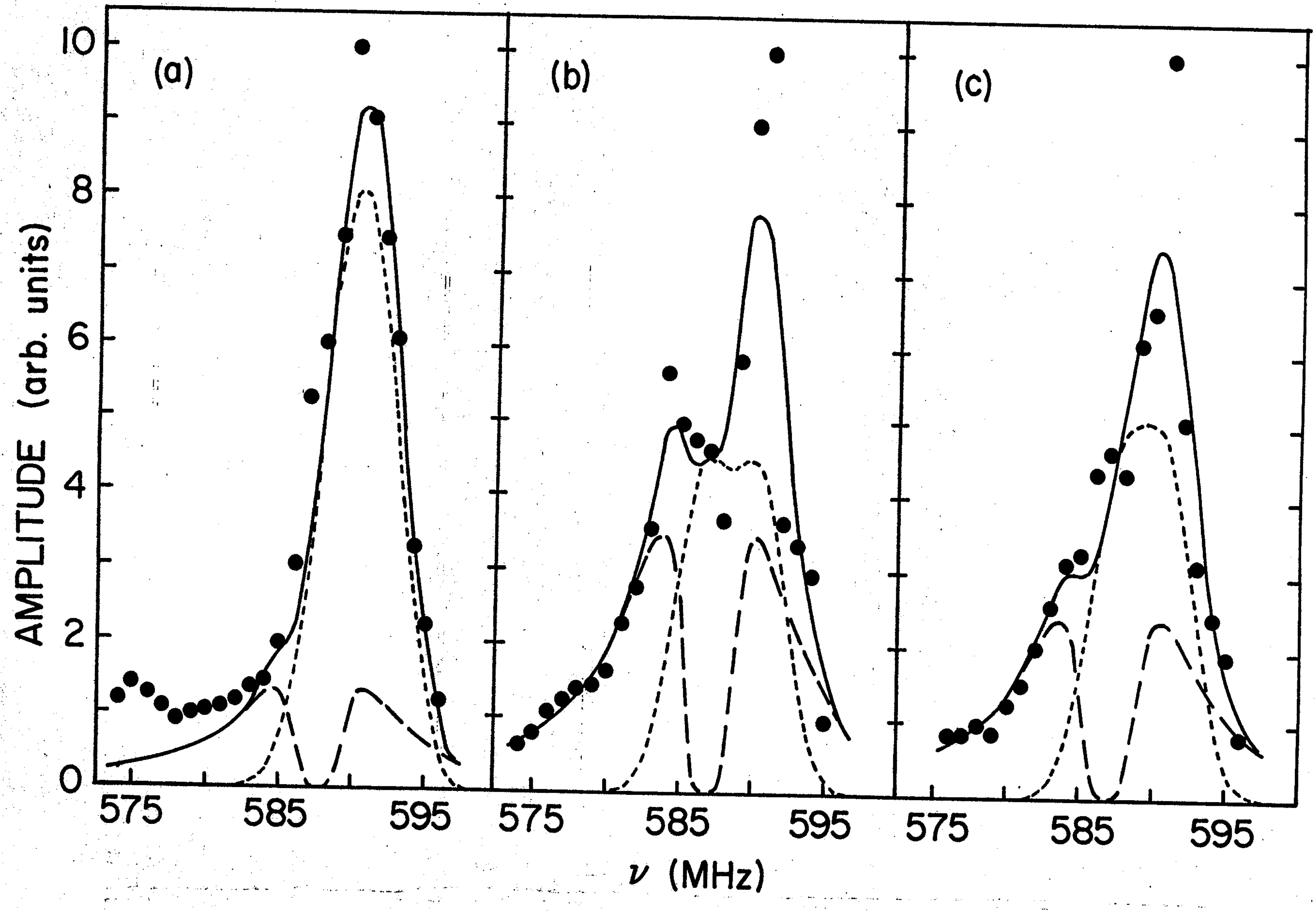

Figure 21. Spectra at T = 4.2 °K in H_o = 3.0 kOe with H_o along a) <100>, b) <110>, and c) <111> directions.

due to the fact that H_o and h_{rf} are parallel, making the domain component of the signal poorly defined for large H_o. The spectra at H_o = 2.0 kOe are fairly well behaved, however, and answer the questions previously raised concerning the spectra for temperatures above 2.10 ^oK. In particular, the resonance is still fairly well described by two overlapping components with the same linewidths (and lineshapes) as used for lower temperatures, and the frequency pulling for both components amounts to only about 1.5 MHz over this temperature range. The angular dependence of the spectra seems to be straightforward in that it doesn't show anything unexpected. The remaining difficulties, in particular the long values of T_{20}, are felt to be due to the difficulty in fitting the spectra because of the "shallow" background relaxation. To illustrate this particular problem somewhat more clearly, Figure 22 shows the total relaxation rates of the two components of the H_o = 2 kOe spectrum for the $\langle 100 \rangle$ orientation. When the relaxation time of one component is nearly independent of frequency it is very difficult to separate it from the background relaxation times, and as shown in the figure, there is little variation with frequency (compared to the case at T = 1.45 ^oK) in the domain component's relaxation time. When the relaxation times of the two components behave as in Figure 1-b for the spectrum at 1.45 ^oK, the signals are relatively easy to separate even though they strongly overlap. This problem prevents the accurate determination of the relaxation time parameters for the spectra at 4.2 ^oK. The only relaxation time which is still well defined is T_{10}, since it is so much shorter than all of the others. There still remains the possibility of separately determining the longitudinal relaxation times by using three pulse techniques.

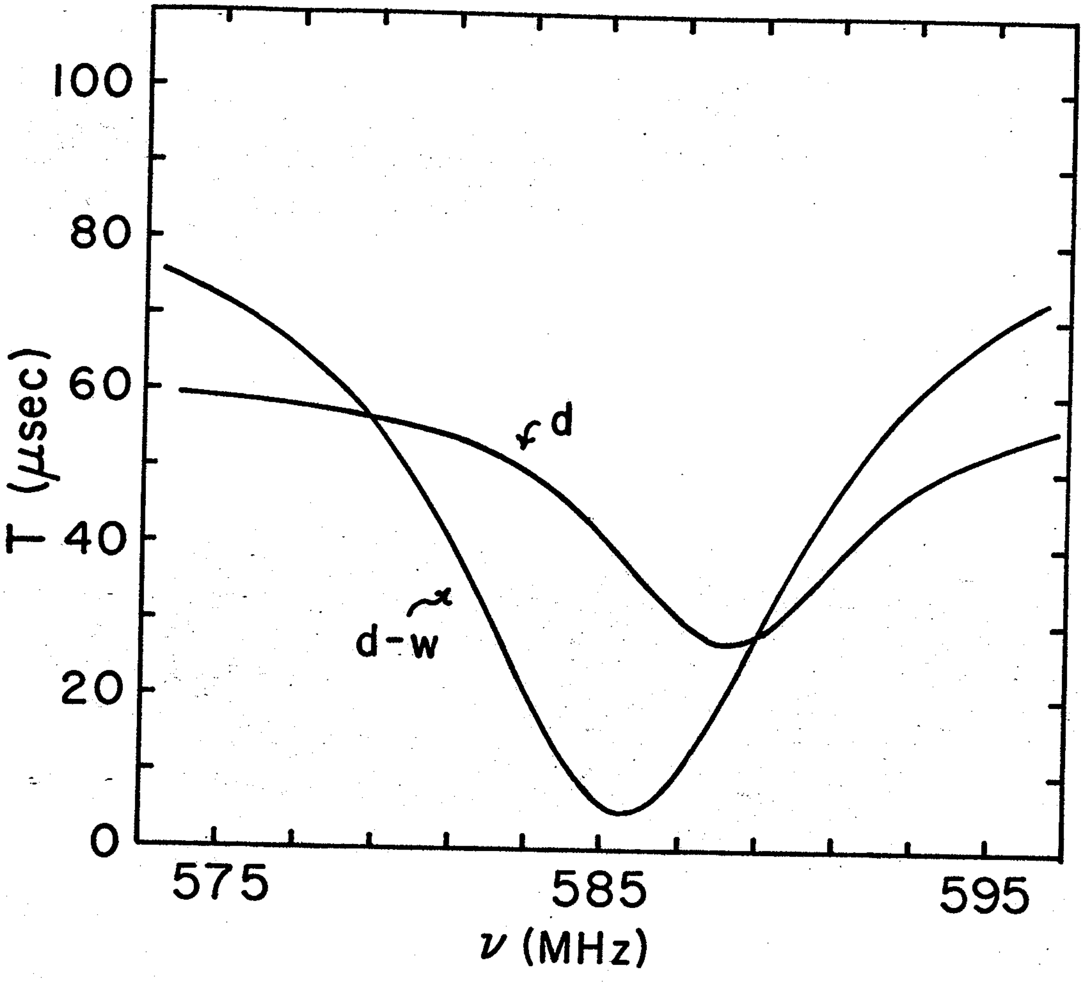

Figure 22. Total relaxation time of the two signal components versus frequency at T = 4.2 °K in H_o = 2.0 kOe.

5. Three-Pulse Experiments--The Stimulated Echo

As pointed out in Chapter I, Section 8.2, if a third rf pulse is applied following the usual pulse pair, a number of spin echoes occur, as shown in Figure I-5. The stimulated echo, occurring at $t = \tau_1 + \tau_2$ (where τ_1 and τ_2 are the separations between the first and second, and first and third pulses, respectively), provides a convenient measure of the longitudinal relaxation time. This technique is especially useful in cases where the line is severly inhomogeneously broadened[73] since in these instances the usual free induction decay techniques cannot be employed. In the presence of spectral diffusion the amplitude of the stimulated echo is given by[71-73]

$$A(\tau_1 + \tau_2) \propto \exp(-\tau_2/T_1) \exp\{-f(\tau_1)\tau_2\} \qquad (14)$$

where $f(\tau_1) = k_G \tau_1^2$ for a Gaussian process,

or $f(\tau_1) = k_L \tau_1$ for a Lorentzian diffusion process.

Thus, the decay of the stimulated echo as a function of τ_2 will always appear exponential, but the decay rate will depend on τ_1. A plot of the effective decay rate, for a given τ_1, versus τ_1 (for a Lorentzian process) or versus τ_1^2 (for a Gaussian process), should give a straight line whose intercept (on the $1/T_m$ axis) gives $1/T_1$ and whose slope gives k_L (or k_G), the diffusion decay constant.

Spectral diffusion decay of the two-pulse echo results in a decay envelope given by[72]

$$A(2\tau) = A_o \exp(-2\tau/T_2) \exp(-k_L \tau^2)$$

or

$$A(2\tau) = A_o \exp(-2\tau/T_2) \exp(-k_G' \tau^3) \qquad (15)$$

for Lorentzian or Gaussian diffusion. This diffusion term in the echo decay envelope has been neglected until now because the decay was always well described by a sum of two independent exponentials. When there are two independently relaxing components to the signal, the contribution due to diffusion is difficult to measure[73].

At high fields the domain-wall component is very small and the contribution due to spectral diffusion should be easy to see. Figure 23 shows the decay rate for the stimulated echo at $\nu = 592$ MHz and at $T = 1.33$ ^{o}K in $H_o = 8.0$ kOe ($H_o \| \langle 100 \rangle$ in (110), $h_{rf} \perp H_o$) plotted versus τ_1. The decay rate does change with τ_1 and seems to favor the Lorentzian diffusion process. The ordinate intercept gives $T_1 \approx 205$ μsec and the slope yields a decay constant $k_L \approx 1.6 \times 10^8$ $(\text{sec})^{-2}$. Thus, spectral diffusion appears to provide an important contribution to the decay of spin echoes in this material, and, in particular, its effects on the decay of the normal two-pulse echo should be included in the analysis of the data discussed earlier. The effect of spectral diffusion on the decay of the two-pulse echo, as given in Equation 15, should be easily visible if k_L is correctly determined by the data in Figure 23. However, this is not the case. The high field spectra at all temperatures and frequencies give echo decay envelopes which are very nearly exponential. Figure 24 illustrates what might be expected if the spectral diffusion is as strong as suggested. Here, an exponential decay of time constant $t_c = 35$ μsec is compared to the spectral diffusion decay envelope using k_L as determined above. The dashed straight line in the figure has a decay constant of 50 μsec, and when multiplied by the spectral decay envelope gives the dashed curve in the figure. This curve is concave downward over the time scale defined in the figure. All of the two-pulse echo decay curves were

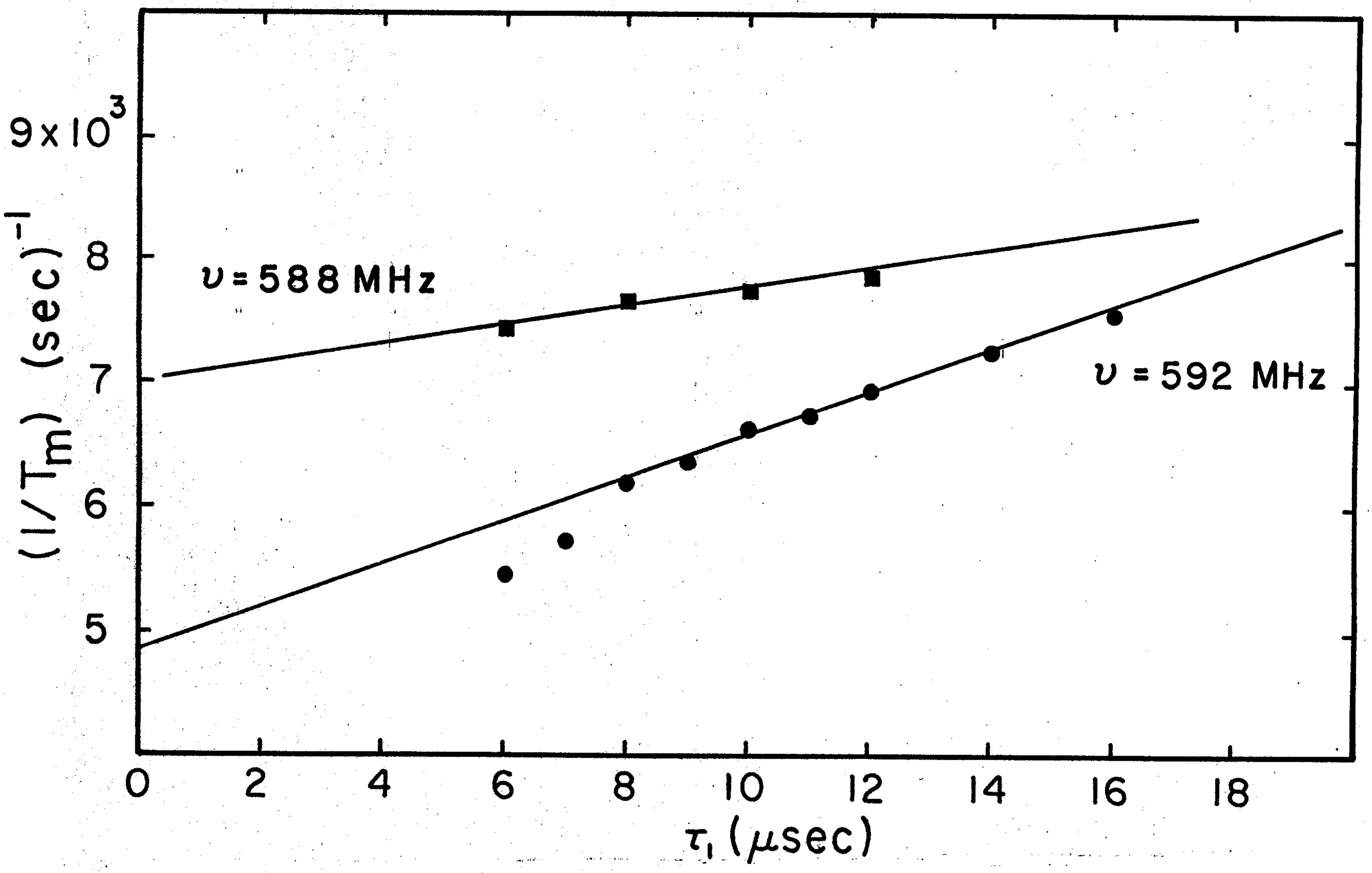

Figure 23. Stimulated echo decay rate versus τ_1 at T = 1.33 °K in H_o = 8.0 kOe ($H_o \| \langle 100 \rangle$), for ν = 588 MHz and ν = 592 MHz.

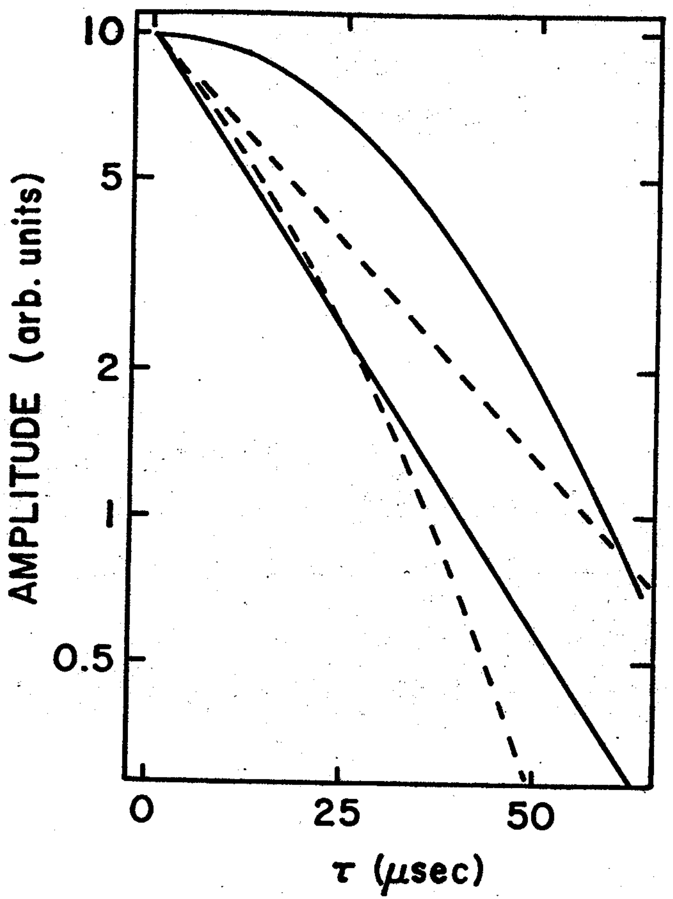

Figure 24. Effect of spectral diffusion on decay of two pulse echo. Upper solid curve is diffusion envelope using $k_L = 1.6 \times 10^8$ $(sec)^{-2}$. Lower dashed curve shows modification of exponential decay curve on including spectral diffusion.

either exponential (as at high fields) or concave upward (well described by the sum of two exponentials)(see, for example, the decay curves shown in Figure III-17). Thus, it seems that the contribution of spectral diffusion to the echo decay has been overestimated.

Figure 25 shows the response of the spin system to the three rf pulses at $t = 0, \tau_1, \tau_2$ used in a stimulated echo experiment. It is readily apparent that, because of the strong echoes and the refocusing effects due to the Suhl-Nakamura interaction (as discussed in Chapter II), this is not a simple three-pulse experiment. Each echo is an effective rf pulse acting on those spins not refocusing to form that particular echo. Thus, the stimulated echo in this case is not expected to behave in precisely the manner predicted by the vector model for a three-pulse experiment. Figure 26-a shows the stimulated echo's characteristic decay time T_s at $T = 4.2\ ^{o}K$ in $H_o = 8.0$ kOe, plotted vs frequency. The slight frequency dependence of this decay time at this temperature might be attributed to a slight admixture of domain-wall signal or to experimental error if not for the very strong frequency dependence shown in Figure 26-b at $T = 1.45\ ^{o}K$. The values of T_s at $4.2\ ^{o}K$ are in good agreement with the value of T_{B_2} obtained from the two pulse echo data and the value $T_{B_2} \simeq 240$ μsec at $1.45\ ^{o}K$ is in the center of the range of T_s shown in this figure.

For nuclei in domain walls the Raman spin-wave scattering process could produce a frequency dependent relaxation since the direction of the nuclear hyperfine field may make some small angle θ with respect to the direction of the ion's electronic moment and $(1/T_{Raman}) \propto \sin^2\theta$. For example, the angle θ may be non-zero because of super-transferred hyperfine field contributions due to neighboring ions, and this angle could

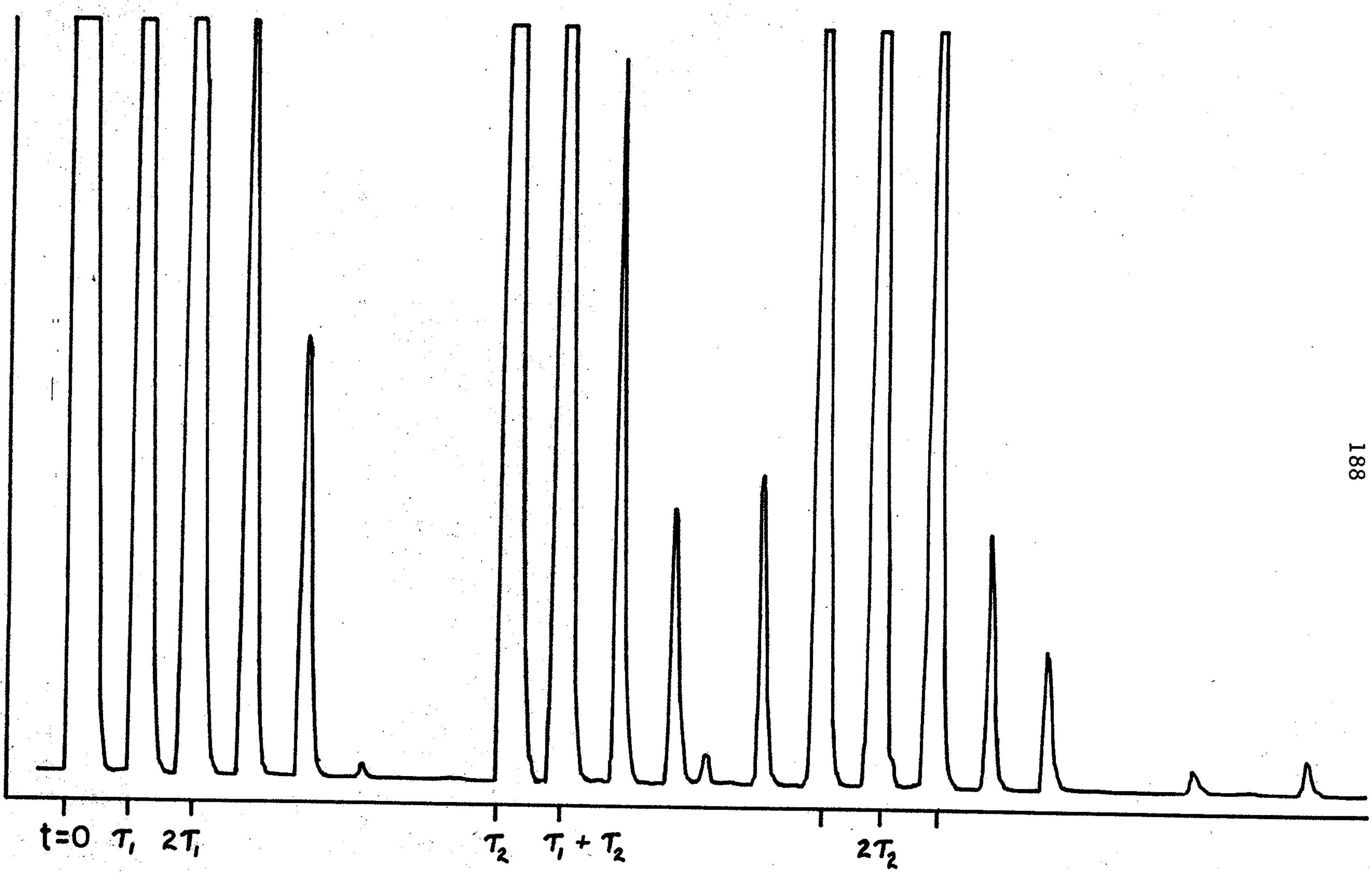

Figure 25. Response of the spin system to three rf pulses at t = 0, τ_1, and τ_2 .

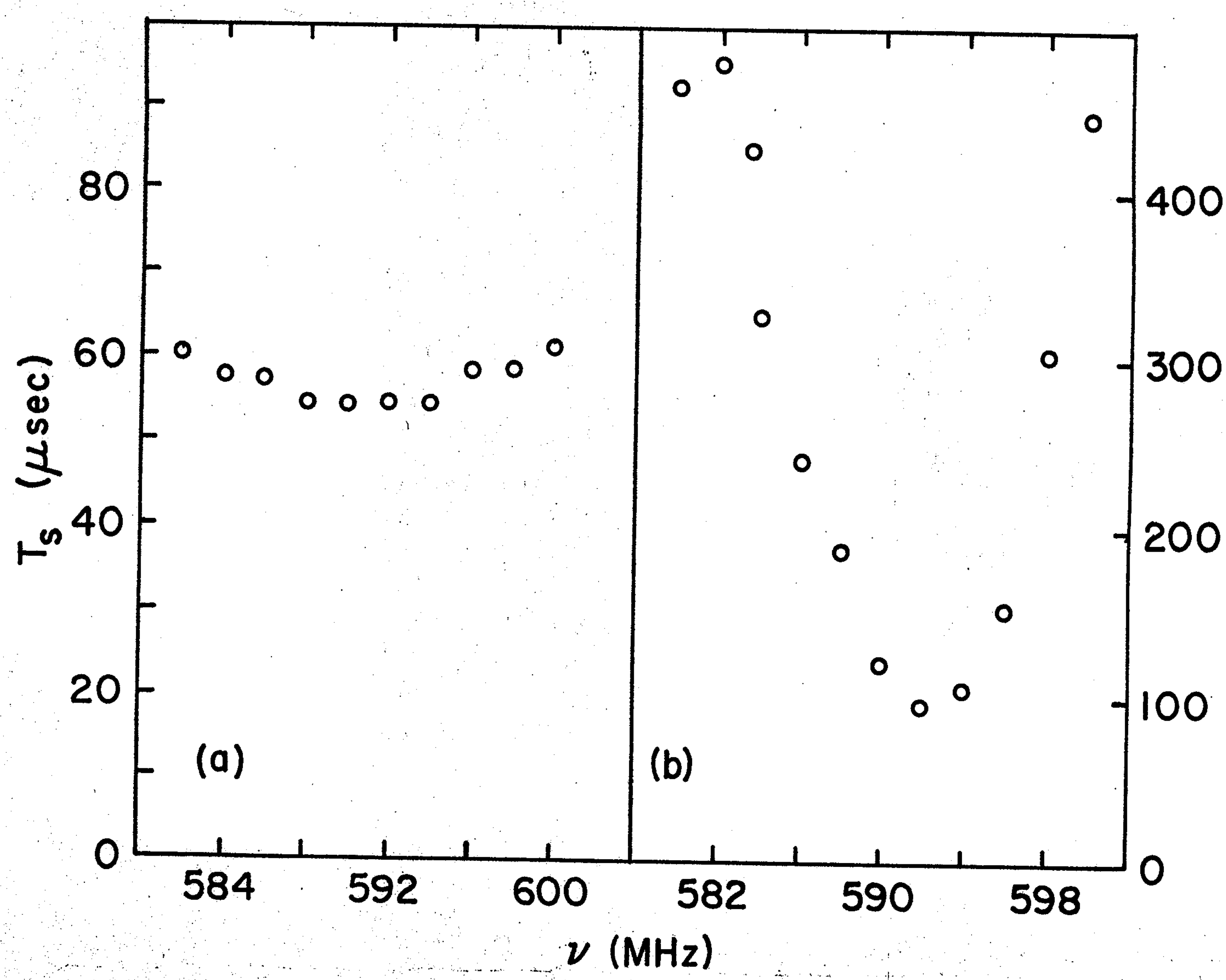

Figure 26. Stimulated echo decay time versus frequency in H_o = 8.0 kOe at a) T = 4.2 °K, and b) T = 1.45 °K.

change with position in the wall since the angle between neighboring electronic spins is a function of wall position. Thus, since the nuclear resonance frequency is also expected to change with position in the wall, whether due to frequency pulling effects by way of the variation in wall enhancement factor or to the variation in the magnitude of the hyperfine field by the same super-transferred hyperfine interaction, the relaxation time can vary with resonance frequency. Further since this relaxation rate is a maximum at the same place that the enhancement factor is a maximum, i.e., where the angle between neighboring spins is a maximum, the relaxation time would show a dip near the center of the domain-wall line.

For nuclei in bulk domains, however, no such variation can be expected since all A-site spins are parallel. Furthermore, at T = 1.45 ^{o}K, even for domain walls, the spin-wave scattering processes should be much weaker than required to explain this effect.

In the presence of appreciable spectral diffusion one might expect a frequency dependent decay of the stimulated echo simply because spins near the center of the resonance line have more spins close to each other in energy and the diffusion process may proceed more rapidly than for spins with resonance frequencies in the wings. For example at ν = 588 MHz, the diffusion constant given in Figure 23 is $k_L \simeq 0.8 \times 10^8$ (sec)$^{-2}$ compared to the value of $k_L \simeq 1.6 \times 10^8$ (sec)$^{-2}$ found at ν = 592 MHz. However, as mentioned earlier, there is considerable uncertainty in the significance of these numbers.

Other relaxation processes either due to spin-wave scattering or to longitudinal spin-spin interactions are not expected to show any frequency dependence (over this frequency range) unless, for some reason, the nuclei with resonance frequencies near the center of the line (which are the most numerous) have more near neighbor magnetic nuclei than do those with Larmor frequencies in the wings of the line (this is possible because there are four types of nuclei occupying the A- and B-sites: Mn nuclei in both Mn^{2+} and Mn^{3+} ions, and ^{57}Fe nuclei, which have nuclear magnetic moments, and the Fe nuclei which do not have moments, distributed on both sites). For a random distribution of nuclei no such frequency dependence is expected.

The difficulty in the interpretation of the stimulated echo experiments is very likely due to the presence during the interval between the second and third externally applied rf pulses, of numerous effective internal rf pulses due to the spin echoes themselves, resulting in the introduction of "T_2-like" decay into the stimulated echo, either by actual decay of part of the stimulated echo by T_2 processes during τ_2, or through changes in the directions of the spins due to the multiple refocusing pulses occurring during τ_2.

At lower fields where both signal components are present the problem becomes even more severe. Spectral diffusion is expected to be more important for domain-wall nuclei and the presence of overlapping signals will require a treatment of the stimulated echo decay in three independent variables τ_1 , τ_2 , and ν . Such a treatment is possible but would require a very large amount of data. Further work along these lines would be fruitful, however; in particular, measurements on the decay of the image echo (occurring at $t = 2(\tau_2 - \tau_1)$) while varying τ_2 and τ_1 in such a way that the difference $\tau_2 - \tau_1$ remains constant[72] may provide a more useful measure of spectral diffusion decay in the present case than that obtained from the stimulated echo.

CHAPTER V

Conclusion

The most interesting features of the A-site ^{55}Mn nuclear magnetic resonance are: the formation of multiple echoes and the strongly frequency dependent transverse relaxation, both well described by the very long ranged Suhl-Nakamura or indirect nuclear spin-spin interaction; and the comparison of the two simultaneously occurring signal components, due to nuclei within domain walls and nuclei within bulk domains, made possible by the non-linear optimization in two independent variables of the fit to the set of partially relaxed spectra (or equivalently the set of echo decay envelopes for the frequency range).

The foregoing analysis of the observed spectra points out many interesting features which are common to a large number of magnetic materials. The Suhl-Nakamura interaction produces the most striking effects (in the liquid helium temperature range), while the readily visible spin-wave scattering relaxation processes and the apparent hyperfine field fluctuations for domain-wall nuclei offer excellent opportunitees for further study. The coexistence of domain and domain-wall signals allows the direct comparison of spin-wave processes within domain walls with the processes in the bulk domains within the same material and under the same experimental conditions. The existence of a strongly frequency dependent transverse relaxation rate results in a significant simplification in the process of separating the two overlapping signals, thereby aiding the study of the separate components.

Several problems remain and further work is required to properly understand the nature of the hyperfine field fluctuations and the spin-wave relaxation processes. In particular, careful T_1 measurements for both signal components should be made over a wide temperature range. The various spin-wave processes will also exhibit characteristic field dependences which will help to identify conclusively the particular processes responsible for the temperature dependent part of the relaxation. The question of the apparent frequency dependent longitudinal relaxation seen in the decay of the stimulated echo—whether due to spectral diffusion, some unknown truly frequency dependent process, or to interference from T_2 processes—can probably be answered by a study of the stimulated echo spectra in conjunction with the two-pulse echo spectra using the same technique as applied here to the two-pulse echo; although the necessity of introducing at least one more relaxation time parameter into the fitting procedure will place a heavy burden on the experimental data which must already support two relaxation times per signal component. (The strong inhomogeneous broadening of the line and the resulting very rapid decay of the free induction signal, persisting only for times of the order of the receiver recovery time, seem to preclude the possibility of the measurement of T_1 by free induction decay measurements, e.g., by a π , $\pi/2$ pulse sequence.)

Manganese ferrites are particularly suitable samples for this type of study because of the relatively narrow inhomogeneous lines (thereby bypassing many experimental difficulties) and because the signal strengths of the two components are roughly comparable. Further, the magnetic properties of these crystals, e.g., anisotropy, exchange, and hyperfine fields are of such magnitudes as to make the various effects readily visible and easily measurable. The main drawback in these materials is the relative complexity of the spinel lattice which may require for an accurate description the inclusion of two (perhaps even three) exchange interactions and a more detailed discussion of spin-waves using a six-sublattice model[84].

A few points brought out in the discussion of the data deserve some final clarification. The resonance condition given by Equations I-54,55 gives the resonance frequency in terms of the anisotropy and hyperfine fields, or alternatively, in terms of the single-domain enhancement factor η'. The frequency pulling observed for the domain component of the signal suggests that the enhancement factor $\eta' \sim 100-300$, implying that the anisotropy field is roughly constant (within a factor of 2) and has a magnitude $H_K \sim 1-2$ kOe in this temperature region. The value of H_K obtained from ferromagnetic resonance measurements ($H_K \simeq 520$ Oe) is smaller than that given by the observed frequency pulling of the NMR lines. Thus it appears that the effective anisotropy field for nuclei may be quite different from that acting on the electrons, perhaps due to some small anisotropy in the hyperfine field. The domain-wall component's resonance frequency appears to follow Equations I-54,55 in the same manner as the domain component, with only a slight adjustment in anisotropy and hyperfine fields. Thus, while the enhancement factor of the signal is very large for the domain-wall component, the frequency pulling is quite small and the line is not distorted very much. However, Equations I-54,55 refer to anti-parallel sublattices (each of which is itself colinear) and cannot be accurately applied to the situation within a domain wall. It is apparent, however, that the situation within a wall will not be very different from the single domain case, at least in this instance where the angle between near magnetic neighbor spins is very small. Measurement of the spectra using shorter values of τ (pulse separation) than those used here would provide useful information on the domain wall structure and its changes with field (in the intermediate field region) and temperature.

Many other magnetic materials can be studied in this manner. Cobalt powders[85] exhibit many of the features observed in manganese ferrites, such as frequency dependent relaxation due to an indirect spin-spin interaction, existence of domain and domain-wall signals, and multiple echoes. The hexagonal phase of cobalt should exhibit a strong quadrupole interaction, introducing another interesting feature, as well as a further complication, into the resonance behaviour of this system. The ^{55}Mn resonance in the $La_{1-x}Pb_xMnO_3$ system[86] shows many of these same features, including quadrupole effects. The ^{153}Eu resonance in EuO is under investigation[60,87] by similar techniques again showing many of the same effects. The antiferromagnetic fluorides, such as MnF_2 which has been extensively studied, exhibit a strong Suhl-Nakamura interaction and the spin-wave relaxation processes in MnF_2 are well explained and provide an excellent verification of the theory[61,68,88].

Thus, the effects observed and reported here occur in a wide class of magnetic materials and a study of these effects using the techniques applied here to manganese ferrite can contribute to the understanding of the magnetic properties of these strongly coupled spin systems.

Appendix I: The Method of Moments

The nth moment of the distribution function $f(\omega)$ is defined as

$$M_n = \int (\omega - \omega_o)^n f(\omega)\, d\omega \qquad (1)$$

Thus, for the case of a Gaussian distribution function,

$$f(\omega) = \frac{1}{\Delta\sqrt{2\pi}} \exp\{-(\omega - \omega_o)^2/2\Delta^2\}$$

all of the moments may be easily evaluated, yielding

$$M_2 = \Delta^2 \quad , \quad M_4 = 3\Delta^4$$

$$M_{2n} = 1\cdot3\cdot5\cdots(2n - 1)\ \Delta^{2n}$$

and, since this function $f(\omega)$ is symmetric about ω_o, all odd moments vanish. The half-width at half-maximum δ, normally used as a measure of the width of a distribution, is given for the Gaussian case by

$$\delta = \Delta\sqrt{2\ln 2} \approx 1.178\ M_2^{\frac{1}{2}}$$

and the second moment gives a good measure of the width of the distribution.

For a Lorentzian distribution function

$$f(\omega) = \frac{\delta}{\pi} \frac{1}{\delta^2 + (\omega - \omega_o)^2}$$

all of the even moments diverge. Some very useful results can be obtained however, if one uses a cut-off Lorentzian and carries out the integration over the interval $|\omega - \omega_o| \lesssim \alpha$, with $\alpha >> \delta$. This gives

$$M_2 = \frac{2\alpha\delta}{\pi} \quad , \quad M_4 = \frac{2\alpha^3\delta}{2\pi} \quad , \quad \text{and} \quad M_4/(M_2)^2 = \frac{\pi\alpha}{6\delta} \qquad (2)$$

thus, since $\alpha >> \delta$, this ratio must be a large number if the distribution is to be described by a cut-off Lorentzian.

In a physical situation one can often calculate the first two even moments M_2 and M_4 by direct summation and obtain the ratio $M_4/(M_2)^2$ and from its value determine the nature of the distribution function (whether more nearly Gaussian or Lorentzian).

To find the connection between these moments of the distribution function $f(\omega)$ and the response of the nuclear spin system to an external rf field of frequency ω we consider the case of a field $H_1\cos\omega t$ applied along the x-axis. Then, the magnetization will be given by

$$M_x = H_1\left[\chi'(\omega)\cos\omega t + \chi''(\omega)\sin\omega t\right] \tag{3}$$

where $\chi'(\omega)$ and $\chi''(\omega)$ are the real and imaginary parts of the nuclear susceptibility.

Alternatively, using the density matrix formalism discussed in Chapter II, the magnetization is given by

$$M_x = \langle \mathcal{M}_x \rangle = \mathrm{tr}(\rho \mathcal{M}_x) \tag{4}$$

where the density matrix at equilibrium is

$$\rho_o = \exp(-\mathcal{H}_o/kT)/\mathrm{tr}\{\exp(-\mathcal{H}_o/kT)\}$$

Then, in the presence of the rf field $H_1\cos\omega t$

$$(\hbar/i)(d\rho/dt) = \left[\rho, \mathcal{H}_o - V\mathcal{M}_x H_1\cos\omega t\right] \tag{5}$$

where V is the sample volume. Transforming to the interaction representation by $\rho^* = \exp(i\mathcal{H}_o t/\hbar)\ \rho\ \exp(-i\mathcal{H}_o t/\hbar)$, the equation of motion becomes

$$(\hbar/i)(d\rho^*/dt) = -VH_1\left[\rho^*, \exp(i\mathcal{H}_o t/\hbar)\mathcal{M}_x\exp(-i\mathcal{H}_o t/\hbar)\right]\cos\omega t \tag{6}$$

Then, assuming $\rho(-\infty) = \rho_o = \rho^*(-\infty)$ the solution at time t, to first order, is

$$\rho^*(t) = \rho^*(-\infty) - (iH_1V/\hbar)\int_{-\infty}^{t}\left[\rho^*(-\infty), \exp(i\mathcal{H}_o t'/\hbar)\mathcal{M}_x\exp(-i\mathcal{H}_o t'/\hbar)\right] \times \cos\omega t'\, dt' \tag{7}$$

or, transforming back to $\rho(t)$,

$$\rho(t) = \rho_o - (iH_1V/\hbar)\int_{0}^{\infty}\left[\rho_o, \exp(-i\mathcal{H}_o t''/\hbar)\mathcal{M}_x\exp(i\mathcal{H}_o t''/\hbar)\right]\cos\omega(t - t'')dt'' \tag{8}$$

Then, assuming $M_x(-\infty) = \mathrm{tr}(\rho_o\mathcal{M}_x) = 0$,

$$\begin{aligned}
<\mathcal{M}_x(t)> &= \mathrm{tr}(\rho\,\mathcal{M}_x) = M_x \\
&= -(iH_1V/\hbar)\sin\omega t\ \mathrm{tr}\left\{\int_0^{\infty}\left[\rho_o, \exp(-i\mathcal{H}_o t'/\hbar)\mathcal{M}_x\exp(i\mathcal{H}_o t'/\hbar)\right] \times \mathcal{M}_x\sin\omega t'\, dt'\right\} \\
&\quad - (iH_1V/\hbar)\cos\omega t\ \mathrm{tr}\left\{\int_0^{\infty}\left[\rho_o, \exp(-i\mathcal{H}_o t'/\hbar)\mathcal{M}_x\exp(i\mathcal{H}_o t'/\hbar)\right] \times \mathcal{M}_x\cos\omega t'\, dt'\right\}
\end{aligned} \tag{9}$$

and, on comparing with the expression in Equation 3, the real and imaginary parts of the nuclear susceptibility are, in the high temperature approximation where $\rho_o \sim (\mathcal{H}/kT)/\mathrm{tr}\{1\}$,

$$\chi''(\omega) = (i/kT)(V/\mathrm{tr}\{1\})\int_0^{\infty}\sin\omega t'\ \mathrm{tr}\left\{\left[\mathcal{H}_o, \exp(-i\mathcal{H}_o t'/\hbar)\mathcal{M}_x\exp(i\mathcal{H}_o t/\hbar)\right] \times \mathcal{M}_x\right\}dt' \tag{10}$$

$$\chi'(\omega) = (i/kT)(V/tr\{1\})\int_0^\infty \cos\omega t'\ tr\{[\mathcal{H}_o, \exp(-i\mathcal{H}_o t'/\hbar)\mathcal{M}_x \exp(i\mathcal{H}_o t'/\hbar)] \times \mathcal{M}_x\}dt'$$

Then, introducing the eigenstates of the Hamiltonian $\mathcal{H}_o$ by $\mathcal{H}_o|n> = E_n|n>$, the trace may be written as

$$\sum_n <n|\ \exp(-i\mathcal{H}_o t'/\hbar)\ [\mathcal{H}_o, \mathcal{M}_x]\exp(i\mathcal{H}_o t'/\hbar)\ \mathcal{M}_x|n>$$

and, the expression for $\chi''(\omega)$ becomes

$$\chi''(\omega) = (i/kT)(V/tr\{1\})\int_0^\infty \sin\omega t'\ \sum_{n,n'} \exp\{-i(E_n - E_{n'})t'/\hbar\}\ (E_n - E_{n'}) \times |<n'|\mathcal{M}_x|n>|^2\ dt' \qquad (11)$$

Then, after integrating by parts,

$$\chi''(\omega) = (\omega V/kT)(1/tr\{1\})\int_0^\infty \cos\omega t'\ \sum_{n,n'} |<n'|\mathcal{M}_x|n>|^2\ \exp\{-i(E_n - E_{n'})t'/\hbar\}dt' \qquad (12)$$

Defining $\mathcal{M}_x(t) = \exp(i\mathcal{H}_o t/\hbar)\mathcal{M}_x \exp(-i\mathcal{H}_o t/\hbar)$ this expression may be written in the form

$$\chi''(\omega) = (\omega V/kT)(1/tr\{1\})\int_0^\infty \cos\omega t'\ tr\{\mathcal{M}_x(t')\mathcal{M}_x\}\ dt' \qquad (13)$$

and the correlation or relaxation function of the magnetization may be defined as

$$G(t') = tr\{\mathcal{M}_x(t')\mathcal{M}_x\} \qquad (14)$$

Thus, since the imaginary part of the nuclear susceptibility, $\chi''(\omega)$, describes the absorbtion of energy from the perturbing field $H_1\cos\omega t$, the nuclear magnetic resonance lineshape function $f(\omega)$ can be written as

$$f(\omega) = A\int_0^\infty G(t)\cos\omega t\ dt \qquad (15)$$

where A is a normalization constant and the line is assumed narrow ($\delta << \omega_o$) so that $\chi''(\omega)/\omega$ describes $f(\omega)$ as well as does $\chi''(\omega)$.

If the unperturbed Hamiltonian can be written as $\mathcal{H}_o = \mathcal{H}_z + \mathcal{H}'$, where $\mathcal{H}_z$ is the Zeeman Hamiltonian, with $[\mathcal{H}_z, \mathcal{H}'] = 0$, then

$$\exp\{i(\mathcal{H}_z + \mathcal{H}')t/\hbar\} = \exp(i\mathcal{H}_z t/\hbar)\exp(i\mathcal{H}' t/\hbar)$$

and

$$\begin{aligned} G(t) &= \mathrm{tr}\{\exp(i\mathcal{H}'t/\hbar)\mathcal{M}_x\exp(-i\mathcal{H}'t/\hbar)\exp(-i\omega_o I_z t)\mathcal{M}_x\exp(i\omega_o I_z t)\} \\ &= \cos\omega_o t \ \mathrm{tr}\{\exp(i\mathcal{H}'t/\hbar)\mathcal{M}_x\exp(-i\mathcal{H}'t/\hbar)\} \qquad (16) \\ &= G_1(t)\cos\omega_o t \end{aligned}$$

where $G_1(t)$ is defined to be the reduced autocorrelation function of $\mathcal{M}_x$. Then, taking the inverse transform of Equation 15,

$$G_1(t)\cos\omega_o t = \frac{2}{\pi A}\int_{-\omega_o}^{\infty} f(\omega_o + u)\cos(\omega_o + u)\,du \quad , \quad \omega = \omega_o + u$$

then, assuming the line is narrow (allowing the extension of the lower limit of the integral to $-\infty$) and symmetric about ω_o, with $h(u) = f(\omega_o + u)$

$$G_1(t) = \frac{2}{\pi A}\int_{-\infty}^{\infty} h(u)\cos(ut)\,du \qquad (17)$$

Then, since $M_n = \int h(u)\,u^n\,du$ and $\cos(ut) = \sum_{k=0}^{\infty}(-1)^k\frac{(ut)^{2k}}{(2k)!}$, the reduced autocorrelation function can be expressed in terms of the moments of the distribution function

$$G_1(t) = \frac{2}{\pi A}\{M_o - \frac{t^2}{2!}M_2 + \frac{t^4}{4!}M_4 - \ +\cdots\} \qquad (18)$$

and, expanding $G_1(t)$ in a Taylor series, expressions for the moments in terms of the derivatives of $G_1(t)$ are obtained

$$M_2 = -(\pi A/2)(d^2G_1(t)/dt^2)_{t=0} \quad , \quad M_4 = (\pi A/2)(d^4G_1(t)/dt^4)_{t=0}$$

$$M_{2n} = (-1)^n(\pi A/2)(d^{2n}G_1(t)/dt^{2n})_{t=0} \tag{19}$$

$$G_1(0) = 2/\pi A$$

Then, expanding $\mathcal{M}'_x(t) = \exp(i\mathcal{H}'t/\hbar)\mathcal{M}_x\exp(-i\mathcal{H}'t/\hbar)$

$$\mathcal{M}'_x(t) = \mathcal{M}_x + \mathcal{M}'^{(1)}_x(t) + \mathcal{M}'^{(2)}_x(t) + \cdots$$

with

$$\mathcal{M}'^{(n)}_x(t) = i\int_0^t [\mathcal{H}', \mathcal{M}'^{(n-1)}_x(t')]\,dt' \tag{20}$$

and, since,

$$\exp(i\mathcal{H}'t/\hbar)\mathcal{M}_x\exp(-i\mathcal{H}'t/\hbar) = \sum_j (i\mathcal{H}'t/\hbar)^j/j!\ \mathcal{M}_x \sum_k (-i\mathcal{H}'t/\hbar)^k/k!$$

$$= \sum_{j,k} (-1)^k(it)^{j+k}(\mathcal{H}'^j\mathcal{M}_x\mathcal{H}'^k/j!k!)/(h)^{j+k} \tag{21}$$

we obtain the expression

$$(d^pG_1(t)/dt^p)_{t=0} = (i)^p\ \mathrm{tr}\{\ \overset{1}{[}\mathcal{H}',\ \overset{2}{[}\mathcal{H}', \overset{\cdots\cdot}{\cdots}\ \overset{p}{[}\mathcal{H}', \mathcal{M}_x]\cdots]]\mathcal{M}_x\}$$

Thus, the first two even moments can be written

$$M_2 = -\ \mathrm{tr}\{[\mathcal{H}', I_x]^2\}\ /\mathrm{tr}\{I_x^2\} \tag{22}$$

and

$$M_4 = \mathrm{tr}\{[\mathcal{H}', [\mathcal{H}', I_x]\ ]^2\}/\ \mathrm{tr}\{I_x^2\} \tag{23}$$

since $I_x \propto \mathcal{M}_x$ and $G_1(0) = \mathrm{tr}\{\mathcal{M}_x^2\}$.

The evaluation of the trace in the denominators is quite straightforward if one introduces the functions $|m_1m_2m_3\cdots m_N\rangle = |m_1\rangle|m_2\rangle\cdots|m_N\rangle$ formed as products of the individual spin functions $|m_k\rangle$. Then,

$$\mathrm{tr}\{I_x^2\} = \sum_{m_1,m_2,\cdots m_N} \langle m_1,m_2,\cdots m_N|I_x^2|m_1,m_2,\cdots m_N\rangle$$

and, using $I_x = \Sigma_j I_{x_j}$ to obtain $I_x^2 = \Sigma_{j,k} I_{x_j} I_{x_k}$, we have, for $j \neq k$, terms of the form

$$\sum_{m_1,m_2,\cdots m_j\cdots m_k\cdots m_N} \langle m_1\cdots m_j\cdots m_k\cdots m_N|I_{x_j} I_{x_k}|m_1\cdots m_j\cdots m_k\cdots m_N\rangle$$

$$= \sum_{m_1\cdots m_j\cdots m_k\cdots m_N} \langle m_j|I_{x_j}|m_j\rangle\langle m_k|I_{x_k}|m_k\rangle = 0$$

since $\Sigma_{m_j} \langle m_j|I_{x_j}|m_j\rangle = 0$, etc. The terms for $j = k$ do not vanish, however, and give terms like

$$\sum_{m_1\cdots m_j\cdots m_N} \langle m_1\cdots m_j\cdots m_N|I_{x_j}^2|m_1\cdots m_j\cdots m_N\rangle$$

$$= (2I+1)^{N-1} \sum_{m_j} \langle m_j|I_{x_j}^2|m_j\rangle \tag{24}$$

since each summation for m_k, $k \neq j$, gives $(2I + 1) \times \Sigma_{m_j} \langle m_j|I_{x_j}^2|m_j\rangle$. Finally, then,

$$\sum_{m_j} \langle m_j|I_{x_j}^2|m_j\rangle = \frac{1}{3} \sum_{m_j} \langle m_j|I_j^2|m_j\rangle = \frac{1}{3} I(I+1)(2I+1)$$

and,

$$\mathrm{tr}\{I_x^2\} = \frac{1}{3} I(I+1)(2I+1)^N N \tag{25}$$

since there are N choices for $j = k$.

The traces in the numerators of Equations 22 and 23 depend on the particular form of the Hamiltonian $\mathcal{H}'$ and can be quite difficult to evaluate. Those for the dipole-dipole Hamiltonian have been evaluated for the cubic lattices. These will be discussed in Chapter III.

References

1. J. H. Hastings and L. M. Corliss, Phys. Rev. 104, 328 (1961)
2. U. König and G. Chol, J. Appl. Cryst. 1, 124 (1968)
3. A. H. Morrish and P. E. Clark, Phys. Rev. B 11, 278 (1975)
4. T. Kubo, A. Hirai, and H. Abe, J. Phys. Soc. Japan 26, 1094 (1969)
5. F. Keffer, "Spin Waves", Handbuch der Physik, vol. 18-2, S. Flügge, ed., Springer-Verlag, Berlin (1966)
6. see e.g., A. J. Freeman and R. E. Watson, "Hyperfine Interactions in Magnetic Materials", Magnetism, vol. 2-a, G. Rado and H. Suhl, eds., Academic Press, New York (1965)
7. see e.g., S. Geschwind, "Special Topics in EPR", Hyperfine Interactions, A. J. Freeman and R. B. Frankel, eds., Academic Press, New York (1967)
8. A. J. Heeger and T. W. Houston, Phys. Rev. 135, A661 (1964)
9. L. Neel, Ann. Phys. (Paris) 3, 137 (1948)
10. P. Anderson, "Exchange in Insulators", Magnetism, vol. 1, G. Rado and H. Suhl, eds., Academic Press, New York (1963)
11. see e.g., J. B. Goodenough, Magnetism and the Chemical Bond, John Wiley and Sons, New York (1963)
12. J. Smit and H. Wijn, Ferrites, John Wiley and Sons, New York (1959)
13. P. Weiss, J. Phys. Radium 4, 661 (1907)
14. J. S. Smart, Effective Field Theories of Magnetism, W. B. Saunders Co., Philadelphia (1966).
15. F. Bloch, Z. Physik 61, 206 (1930)
16. L. R. Walker, "Spin Waves and Other Magnetic Modes", Magnetism, vol. 1, G. Rado and H. Suhl, eds., Academic Press, New York (1963)
17. for a general discussion see A. R. Edmunds, Angular Momentum in Quantum Mechanics, Princeton Univ. Press, Princeton, N. J., (1960)

18. T. Holstein and H. Primakoff, Phys. Rev. 58, 1098 (1940)

19. for a more complete discussion of this expansion see, T. Oguchi, Phys. Rev. 117, 117 (1960)

20. M. Sparks, Ferromagnetic Relaxation Theory, McGraw-Hill, New York, (1964)

21. see e.g., S. Chikazumi, Physics of Magnetism, John Wiley and Sons, New York, (1964)

22. J. H. Davis, unpublished data

23. J. F. Dillon, S. Geschwind, and V. Jaccarino, Phys. Rev. 100, 750 (1955)

24. J. H. Van Vleck, Phys. Rev. 52, 1178 (1937)

25. K. Yosida and M. Tachiki, Prog. Theor. Phys. 17, 331 (1957)

26. P. Novak, Czech. J. Phys. B 16, 723 (1966)

27. for an extensive discussion of domain walls see C. Kittel and J. K. Galt, "Ferromagnetic Domain Theory", Solid State Physics, vol. 3, F. Seitz and D. Turnbull, eds., Academic Press Inc., New York, (1956)

28. Gossard, Portis, Rubenstein, and Lindquist, Phys. Rev. 138, A1415 (1965)

29. A. Hirai, J. Eaton, and C. Searle, Phys. Rev. B 3, 68 (1971)

30. J. H. Davis and C. W. Searle, Phys. Rev. B 9, 323 (1974)

31. de Gennes, Pincus, Hartmann-Boutron, and Winter, Phys. Rev. 129, 1105 (1963)

32. E. L. Hahn, Phys. Rev. 80, 580 (1950)

33. H. Y. Carr and E. M. Purcell, Phys. Rev. 94, 630 (1954)

34. S. Meiboom and D. Gill, Rev. Sci. Instrum. 29, 688 (1958)

35. I. J. Lowe and R. E. Norberg, Phys. Rev. 107, 46 (1957)

36. W. B. Mims, Phys. Rev. 141, 499 (1966)

37. E. L. Hahn and D. E. Maxwell, Phys. Rev. 88, 1070 (1952)

38. N. Bloembergen and T. J. Rowland, Phys. Rev. 97, 1679 (1955)

39. M. A. Ruderman and C. Kittel, Phys. Rev. 96, 99 (1954)

40. H. Suhl, Phys Rev. 109, 606 (1958); J. Phys. Radium 20, 333 (1959)

41. T. Nakamura, Prog. Theor. Physics 20, 547 (1958)

42. see e.g., C. P. Slichter, Principles of Magnetic Resonance, Harper and Row, New York (1963), chapter 4.

43. see e.g., A. Abragam, Principles of Nuclear Magnetism, Oxford Univ. Press, London (1961), chapter 2.

44. H. Abe, H. Yasuoka, and A. Hirai, J. Phys. Soc. Japan 21, 77 (1966)

45. see e.g., R. Bracewell, The Fourier Transform and its Applications, McGraw-Hill, New York (1965)

46. A. Narath, "Nuclear Magnetic Resonance", Hyperfine Interactions, A. J. Freeman and R. B. Frankel, eds., Academic Press, New York (1967)

47. I. Solomon, Phys. Rev. 110, 61 (1958)

48. L. G. Rowan, Phys. Rev. 110, 61 (1958)

49. see reference 43, chapter 7.

50. Searle, Davis, Hirai, and Fukuda, Phys. Rev. Lett. 27, 1380 (1971)

51. J. H. Davis and C. W. Searle, Phys. Rev. B 9, 323 (1974)

52. for a general discussion see, A. M. Stoneham, Revs. Mod. Phys. 41, 82 (1969)

53. J. H. Van Vleck, Phys. Rev. 74, 1168 (1948)

54. see reference 43, chapter 4.

55. see reference 42, chapter 3.

56. E. T. Cheng and J. D. Memory, Phys. Rev. B 6, 1714 (1972)

57. W. F. Wurzbach and S. Gade, Phys. Rev. B 6, 1724 (1972)

58. see reference 43, chapter 4.

59. see reference 42, chapter 3.

60. Barak, Siegelstein, Gabai, and Kaplan, Phys. Rev. B 8, 5282 (1973)

61. Hone, Jaccarino, Ngwe, and Pincus, Phys. Rev. 186, 291 (1969)

62. L. B. Vatova, Fiz. Tverd. Tela 7, 2133 (1965): English translation; Soviet Phys.--Solid State 7, 1717 (1966)

63. G. W. Canters and C. S. Johnson, Jr., J. Mag. Res. 6, 1 (1972)

64. D. Beeman and P. Pincus, Phys. Rev. 166, 359 (1968)

65. P. Pincus, Phys. Rev. Lett. 16, 398 (1966)

66. T. Oguchi and F. Keffer, J. Phys. Chem. Solids 25, 405 (1964)

67. A. Narath and A. T. Fromhold, Phys. Rev. Lett. 17, 354 (1966)

68. F. Freyne, Phys. Rev. B 9, 4824 (1974)

69. see reference 5, pages 199-200.

70. crystal supplied by R. Poplowsky, University of Toledo, Toledo, Ohio

71. J. R. Klauder and P. W. Anderson, Phys. Rev. 125, 912 (1962)

72. S. K. Ghosh, Phys. Rev. B 5, 174 (1972)

73. W. R. Mims, K. Nassau, and J. D. McGee, Phys. Rev. 123, 2059 (1961)

74. J. H. Davis and C. W. Searle, submitted to Phys. Rev. B

75. $MnFe_2O_4$ crystal supplied by A. Hirai, Kyoto University, Kyoto, Japan

76. J. M. Winter, Phys. Rev. 124, 452 (1961)

77. G. W. Westley and J. A. Watts, eds., The Computing Technology Center Analysis Library, report number CTC-39, Union Carbide Corporation, Nuclear Division, Computing Technology Center, Scientific Applications Department, Oak Ridge, Tennessee (1970), page 356

78. D. Marquardt, J. SIAM 11, 431 (1963)

79. for other points of view see: M. A. Butler, et al., Phys. Rev. B 5, 990 (1972); A. C. Gossard, et al., J. Appl. Phys. 73 Suppl., 1187 (1962); or reference 76 cited above.

80. W. Palmer, J. Appl. Phys. 33 Suppl., 1201 (1962)

81. see e.g., P. W. Anderson, J. Phys. Soc. Japan 9, 316 (1954); or reference 43, chapters 8 and 10.

82. R. E. Walstedt, Phys. Rev. B 5, 41 (1972)

83. see e.g., reference 42, chapter 5; and reference 43, chapters 8 and 10

84. T. Kaplan, Phys. Rev. 109, 782 (1958)

85. J. Barak and N. Kaplan, Phys. Rev. Lett. 23, 925 (1969)

86. L. K. Leung, PhD thesis, Univ. of Manitoba, Winnipeg, Manitoba, Canada, unpublished.

87. J. Barak, A. Gabai, and N. Kaplan, Phys. Rev. B 9, 4914 (1974); J. Barak, Il Siegelstein, A. Gabai, and N. Kaplan, Phys. Rev. Lett. 27, 817 (1971)

88. D. Paquette, A. R. King, and V. Jaccarino, Phys. Rev. B 11, 1193 (1975)